

J. Sebastian Escobar Niño

## **On the soil – structure interaction induced by shallow tunnelling in urban area**



Numerical modelling predictions for the Metro-Line 2 of Torino, Italy

Master's degree in civil engineering – geotechnics

---



**Politecnico di Torino**

**Master's degree in civil engineering – geotechnics**

Politecnico di Torino

---

NOVEMBER 2024



**On the soil – structure interaction induced by  
shallow tunnelling in urban area**

Numerical modelling predictions for the Metro-Line 2 of Torino, Italy

.....  
J. Sebastian Escobar Niño  
Author

.....  
Prof. M. Rita Migliazza  
Supervisors

.....  
Prof. Renato M. Cosentini

.....  
Prof. Valerio De Biagi

.....  
Prof. Sebastiano Foti  
Head of Department

*Soil mechanics has arrived at the  
borderline between science and art.*  
- Karl von Terzaghi, 1957

## **Acknowledgments**

I thank from the bottom of my heart unconditionally everyone who has supported me from my birth up until this point. Even you, dear reader.

Thank you.

## Contents

<b>ACKNOWLEDGMENTS .....</b>	<b>II</b>
<b>CONTENTS.....</b>	<b>III</b>
<b>LIST OF FIGURES .....</b>	<b>VII</b>
<b>LIST OF TABLES.....</b>	<b>XVII</b>
<b>CHAPTER 1</b>	
<b>INTRODUCTION.....</b>	<b>1</b>
<b>CHAPTER 2</b>	
<b>SHALLOW TUNNELING IN URBAN AREA .....</b>	<b>2</b>
2.1 TUNNELS FOR CITIES .....	2
2.2 THE TUNNELLING PROCESS.....	3
2.3 BASIN OF SUBSIDENCE .....	6
2.3.1 <i>Empirical methods</i> .....	14
2.3.2 <i>Analytical methods</i> .....	17
2.3.3 <i>Numerical methods</i> .....	19
2.4 BUILDING RISK OF DAMAGE ESTIMATION .....	19
2.4.1 <i>The EBA method</i> .....	22
2.4.2 <i>Procedure for the risk of damage estimation</i> .....	25
<b>CHAPTER 3</b>	
<b>NUMERICAL METHODS FOR THE SUBSIDENCE AND BUILDING RISK OF DAMAGE ASSESSMENT.....</b>	<b>26</b>
3.1 THE MODEL OF THE TUNNEL EXCAVATION.....	26
3.1.1 <i>Geometrical model and discretization</i> .....	27
3.1.2 <i>Boundary conditions</i> .....	31
3.1.3 <i>Material properties</i> .....	33
3.1.4 <i>Single-step procedure for the tunnel excavation</i> .....	43
3.1.5 <i>Step-by-step procedure for the tunnel excavation</i> .....	43
3.2 THE MODEL OF THE BUILDING .....	57
3.2.1 <i>Geometrical model, discretization and boundary conditions</i> .....	57

3.2.2 <i>Material properties</i> .....	60
--	----

## CHAPTER 4

### THE METRO-LINE 2 OF TORINO PROJECT..... 67

4.1 GENERAL INFORMATION .....	67
4.1.1 <i>Requirements for the mechanized excavation</i> .....	70
4.2 THE SOIL OF TORINO .....	71
4.2.1 <i>Geology</i> .....	71
4.2.2 <i>Hydrology</i> .....	74
4.2.3 <i>Geotechnical investigations</i> .....	75
4.2.4 <i>Geomechanical characteristics</i> .....	77
4.3 PREDICTION OF THE BASIN OF SUBSIDENCE AND BUILDING DAMAGE RISK .....	80
4.3.1 <i>Palazzo Campana</i> .....	80
4.3.2 <i>Damage risk assessment</i> .....	83
4.3.3 <i>Soil improvement, jet grouting or permeation grouting umbrella</i> .....	85
4.3.4 <i>A 2D numerical approach for the subsidence and building risk of damage prediction</i> .....	86

## CHAPTER 5

### A 3D NUMERICAL MODEL FOR THE SUBSIDENCE AND BUILDING RISK OF DAMAGE PREDICTION IN THE METRO-LINE 2 OF TORINO PROJECT..... 89

5.1 GREENFIELD MODELS .....	89
5.1.1 <i>Geometrical model and discretization</i> .....	89
5.1.2 <i>Boundary conditions</i> .....	94
5.1.3 <i>Material properties</i> .....	96
5.1.4 <i>Initial state of stress and geostatic step</i> .....	101
5.1.5 <i>Stages</i> .....	102
5.1.6 <i>Parametrical analyses</i> .....	105
5.2 UNCOUPLED BUILDING MODELS .....	108
5.2.1 <i>Geometrical model and discretization</i> .....	108
5.2.2 <i>Boundary conditions</i> .....	115
5.2.3 <i>Material properties</i> .....	119
5.2.4 <i>Stages</i> .....	122
5.2.5 <i>Parametric analyses</i> .....	122
5.3 COUPLED MODELS: SOIL – STRUCTURE INTERACTION .....	123

5.3.1 Geometrical model, discretization .....	123
5.3.2 Boundary conditions .....	125
5.3.3 Material properties .....	125
5.3.4 Stages .....	125
<b>CHAPTER 6</b>	
<b>RESULTS.....</b>	<b>126</b>
6.1 GREENFIELD MODELS.....	126
6.1.1 The Reference (REF) model and related closed-form solutions .....	127
6.1.2 Parametric analyses.....	132
6.1.3 Greenfield volume loss models.....	140
6.2 UNCOUPLED BUILDING MODELS .....	142
6.2.1 VLMAX subsidence .....	144
6.2.2 VLMEAN subsidence .....	155
6.2.3 VLMIN subsidence.....	166
6.2.4 Comparison between uncoupled model results.....	177
6.3 BUILDING RISK OF DAMAGE ESTIMATION WITH THE EBA METHOD .....	181
6.4 COUPLED MODELS: SOIL – STRUCTURE INTERACTION.....	188
6.4.1 Steady-state, permanent deformations at the end of tunnelling.....	188
6.4.2 Most critical excavation steps and the influence of three-dimensionality	196
<b>CHAPTER 7</b>	
<b>CONCLUSIONS AND RECOMMENDATIONS .....</b>	<b>200</b>
7.1 CONCLUSIONS .....	200
7.1.1 Greenfield models .....	200
7.1.2 Uncoupled building models .....	201
7.1.3 Coupled soil – structure interaction models .....	202
<b>REFERENCES.....</b>	<b>204</b>
<b>APPENDIX A</b>	
<b>GEOTECHNICAL STUDIES NEAR PIAZZA CARLO ALBERTO.....</b>	<b>212</b>
A.1 SP-D12 STRATIGRAPHY, COURTESY OF INFRATRASPORTI.TO S.R.L. (2024).	212
A.2 DETAILS OF THE SAMPLES FROM THE SP-D12 STRATIGRAPHIC BOREHOLE ..	213
A.3 PERMEABILITY TESTS IN THE SP-D12 BOREHOLE.....	215
A.4 SP-D13 STRATIGRAPHY, COURTESY OF INFRATRASPORTI.TO S.R.L. (2024).	217
A.5 DETAILS OF THE SAMPLES FROM THE SP-D13 STRATIGRAPHIC BOREHOLE ..	218

A.6	PERMEABILITY TESTS IN THE SP-D13 BOREHOLE.....	220
-----	--	-----

## **APPENDIX B**

### **BLUEPRINTS OF PALAZZO CAMPANA ..... 222**

B.1	CELLAR, TOP VIEW .....	222
B.2	FIRST FLOOR, TOP VIEW .....	223
B.3	SECOND FLOOR, TOP VIEW.....	224
B.4	THIRD FLOOR, TOP VIEW.....	225
B.5	FOURTH FLOOR, TOP VIEW .....	226
B.6	INTERIOR COURTYARD ELEVATION, VIA CARLO ALBERTO WING.....	227
B.7	INTERIOR COURTYARD ELEVATION, VIA PRINCIPE AMEDEO WING .....	228
B.8	INTERIOR COURTYARD ELEVATION, VIA ACCADEMIA DELLE SCIENZE WING	229
B.9	INTERIOR COURTYARD ELEVATION, VIA MARIA VITTORIA .....	230

## **APPENDIX C**

### **BUILDING RISK OF DAMAGE ASSESSMENT..... 231**

C.1	EMPIRICAL ASSESSMENT FOR PALAZZO CAMPANA (PNCA43) WITH A VOLUME LOSS OF 1.0%, COURTESY OF INFRATRASPORTI.TO (2024) .....	231
-----	--	-----



## List of figures

Figure 2.1. Evolution of Italian metro lines throughout history .....	2
Figure 2.2. Transversal circular tunnel section nomenclature .....	3
Figure 2.3. Balance of the pressures at the face of the excavation, modified from Herrenknecht AG (2024).....	4
Figure 2.4. Emulation of the soil conditioning of an EPB-TBM.....	4
Figure 2.5. EPB-TBM nomenclature, modified from Herrenknecht AG (2024).....	5
Figure 2.6. Detail of the tail of the shield and annulus backfilling, as seen in Pelizza et al. (2012).....	6
Figure 2.7. Basin of subsidence, as seen in Peila (2023).....	7
Figure 2.8. Causes of the settlement trough during mechanized tunnelling.....	8
Figure 2.9. Detail of the shield – ground gaps and their causes at the crown of the excavation, modified from Thewes & Budach (2009) as seen in Todaro, Saltarin & Cardu (2022).....	9
Figure 2.10. Basin of subsidence in greenfield conditions, modified from Burland (Assessment methods used in design, 2001).....	10
Figure 2.11. Longitudinal settlement trough, adapted from Uriel & Sagaseta (1989)	11
Figure 2.12. Transversal settlement trough.....	12
Figure 2.13. Tunnel walls deformation modes, as presented by Pinto & Whittle (2014).....	13
Figure 2.14. Definition of gap as a physical distance, after Rowe & Kack (1983).....	14
Figure 2.15. Measurements of foundation movement, modified from Burland & Wroth (1974).....	19
Figure 2.16. Cracking of a beam in bending and shearing deformation modes (Burland & Wroth, 1974).....	22
Figure 2.17. Sagging and hogging zone parameters for the deflection ratio (Burland, Assessment methods used in design, 2001).....	23
Figure 2.18. Damage category chart for hogging deformation mode with $L/H=1$ (Mair, Taylor, & Burland, 1996).....	24
Figure 2.19. Framework for the building risk of damage assessment, after Burland (Assessment methods used in design, 2001).....	25
Figure 3.1. Typical configuration of a 3D geometrical model of the soil of a shallow tunnel excavation .....	26
Figure 3.2. Typical configuration of a 3D geometrical model of the TBM shield and liner plus grout.....	27
Figure 3.3. Portion of the model mesh by Kasper & Meschke (2004).....	28
Figure 3.4. Half of the model's mesh by Kavvadas et al. (2017).....	28
Figure 3.5. Mesh and geometrical model of the EPB machine (Kavvadas et al., 2017).....	29

Figure 3.6. Soil – structure interaction model mesh by Amorosi & Sangirardi (2021)	29
Figure 3.7. Model mesh by Mollon, Dias & Soubra (2012)	30
Figure 3.8. Influence of the boundary conditions on the numerical model along the longitudinal direction (Mollon, Dias, & Soubra, 2012)	31
Figure 3.9. Faces of the rectangular prism, dominion of the 3D model	32
Figure 3.10. TBM layout and boundary conditions affecting the excavation, as presented by Mollon et al. (2012)	39
Figure 3.11. Imposed soil convergence around the tunnel following a) uniform radial tunnel contraction, b) oval-shaped tunnel contraction	43
Figure 3.12. EPB-TBM face pressure in the step-by-step procedure	44
Figure 3.13. Step-by-step advancement simulation of the tunnelling process	45
Figure 3.14. Relationship between the normalized face extrusion $\Omega F$ and the Tunnel Stability Parameter $\Lambda FP$ , modified from Kavvadas et al. (2017)	46
Figure 3.15. Forced soil displacement along the shield, modified from Amorosi & Sangirardi (2021)	47
Figure 3.16. Enforced pressure at the tunnel excavation walls, around the shield, modified from Epel et al. (2021)	48
Figure 3.17. Spring rings to limit the soil's convergence around the shield, modified from Nemorini (2010)	49
Figure 3.18. Master-to-slave surface interaction, adapted from Dassault Systemes (2024)	50
Figure 3.19. Hard contact pressure-overclosure property (Dassault Systemes, 2024)	51
Figure 3.20. Scheme of the machine showing the overcut, steering and annular gap (Litsas, Sitarenios, & Kavvadas, 2017)	52
Figure 3.21. Scheme of the machine showing the overcut, steering and annular gap, modified from Losacco & Viggiani (2019)	53
Figure 3.22. Causes of the steering gap pressure, modified from Epel et al. (2021)	54
Figure 3.23. Steering gap pressure scenarios, as presented by Litsas et al. (2017)	54
Figure 3.24. Results of ground settlements obtained by Mollon et al. (2012), modified to draw especial attention to the effect of the grout pressure	56
Figure 3.25. Soil – structure interaction model mesh by Yiu (2018)	59
Figure 3.26. Soil – structure interaction model mesh by Losacco (2011)	59
Figure 3.27. Soil – structure interaction model mesh of the a) building and b) equivalent solid by Rampello, Callisto, Viggiani & Soccodato (2012)	60
Figure 3.28. Results presented by Lasciarrea et al. (2019): comparison between tensile total strain in masonry provided by the elastic and JMM constitutive models	61
Figure 3.29. Typical CDP model response for uniaxial tensile loading (Dassault Systemes, 2024)	62
Figure 3.30. Typical CDP model response for uniaxial compression loading (Dassault Systemes, 2024)	63
Figure 4.1. First phase of the Metro-Line 2 project (Infratrasporti.To S.r.l., 2024)	67
Figure 4.2. Metro-Line 2 of Torino complete development	68
Figure 4.3. From left to right: a) population density and b) public transport usage in the City of Torino, modified from Infratrasporti.To S.r.l. (2024)	69

Figure 4.4. Revitalization of Torino's north, driver of the Metro-Line 2 project (Infratrasporti.To S.r.l., 2024) .....	69
Figure 4.5. Transversal section of the tunnel, dimensions in meters (Infratrasporti.To S.r.l., 2024).....	70
Figure 4.6. Geology of western Piemonte, modified from Irace et al. (2024).....	71
Figure 4.7. Elevation scheme of the A-A section of the geological map, modified from Bottino & Civita (1986) .....	72
Figure 4.8. Bare excavation front of the Underground Railway Link of Torino (Barla & Barla, 2012) .....	72
Figure 4.9. Degrees of cementation in the Torino subsoil at: a) 15 m below the ground surface and b) 20 m, after De Rienzo & Oreste (2011) .....	73
Figure 4.10. Stratigraphy in the Piazza Carlo Alberto zone, below Palazzo Campana (Infra.To S.r.l., 2024) .....	73
Figure 4.11. Flow direction and isopiezometric curves of the superficial water table of Torino, as seen in Infratrasporti.To S.r.l. (2024).....	74
Figure 4.12. Superficial water table depth in the City of Torino (Infratrasporti.To S.r.l., 2024) .....	75
Figure 4.13. From left to right: inside of a borehole drilling and the survey activity (Infratrasporti.To S.r.l., 2023) .....	76
Figure 4.14. a) FLAC and b) PFC numerical models configured by Barla & Barla (2012) to numerically estimate the characteristics of the Torino soil with a given degree of cementation (percentage).....	77
Figure 4.15. Results presented by Barla & Barla (2012): deformation modulus of the numerical Torino soil samples in FLAC and PFC .....	78
Figure 4.16. Results presented by Barla & Barla (2012): yield criteria in function of the degree of cementation of the Torino soil.....	79
Figure 4.17. Fires of 1943 in Palazzo Campana (Designers Riuniti, 1983; ISTORETO, 2002) .....	81
Figure 4.18. Blueprint of the first floor of Palazzo Campana.....	81
Figure 4.19. From left to right: Palazzo Campana's NORTH, SOUTH and EAST facades.....	82
Figure 4.20. Internal halls of Palazzo Campana and localized damage below a slab..	82
Figure 4.21. Development of the basin of subsidence for $VLT = 0.5$ and $1.0$ , according to Infratrasporti.To (2024) based on empirical methods.....	83
Figure 4.22. Risk of building damage assessment, with minor modifications as seen in Infratrasporti.To (2024).....	84
Figure 4.23. Planimetry of the jet grouting injections (Infratrasporti.To S.r.l., 2024).....	85
Figure 4.24. Profile view of the jet grouting injections below Palazzo Campana, modified from (Infratrasporti.To S.r.l., 2024).....	85
Figure 4.25. Detailed configurations of the jet grouting umbrella in sections B-B and C-C of the profile view, modified from (Infratrasporti.To S.r.l., 2024).....	86
Figure 4.26. 2D numerical model in natural conditions and transversal subsidence results, modified from Infratrasporti.To S.r.l. (2024) .....	87
Figure 4.27. 2D numerical model in natural conditions and transversal subsidence results, modified from Infratrasporti.To S.r.l. (2024) .....	87

Figure 4.28. From left to right: a) plan view of the air raid shelter in the courtyard of Palazzo Campana and b) insides of the shelter .....	88
Figure 5.1. Top view of the excavation model and recommended size based on the extension of Palazzo Campana .....	89
Figure 5.2. Elevation of the different layers of the soil model .....	90
Figure 5.3. Model mesh of the soil .....	91
Figure 5.4. From left to right: a) model mesh of the shield, b) model mesh of the lining segments (black) and the grout (red) .....	91
Figure 5.5. Jointed model of the excavation (assembly), featuring the parts of the soil, shield and liners plus grout in interaction .....	92
Figure 5.6. Detail of the model of the excavation.....	92
Figure 5.7. Detail of the model of the excavation with the jet grouting umbrella.....	93
Figure 5.8. Transversal section of the tunnel assembly .....	94
Figure 5.9. Applied topsoil and shield/liner pressures to account for their weights....	95
Figure 5.10 Young's modulus of the two-component grout at an early curing time frame .....	98
Figure 5.11. Young's modulus of the two-component grout in time.....	99
Figure 5.12. Modelling the time-dependent Young's modulus of the grout .....	100
Figure 5.13. Step-function representing the stiffening of the two-component grout in the model, function of time .....	100
Figure 5.14. Step-function representing the stiffening of the two-component grout in the model, function of the distance from the tail of the shield .....	101
Figure 5.15. Effective horizontal stresses and unit weights assumed for the simulation of the geostatic stress .....	102
Figure 5.16. Step-by-step excavation process.....	103
Figure 5.17. Simulation of the EPB-TBM face pressure .....	104
Figure 5.18. Workflow of the greenfield parametrical analyses .....	106
Figure 5.19. Model mesh of Palazzo Campana's perimetral facades, top view and facade nomenclature .....	109
Figure 5.20. EAST facade. Simplified exterior elevation, Via Carlo Alberto wing ..	109
Figure 5.21. NORTH facade. Simplified exterior elevation, Via Principe Amedeo wing.....	110
Figure 5.22. Model mesh of Palazzo Campana's perimetral facades, front view from Via Principe Amedeo .....	110
Figure 5.23. Model mesh of Palazzo Campana's perimetral facades, rear view from Via Maria Vittoria .....	111
Figure 5.24. Model mesh of the NORTH facade .....	111
Figure 5.25. Model mesh of the EAST facade.....	112
Figure 5.26. Model mesh of the SOUTH facade .....	112
Figure 5.27. Model mesh of the CSOUTH facade.....	113
Figure 5.28. Model mesh of the CEAST facade .....	113
Figure 5.29. Model mesh of the CNORTH facade .....	114
Figure 5.30. Model mesh of the WEST facade.....	114
Figure 5.31. Halls of Palazzo Campana, showing vaulted slabs with metal tendons	115
Figure 5.32. Portion of the facades at the level of the slabs .....	116
Figure 5.33. Diaphragm constraint for the last floor of the building model.....	116

Figure 5.34. Mesh model of the facades on top of a supporting layer for the subsidence application .....	118
Figure 5.35. Side by side numerical and laboratory masonry facade models from: Giardina et al. (2013) a) elastic and c) cracking models; and Dalgic et al. (2023) b) lower versus d) higher area of openings .....	118
Figure 5.36. Stress-strain proposed curves for the Palazzo Campana masonry building .....	121
Figure 5.37. Workflow of the parametrical analyses for the uncoupled building model .....	122
Figure 5.38. Jointed coupled model (assembly), featuring the parts of the soil with the jet grouting improved zone, shield, liners plus grout and the building in interaction	124
Figure 5.39. Detail of the coupled model .....	124
Figure 6.1. Control section A-A for the longitudinal troughs .....	126
Figure 6.2. REF model. Longitudinal trough for FEM results and with the cumulative distribution .....	127
Figure 6.3. Location of the nodes for the plot of the longitudinal trough.....	128
Figure 6.4. REF model. Longitudinal trough for the nodes at the surface, crown and invert .....	128
Figure 6.5. REF model. Transversal trough in FEM for different moments of the excavation .....	129
Figure 6.6. REF model. Transversal trough with FEM and empirical and analytical formulations .....	130
Figure 6.7. REF model. Horizontal displacements with FEM and O'Reilly & New's formulation.....	131
Figure 6.8. REF model. Horizontal strains with FEM and O'Reilly & New's formulation.....	131
Figure 6.9. GS models. Longitudinal trough .....	132
Figure 6.10. GS models. Transversal trough.....	132
Figure 6.11. GS models. Horizontal displacements .....	132
Figure 6.12. GS models. Horizontal strains .....	132
Figure 6.13. GS models. Longitudinal trough .....	133
Figure 6.14. GS models. Transversal trough.....	133
Figure 6.15. GS models. Horizontal displacements.....	133
Figure 6.16. GS models. Horizontal strains .....	133
Figure 6.17. GAP models. Longitudinal trough.....	134
Figure 6.18. GAP models. Transversal trough.....	134
Figure 6.19. GAP models. Horizontal displacements.....	134
Figure 6.20. GAP models. Horizontal strains .....	134
Figure 6.21. GAP models. Longitudinal trough for the nodes at the crown and invert .....	135
Figure 6.22. FP models. Longitudinal trough .....	136
Figure 6.23. FP models. Transversal trough .....	136
Figure 6.24. FP models. Horizontal displacements .....	136
Figure 6.25. FP models. Horizontal strains.....	136
Figure 6.26. Tunnel face extrusion results with the parametrical variations. Tunnel face centered at zero.....	137

Figure 6.27. Results of the parametric analyses against Proutzopoulos' (2012) $\Omega F - AFP$ curve .....	137
Figure 6.28. Maximum absolute plastic strains for the FP0 face pressure model .....	138
Figure 6.29. SOIL models. Longitudinal trough.....	139
Figure 6.30. SOIL models. Transversal trough.....	139
Figure 6.31. SOIL models. Horizontal displacement.....	139
Figure 6.32. SOIL models. Horizontal strains .....	139
Figure 6.33. JET model. Longitudinal trough.....	140
Figure 6.34. JET model. Transversal trough.....	140
Figure 6.35. JET model. Horizontal displacement.....	140
Figure 6.36. JET model. Horizontal strains .....	140
Figure 6.37. VL models. Longitudinal trough .....	142
Figure 6.38. VL models. Transversal trough.....	142
Figure 6.39. VL models. Horizontal displacements.....	142
Figure 6.40. VL models. Horizontal strains.....	142
Figure 6.41. Subsidence fields applied below the facades of Palazzo Campana.....	143
Figure 6.42. Uncoupled model: Major principal strains of the facades for the VLMAX models with both ELAS and CDP masonry constitutive behaviors .....	145
Figure 6.43. Uncoupled model: Cumulative portions of the facades belonging to the damage categories based on the limiting tensile strain, for the VLMAX models with the ELAS masonry constitutive behavior .....	146
Figure 6.44. Uncoupled model: Cumulative portions of the facades belonging to the damage categories based on the limiting tensile strain, for the VLMAX models with the CDP masonry constitutive behavior.....	147
Figure 6.45. Uncoupled model: Major principal strains of the NORTH facade for the VLMAX models with both ELAS and CDP masonry constitutive behaviors.....	148
Figure 6.46. Uncoupled model: Major principal strains of the CNORTH and CEAST facades for the VLMAX models with both ELAS and CDP masonry constitutive behaviors .....	149
Figure 6.47. Uncoupled model: Major principal strains of the SOUTH facade for the VLMAX models with both ELAS and CDP masonry constitutive behaviors.....	150
Figure 6.48. Uncoupled model: Cumulative portions of the NORTH facade belonging to the damage categories based on the limiting tensile strain, for the VLMAX models with the ELAS masonry constitutive behavior .....	151
Figure 6.49. Uncoupled model: Cumulative portions of the NORTH facade belonging to the damage categories based on the limiting tensile strain, for the VLMAX models with the CDP masonry constitutive behavior .....	151
Figure 6.50. Uncoupled model: Damage category map of the NORTH facade for the VLMAX models with the CDP MAX masonry constitutive behavior .....	152
Figure 6.51. Uncoupled model: Cumulative portions of the SOUTH facade belonging to the damage categories based on the limiting tensile strain, for the VLMAX models with the ELAS masonry constitutive behavior .....	152
Figure 6.52. Uncoupled model: Cumulative portions of the SOUTH facade belonging to the damage categories based on the limiting tensile strain, for the VLMAX models with the CDP masonry constitutive behavior .....	153

Figure 6.53. Uncoupled model: Damage category map of the SOUTH facade for the VLMAX models with the CDP MAX masonry constitutive behavior .....	153
Figure 6.54. Uncoupled model: Cumulative portions of the CEAST and CNORTH facades belonging to the damage categories based on the limiting tensile strain, for the VLMAX models with the ELAS masonry constitutive behavior .....	154
Figure 6.55. Uncoupled model: Cumulative portions of the CEAST and CNORTH facades belonging to the damage categories based on the limiting tensile strain, for the VLMAX models with the CDP masonry constitutive behavior .....	154
Figure 6.56. Uncoupled model: Damage category map of the CEAST and CNORTH facades for the VLMAX models with the CDP MAX masonry constitutive behavior .....	155
Figure 6.57. Uncoupled model: Major principal strains of the facades for the VLMEAN models with both ELAS and CDP masonry constitutive behaviors .....	156
Figure 6.58. Uncoupled model: Cumulative portions of the facades belonging to the damage categories based on the limiting tensile strain, for the VLMEAN models with the ELAS masonry constitutive behavior .....	157
Figure 6.59. Uncoupled model: Cumulative portions of the facades belonging to the damage categories based on the limiting tensile strain, for the VLMEAN models with the CDP masonry constitutive behavior .....	158
Figure 6.60. Uncoupled model: Major principal strains of the NORTH facade for the VLMEAN models with both ELAS and CDP masonry constitutive behaviors .....	159
Figure 6.61. Uncoupled model: Major principal strains of the CNORTH and CEAST facades for the VLMEAN models with both ELAS and CDP masonry constitutive behaviors .....	160
Figure 6.62. Uncoupled model: Major principal strains of the SOUTH facade for the VLMEAN models with both ELAS and CDP masonry constitutive behaviors .....	161
Figure 6.63. Uncoupled model: Cumulative portions of the NORTH facade belonging to the damage categories based on the limiting tensile strain, for the VLMEAN models with the ELAS masonry constitutive behavior .....	162
Figure 6.64. Uncoupled model: Cumulative portions of the NORTH facade belonging to the damage categories based on the limiting tensile strain, for the VLMEAN models with the CDP masonry constitutive behavior .....	162
Figure 6.65. Uncoupled model: Damage category map of the NORTH facade for the VLMEAN models with the CDP MAX masonry constitutive behavior .....	163
Figure 6.66. Uncoupled model: Cumulative portions of the SOUTH facade belonging to the damage categories based on the limiting tensile strain, for the VLMEAN models with the ELAS masonry constitutive behavior .....	163
Figure 6.67. Uncoupled model: Cumulative portions of the SOUTH facade belonging to the damage categories based on the limiting tensile strain, for the VLMEAN models with the CDP masonry constitutive behavior .....	164
Figure 6.68. Uncoupled model: Damage category map of the SOUTH facade for the VLMEAN models with the CDP MAX masonry constitutive behavior .....	164
Figure 6.69. Uncoupled model: Cumulative portions of the CEAST and CNORTH facades belonging to the damage categories based on the limiting tensile strain, for the VLMEAN models with the ELAS masonry constitutive behavior .....	165

Figure 6.70. Uncoupled model: Cumulative portions of the CEAST and CNORTH facades belonging to the damage categories based on the limiting tensile strain, for the VLMEAN models with the CDP masonry constitutive behavior.....	165
Figure 6.71. Uncoupled model: Damage category map of the CEAST and CNORTH facades for the VLMEAN models with the CDP MAX masonry constitutive behavior .....	166
Figure 6.72. Uncoupled model: Major principal strains of the facades for the VLMIN models with both ELAS and CDP masonry constitutive behaviors .....	167
Figure 6.73. Uncoupled model: Cumulative portions of the facades belonging to the damage categories based on the limiting tensile strain, for the VLMIN models with the ELAS masonry constitutive behavior .....	168
Figure 6.74. Uncoupled model: Cumulative portions of the facades belonging to the damage categories based on the limiting tensile strain, for the VLMIN models with the CDP masonry constitutive behavior.....	169
Figure 6.75. Uncoupled model: Major principal strains of the NORTH facade for the VLMIN models with both ELAS and CDP masonry constitutive behaviors .....	170
Figure 6.76. Uncoupled model: Major principal strains of the CNORTH and CEAST facades for the VLMIN models with both ELAS and CDP masonry constitutive behaviors.....	171
Figure 6.77. Uncoupled model: Major principal strains of the SOUTH facade for the VLMIN models with both ELAS and CDP masonry constitutive behaviors .....	172
Figure 6.78. Uncoupled model: Cumulative portions of the NORTH facade belonging to the damage categories based on the limiting tensile strain, for the VLMIN models with the ELAS masonry constitutive behavior .....	173
Figure 6.79. Uncoupled model: Cumulative portions of the NORTH facade belonging to the damage categories based on the limiting tensile strain, for the VLMIN models with the CDP masonry constitutive behavior .....	173
Figure 6.80. Uncoupled model: Damage category map of the NORTH facade for the VLMIN models with the CDP MAX masonry constitutive behavior .....	174
Figure 6.81. Uncoupled model: Cumulative portions of the SOUTH facade belonging to the damage categories based on the limiting tensile strain, for the VLMIN models with the ELAS masonry constitutive behavior .....	174
Figure 6.82. Uncoupled model: Cumulative portions of the SOUTH facade belonging to the damage categories based on the limiting tensile strain, for the VLMIN models with the CDP masonry constitutive behavior .....	175
Figure 6.83. Uncoupled model: Damage category map of the SOUTH facade for the VLMIN models with the CDP MAX masonry constitutive behavior .....	175
Figure 6.84. Uncoupled model: Cumulative portions of the CEAST and CNORTH facades belonging to the damage categories based on the limiting tensile strain, for the VLMIN models with the ELAS masonry constitutive behavior .....	176
Figure 6.85. Uncoupled model: Cumulative portions of the CEAST and CNORTH facades belonging to the damage categories based on the limiting tensile strain, for the VLMIN models with the CDP masonry constitutive behavior.....	176
Figure 6.86. Uncoupled model: Damage category map of the CEAST and CNORTH facades for the VLMIN models with the CDP MAX masonry constitutive behavior .....	177



Figure 6.87. Uncoupled model: Comparison of the potential effects of the greenfield volume loss models in the NORTH facade.....	179
Figure 6.88. Uncoupled model: Comparison of the potential effects of the greenfield volume loss models in the CEAST and CNORTH facades .....	180
Figure 6.89. Uncoupled model: Comparison of the potential effects of the greenfield volume loss models in the SOUTH facade .....	181
Figure 6.90. Greenfield settlements and horizontal displacements induced below the NORTH facade.....	182
Figure 6.91. Parameters for the calculation of the deflection ratio of the NORTH facade in greenfield conditions .....	183
Figure 6.92. Damage category charts for the NORTH facade in greenfield conditions and ELAS MAX parameters, for a) sagging and b) hogging deformation modes ....	183
Figure 6.93. Greenfield settlements and horizontal displacements induced below the CNORTH facade .....	184
Figure 6.94. Parameters for the calculation of the deflection ratio of the CNORTH facade in greenfield conditions .....	185
Figure 6.95. Damage category charts for the CNORTH facade in greenfield conditions and ELAS MAX parameters, for a) sagging and b) hogging deformation modes ....	185
Figure 6.96. Greenfield settlements and horizontal displacements induced below the SOUTH facade.....	186
Figure 6.97. Parameters for the calculation of the deflection ratio of the SOUTH facade in greenfield conditions .....	187
Figure 6.98. Damage category charts for the SOUTH facade in greenfield conditions and ELAS MAX parameters, for a) sagging and b) hogging deformation modes ....	187
Figure 6.99. Interaction model: Major principal strains of the entire building for the INT_VLMIN condition with ELAS MAX masonry constitutive behavior.....	189
Figure 6.100. Interaction model: Major principal strains of the individual facades for the INT_VLMIN condition with ELAS MAX masonry constitutive behavior.....	190
Figure 6.101. Interaction model: Major principal strains of the entire building for the INT_VLMIN condition with CDP MAX masonry constitutive behavior .....	191
Figure 6.102. Interaction model: Major principal strains of the individual facades for the INT_VLMIN condition with CDP MAX masonry constitutive behavior .....	192
Figure 6.103. Comparison of major principal strains between individual facades of the uncoupled and coupled interaction models, for the VLMIN condition with ELAS MAX masonry constitutive behavior.....	193
Figure 6.104. Comparison of major principal strains between individual facades of the uncoupled and coupled interaction models, for the VLMIN condition with CDP MAX masonry constitutive behavior .....	194
Figure 6.105. Comparison of damage category maps between individual facades of the uncoupled and coupled interaction models, for the VLMIN condition with CDP MAX masonry constitutive behavior.....	195
Figure 6.106. Total tensile strains of the uncoupled VLMIN_CDP_MAX model of CEAST and CSOUTH facades .....	196
Figure 6.107. Effect (tensile) of the step-by-step excavation and the three-dimensionality in the CSOUTH facade .....	197

Figure 6.108. Displacements (U2 in meters for the labels, exaggerated deformation by 500 times) of the CNORTH, CEAST and CSOUTH facades and their three-dimensional interaction in the step-by-step excavation.....	198
---	-----

## List of tables

Table 2.1. Damage categories for brickwork masonry, as presented by Mair, Taylor & Burland (1996) and Boscardin & Cording (1989) .....	21
Table 3.1 Mix dosage and time-dependent elastic properties of different two-component grouts in the literature .....	42
Table 3.2 Elastic and CDP properties of different masonry buildings and samples in the literature .....	65
Table 4.1. Mohr-Coulomb elasto-plastic parameters for the Torino cemented soil, after Barla & Barla (2012) .....	79
Table 4.2. Minimum requirements for the improved soil (Infratrasporti.To S.r.l., 2024) .....	86
Table 5.1. Parameters selected for the model of the Torino soil .....	96
Table 5.2 Proposed Metro-Line 2 of Torino's two-component grout elastic parameters .....	97
Table 5.3. Parameters selected for the model of the jet grouting umbrella .....	101
Table 5.4. Nomenclature for the greenfield models .....	107
Table 5.5. Proposed elasto-plastic parameters for the Palazzo Campana masonry building .....	120
Table 5.6. Nomenclature for the uncoupled building models .....	123
Table 6.1. Settlement volume losses calculated for each model of the greenfield parametric analysis.....	141



# Chapter 1

## Introduction

In comparison to the existent Metro-Line 1 of Torino, Italy, which exclusively dug its way below three main and one secondary urban roads (C.so Francia, C.so Bolzano, C.so Vittorio Emanuele II and Via Nizza) reducing its direct interaction with surface structures and furthermore, avoiding completely the city's historical center; the Metro-Line 2 phase 1 project (north alignment from Rebaudengo to Porta Nuova) poses a challenge in the sense that it foresees excavations directly passing below several buildings in the north of the city, towards the Aurora and Vanchiglia districts, with an especially long portion proceeding underneath historical masonry buildings in the Centro Storico (historical center) quarter of Torino. For this reason, both the City of Torino and its society Infratrasporti.To S.r.l., in charge of the preliminary designs of the works, supervision, in-situ surveys, feasibility studies and contract administration, are rightfully interested in guaranteeing the successful completion of the tunnelling works with negligible effects on the surface structures. For this purpose, in the design stage the society studied the interaction between the excavation and the buildings on top of the tunnel path, and through simplified empirical and two-dimensional numerical alternatives, they identified 11 buildings at risk of experiencing moderate to severe damage, from which only one building, Palazzo Campana, fell in the highest degree of severity. Acknowledging that simplified methods for building damage estimation are regarded as conservative, it is the motivation of the current thesis to evaluate such statement with more advanced methods, such as three-dimensional parametric numerical modelling, in an effort to provide more representative predictions of what the real tunnelling process will be, its interaction with Palazzo Campana and the potential building risk of damage.

## Chapter 2

### Shallow tunneling in urban area

#### 2.1 Tunnels for cities

Italian metro lines have been active since the 1920s. In an effort to show the magnitude of these significant works in Italy, the next graph shows a summary of the inauguration dates and lengths of Italian metro lines throughout history, suggesting, furthermore, that since 1955 there has not been a single decade in which the construction of tunnels under the main Italian cities has stopped. It is ever present, starting from the Line 2 of Naples, continuing with Rome's Line B, Milan's Line 1, in 2006 the first line of the metro of Torino, and so forth; accumulating nearly 300 kilometers of metro lines in almost 100 years.

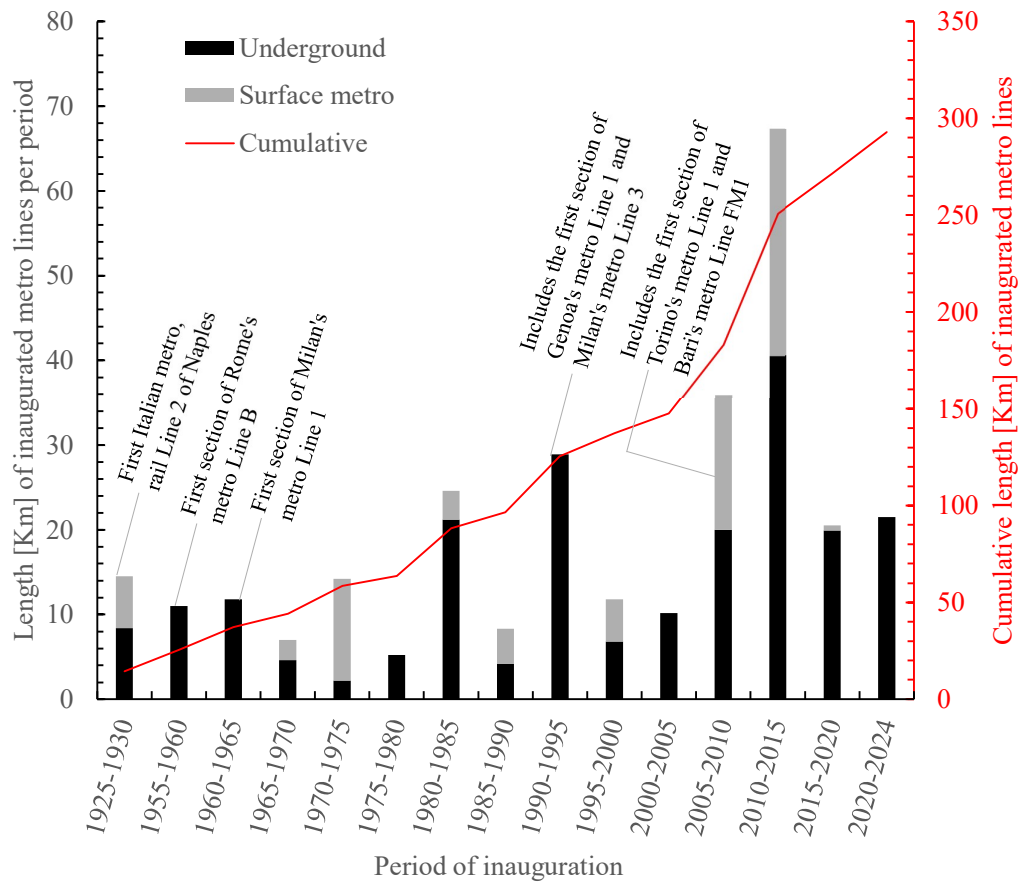


Figure 2.1. Evolution of Italian metro lines throughout history

## 2.2 The tunnelling process

Tunnelling in urban areas, especially in highly urbanized zones, is commonly performed with tunnel boring machines (TBMs). These machines course through the subsoil by cutting the ground ahead with spinning cutterheads and moving, ideally, with near constant and steady advancement rates by thrusting on rear installed segmental liners, which are prefabricated concrete elements built to support the crown, invert and springline of the circular-shaped excavation (all in junction called the walls of the excavation, detailed in Figure 2.2). The TBM itself supports the excavation walls with the shield and at the front of the excavation with an induced face pressure, bearing in mind that loose soil can freely displace inside the void if support is not provided. In this way, the aim of the machine is to cruise the subsoil marginally disturbing the surrounding ground, avoiding undesirable effects on the surface such as settlements and sinkholes, while continuously advancing the excavation at a formidable pace.

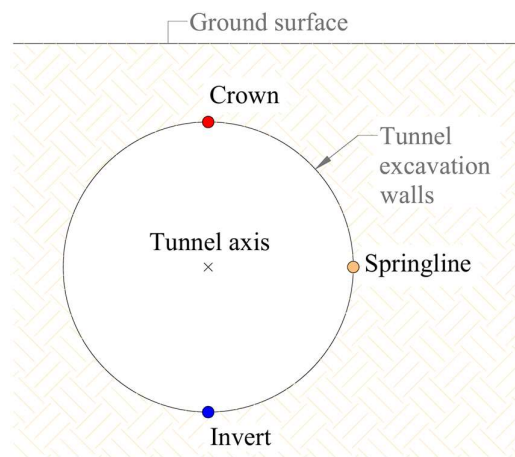


Figure 2.2. Transversal circular tunnel section nomenclature

Usually, two types of TBMs are employed in urban tunnelling: Earth Pressure Balance (EPB) and slurry-shield. If the stratigraphy is composed of capable or even soft rock, open-faced TBMs are also an option. In soft homogeneous ground, prevailing condition in urban tunnelling where the geological setting seldom varies, the EPBs and slurry-shields are the go-tos. Given that the soft ground is weakened and loosened up by the decompression and variable changes in the stress state induced by the excavation, both the EPB and slurry-shield technologies offer the possibility to control the amount of loose material being excavated, preventing the possibility of incurring in excessive over-excavations, and to exert pressure at the face of the tunnel to thwart the inflow of loose soil coming into the machine. In this way, with a good steering of the TBM, the surface settlements are effectively reduced and the odds of having sinkholes become almost null.

The difference between both technologies is principally the material used for the pressure application. The EPB, as illustrated in the next Figure 2.3, applies the face pressure to balance the geostatic and hydrostatic thrusts with the same material that is being excavated, while the slurry-shield, as its name implies, uses foreign clays or bentonite slurries to exert said pressure.

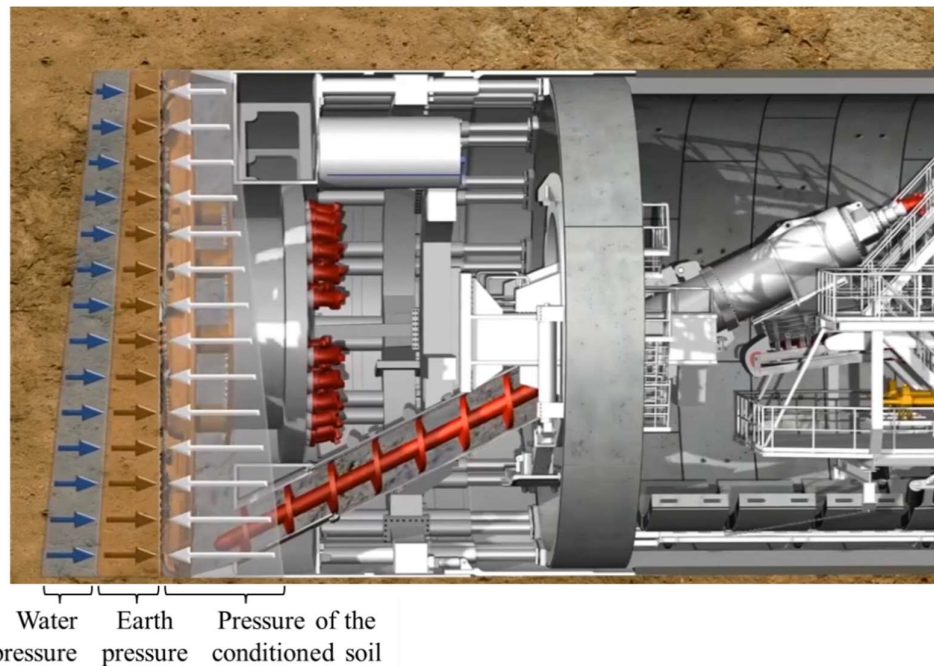


Figure 2.3. Balance of the pressures at the face of the excavation, modified from Herrenknecht AG (2024)

The advantage of the EPB over the slurry-shield is that it does not need to introduce foreign materials to put forth the face support, saving on environmental and economic costs of the slurries and management of the muds. Instead, the EPB machine needs to condition the soil in the face of the tunnel by injecting foam through nozzles in the cutterhead. This foam, as shown in Figure 2.4, plasticizes the soil which is initially unable to be pressurized because of its altered loose conditions or natural coarse structure, turning it into a pressured paste of reduced permeability, both supporting the excavation front and impermeabilizing it.



Figure 2.4. Emulation of the soil conditioning of an EPB-TBM

However, if the EPB-TBM is forced to stop for long periods of time, the foam is known to degrade (the foam stability can be experimentally tested with the half-time life procedure, deriving the  $t_{50}$  parameter) losing its original plasticizing properties, rendering the soil loose once more and unable to maintain the pressurization. It is in this case that multi-mode alternatives, mixing the EPB and slurry-shield technologies



such as Herrenknecht's Variable Density, work best. With a multi-mode TBM, when the foam degrades it is possible to keep the face support by injecting pressurized slurry; rendering it a desirable alternative in geologically complex conditions. The Metro of Catania, Italy, comes to mind, and the desire of the Head of Design to have employed from the beginning a multi-mode machine in response to the very heterogeneous soil: mixture of magmatic rock, loose silty-clays, volcanic sand and breccias of different degrees of cementation, that increased the risk of the EPB-TBM dropping the pressure at the front after getting jammed inside the cavity, and the flexibility that a multi-mode machine would have provided with the injection of slurry to resume the pressure. These more flexible machines are, expectedly, more expensive and therefore rarely used if the stratigraphy is simple. The preferred alternative is to avoid at all costs the stopping of the TBM, having the excavation active 24 hours a day with different work shifts for the operators.

The main principle of the EPB and the reason it can maintain the pressure at the front is the balance between the advancement rate and the extraction of the soil. The ground is first loosened up by the cutterhead (in the next figure number 1). Then, the extraction of the muck is facilitated by a screw conveyor (4) and the advancement of the TBM by the thrust jacks (7) pushing on the installed prefabricated lining segments (10). As the TBM pushes forward, the material in the pressure chamber (3) is compressed against the face of the excavation, increasing the applied pressure. Conversely, this pressure cannot be too high to induce instability in the soil ahead of the face. To reduce it, the conditioned soil in the pressurized chamber must be progressively removed by the screw conveyor. In summary, the advancement of the machine increases the pressure on the face and the extraction of the conditioned soil decreases it. By balancing these two actions, the seamless support at the front is targeted to counter the geostatic and hydrostatic horizontal stresses.

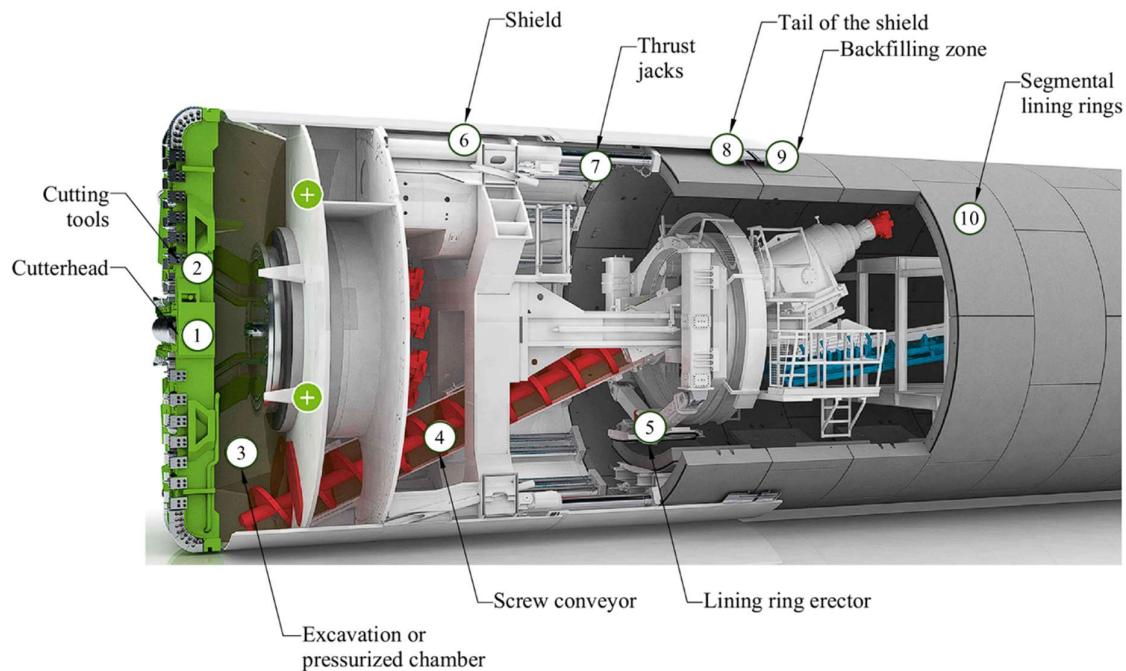


Figure 2.5. EPB-TBM nomenclature, modified from Herrenknecht AG (2024)

While the machine is advancing, the soil at the excavation walls is supported by the presence of the rigid shield (6). Once the shield has passed, the soil is able to freely displace into the cavity until it meets the segmental lining (10) or, if backfilling (9) is performed, until it meets the injected grout or pea gravel. A detail of the backfilling zone is presented in Figure 2.6 below, highlighting the importance of this operation to reduce the soil displacements around the excavation.

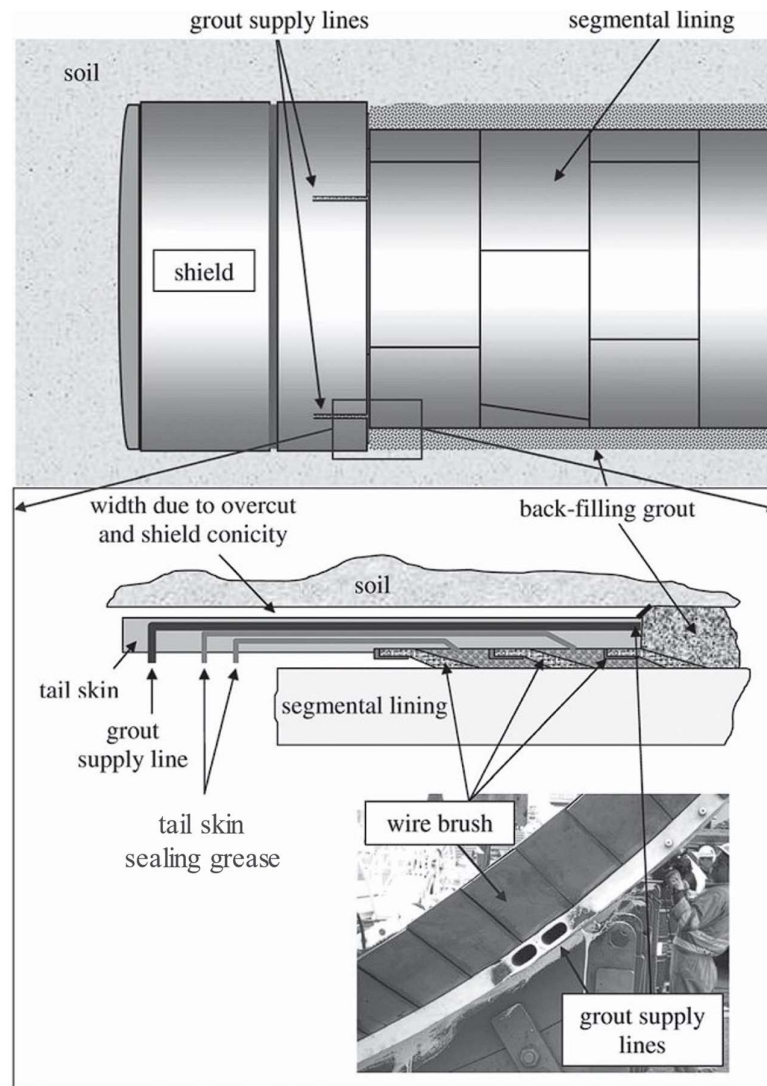


Figure 2.6. Detail of the tail of the shield and annulus backfilling, as seen in Pelizza et al. (2012)

### 2.3 Basin of subsidence

The socio-economic impact of metro tunneling works in urban areas has been well exposed in a past heading, and some hints have been given regarding the problem of the interaction between the settling soil and the existing structures above the excavation. Truly, with the excavation of a shallow tunnel, the soil's initial equilibrium state is

disturbed and consequently, a displacement field is initialized around and beyond the boundaries of the excavation. How farther away from the tunnel walls the perturbations extend depends on the tunneling technique, the ground compensation activities, the overburden and the overall geological characteristics of the domain; yet it is true at all times that the displacement field is never null, regardless of how precise and cautious the tunnelling process is.

This displacement field, closely followed by the stresses the liner rings must resist, is undeniably the most important tensor in the design stages of a shallow tunnelling project. At the ground surface it becomes of such relevance, that it has been identified with various names, among which: basin of subsidence, settlement trough and surface settlements. Directly, the basin of subsidence is the evolution of this displacement field towards the ground surface, taking the shape of an elongated bowl that follows the tunnel axis, extends ahead of the tunnel face and widens to the sides beyond the tunnel sidewalls, as better depicted in the next Figure 2.7.

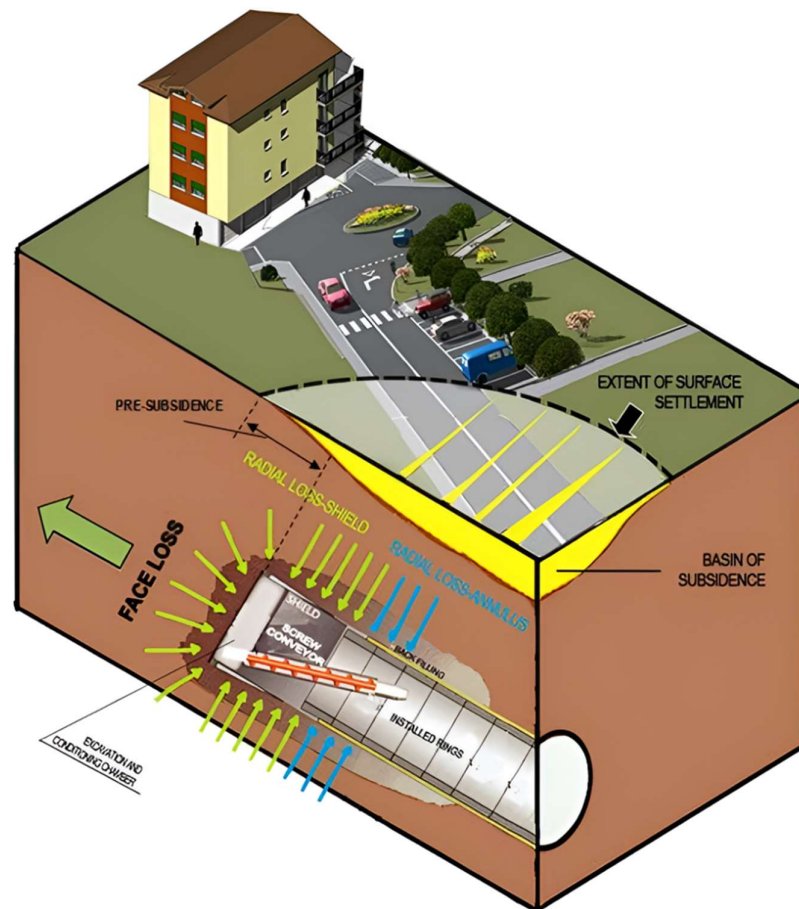


Figure 2.7. Basin of subsidence, as seen in Peila (2023)

This past figure is highly relevant, as it not only depicts the subsidence basin, but it also demonstrates how the basin can enter in interaction with superficial infrastructure, common goods and services, and structures such as residential buildings. This soil –

structure interaction is a crucial phenomenon that must be analyzed at the design stage, to determine potential building damage and to plan accordingly the compensation and monitoring strategies that will guarantee a safe execution of the underground works.

Furthermore, the figure well introduces the sources of the surface settlements, that belong to the mechanized excavation technique. In more detail these are:

- 1) Intrusion of the soil from the excavation face. The loose soil is ‘pressed’ towards the cutterhead producing an over-excitation.
- 2) Overcut because of the peripheral tools and soil convergence due to the shield’s conicity. The overcut can increase if the machine is steered poorly.
- 3) Annulus void. The distance between the shield and segmental lining’s extradoses.
- 4) Lining deformation caused by the earth pressure.
- 5) Long term deformations. In clays due to the consolidation or creep, and in soft rocks owing to delayed deformations.

These causes are respectively illustrated in Figure 2.8.

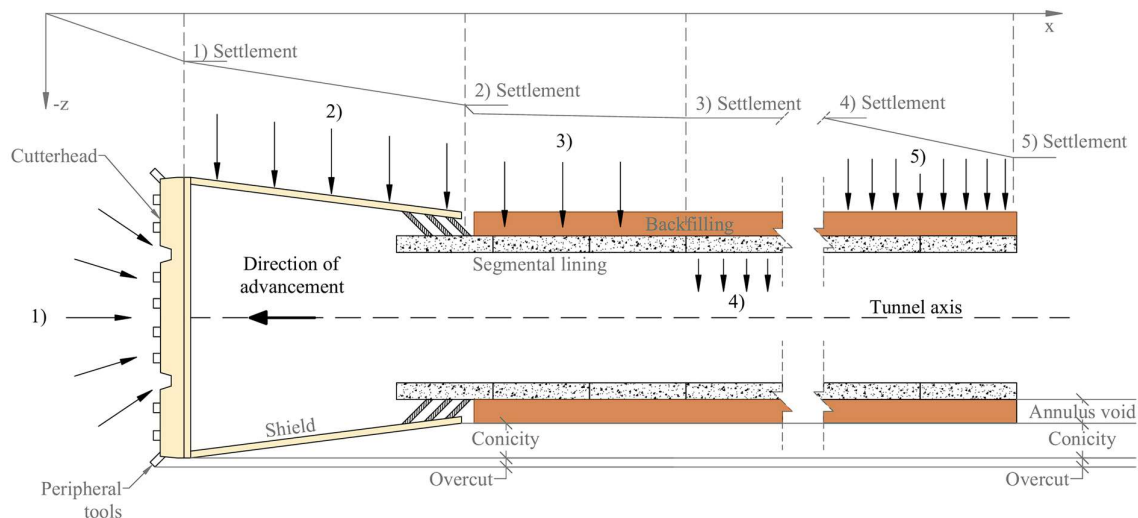


Figure 2.8. Causes of the settlement trough during mechanized tunnelling

As readily apparent, the greatest settlements are mobilized ahead of the face, along the shield length and in long-terms, depending on the soil’s granulometry. Concerning the first cause of Figure 2.8, with the perturbations induced by the cutterhead the soil’s effective stresses change ahead of the face of the excavation, boosting a decompression of the ground that can extend immediately in front of the face for one to two tunnel diameters at the depth of the excavation; while reaching significantly higher extensions as one approaches the ground surface. With this decompression, the soil loosens up and extrudes towards the void. To counter this effect, the EPB-TBMs exert a ‘face pressure’ (same pressure of the conditioned soil in the pressurized chamber), as depicted in the past Figure 2.3, not ever entirely nullifying the perturbations and consequently, minor surface settlements should still be expected.

For the second and third causes, the next Figure 2.9 excellently depicts the gaps that form around the machine during the excavation, detailing the overcut and conicity widths that account for the *shield steering gap*, and the shield and grout thicknesses that create the *annulus void* jointly with the former gaps. The reader is encouraged to remember this terminology by heart, as this figure will be recalled several times within the essay, echoing the importance that the gaps have in the tunnelling process.

These gaps, that appear vacant in the figure below, allow for the free convergence of the surrounding ground increasing the surface settlements, if no countering measures are taken. These concepts are, however, explored in more detail in Chapter 3.

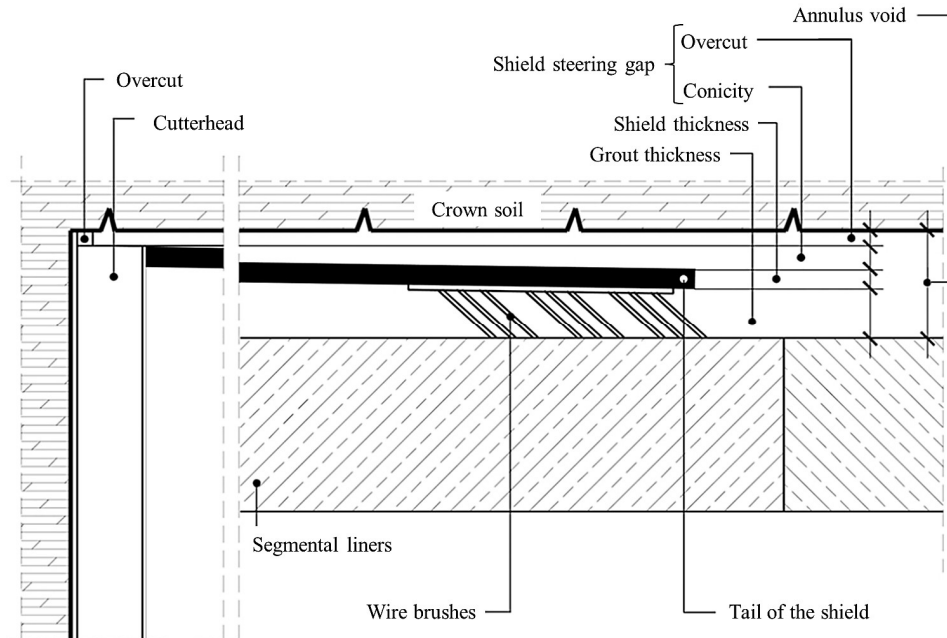


Figure 2.9. Detail of the shield – ground gaps and their causes at the crown of the excavation, modified from Thewes & Budach (2009) as seen in Todaro, Saltarin & Cardu (2022)

For what concerns the fourth cause, from Figure 2.8 it is hinted that the cumulative settlements immediately after cause 3) have not increased. Indeed, it is usual to neglect the deflection of the lining, since from the structural design the segments and their connections are envisioned to resist normal forces and bending moments, indirectly diminishing possible deflections by assigning to them capable thicknesses and abundant reinforcement, originally to counter the earth pressure and most importantly, the jacking forces of the TBM. Furthermore, if fast-hardening backfilling is used, such as the two-component grout, the liners are expected to remain rigidly fixed in position, nullifying any possible deflection.

The fifth and final cause is the long-term ground deformation, especially the consolidation in clayey soils. In foundation engineering, the consolidation settlement in fine grained soils is typically the most concerning component of the settlements in comparison to the immediate one. Tunnelling is no exception to the rule; nevertheless, here the reason is not simply the natural dissipation of the excess water pressure into the soil. In fact, even though ahead of the excavation and around the segmental liners where the backfilling is injected the pore water pressure increases significantly, it

returns naturally to its original state in a relatively short period (depending on the soil's permeability, i.e. in less than one week for Kasper & Meschke (2004)). Still, the truly significant long-term settlements caused by tunnel excavations in clay have been recorded to be active for years and even decades after the conclusion of the works, increasing in magnitude up to three times the immediate settlement (Bowers, Hiller, & New, 1996; Burland, 2001; Avgerinos, Potts, & Standing, 2016; Rampello, Callisto, Viggiani, & Soccodato, 2012). This has been justified, in certain cases, by acknowledging the effect that the permeability of the tunnel segmental lining has (Mair & Taylor, 1997), rendering it an artificial water drain that dissipates the pore water pressure around the excavation walls, increasing the effective stresses and with it, increasing the consolidation settlement (Yiu, 2018).

Now, returning to Figure 2.7 it is never made direct reference to the surface settlements but to 'losses', precisely the face loss and the shield and annulus radial losses. These losses, product of the soil's stress relaxation, are excess ground movements towards the cavity that accumulate to render the real excavated soil volume much larger than the theoretical one. The relationship between these two volumes is called the tunnel volume loss, and one of its consequences is the formation of the settlement trough. In a cartesian reference system, this trough can be represented in free field conditions (or greenfield, meaning no surface structures are present) as shown next (the same orientation of the X, Y and Z axes will be retained along the document, unless stated otherwise).

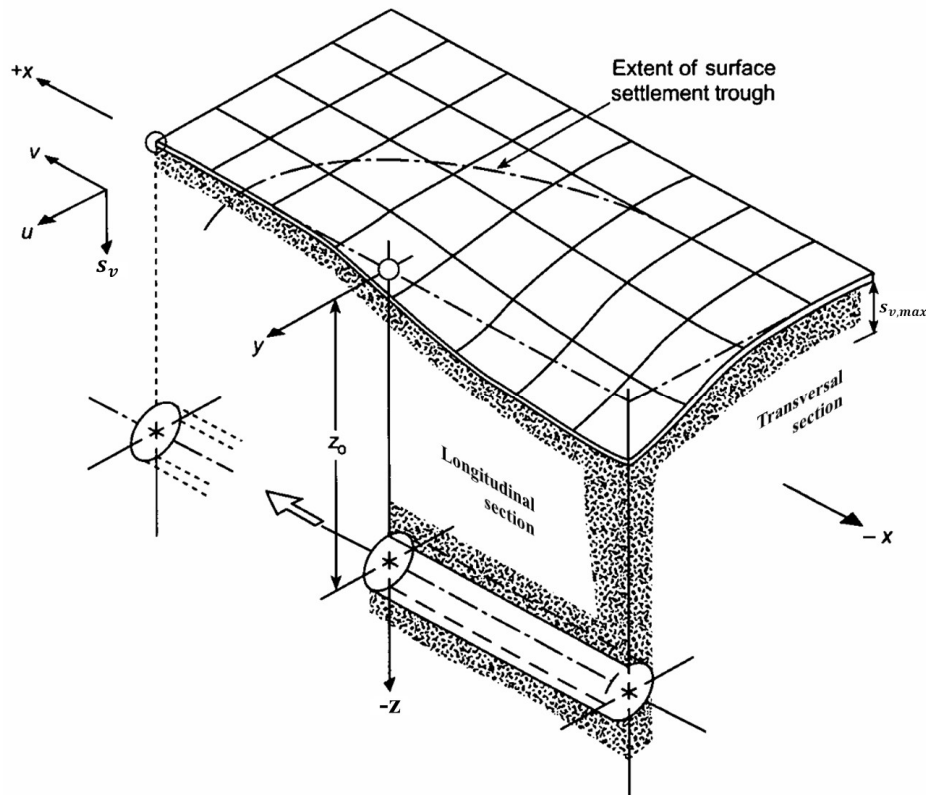


Figure 2.10. Basin of subsidence in greenfield conditions, modified from Burland (*Assessment methods used in design*, 2001)

In the longitudinal section of the previous figure, the settlement trough above the tunnel axis and the companion horizontal displacements can be illustrated as follows.

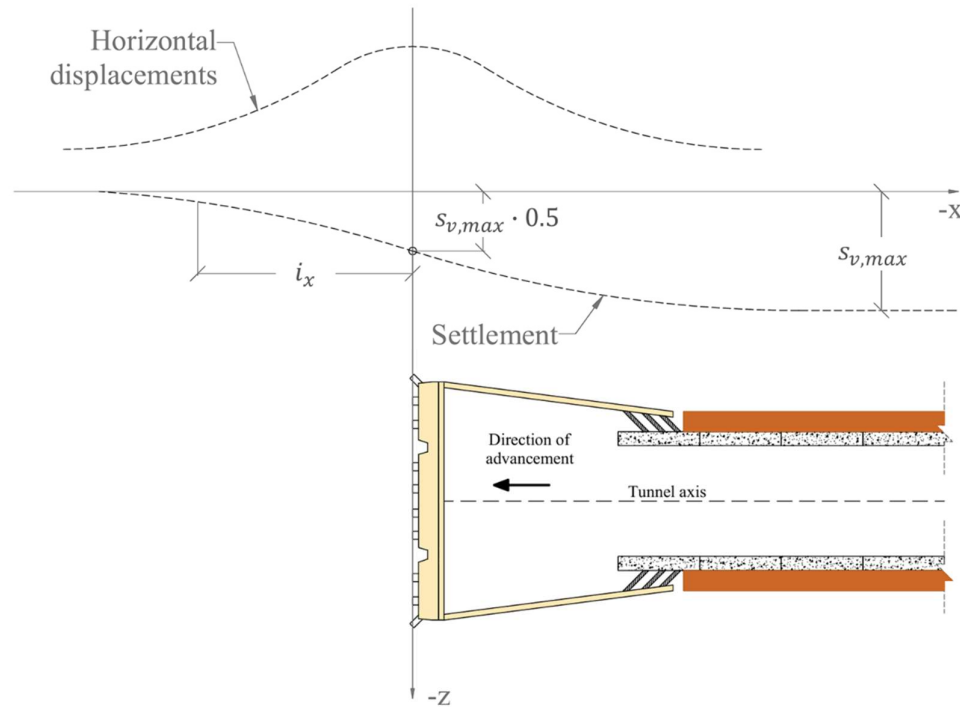


Figure 2.11. Longitudinal settlement trough, adapted from Uriel & Sagaseta (1989)

The longitudinal trough is often approximated to a cumulative normal distribution, as per Attewell & Woodman (1982):

$$s_v(x)_{y=0} = s_{v,max} \cdot \frac{1}{i_x \sqrt{2\pi}} \int_{-\infty}^x e^{-\frac{x^2}{2i_x^2}} \quad (2.1)$$

Here, as also depicted in the figure above,  $s_{v,max}$  is the maximum value of the settlement at steady-state and  $i_x$  is the distance equal to half one standard deviation from the inflection point of the curve, most often than not located above the tunnel face where typically  $s_v(0)_{y=0} = 0.5 \cdot s_{v,max}$ .

Conversely, in the transversal section of the figure the settlement trough above the tunnel axis and the companion horizontal displacements are illustrated in the following Figure 2.12. The transversal settlement trough at steady-state (or permanent) deformations is often approximated to a normal probability distribution, idea first proposed by Peck (1969) and then mathematically expressed by Attewell & Woodman (1982) as:

$$s_v(y)_{x=-\infty} = s_{v,max} \cdot e^{-\frac{y^2}{2i_y^2}} \quad (2.2)$$

Here,  $i_y$  is the inflection point of the curve, also known as the trough half-width parameter, that separates the sagging from the hogging zones of the settlement curve. Mathematically it represents the standard deviation of the normal distribution, yet in tunnelling it can be related to the ground conditions and depth of the tunnel axis  $z_0$  (O'Reilly & New, 1982; Mair & Taylor, Bored tunnelling in the urban environment, 1997; Chirioti, Marchionni, & Grasso, 2001). It should be noted that, from the same figure, the maximum horizontal displacements occur in correspondence with the inflection point of the settlement trough.

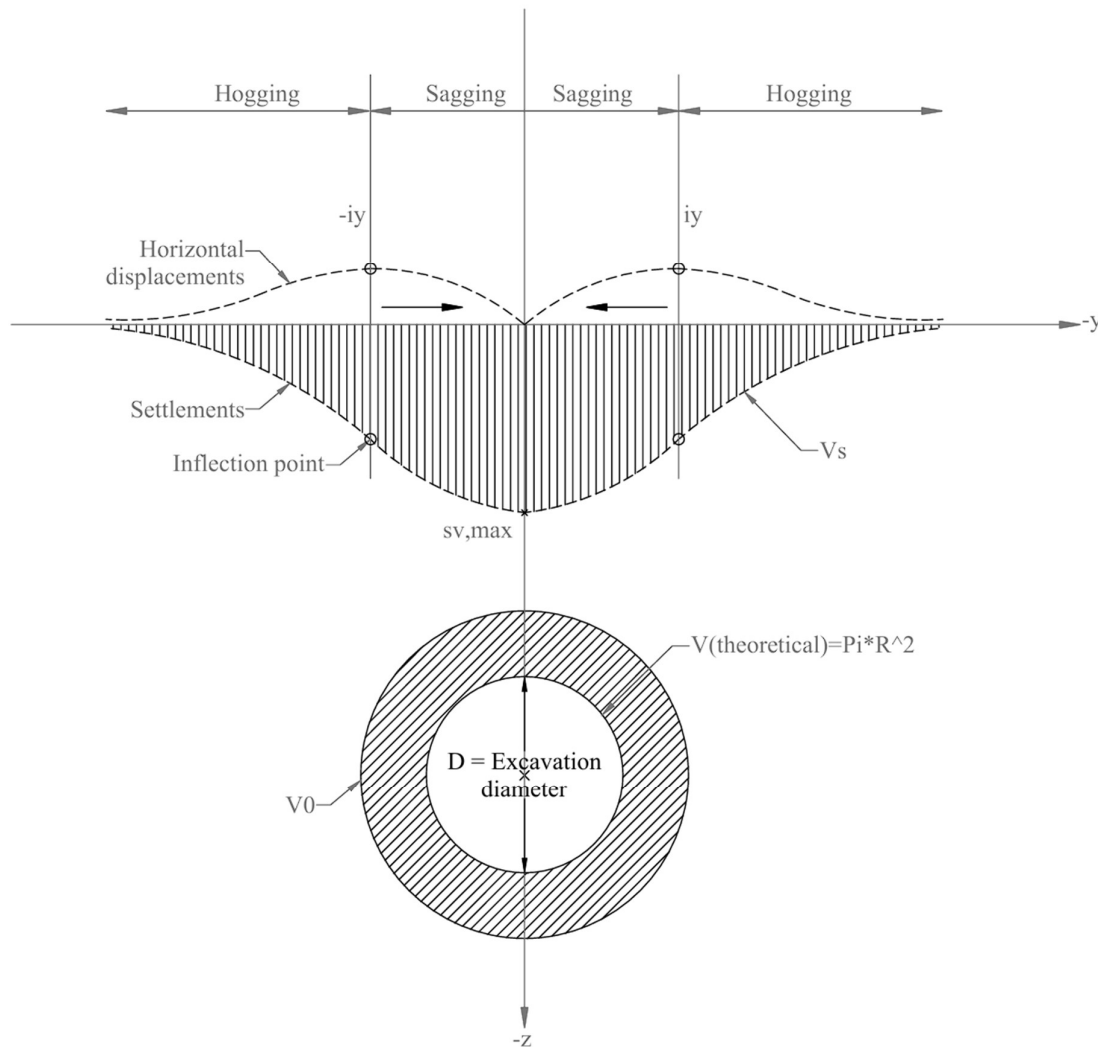


Figure 2.12. Transversal settlement trough

In the previous figure,  $V_0$  is the extra excavated soil volume,  $V_s$  is the volume of the settlement trough and  $V_{Theoretical}$  is the design or theoretical excavation volume. These volumes can be related by two different 'volume losses' to provide a measurement of the soil disturbance due to the excavation (Yiu, 2018). The tunnel volume loss can be calculated as:

$$V_L^T = \frac{V_0}{V_{Theoretical}} \cdot 100\% \quad (2.3)$$



And the settlement volume loss as the relationship:

$$V_L^S = \frac{V_s}{V_{Theoretical}} \cdot 100\% = \frac{V_s}{\pi \cdot \left(\frac{D}{2}\right)^2 \cdot L_{exc,T}} \cdot 100\% \quad (2.4)$$

Where  $D$  is the diameter of the excavation and  $L_{exc,T}$  is the total excavation length of interest, in steady state. If the volume of the settlement trough is defined as  $V_s = A_s \cdot L_{exc,T}$ , with  $A_s$  being the area of the settlement trough, calculated as:

$$A_s = \int_{-\infty}^{\infty} s_v(y)_{x=-\infty} dy = \sqrt{2\pi} i_y \cdot s_{v,max} \quad (2.5)$$

Then the settlement volume loss can be rewritten as:

$$V_L^S = \frac{4\sqrt{2\pi} i_y \cdot s_{v,max}}{\pi \cdot D^2} \cdot 100\% \quad (2.6)$$

Contrary to the concentric deformation mode hinted by the tunnel volume loss in the past figure, some authors have suggested to account for a more realistic composite deformation sequence. As fittingly illustrated by Pinto & Whittle (2014) in the next Figure 2.13, the d) final shape of the deformed tunnel void is the addition of the well-known a) uniform convergence due to changes in the volumetric stress, with b) an ovalization given the long-term changes in the deviatoric stress and c) a rigid vertical translation that counters the buoyancy effect.

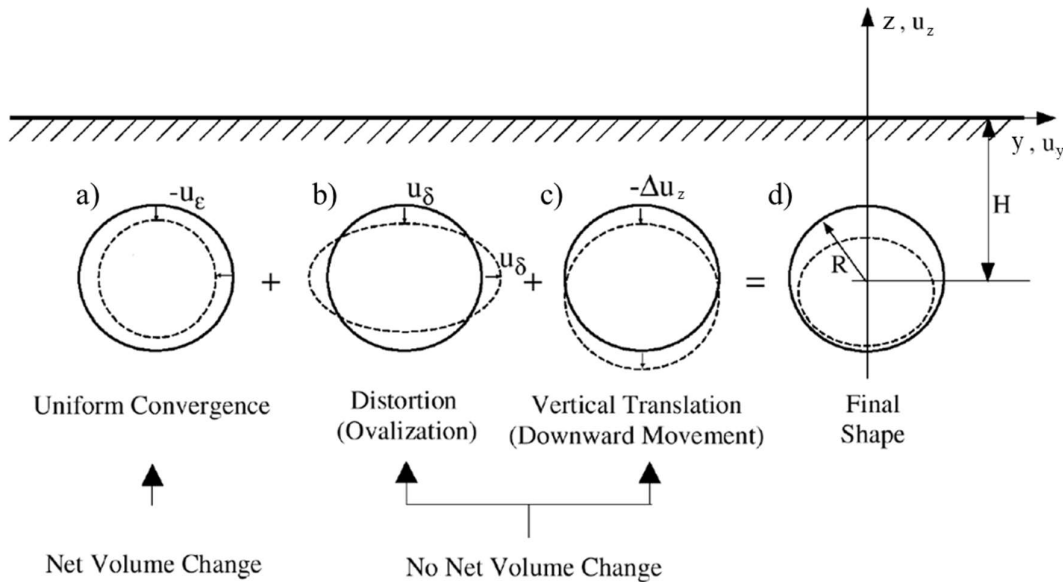


Figure 2.13. Tunnel walls deformation modes, as presented by Pinto & Whittle (2014)

A simpler, more straightforward alternative is to disregard the ovalization of the walls to only concentrate on the a) and c) deformation modes. Rowe & Kack (1983) were the first to visualize these modes; nevertheless, the authors did not give them a theoretical meaning as Pinto & Whittle after them, but they attributed these deformations to the construction technique: a) uniform convergence due to an uniform gap formed out of the difference of diameters between the excavation and the segmental liners, and b) rigid vertical displacement due to the weight of the lining that forces the rings to rest at the invert. From this, the *gap* physical distance is defined as in the following Figure 2.14.

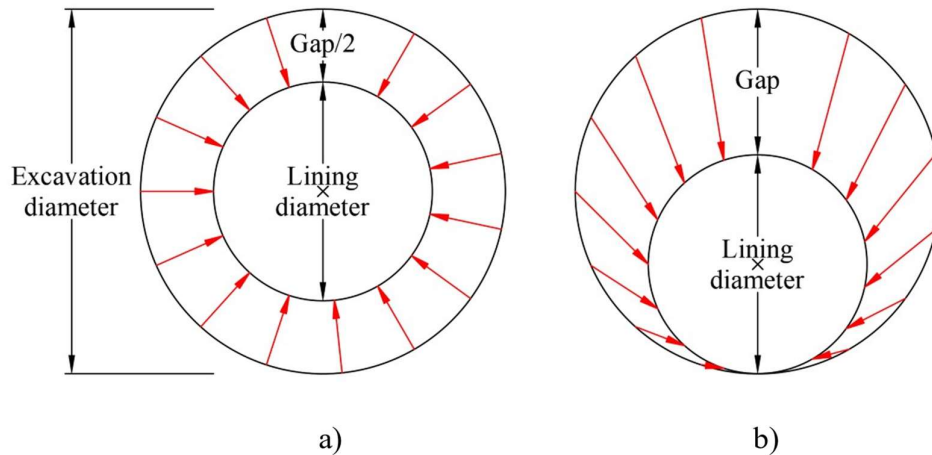


Figure 2.14. Definition of gap as a physical distance, after Rowe & Kack (1983)

In the literature, however, the definition of the gap as a measure is not well standardized, with some authors referring to the *gap* as the distance between the excavation intrados and the lining extrados (in contrast with Figure 2.14 with this distance being half the gap), instead of it being the difference between both diameters. In the present text, the definition of gap by Rowe & Kack is consistently employed, while in some cases denominations such as *width* or *thickness* are used to refer to specific voids left during the excavation.

### 2.3.1 Empirical methods

With the objective of predicting surface settlements induced by tunnelling works, several authors have proposed empirical relations resulting from their experience and monitoring data collected from completed excavations. From Peck (1969), Attewell & Woodman (1982) and O'Reilly & New (1982) to Oteo & Moya (1979), Romo & Diaz (1981) and Loganathan & Poulos (1998), various empirical and semi-empirical well-known expressions have been derived to describe the problem in three dimensions. Here, only a selected few are hastily explained because these will be used to compare the numerical results obtained in this thesis.

### 2.3.1.1 Probability distributions for the settlement estimation

As anticipated by Equation (2.1), the shape of the transversal settlement trough can be approximated to a normal distribution. The first to propose this was Peck (1969), based on a literature review of tunnelling case studies which stratigraphies ranged from stiff to plastic and expansive clays, cohesionless to cohesive granular soils, with the water table both above and below the tunnel, excavated both with shielded machines and conventional methods, being mono or twin tunnels of different diameters and overburdens. The variety of the cases gave a strong credibility to Peck's method to predict surface settlements induced by tunnelling, although it remains an empirical approach for which the parameters of the maximum settlement  $s_{v,max}$  and trough widths  $i_x$  and  $i_y$  must be proposed. In a gambling attempt, the current practice in the industry is to assume an 'average' and a 'conservative' value of the settlement volume loss, respectively equal to, for example, 0.5 and 1.0% (although it truly depends on the experience with past excavation labors) and from it, deriving the unknown statistical parameters. If this practice is not coupled with an extensive monitoring phase during the excavation it truly becomes a gamble, against Peck's sentiments on the matter and directly, the transience that he himself assigns to the method when declaring: "the use of this curve has no theoretical justification, it provides at least a temporary expedient for estimating the settlements to be expected at varying distances laterally from the center line of a tunnel" (Peck, 1969).

Building upon Peck's proposal, Attewell & Woodman (1982) subsequently suggested to approximate the longitudinal settlement trough to a cumulative probability function as per Equation (2.1), comparing successfully the method with monitoring data from tunnels in the United Kingdom.

### 2.3.1.2 Loganathan & Poulos' (1998) method for the settlement estimation

The authors' method for the prediction of the settlements builds upon Verruijt & Booker's (1996) analytical proposal in plane strain, which calculated the displacements of an elastic semi-infinite half space around a cavity, without distinguishing the granulometry of the material. Contrary to the latter, Loganathan & Poulos particularize the solution by neglecting the long-term ovalization of the cavity and furthermore, by introducing a parameter named the equivalent undrained ground loss  $\varepsilon_0$ , different from the volume losses studied previously, which was stated in function of the radius  $R$  of the tunnel as:

$$\varepsilon_0 = \frac{4 \cdot GAP \cdot R + GAP^2}{4R^2} \quad (2.7)$$

This parameter, as its name suggests, is only applicable in undrained scenarios given that it depends on the GAP parameter, not to be confused with Rowe & Kack's (1983) *gap* physical distance studied before. The GAP parameter, for Loganathan & Poulos, can only exist in undrained conditions because they declare that the oval-shaped physical *gap* forms in a limited time frame just after the passing of the cutterhead, disregarding consolidation or creep ground losses. The expression is:

$$GAP = gap + U_{3D}^* + w \quad (2.8)$$

Here the *gap* is the same as Rowe & Kack's (1983) physical distance equal to the difference of diameters between the excavation and the segmental liners,  $U_{3D}^*$  is half the soil extrusion at the front of the excavation and  $w$  is a value to account for workmanship when the lining rings are erected and to the overcut produced by the TBM's peripheral tools (Lee, Rowe, & Lo, 1992). In particular, the *gap* distance can be reduced to 7~10% because the void is typically filled with grout, only accounting in this case for the shrinkage of this material.

With the newly defined equivalent undrained ground loss  $\varepsilon_0$ , Loganathan & Poulos modified Verruijt & Booker's (1996) analytical proposal and expressed the ground surface settlements, also in function of the depth of the axis of the tunnel  $z_0$ , the Poisson's ratio of the soil  $\nu$  and the transversal distance  $y$  from the tunnel axis, as:

$$s_\nu(y)_{x=-\infty} = 4(1 - \nu)R^2 \cdot \frac{z_0}{R^2 + z_0^2} \varepsilon_0 \cdot e^{\left[-\frac{1.38y^2}{(R+z_0)^2}\right]} \quad (2.9)$$

If this is an analytical formulation, as it was derived from Verruijt & Booker (1996), why is it included in the empirical methods in the present essay? The reader is exhorted to write this expression in a spreadsheet and to vary the GAP parameter by just half a centimeter to see how sensible the settlement volume loss is to this value. Indeed, the entire expression is heavily dependent on  $\varepsilon_0$ , which in turn is function of the GAP, that once again is function of other three parameters, the *gap*,  $U_{3D}^*$  and  $w$ , that are entirely empirical and even idealistic, as no one has stepped in front of an active TBM to measure the face extrusion or the overcut. Therefore, here it is argued that the same equivalent undrained ground loss  $\varepsilon_0$ , which depends on the value of the GAP, can be adjusted to fit any condition that the designer may consider reasonable. As an example, in 1992 (by Lee, Rowe & Lo) it was declared that the *gap* distance could be reduced by the 7~10% when grout was injected around the liners to reduce the convergence. However, shrinkage effects are mostly true for mono-component cement-based grouts, not two-component grouts. If the project involves the use of two-component grouts, common contemporary choice, the *gap* parameter can therefore be reduced without constraint, even nullified, as no data exists for its contraction around the liners and some researches even argue that it immediately locks the displacements of the soil (Pelizza, Peila, Sorge, & Cignitti, 2012); and in this way, the values of the GAP and of the  $\varepsilon_0$  are immensely altered. In prediction, always the most conservative alternative is to be chosen. In monitoring, on the other hand, the advantage is that the value of the GAP can be calibrated to produce the best fit with the obtained in-situ settlements, allowing to use Loganathan & Poulos' method in a wider variety of cases and not only in soils of fine granulometry (undrained), remembering that the original solution by Verruijt & Booker (1996), before the invention of the empirical  $\varepsilon_0$ , was a general solution.

Loganathan & Poulos also provide the formulation for the subsurface settlements at a depth  $z$ :

$$s_v(y)_{x=-\infty}^{z>0} = R^2 \left\{ -\frac{z - z_0}{y^2 + (z - z_0)^2} + (3 - 4\nu) \frac{z + z_0}{y^2 + (z + z_0)^2} - \frac{2z[y^2 + (z + z_0)^2]}{[y^2 + (z + z_0)^2]^2} \right\} \varepsilon_0 \cdot e^{\left\{ -\left[ \frac{1.38y^2}{(R+z_0)^2} + \frac{0.69z^2}{z_0^2} \right] \right\}} \quad (2.10)$$

### 2.3.1.3 Horizontal displacements and strains

As depicted in the past Figure 2.12, surface horizontal soil movements are also induced with the formation of the basin of subsidence. Empirically, following O'Reilly & New (1982) these can be estimated with:

$$u(y)_{x=-\infty} = -\frac{y \cdot s_v(y)_{x=0}}{z_0} \quad (2.11)$$

Here  $s_v(y)_{x=-\infty}$  are the steady-state (or permanent) transversal surface settlements and  $z_0$  is the depth of the tunnel axis. And with horizontal displacements horizontal strains follow. Indeed, the same O'Reilly & New (1982) formulated the next expression for the horizontal strains:

$$\varepsilon(y)_{x=-\infty} = \frac{s_v(y)_{x=0}}{z_0} \cdot \left( \frac{y^2}{i_y^2} - 1 \right) \quad (2.12)$$

## 2.3.2 Analytical methods

Analytical methods take advantage of simplifications, such as assuming homogeneous and undrained stratigraphies, to fit the prediction of the surface settlements in either the transversal or longitudinal directions with mathematical closed form expressions. In the same spirit as done for the empirical methods, here only a selected few analytical methods are reviewed because these will be used to compare the numerical results obtained in this thesis.

### 2.3.2.1 Sagaseta's (1987) method for the transversal settlement estimation

Prof. Sagaseta was the first to solve the problem of the estimation of tunnelling induced surface settlements in an analytical, closed form scheme. And as a first approximation in 1987, it came with various limitations as it considered the tunnel cavity to inhabit a half space soil of isotropic, homogeneous and incompressible characteristics, the incompressibility being the most discussed assumption, yet according to the author it is applicable in undrained conditions (i.e. soft saturated clays) when short-term displacements are the primary concern. With these assumptions, the surface displacements are easily obtainable as vertical point loads at the surface of the half space produce zero horizontal displacements and horizontal point loads at the surface produce zero vertical displacements. Following Uriel and Sagaseta (1989), this

indicates that the surface displacements in a half space due to the ground loss double the value of the displacements in the same plane for an infinite medium. The original solution obtained by Sagaseta (1987) for the transversal settlements is:

$$s_v(y)_{x=-\infty} = \frac{V_s}{\pi} \cdot \frac{z_0}{y^2 + z_0^2} \quad (2.13)$$

Where  $V_s$  is the volume of the settlement trough from Figure 2.12. This solution is, however, known to underestimate the settlements for which further updates to the method were performed to include elastic anisotropy and compressibility (Uriel & Sagaseta, 1989) and the effects of volume loss and the ovalization deformation mode of the tunnel (González & Sagaseta, 2001).

### 2.3.2.2 Verruijt & Booker's (1996) method for the settlement estimation

Working in plane strain, the authors proposed a closed form solution to calculate the displacements of a linear elastic semi-infinite half space around a cavity, building upon Sagaseta's (1987) isotropic, homogeneous and incompressible soil half space. Verruijt & Booker removed the incompressible soil assumption, allowing the use of arbitrary Poisson ratios, and they further added the possibility to account for the ovalization mode of the tunnel deformation. For their formulations, the authors considered only deformation modes a) uniform radial convergence and b) ovalization (retrieving Figure 2.13), respectively with the parameters  $\varepsilon$  and  $\delta$  representing the relative displacement of the tunnel excavation walls (written as percentages). The proposed equation for the surface settlements is:

$$s_v(y)_{x=-\infty} = 4\varepsilon(1 - \nu)R^2 \cdot \frac{z_0}{y^2 + z_0^2} - 2\delta z_0 R^2 \cdot \frac{y^2 - z_0^2}{(y^2 + z_0^2)^2} \quad (2.14)$$

The settlement trough area can be found by integrating this equation in the domain  $-\infty < y < +\infty$ . The result is:

$$A_s = 4\varepsilon\pi(1 - \nu)R^2 \quad (2.15)$$

Which can be rewritten as:

$$\varepsilon = \frac{1}{4(1 - \nu)} \cdot \frac{A_s}{\pi R^2} \quad (2.16)$$

The fraction to the right is reminiscent of the settlement volume loss relationship studied in Equation (2.4). Then the relative uniform radial convergence is:

$$\varepsilon = \frac{V_s}{4(1 - \nu)} \quad (2.17)$$

The ovalization  $\delta$  is suggested to be calculated as the fraction between the maximum value of the radial displacement of the tunnel walls and the radius of the tunnel (González & Sagasetta, 2001).

### 2.3.3 Numerical methods

In complex stratigraphic conditions, when the soil cannot be considered as an isotropic homogeneous medium, and when more intricate analyses are needed regarding the full mechanized excavation and its effect on surface structures, empirical and analytical methods become unable to provide reliable predictions of the subsidence basin. It is in these cases that numerical methods are used, especially based in the finite element method (FEM) which uses a discretized domain, predefined boundary conditions, material constitutive equations and iterative solving algorithms to resolve boundary value problems in terms of a primary value, typically the displacements of the nodes of the domain. An in-depth review of numerical models for the estimation of the subsidence is presented in the next Chapter 3.

## 2.4 Building risk of damage estimation

Until this point it has been well established that shallow tunnelling activities induce displacements in the surrounding soil, propagating towards the surface or, if buildings are present, towards the base of the foundations generating settlements. The influence of the settlements on building risk of damage has been well studied in foundation engineering, with Terzaghi & Peck (1948) suggesting a limiting value of 25 mm for the maximum settlements of footings in sand and 75% of this value for the differential settlements or Rankin (1988) proposing a limiting value for the rotation of 1/500 and maximum settlement of 10 mm to avoid building damage.

These parameters: maximum settlement  $s_{v,max}$ , differential settlement  $\delta s_v$  and rotation  $\theta$  are highlighted in the figure below for an initially horizontal foundation A-B-C-D that subsides with a given settlement.

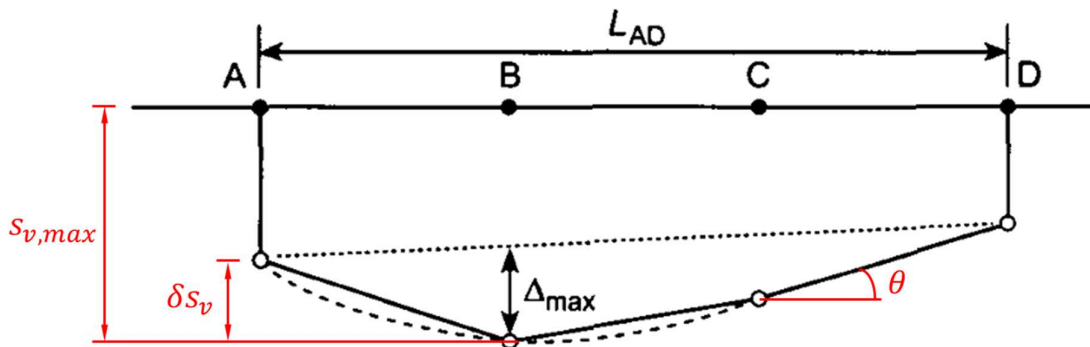


Figure 2.15. Measurements of foundation movement, modified from Burland & Wroth (1974)

The parameter not mentioned in the first paragraph is the relative deflection  $\Delta_{max}$  (existent both in sagging and hogging modes of deformation) that is the maximum displacement relative to the straight line connecting two reference points at a distance  $L$  apart (Burland & Wroth, 1974). From this, the deflection ratio is denoted as  $\Delta/L$ .

Now, specifically for buildings of masonry load-bearing walls, according to Burland and Worth (1974), from a series of experimental tests regarding numerous masonry walls in the UK, the material starts cracking from a well-defined value of the average tensile strain, independently of the mode of deformation: either bending or shear. After this realization, the authors defined the critical tensile strain  $\varepsilon_{crit}$ , measured as the average tensile strain in a length of 1 meter or more at which the onset of masonry visible damage occurs, and has no saying in the prediction of loss of serviceability or structural collapse. In this sense,  $\varepsilon_{crit}$  is not a replacement of the ultimate tensile strain of the material, obtained from indirect tensile tests, for example.

After Burland & Wroth, Boscardin & Cording (1989) developed the concept of limiting tensile strain  $\varepsilon_{lim}$  from a little less than 20 case records of masonry building damage registered during tunnel excavations. The authors defined five ranges of  $\varepsilon_{lim}$  and correlated them with a “degree of severity” of building risk of damage (this term will be often used in this thesis to describe potential building damage) from *negligible* to *very severe*. At this point, the concept of critical tensile strain evolved to the limiting tensile strain, now being able to provide serviceability limit states.

The next Table 2.1 lists the suggested damage categories for masonry buildings, integrating the proposals of Burland (as seen in Mair, Taylor & Burland (1996), based on the ease of repair) and Boscardin & Cording (1989). As emphasized by the authors, the listed crack widths are only one factor in assessing the category of damage and should not be used on its own as a direct measure of it.



Table 2.1. Damage categories for brickwork masonry, as presented by Mair, Taylor & Burland (1996) and Boscardin & Cording (1989)

Category of damage	Normal degree of severity	Description of typical damage	Limiting tensile strain [%] (Boscardin & Cording, 1989)
0	Negligible	Hairline cracks less than about 0.1 mm	0 – 0.05
1	Very slight	Fine cracks which are easily treated during normal decoration. Damage generally restricted to internal walls finishes. Close inspection may reveal some cracks in external brickworks or masonry. Typical crack widths up to 1 mm.	0.05 – 0.075
2	Slight	Cracks easily filled. Re-decoration is probably required. Recurrent cracks can be masked by suitable linings. Cracks may be visible externally and some repointing may be required to ensure weather tightness. Doors and windows may stick slightly. Typical crack width up to 5 mm.	0.075 – 0.15
3	Moderate	The cracks require some opening up and can be patched by mason. Repointing of external brick work and possibly a small amount of brickwork to be replaced. Doors and windows sticking. Service pipes may fracture. Weather tightness is often impaired. Typical crack widths are 5 to 15 mm or several up to 3 mm.	0.15 – 0.30
4	Severe	Extensive repair work involving breaking-out and replacing sections of walls, especially over doors and windows. Windows and door frames distorted, floor sloping noticeably. Walls leaning or bulging noticeably, some loss of bearing in beams. Service pipes disrupted. Typical crack widths are 15 to 25 mm but also depends on the number of cracks.	> 0.30
5	Very severe	This requires a major repair job involving partial or complete rebuilding. Beams lose bearing, walls lean badly and require shoring. Windows broken with distortion. Danger of instability. Typical crack widths are greater than 25 mm but depends on the number of cracks.	> 0.30

### 2.4.1 The EBA method

The great advantage of Burland & Wroth's proposal is that the authors proposed a way to relate the deflection ratio  $\Delta/L$  of a masonry wall with the critical (or limiting) tensile strain, the authors pointed out two modes for the crack formation in simple beams: bending and shearing, producing respectively vertical and diagonal cracks as show in

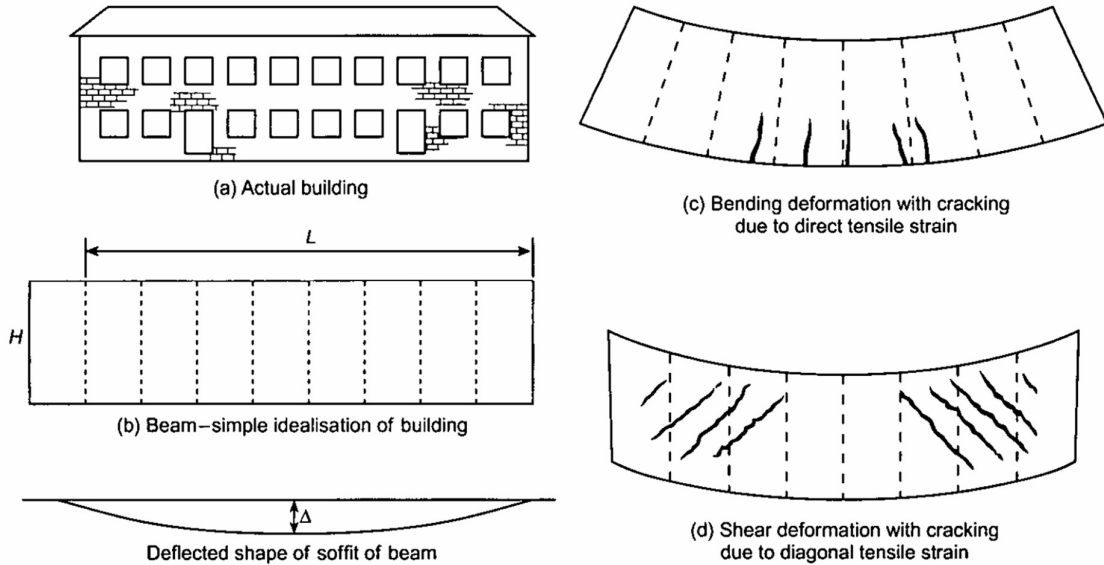


Figure 2.16. Cracking of a beam in bending and shearing deformation modes (Burland & Wroth, 1974)

In a Timoshenko deep beam analysis, also referred to as the elastic beam assessment (EBA) method, the relative deflection  $\Delta$  of the beam can be produced from a distributed or central point load. Burland & Wroth suggested that the differences between the two forms of loading had a small impact on the final result. In this way, the authors related the deflection ratio  $\Delta/L$  with the extreme fiber strain  $\varepsilon_b$  produced in bending and the maximum diagonal strain  $\varepsilon_d$  produced in shearing as:

$$\frac{\Delta}{L} = \left( \frac{L}{12t} + \frac{3I}{2tLH} \cdot \frac{E}{G} \right) \cdot \varepsilon_b \quad (2.18)$$

$$\frac{\Delta}{L} = \left( 1 + \frac{HL^2}{18I} \cdot \frac{G}{E} \right) \cdot \varepsilon_d \quad (2.19)$$

Here  $H$  is the height of the building from the foundation bottom to the eaves,  $I$  the inertial,  $L$  is the length of the foundation,  $E$  and  $G$  are the elastic parameters and  $t$  is the distance from the neutral axis to the fiber of interest. Accounting for hogging or sagging deformation modes of a wall, the length can be divided into two at the inflection point of the trough and thus, it is possible to consider two different values of  $L$  and  $\Delta$ , as depicted in the next (2.17).

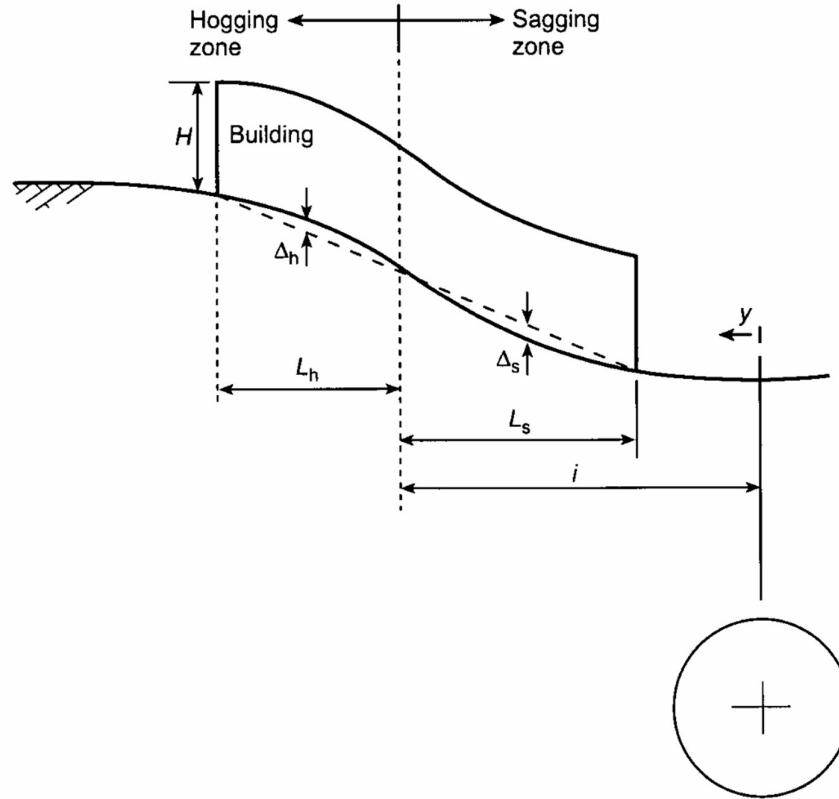


Figure 2.17. Sagging and hogging zone parameters for the deflection ratio (Burland, *Assessment methods used in design*, 2001)

Horizontal strains  $\varepsilon_h$  from the soil can also influence the bending and diagonal strains alike, therefore the total bending and diagonal strains accounting for the action of the horizontal strains can be obtained from:

$$\varepsilon_{bt} = \varepsilon_h + \varepsilon_b \quad (2.20)$$

$$\varepsilon_{dt} = 0.35\varepsilon_h + [(0.65\varepsilon_h)^2 + \varepsilon_d^2]^{0.5} \quad (2.21)$$

Setting  $\varepsilon_{bt} = \varepsilon_{lim}$  and  $\varepsilon_{dt} = \varepsilon_{lim}$  while varying the value of  $\varepsilon_h$  and then replacing in Equation (2.18) and (2.19), the next damage category charts can be obtained.

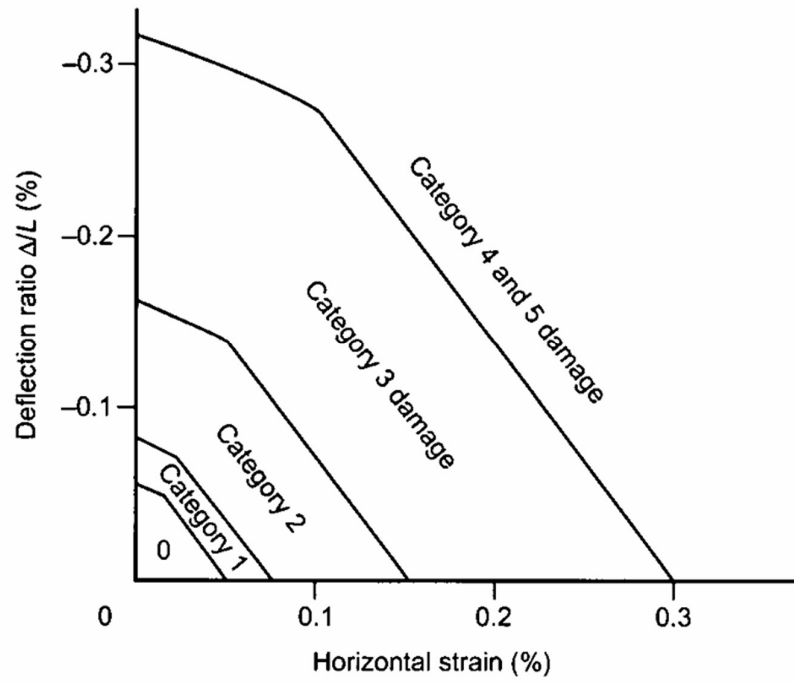


Figure 2.18. Damage category chart for hogging deformation mode with  $L/H=1$  (Mair, Taylor, & Burland, 1996)

### 2.4.2 Procedure for the risk of damage estimation

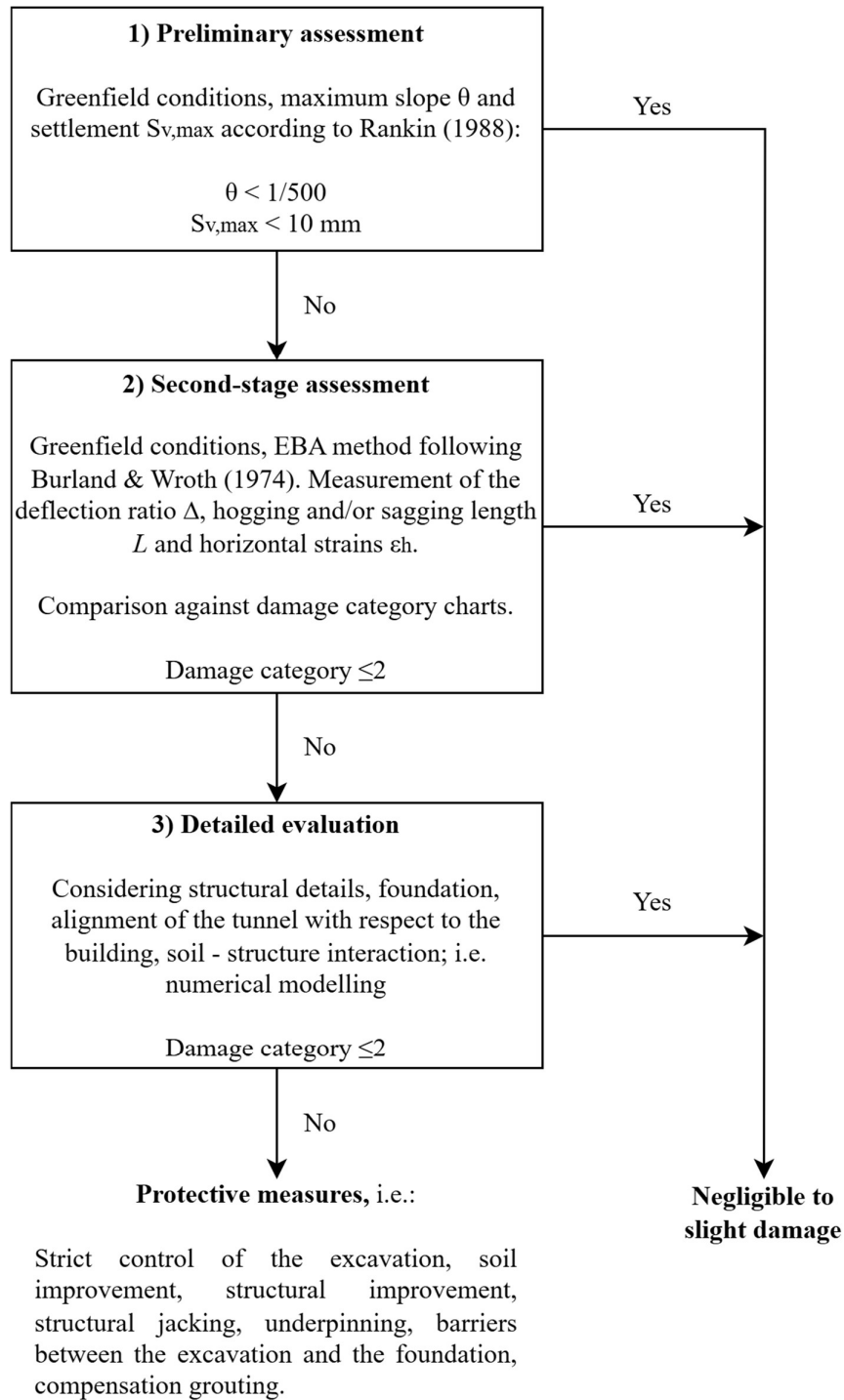


Figure 2.19. Framework for the building risk of damage assessment, after Burland (*Assessment methods used in design*, 2001)

## Chapter 3

# Numerical methods for the subsidence and building risk of damage assessment

### 3.1 The model of the tunnel excavation

In this chapter, emphasis is made on three-dimensional numerical models from the literature following the finite element method (FEM), that are built to simulate the excavation of a shallow tunnel, as these can be configured to well emulate the multiple complex mechanisms of the tunnelling process and the behavior of an equivalent continuum medium, such as the soil, as it is disturbed by the excavation. The cases here studied will then be the inspiration for the model used to analyze the subsidence in the Metro-Line 2 of Torino, later in Chapter 5.

In the next Figure 3.1, the standard configuration of a 3D geometrical mesh for the soil of a shallow tunnel excavation is shown, where the notation for the dimensions of width, length, and depth of the soil rectangular prism (or cuboid) are exhibited.

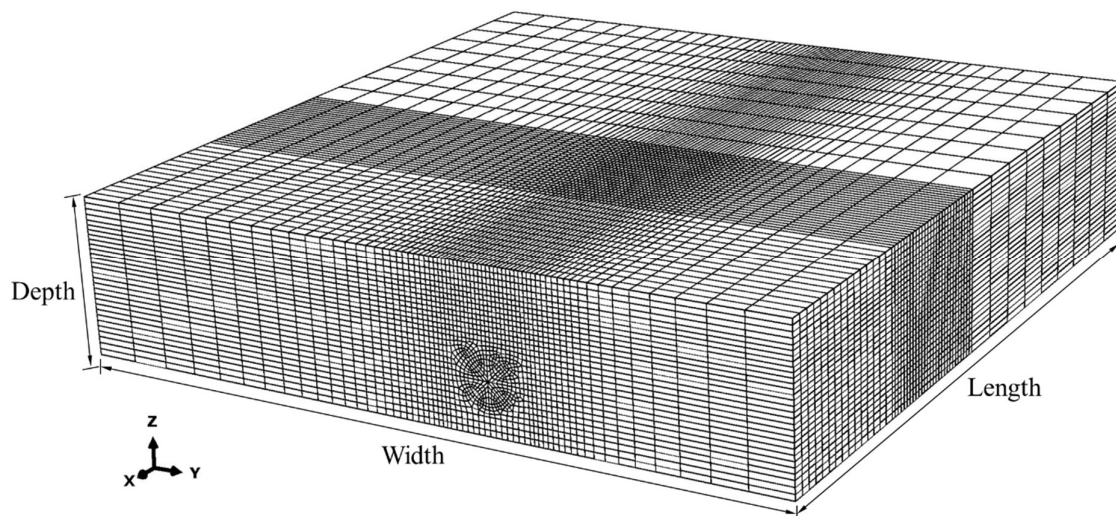


Figure 3.1. Typical configuration of a 3D geometrical model of the soil of a shallow tunnel excavation

Apart from the model of the soil, in some studies, especially those developed using numerical software that can handle contact interactions, the models of the segmental lining, the grout and the shield of the TBM are also incorporated as isolated parts that enter in interaction with the model of the soil. The word *parts* will be hereon used to refer to these separate models that can be assembled and, in this condition, are the base

to build the global numerical model. The standard configuration of the 3D geometrical model for the shield of the TBM and the lining plus grout are displayed in Figure 3.2. It must be remarked that the shield of the machine, accounting for its limited thickness, is usually modelled with shell elements while the lining and ground can be structured with solid elements. For both, the notations for the dimensions of the excavation length, liner internal diameter, liner thickness, annulus void and the shield diameter are exhibited.

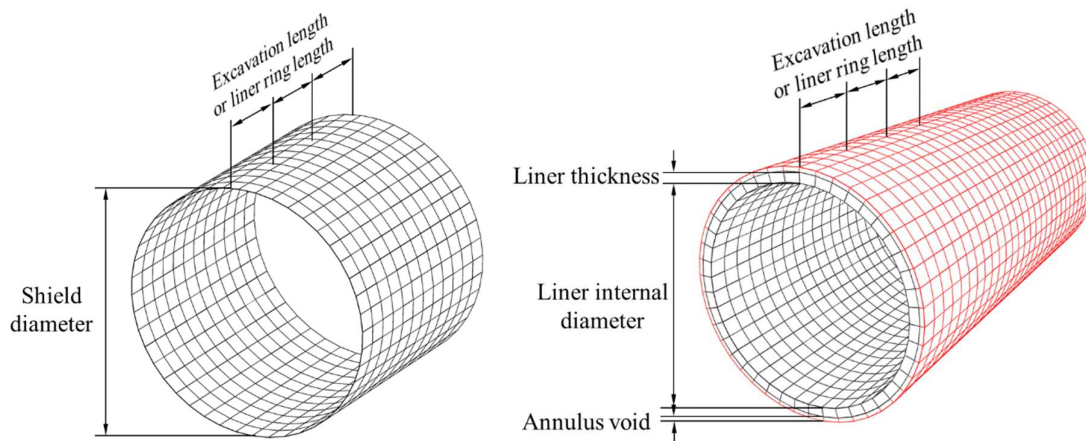


Figure 3.2. Typical configuration of a 3D geometrical model of the TBM shield and liner plus grout

### 3.1.1 Geometrical model and discretization

Here both the geometry and the mesh of various tunnel excavation models (for each part if present) are described, for a list of relevant research articles that successfully simulated the tunnelling process in three dimensions.

Starting with one of the most influential, intricate three-dimensional tunnelling models produced to date, which considered to an extreme level of detail the mechanized tunnel step-by-step excavation to even simulate the thrust force of the jacks of the machine, pitch and yawning of the TBM (to simulate also curved tunnels!), hydraulic conditions, grout permeability and time-dependent stiffness, contact between the separate parts of the shield, grout, converging soil and pressure chamber, and a multipart constitutive behavior for the soil such as the Cam Clay model; Kasper & Meschke's (2004) efforts to provide a generalized model (without reference to a specific project) would much later inspire other authors to prepare simpler yet well thought-out greenfield models that encompassed the main characteristics of the tunnelling process, to assess the sensibility of the overall excavation to each parameter.

A portion of the model mesh is presented in Figure 3.3, with the complete mesh being of a length of 108 m, width of 106m and depth of 55 m, with an excavation diameter of 6.3 m and an overburden of 9.45m; constituted by 3548 hexahedral solid elements with second-order integration for the soil, the grout and the lining, and nine truss elements for the jacks. From here, it can be concluded that the authors used a length of about

eight times the diameter of the excavation to widen the geometry to the sides beyond the tunnel sidewalls, avoiding the interference of the boundary conditions. In the vertical, the authors provided below the invert a depth of around six tunnel diameters with the same purpose.

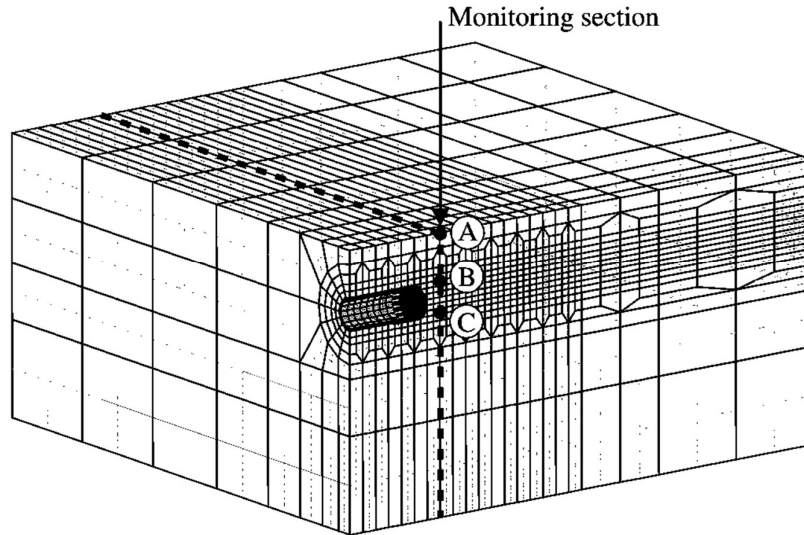


Figure 3.3. Portion of the model mesh by Kasper & Meschke (2004)

Inspired by Kasper & Meschke (2004), Kavvadas, Litsas, Vazaios & Fortsakis (2017) and then revised by Litsas, Sitarenios & Kavvadas (2017), in ABAQUS CAE (Dassault Systemes, 2024) presented a 220 m wide, 210 m long, 50 m deep rectangular prism for the soil model, with the excavation of a 10 m diameter tunnel centered in the width of the cuboid and advancing parallel to its length for 130 m, with an overburden of 15 m. Half of the model's mesh is shown in the Figure 3.4 below, in which the main dimensions of the problem are displayed in terms of the excavation diameter (this again, was not based on any specific project). This mesh was composed of 8-noded, fully integrated hexahedral solid elements (C3D8), and although no mention was made of the number of finite elements, from the picture alone it is expected to have around 200 thousand elements.

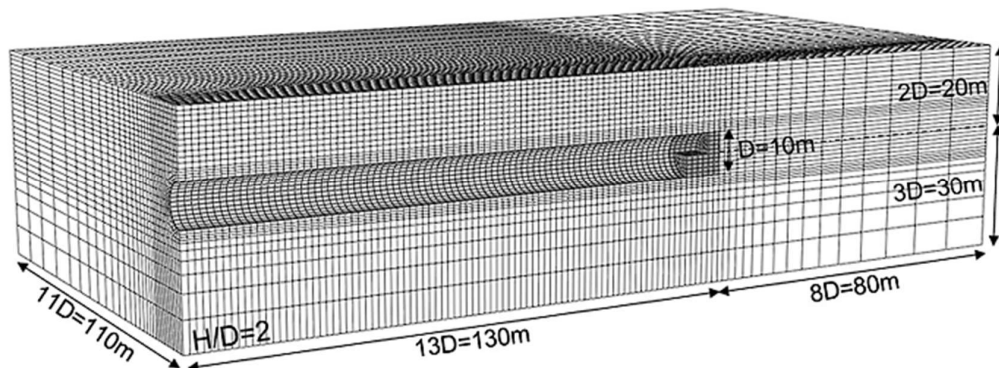


Figure 3.4. Half of the model's mesh by Kavvadas et al. (2017)



The authors comment that the choice of modelling the complete cuboid instead of exploiting the symmetry of the problem was made considering that the segmental liners were not modelled only as continuous entities, but some parametrical analyses included the joints between the rings and the segments. At the excavation front, the excavation chamber and EPB equipment were also modelled with C3D8 elements. Then, 4-noded shell elements (S4) were employed for the segmental lining, shield and the cutterhead (see Figure 3.5). Particularly, the liner segments and the shield were created as separate parts from the soil model and thus, it was required for the parts to interact through contact formulations (more on that under the headings 3.1.5.2 and 3.1.5.3).

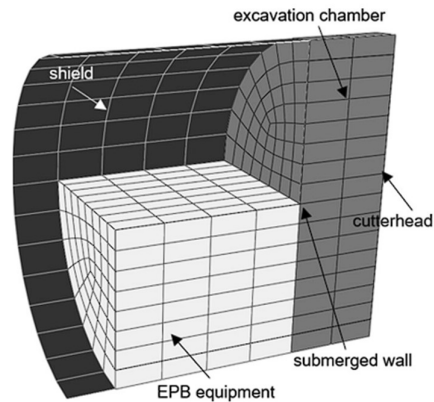


Figure 3.5. Mesh and geometrical model of the EPB machine (Kavvas et al., 2017)

Based on Yiu's (2018) detailed short- and long-term soil – structure interaction models, Amorosi & Sangirardi (2021) studied the necessity of formulating complex three-dimensional numerical models to study the damaging effect in surface masonry structures. Their model was, in any case, more simplified in comparison to those of the authors cited earlier (i.e. it did not consider explicitly the TBM machine or the thrusting jack forces to simulate the step-by-step advancement).

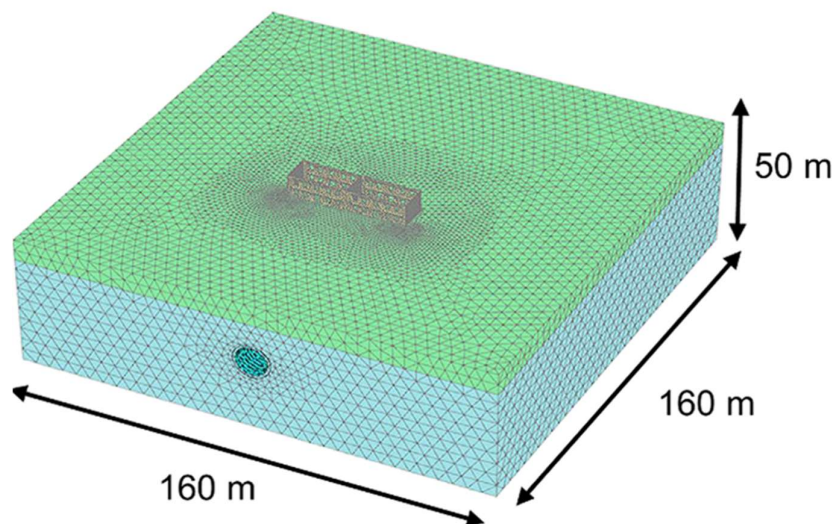


Figure 3.6. Soil – structure interaction model mesh by Amorosi & Sangirardi (2021)

The complete model mesh is in Figure 3.6 above, with the soil cuboid being built on 205 thousand 10-noded tetrahedral elements (second-order integration), and the shield and the lining with six-noded triangular plate elements. It can be noticed from the same figure that a higher mesh density was needed to transition from the soil to the building, given that in PLAXIS both entities belong to the same mesh and therefore, they must share nodes. Furthermore, in this numerical software it is not possible to simulate genuine contact interactions, and for the purpose of the interaction between the soil and the shield or the liners, interface elements were included. Having an overburden of 25.5 m and a tunnel diameter of 11.0, it can be deduced that the authors set the lateral boundaries of the model at around seven times the tunnel diameter, and a depth below the invert equal to about one tunnel diameter.

The most simplified numerical model in terms of discretization and geometrical complexity here revised is that of Mollon, Dias & Soubra (2012), precisely devised for simplicity and wide representation of multiple tunnelling cases. If from the next Figure 3.7 the shield or the TBM cannot be identified, it is because they were not explicitly modelled. The authors included a boundary condition at the nodes of the excavation boundaries to limit their free convergence when the displacement was equal to the shield gap.

The entire geometry of the model in FLAC3D is presented in the figure below, and it only represents half of the soil cuboid because the authors exploited the symmetry of the tunnelling problem in greenfield conditions, allowing them to reduce the number of hexahedral elements (or zones, as named in FLAC) to less than 100 thousand.

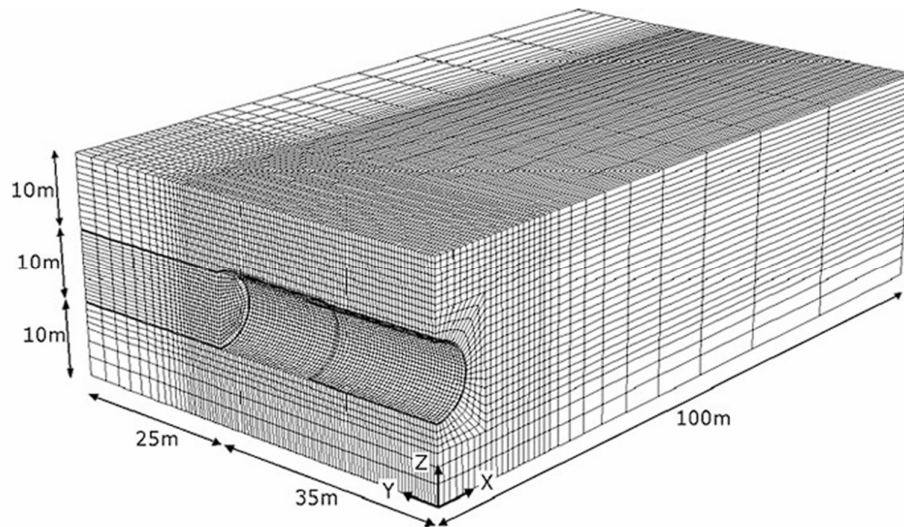


Figure 3.7. Model mesh by Mollon, Dias & Soubra (2012)

From the measures of the soil cuboid, especially the length in comparison to formerly revised proposals that allocated lengths higher than 100 meters (up to 210 meters for that of Kavvas et al. (2017)), the model of Mollon et al. only considered a length equal to 60 meters. This is a rather courageous modelling choice, since longitudinal settlement troughs are expected to extend ahead of the face of the excavation for several meters, at times reaching the 30 meters or more. Indeed, with such a near boundary in

the length, the authors reported some strong influences of the boundary as illustrated in Figure 3.8, where the soil body did not behave steadily after the passing of the TBM but rather showed an important uplift and spurious horizontal displacements. The solution provided by the authors was not increasing the geometrical length, because probabilistic analyses were to be performed and increasing the length signifies higher computational times both due to a larger number of finite elements and excavation steps. Instead, the authors proposed an alternative to superpose individual basins of subsidence, worth examining directly from their article.

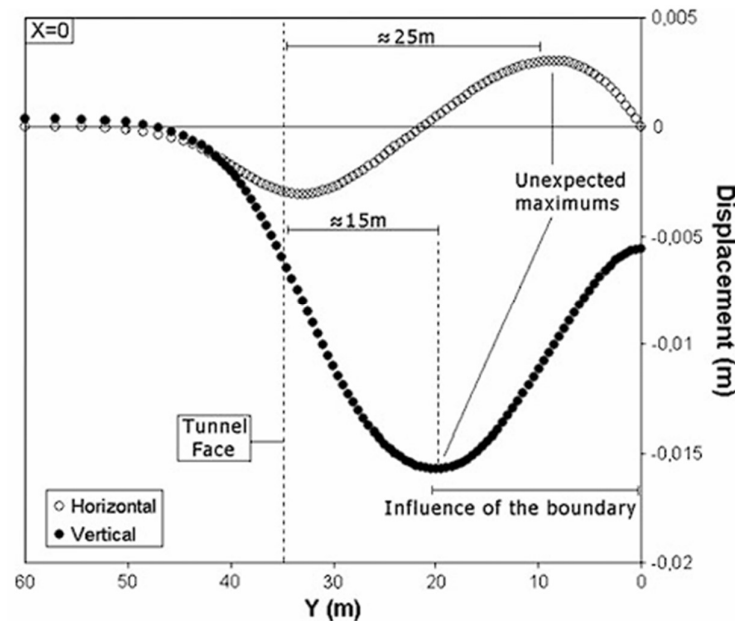


Figure 3.8. Influence of the boundary conditions on the numerical model along the longitudinal direction (Mollon, Dias, & Soubra, 2012)

### 3.1.2 Boundary conditions

Boundary conditions are what encloses the numerical problem, and the behavior of the domain is strictly linked to them. Their effects in well-defined models can provide for expected field, loading, displacement or contacting conditions; however, they can also play against the modelling purpose if not configured correctly or not placed at a prudent distance. Here, the most important boundary conditions of the excavation model are listed, with an important lot left to discuss in section 3.1.4 and 3.1.5.

#### 3.1.2.1 Soil external constraints

It is usual to find in the literature that the boundary conditions at the outer-most faces of the soil cuboid are assigned as described next: Regarding the following Figure 3.9, the nodes at the Top face are left free to displace, the nodes at the Lateral faces are restricted to move in Y direction ( $U_2=0$ ), those at the Front and Rear faces are restricted

to move in X direction ( $U1=0$ ) and those at the Bottom face are restricted to move in the Z direction ( $U3=0$ ). All the nodes of continuous solid hexahedral elements are, by definition, allowed only to translate but not to rotate (Dassault Systemes, 2024), thus their corresponding restraints at the listed faces are only concerned with their translations, characterizing them as the pinned roller type.

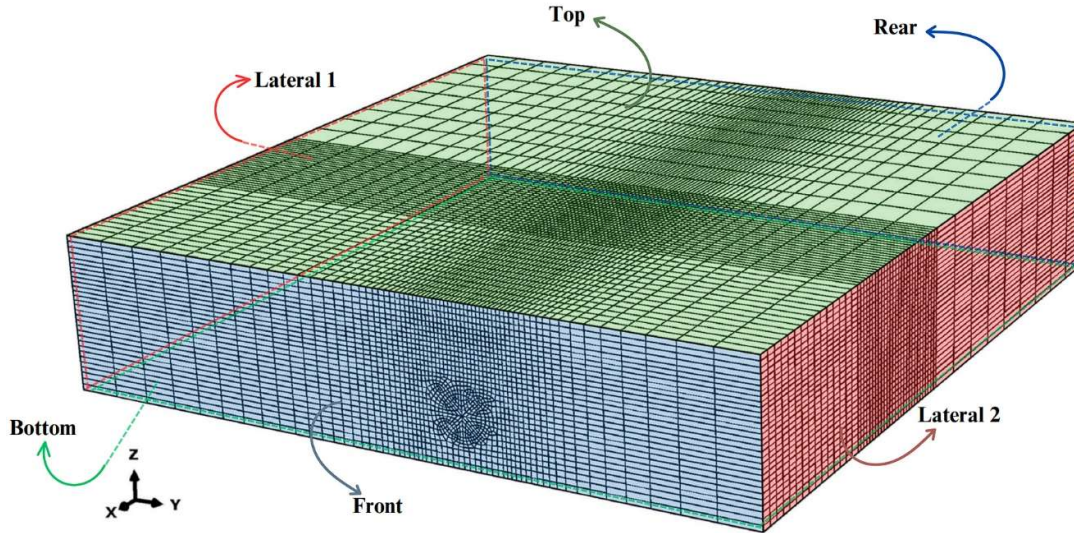


Figure 3.9. Faces of the rectangular prism, dominion of the 3D model

These boundary conditions are imposed because, ideally, an undisturbed soil cuboid such as the one presented above has no original displacements, with its perturbations only starting around the tunnel boundaries at the start of the excavation steps. For deep tunnels, such perturbations in terms of displacements only converge to zero (they return to their initial state) at an infinite distance from the tunnel walls, based on the theory of Kirsch (1898) for the stress concentrations around circular holes in linear-elastic infinite plates of homogeneous material. In FEM modelling, nevertheless, it is not possible to reproduce an infinitely large model expecting the soil to recover its initial state (or be completely unaffected by the tunnel excavation) at a far boundary (as it is likely to happen in real life) and therefore, the displacements must be forced to converge to zero at a finite distance, chosen prudently to not affect the behavior of the target event, as explained earlier. The same is true for shallow tunnelling applications, yet in this case because the target event, directly the tunnel excavation, is close to the surface, the Top face of the dominion cannot be constrained as it must be allowed to affect the tunnel and vice versa, to be able to analyze their mutual influence: the formation of the basing of subsidence and the tunnel walls/face convergence.

### 3.1.2.2 The shield and the lining segments

In the literature there are several ways to constrain the shield and lining segments, if these are explicitly included as individual geometrical parts. In some cases they are not, as hinted before for Mollon et al.'s (2012) model, for example the shield is not modelled explicitly and instead a condition of limited displacement is introduced at the excavation boundary nodes; or in the case of Migliazza, Chiorboli & Giani (2009) and

Nemorini (2010), the lining is not included as a separate geometry but instead, the ground elements are deactivated and reactivated with the properties of the segmental lining, being perfectly attached to the surrounding soil.

When the shield and segmental liners are modelled explicitly as separate parts from the soil, it is because the numerical software employed allows to emulate contact interactions as boundary conditions. This is the case of Kavvadas et al. (2017), who configured a contact interaction between the shield, the liner rings, the grout and the converging soil, leaving the shield and the lining free to displace within the domain and to transfer their weights to the invert of the tunnel in the most realistic manner, only constrained by the normal and frictional contact properties between the parts of the assembly. A similar approach was adopted by Losacco & Viggiani (2019), however they did constrained the movement of the lining rings at the beginning of their installation, behind the tail of the shield, to account for the rigid locking action of the thrust jacks of the TBM.

### 3.1.2.3 Additional boundary conditions

Other boundary conditions, such as those concerning the convergence of the tunnel's walls, the application of the face pressure, the contact interactions, and so on; are closely related to the excavation stages and therefore, will be later discussed under the headings 3.1.4 and 3.1.5.

## 3.1.3 Material properties

### 3.1.3.1 Soil constitutive models

Across the literature concerning three-dimensional numerical simulations of the EPB or slurry shield tunnel excavation, the most used soil constitutive model is by far the *linear elastic-perfectly plastic behavior with Mohr-Coulomb failure criterion* (Barla G., Barla, Bonini, & Gamba, 2005; Migliazza, Chiorboli, & Giani, 2009; Nemorini, 2010; Barla, Barla, & Leuzzi, 2012; Mollon, Dias, & Soubra, 2012; Mooney, Grasmick, Kenneally, & Fang, 2016; Kavvadas, Litsas, Vazaios, & Fortsakis, 2017; Litsas, Sitarenios, & Kavvadas, 2017; Boldini, Losacco, Bertolin, & Amorosi, 2018). In recent years, however, the tendency is to implement more advanced constitutive models, particularly highlighting the *hardening soil model with small-strain stiffness* (Benz, 2007), also known as HSsmall in PLAXIS software, being the second most used constitutive behavior among the authors consulted who had successfully modelled the shallow tunnelling excavation (Fargnoli, 2015; Epel, Mooney, & Gutierrez, 2021; Amorosi & Sangirardi, 2021; Mohammadzamani, Lavasan, & Wichtmann, 2023); with a minor number of other authors including different formulations such as the *Cam-Clay plasticity* (Kasper & Meschke, 2004), *Extended Mohr-Coulomb, multiple yield surface kinematic hardening* and *modified two-surface kinematic hardening* (Yiu, 2018) and *hypoplasticity extended with intergranular strain* (Oh & Ziegler, 2014; Losacco & Viggiani, 2019).

The scope of the present thesis is not to discuss each model; nonetheless, it is recognized that most of these advance models, if correctly selected for the types of soils present in the job site, can better reproduce the behavior of these materials in tunnelling applications, in comparison to the classical Mohr-Coulomb formulation. For example, some of these (i.e., HSsmall) are able to simulate the hardening plasticity of the soil and early plastic deformations, while in their elastic regime the stiffness is related to the state of stress, at low levels assigning very high stiffnesses and at high levels considering the stiffness degradation, consequently producing reasonable results in loading/unloading regimes, which are expected to occur at least ahead of the face of the excavation due to the soil decompression (unloading) and at the pressurized grouting zone (loading) behind the tail of the shield (Epel, Mooney, & Gutierrez, 2021). All these multifaceted non-linear behaviors have been observed vastly during experimental campaigns on the soil (Benz, 2007) and therefore, the constitutive models that are able to reproduce them can be deemed to realistically represent the behavior of the soil, improving over the elementary Mohr-Coulomb constitutive model.

However, none of the authors that worked with the complex constitutive models cited before had to analyze heavily cemented granular soils, interesting for this thesis as the Torino soil, host of the Metro-Line 2, is of variable degree of cementation. These soils have a particularity: they can be considered to have a rock-like behavior when the volume of the cemented clusters governs over the loose granular portion and, conversely, if the volume of the clusters in the matrix is marginal, the material can be considered to have a soil-like behavior. For this, as seen in Barla & Barla (2005) and Barla & Barla (2012), Papantonopoulos & Atmatzidis (1993) proposed a failure criterion that varies between the Mohr-Coulomb and Hoek & Brown models, to respectively emulate that variation between soil-like and rock-like behaviors.

Firstly, the Mohr-Coulomb failure criterion, dear to all geotechnical engineers, relates the available shear strength  $\tau$  of a material, frequently a soil, with the acting normal stress  $\sigma_n$  and two parameters known as the cohesion  $c$  and the friction coefficient  $\tan \varphi$ , which geo-practitioners can directly associate with the behaviors of different types of soils; for example, a coarse granular soil is expected to be deprived of cohesion yet to have a relatively capable frictional coefficient. Another parameter is also included by means of the flow rule: the dilatancy angle  $\psi$ , which for soils is typically smaller than the friction angle, characterizing the flow rule as non-associative, and represents the plastic volumetric change of the material in comparison to its shear plastic strains (Vermeer & de Borst, 1984). The criterion in terms of effective stress is as follows:

$$\tau = c' + \sigma'_n \tan \varphi' \quad (3.1)$$

And in the principal plane it is rewritten as:

$$\sigma'_1 = \sigma'_3 \cdot \frac{1 + \sin \varphi'}{1 - \sin \varphi'} + \sigma_{ci} \quad (3.2)$$

Where,

$$\sigma_{ci} = \frac{2c' \cos \varphi'}{1 - \sin \varphi'} \quad (3.3)$$

Secondly, the Hoek & Brown failure criterion for rock masses, first introduced in 1980 in the book *Underground Excavations in Rock*, was conceived with a heavy partiality towards the behavior of hard rock as it was related to very strong andesites from Papua New Guinea (Hoek & Marinos, 2007). Then, through the years it evolved to further represent the behavior of the rock masses of variable qualities via the geological strength index (GSI), in a publication by E. Hoek in the ISRM's News Journal, 1994. Eight more years had to pass for the criterion to be completely re-examined, using the rock masses' excavation disturbance factor D in 2002's publication by the same author in conjunction with C. Carranza-Torres and B. Corkum, of the name *Hoek-Brown criterion – 2002 edition*. This version of the criterion represents one of the most used strength criteria for rock masses worldwide, as it permits to estimate the failure conditions of an equivalent continuum rock-like material in the plane of principal stresses ( $\sigma'_1$  and  $\sigma'_3$ ). The criterion is as follows.

$$\sigma'_1 = \sigma'_3 + \sigma_{ci} \left( m_b \frac{\sigma'_3}{\sigma_{ci}} + s \right)^a \quad (3.4)$$

Where,

$$m_b = m_i e^{\left(\frac{GSI-100}{28-14D}\right)} \quad (3.5)$$

$$s = e^{\left(\frac{GSI-100}{9-3D}\right)} \quad (3.6)$$

$$a = \frac{1}{2} + \frac{1}{6} \left( e^{-GSI/15} - e^{-20/3} \right) \quad (3.7)$$

Here  $\sigma_{ci}$  is the unconfined compressive strength of the intact rock (or the cemented clusters) and  $m_i$  is a parameter that depends on the lithotype of the intact rock. The same authors indicate that the criterion also applies for the intact rock if  $m_b = m_i$ ,  $s = 1$  and  $a = 0.5$ , obtaining:

$$\sigma'_1 = \sigma'_3 + \sigma_{ci} \left( m_i \frac{\sigma'_3}{\sigma_{ci}} \right)^{0.5} \quad (3.8)$$

Now, following Papantonopoulos & Atmatzidis (1993), the Mohr-Coulomb and Hoek & Brown failure criteria can be rewritten respectively as:

$$(\sigma'_1 - \sigma'_3) = (K_p - 1) \cdot \sigma'_3 \quad (3.9)$$

And,

$$(\sigma'_1 - \sigma'_3)^2 = m_i \sigma_{ci} \cdot \sigma'_3 + \sigma_{ci}^2 \quad (3.10)$$

Where  $K_p$  is the coefficient of passive earth pressure of the loose granular soil. Then, to transition from one formulation to the other, the authors propose:

$$(\sigma'_1 - \sigma'_3)^{(1+k)} = m \cdot \sigma_{ci}^k \cdot \sigma'_3 + \sigma_{ci}^{(1+k)} \quad (3.11)$$

Notice in this equation that if the parameter  $k = 1$  the expression returns to the rearranged Hoek & Brown failure criterion representing a rock-like behavior, while if  $k = 0$  it is representative of a soil-like Mohr-Coulomb behavior.  $k$  is consequently the parameter that governs the transition between the models, and  $m$  can be related to  $k$  as:

$$k = \frac{1 + m - K_p}{1 + m_i - K_p} \quad (3.12)$$

According to Barla & Barla (2012), the soil can be considered loose if  $m = 3$  (or takes a low value), and fully cemented if  $m = 20$  (i.e. the parameter  $m_i$  takes values near 20 for very capable rocks, such as breccias, conglomerates and basalt (Hoek & Brown, 1997)).

In this way, it is possible to model the constitutive behavior of a partially cemented soil by assuming linear elasticity before yield, with a perfectly plastic Papantonopoulos & Atmatzidis failure criterion for the transitional material. The application of this model to the Torino soil will be explained with more detail in Chapter 4.

### 3.1.3.2 The shield and the lining segments

It is most usual to find the shield and the lining segments being modelled with isotropic elastic constitutive formulations. The shield commonly takes the properties of the steel, with a Young's modulus of 200 GPa and Poisson's ratio of 0.3, while the segmental lining the properties of the reinforced concrete, with a Young's modulus of 30 GPa and a Poisson's ratio of 0.2. These properties are normally only included to characterize these elements as significantly more rigid than the surrounding soil and therefore, their deformability is neglected in the analysis of the subsidence.

Only in the cases where the aim is to study the response of the segmental liners to the convergence of the tunnel walls and applied pressures (i.e. jacking forces or grout injection pressures), like in the case of Kavvas et al. (2017) or Epel, Monney & Gutierrez (2021), both the geometrical and constitutive models of the lining rings are devised in more detail, even simulating the longitudinal joints between the segments or transversal joints between one liner ring and the next.



### 3.1.3.3 *Annulus grout*

As expressed once by esteemed Prof. D. Peila at the Politecnico di Torino, if we were able to fill the annulus void (recall Figure 2.6) with water, we might as well do it as the incompressibility of water would lock in place the soil convergence around the liners. Unfortunately, as properly concluded by himself, the surrounding soil's permeability would permit the water to drain through its pores, leaving vacant once more the annulus gap for the soil to freely displace.

As stark as this example appears, it does well to remind us that any material is suitable to fill the annulus void to lessen the soil convergence, independently of its strength characteristics, as long as its composition (in terms of granulometry) or viscosity impedes its escape through the soil while also retaining a low volumetric compressibility. These are characteristics effectively emulated by mono-component (cement-based or mortar) or two-component grouts (Pelizza, Peila, Sorge, & Cignitti, 2012), as well as pea gravel, all used frequently in tunnelling applications as backfills.

In numerical models, as performed before by various authors (Losacco & Viggiani, 2019; Kavvadas, Litsas, Vazaios, & Fortsakis, 2017; Kasper & Meschke, 2004; Epel, Mooney, & Gutierrez, 2021), the tail void grout can be simulated with a time-dependent behavior, since the material hardens in time changing progressively its properties. From these characteristics, some authors have concentrated mainly in the variation of the elastic parameters, directly the Young's modulus and Poisson's ration (Losacco & Viggiani, 2019; Kavvadas, Litsas, Vazaios, & Fortsakis, 2017), while others, aiming to reproduce more complex physics in their models, such being the case of coupled hydromechanical approaches, also considered the material's permeability variation (Kasper & Meschke, 2004), shrinkage and creep (Mohammadzamani, Lavasan, & Wichtmann, 2023).

Following the ample (in terms of parameters implemented) investigations presented by Mohammadzamani et al. (2023), the hardening rate of the grout apparently has the most significant impact on the surface settlements, compared to the other parameters included, such as the elastic modulus at 28 days of hardening  $E_{28}$ , the permeability, shrinkage strains and creep of the grout.

The hardening rate, represented by the fraction  $E_1/E_{28}$ , denotes the proportion of the material's stiffness at an early stage, day-one for  $E_1$ , to that at 28 days. In this sense, a slow-hardening grout has low values of  $E_1/E_{28}$  while a fast-hardening grout has higher values of the fraction. As an example, a mono-component mortar grout can reach stiffnesses of 1.0 GPa after 28 days (Kasper & Meschke, 2004), and for the authors, supposing it is a slow-hardening type of material, with a hardening rate of  $E_1/E_{28} = 0.3$  it would have a day-one stiffness of 0.3 GPa. On the contrary, if some accelerating agent were to be used on the same type of mix, being mindful of only altering the hardening rate at early stages, at 28 days the material would have the same 1.0 GPa of elastic modulus, and for the authors, knowing it is a fast-hardening type of material, with a hardening rate of  $E_1/E_{28} = 0.5$  in day-one its stiffness would be equal to 0.5 GPa. Simply for comparison, it is known that shotcrete can reach hardening ratios up to 0.84 (Meschke, Kropik, & Mang, 1996), clearly exhibiting its speedy stiffening, even compared to the grout.

Indeed, the authors used a range of hardening rates for the grout from 0.3 to 0.5, with steps of 0.05, fixing the value of  $E_{28}$  in a range from 0.5 to 2.0 GPa. With this, they witnessed that the fastest hardening rate of 0.5 compared to the slowest of 0.3, produced considerably smaller surface settlements, hinting that two-component grouts, with their ability to harden in shorter time frames, would be especially effective in controlling the soil convergence around the lining segments and consequently, the basin of subsidence. In this way, their research also supported the earlier declarations of various authors such as Pelizza (2012), Peila (2015) and Oreste (2021), claiming that, ideally, the grout should be applied immediately with the advancement of the TBM to avoid the presence of voids and that it should harden instantaneously, filling completely the annulus to minimize the surface settlements. Mohammadzamani et al., nevertheless, did not explicitly disclose the values used for the couple  $E_1$  and  $E_{28}$  to evaluate a certain hardening ratio  $E_1/E_{28}$ , in the sense that the ratio  $E_1/E_{28} = 0.4$  can be easily fulfilled by assuming  $E_1$  equal to 0.2 GPa and  $E_{28}$  equal to 0.5 GPa, but it is also true if one assumes  $E_1$  equal to 0.4 GPa and  $E_{28}$  equal to 1.0 GPa or  $E_1$  equal to 0.8 GPa and  $E_{28}$  equal to 2.0 GPa; the first couple being the softest and ending at the last couple, being the most rigid of the three.

The impact of this softer-to-stiffer gradient of grouts was numerically studied by Nikakhtar et al. (2020). Because their type of material acquired its solid state early, the Young's moduli regarded were  $E_{gel}$  for a freshly applied grout to  $E_{solid}$  for the same material after eight hours of hardening. For their particular case, a new type of hardening rate can be defined as  $E_{gel}/E_{solid}$ . In their research, the authors fixed the value of  $E_{solid}$  in a range from 10 to 60 MPa (typical values for two-component grouts) and derived the Young's modulus of the fresh material assuming  $E_{gel} = 1/4 E_{solid}$ ; in other words, it can be interpreted that they investigated for all cases an early hardening rate  $E_{gel}/E_{solid} = 0.25$ , from softer ( $E_{gel} = 2.5$  MPa and  $E_{solid} = 10$  MPa) to stiffer ( $E_{gel} = 15$  MPa and  $E_{solid} = 60$  MPa) grouts. Once again, what we call a 'gradient' of softer-to-stiffer grouts, proved to also have an impact on the basin of subsidence with, evidently, the stiffer grouts reducing considerably the surface settlements in comparison to their softer counterparts.

From the past two examples, it is apparent that the elastic properties of the backfilling material, evolving in time, have a definitive impact on the surface settlements. In a broader investigation yet with a more simplified numerical model, Mollon, Dias & Soubra (2012) evaluated the probabilistic impact of the elastic parameters of the backfill, to that of other model parameters such as the soil's internal friction angle and cohesion (based on the Mohr-Coulomb perfect plasticity), the Young's modulus of the soil and the applied face pressure. The impact of additional parameters was also compared, such as that of the grout injection pressure  $\sigma_{inj}$  and the grout solidification length  $L_{inj}$ , yet these can be related to the time-dependent properties of the material, considering that the hardening process of the grout, before reviewed in terms of time by Mohammadzamani and Nikakhtar, can here be assessed in terms of the solidification length  $L_{inj}$  by linking the advancement rate of the TBM to the length of each excavation step; whereas the injection pressure  $\sigma_{inj}$  is solely a property of the liquid grout that

disappears as the material hardens, and will be discussed further under the next heading 3.1.5. Both parameters can be identified in the next Figure 3.10.

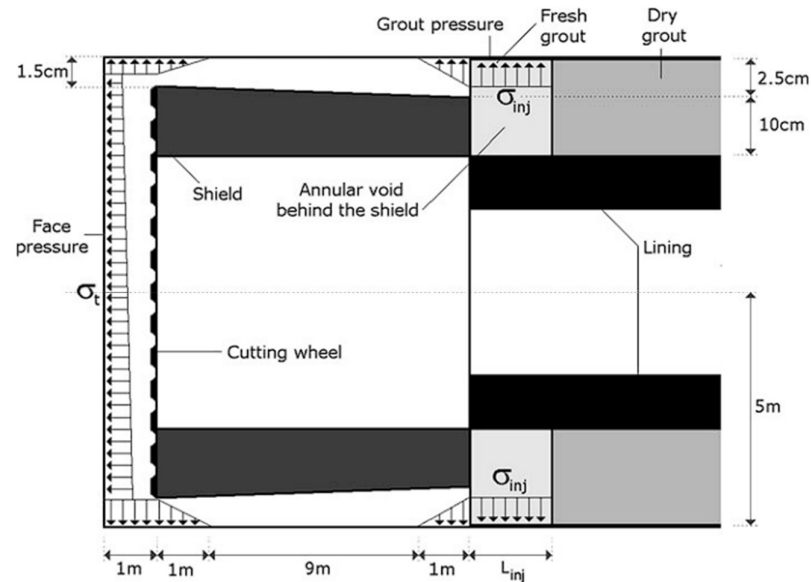


Figure 3.10. TBM layout and boundary conditions affecting the excavation, as presented by Mollon et al. (2012)

In their research, Mollon et al. (2012) used a modified form of the probabilistic method called Collocation-Based Stochastic Response Surface Methodology (CSRSM) to analyze the global sensibility of the system to the parameters listed before (assumed to be independent random variables, each with its own probability distribution, mean and coefficient of variation). The CSRSM is presented to be a powerful alternative to the Monte-Carlo Sampling method, that allows the users to run a significantly lower number of computations if the quantity of random variables is fairly low, as it uses a meta-model in the form of a Polynomial Chaos Expansion (PCE) of a given order  $n$ , instead of running a large number of parametric analyses with the deterministic numerical model. The unknown variables of the PCE are in turn obtained by regressions depending on the results of the numerical model (Mollon, Dias, & Soubra, 2012). Then, the sensibility analysis is to be performed by calculating the Sobol indexes of each random variable using the coefficients of each PCE. These indexes allowed the authors to quantify, in a percentage from 0 to 100%, the contribution of each variable (for example, the Young's modulus of the grout) to the variance of each output (for example, the maximum settlement). In this way, they were able to identify that the maximum settlement's variance was mainly affected by the Young's modulus of the grout, while the maximum longitudinal superficial displacement was particularly sensible to the grout's solidification length (or by extension, is hardening time). This, however, does not indicate that these two parameters have necessarily the greatest deterministic impact on the maximum ground displacements as previously proven by Mohammadzamani and Nikakhtar, yet it does show the importance of considering their variability in comparison to the real tunnelling process, inviting the practitioners to perform more detailed parametric analyses focused on evaluating the effect of these 'critical' random variables, with the aim of producing more reliable outputs.

Both deterministically and probabilistically, the elastic and time-dependent properties of the grout most definitely play a key role. Nevertheless, these parameters are usually clouded by the uncertainties of the construction site and most of the time, from a design stage, the properties of the final material that is to be installed as backfill are unknown. This is the case with the Metro-Line 2 of Torino, for the civil contracts are still to be formalized and consequently, the detailed information regarding the boring machine and the materials for the works has not yet been presented. For this reason, it is necessary to recur to the literature to determine a range of possible behaviors that the grout can assume.

To narrow the number of possibilities, only the elastic properties of two-component grout mixes will be studied, given that during the past decade this material has risen to become the most used backfill in shielded tunnelling (Antunes, 2012; Pelizza, Peila, Sorge, & Cignitti, 2012; Peila, et al., 2015; Oggeri, Oreste, & Spagnoli, 2021; Todaro, Saltarin, & Cardu, 2022; Rahmati, Chakeri, Sharghi, & Dias, 2022), especially in urban environments where the subsoil tends to be soft and unstable. In the next Table 3.1, a collection of different laboratory and numerical investigations concerning the characteristics of the two-component grout is presented, in order to determine a probable range for the time-dependent elastic properties that the material will exhibit in-situ. The table is precisely that, a *collection of different* studies for exhibition, and should not be approached as a comparative unit. Some comments regarding each investigation are presented below.

Firstly, it is paramount to remark that the number of research articles concerned with the time-dependent elastic properties of the two-component grout is scarce, as before also pointed out by Oreste et al. (2021), on top of the lack of standard regulations to assess such properties (Todaro & Pace, 2022). The next Table 3.1 should consequently be considered as a first draft of a future state of the art review, and an encouragement to researchers in the field of material sciences to fill in the knowledge gaps surrounding the behavior of this type of grout, both at short and long terms.

Apropos the numerical investigation conducted by Epel et al. (2021), the authors used the hardening function proposed by Meschke et al. (1996), related to the time-dependent stiffening of the shotcrete, and based the two-component grout design on that of Flores (2015). This mix design contained a cement replacement of 50% with fly ash, which the author associates with a significant late increase of the elastic modulus, right after the 28 days until the 98 days of hardening. This justifies, as a result, the relatively high value of the Young's modulus reported by the author at 28 days of curing.

The rest of the collected scientific articles were focused on laboratory work, here especially highlighting the tests to determine the material's Young's modulus. This, however, was not similarly obtained from one study to the other. For example, even though both Todaro et al. (2019) and Rahmati et al. (2022) conducted uniaxial compression (UCS) tests to determine the elastic modulus of the material, the former used a modified form of the Italian regulations UNI EN 196-1 for cement paste, while the latter used the American ASTM C109 for cement mortars, differing both in the sizes of the cubic samples and compression speeds.

Especial attention is directed towards Todaro & Pace's (2022) work, since they obtained the dynamic elastic parameters instead of their static equivalents, this by preparing cylindrical samples and subjecting them to ultrasonic pulse velocity (UPV) tests, from which the S- and P-wave's first arrival velocities could be read and related to the dynamic mechanical properties of the two-component grout. It is well known, however, that for concrete and mortar the static Young's moduli obtained from UCS tests is frequently lower than the dynamic modulus obtained from UPV tests. As an example, for concrete Thomaz et al. (2021) proposed that  $E_{stat} \approx 0.7E_{dyn}$ , and for mortar Marques et al. (2020) found a range of  $E_{stat} = 0.67 \sim 0.90E_{dyn}$ , yet both these studies were conducted in stiff samples, after 28 or more days of hardening. For two-component grouts, on the contrary, this static-dynamic ratio has not been fully explored. Oreste et al. in 2021, nevertheless, did conduct UCS and UPV tests on two-component grout samples and, while the authors never proposed a ratio between  $E_{stat}$  and  $E_{dyn}$ , from the data that they gathered for the curing ages of 7, 10 and 28 days, it is hereby proposed that, approximately,  $E_{stat} = 0.20E_{dyn}$ . This ratio is then used to process Todaro & Pace's dynamic parameters, after obtaining them by graphical interpolation, and it is noticed that the resulting values are reasonably close to their counterparts from other studies.

In general, all the reported values of the Young's modulus in the next table refer to the tangent modulus at 50% of the elastic domain, except for those from Epel et al. (2021) which come from constitutive modelling, and those from Todaro & Pace (2022) which, as detailed before, were processed to obtain their static equivalents.

Lastly, the values of the Poisson's ratio appear to behave as expected, for the gel-like material at early stages and even after hardening, the ratio remains above 0.4. Only the findings of Oggeri et al (2021) seem to deviate from this value, with the authors themselves commenting that a larger database is required to plausibly judge the Poisson's ratio as it is "one of the most sensitive features of the grout behavior".

*Table 3.1 Mix dosage and time-dependent elastic properties of different two-component grouts in the literature*

	Epel et al. (2021)	Todaro et al. (2019)	Oggeri et al. (2021)	Oggeri et al. (2022)	Oreste et al. (2021)	Todaro & Pace (2022)	Rahmati et al. (2022), MIN	Rahmati et al. (2022), MAX
Investigation	Numerical	Laboratory	Laboratory	Laboratory	Laboratory	Laboratory	Laboratory	Laboratory
-----								
Mix dosage [kg/m <sup>3</sup> ]								
Water		853.0	800.0	800.0	819.9	853.0	~ 800.0	~ 800.0
Bentonite		30.0	35.0	35.0	35.2	30.0	40.0	40.0
Portland Cement		230.0	350.0	350.0	295.9	230.0	400.0	400.0
Retarding/fluidifying agent	NR	3.5	17.5	17.5	5.0	3.5	NR	NR
Accelerator		81.0	85.0	85.0	90.5	81.0	90.0	90.0
Additional comment	Fly ash replacement >50%	NR	NR	NR	NR	NR	Sodium silicate ratio 2.3	Sodium silicate ratio 2.6
-----								
Young's modulus [MPa]								
1 [hr]	NR		1.3		10.0	1.3***	1.1	2.5
8 [hrs]	25.0	NR	11.0*	NR	NR	24.0***	NR	NR
16 [hrs]	40.0		21.0*			40.0***		
1 [day]	50.0	57.5**	26.1	23.0	250.0	40.4***	32.1	82.3
7 [days]	145.0	NR	35.9	91.2	260.0		155.7	172.0
28 [days]	350.0	136.6**	64.3	98.2	270.0	NR	NR	NR
-----								
Poisson's ratio [-]								
1 [hr]	No explicitly		0.09			0.5		
8 [hrs]	mentioned, yet					0.49*		
16 [hrs]	because it is based on		NR		NR	0.49*		
1 [day]	Meschke et al. (1996)	NR		NR			NR	NR
7 [days]	material model, it		0.08			0.48		
28 [days]	could take a range		0.09		0.43	NR		
	from 0.30 to 0.38		0.06		0.42			

\* Obtained from graphical interpolation

\*\* Obtained from graphical interpretation of UCS tests

\*\*\* Static parameters computed from the correlation  $E_{stat} = 0.2 \cdot E_{dyn}$  discussed in the paragraphs above

NR: Not reported by the authors

### 3.1.4 Single-step procedure for the tunnel excavation

In some of the cases studied in the former heading 3.1.1, the shield and the liner rings were explicitly modelled. This, however, only occurs when step-by-step excavation procedures are employed, which will be discussed in more detail in the following section. In a more simplified scheme, neither the shield, segmental lining nor the grout are explicitly modelled but instead, a fictitious uniform or oval-shaped displacement (as seen in Figure 3.11) can be applied at the nodes of the excavation walls to emulate the ground convergence due to the shield's overcut, conicity or grout shrinkage under pressure (Boldini, Losacco, Bertolin, & Amorosi, 2018; Miraei, 2020). The key point is to guarantee that these forced contractions correspond to the most accurate approximation of the soil's behavior during the excavation and well reproduce the observed volume loss; and for this it is necessary to know beforehand the effects of the tunnelling process at least at the ground surface and at the tunnel walls. Plainly, a calibration of the model is imperative, comparing it to existent in-situ data.

For a prediction model such as the one of the present effort, crafted before the beginning of the civil works, the selection of a representative forced contraction is challenging. In these cases, a more sensible approach might be explicitly modelling the shield, liners and the grout.

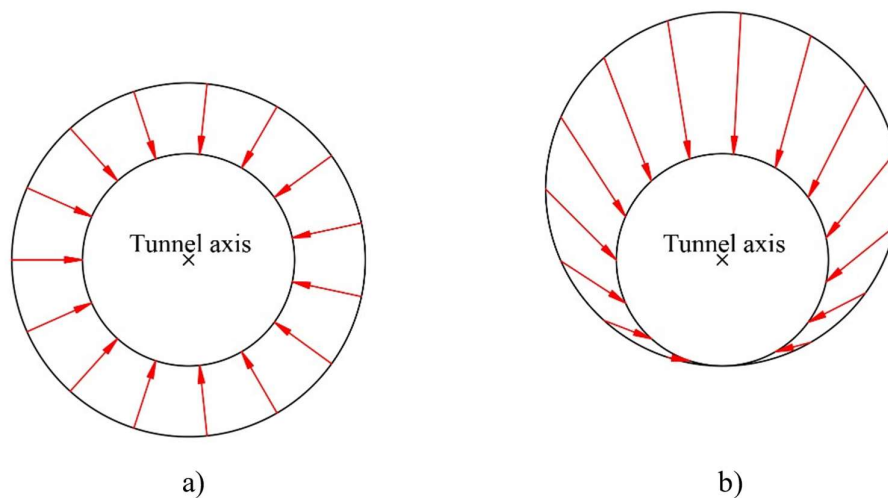


Figure 3.11. Imposed soil convergence around the tunnel following a) uniform radial tunnel contraction, b) oval-shaped tunnel contraction

### 3.1.5 Step-by-step procedure for the tunnel excavation

#### 3.1.5.1 Excavation advancement

In literature the step-by-step excavation procedure is commonly simulated as listed next, in correspondence to the steps illustrated in Figure 3.13.

- 1) At the beginning of the simulation, the shield of the TBM is advanced a certain distance until it is completely introduced inside the soil, this by deactivating the soil elements in

the excavation length which usually coincides with the length of the discretized elements in the direction of the tunnel alignment, and then activating either explicit rigid elements simulating the shield or displacement/pressure boundary conditions around the tunnel walls. In some cases, an applied pressure simulating the weight of the TBM is also included at the invert of the excavation. In other cases, when contact interactions are emulated, the TBM is let free to fall on top of the soil transmitting its weight.

- 2) The shield is advanced once again by one excavation length and immediately behind the tail of the shield, the elements of the segmental lining and the grout are activated. Again, in some cases an applied pressure simulating the weight of the segmental liners and grout is also included at the invert of the excavation. In other cases, when contact interactions are emulated, these elements are let free to fall on top of the soil transmitting their weight.
- 3) A grout injection pressure is included on the first segmental rings behind the tail.
- 4) The process is repeated by activating the shield and liner plus grout elements, and their respective pressures, while deactivating the corresponding ground elements at the front of the tunnel.

In every step, a horizontal and either constant or trapezoidal pressure is activated at the front face of the tunnel as depicted in Figure 3.12, to simulate the supporting pressure exerted by the conditioned soil in the excavation chamber of the EPB-TBM.

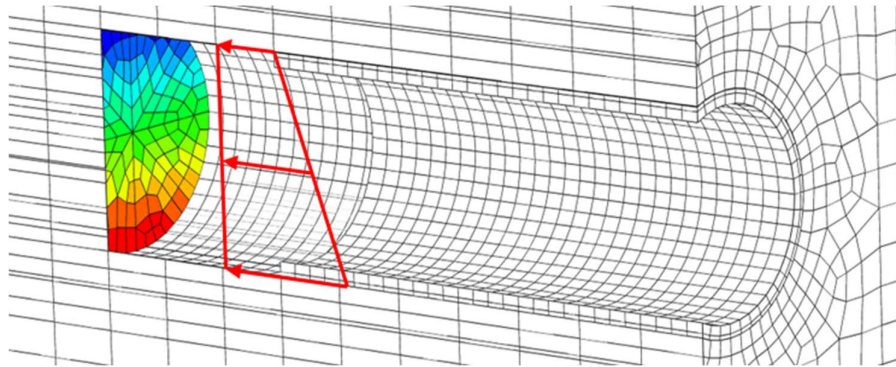


Figure 3.12. EPB-TBM face pressure in the step-by-step procedure



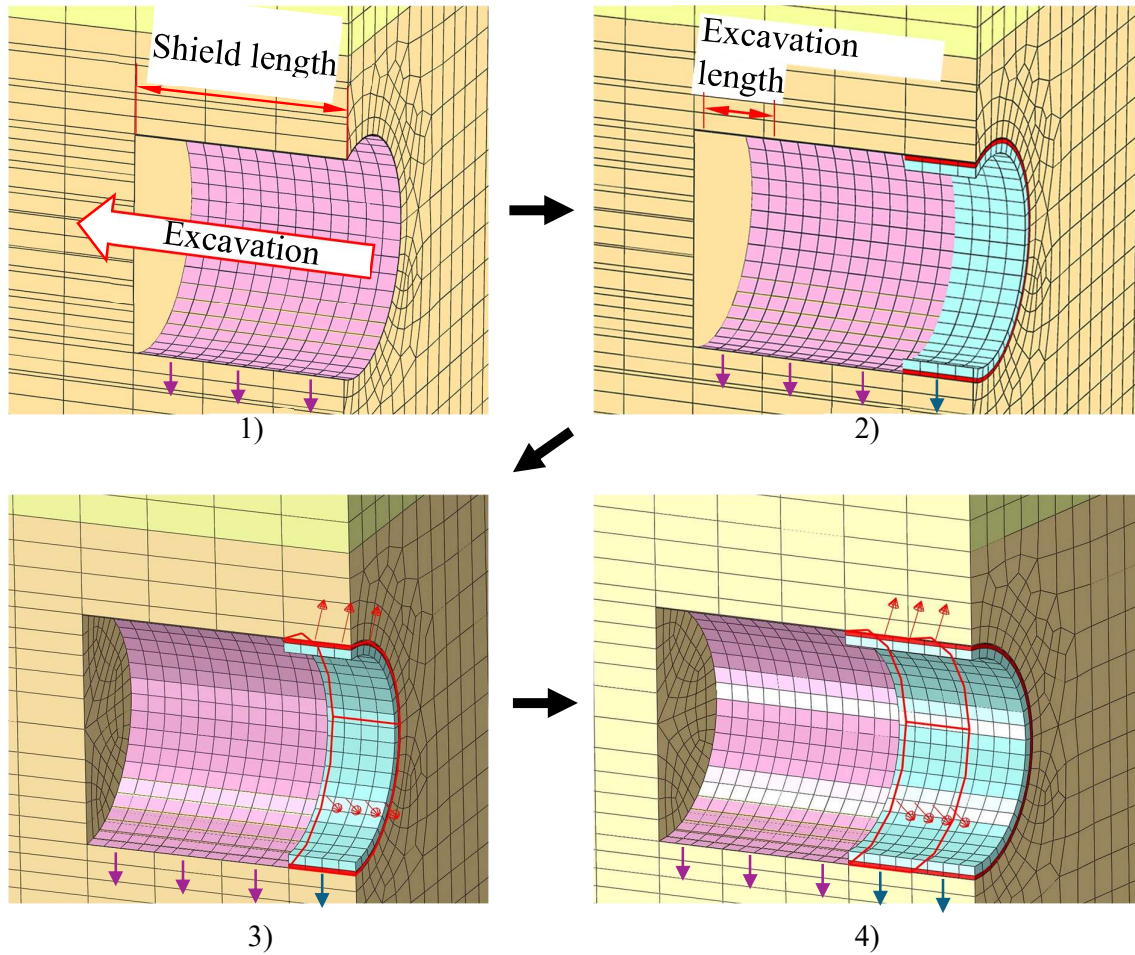


Figure 3.13. Step-by-step advancement simulation of the tunnelling process

For the applied supporting face pressure, in the real application it is usually recommended to completely counter the effective horizontal earth stress and the hydrostatic thrust. In some situations, nevertheless, for example when the TBM is abruptly stopped, the pressure at the front can drop with the degradation of the foams that condition the soil in the pressurized chamber. In this situation, it is beneficial knowing the minimum value of the supporting face pressure to avoid hazardous effects in the surface, such as sinkholes.

With the objective of determining the conditions that trigger the instability at the front, Proutzopoulos (2012) executed around 400 three-dimensional numerical studies in ABAQUS with different tunnelling configurations, varying the tunnel diameter  $D$ , tunnel overburden  $H$ , soil Young's modulus  $E$ , cohesion  $c$ , unit weight  $\gamma$  and friction angle  $\varphi$  considering Mohr-Coulomb perfect-plasticity; to finally formulate the normalized face extrusion as:

$$\Omega_F = \frac{U}{D} \cdot \frac{E}{P_0} \quad (3.13)$$

Here  $U$  is the face extrusion as an output of the numerical model and  $P_0$  is the average geostatic effective stress at the level of the tunnel axis.

The product of the analysis was a data cloud that found an ideal correlation with a face stability ratio  $\Lambda_{FP}$ , known as the Tunnel Stability Parameter. The relationship is better plotted in the next Figure 3.14.

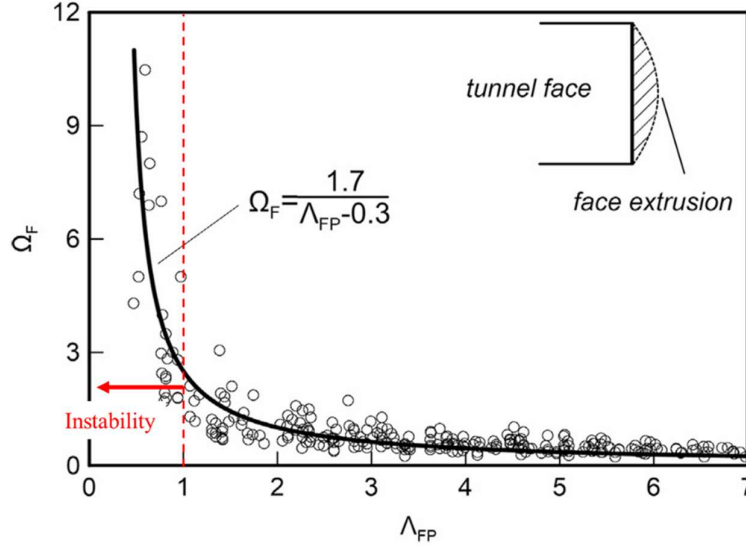


Figure 3.14. Relationship between the normalized face extrusion  $\Omega_F$  and the Tunnel Stability Parameter  $\Lambda_{FP}$ , modified from Kavvadas et al. (2017)

The stability parameter of the face can be calculated from the best fit provided by the previous curve, written as:

$$\Lambda_{FP} = \frac{1.7}{\Omega_F} + 0.3 \quad (3.14)$$

Or, alternatively, it can be obtained from the original process the author followed to define the meta-model. A Stability Factor was initially stated as:

$$\Lambda_F = \frac{5.25 \cdot c \cdot (N_\varphi)^a}{\gamma \cdot H^{1-b} \cdot D^b} \quad (3.15)$$

And here,

$$N_\varphi = \tan^2 \left( 45 + \frac{\varphi}{2} \right)$$

$$a = 0.16 \cdot \frac{H}{D} + 0.59 \quad (3.16)$$

$$b = \left( \frac{H}{D} \right)^{-0.37}$$

For then receiving a modification (Kavvadas, Litsas, Vazaios, & Fortsakis, 2017) to include the average face pressure  $P_F$  exerted by the TBM at the excavation front. If the value of  $\Lambda_{FP}$  from the most conservative equation, either (3.14) or (3.17) is lower than the unit, as shown in the past Figure 3.14 instability is predicted.

$$\Lambda_{FP} = \Lambda_F + 8 \cdot \frac{H}{D} \cdot \left( \frac{P_F}{P_{h0}} \right)^{1+0.1\left(\frac{H}{D}\right)} \quad (3.17)$$

### 3.1.5.2 Soil convergence around the shield

As depicted in Chapter 2, the surface settlements are, among other things, a product of the convergence of the excavation walls around the TBM's shield. In turn, the convergence around the shield is due to the cutterhead's overcut and the shield's conicity, that collectively leave a gap (referred to as shield steering gap) for the soil to freely displace, under the assumption that this gap is not filled with slurry or conditioned soil intruding from the face of the excavation. This intruding mix, as reviewed below, can generate a radial pressure that limits the deformation of the soil around the shield, and depending on the considered shape of the pressurized area, it can significantly reduce the surface settlements.

Borrowing from the single-step procedure, it is also possible to force the soil convergence by applying a fictitious displacement at the tunnel walls but, instead of doing it for the entire tunnel length, it can be applied only along the length of the shield as the excavation advances step-by-step, as a form of constant or incremental displacement. As an example, the next picture shows the scheme adopted by Amorosi & Sangirardi (2021) to simulate said displacement, which aims to reproduce either the real gap between the shield and the soil enabled by the shield's conicity (Amorosi & Sangirardi, 2021) or a target volume loss which can be conservatively assumed or calibrated by observing similar case studies (Fargnoli, 2015). These displacements can also be imposed to reproduce both uniform-radial and oval-shaped ground movements, as depicted in Figure 3.11 a) and b) for the single-step procedure.

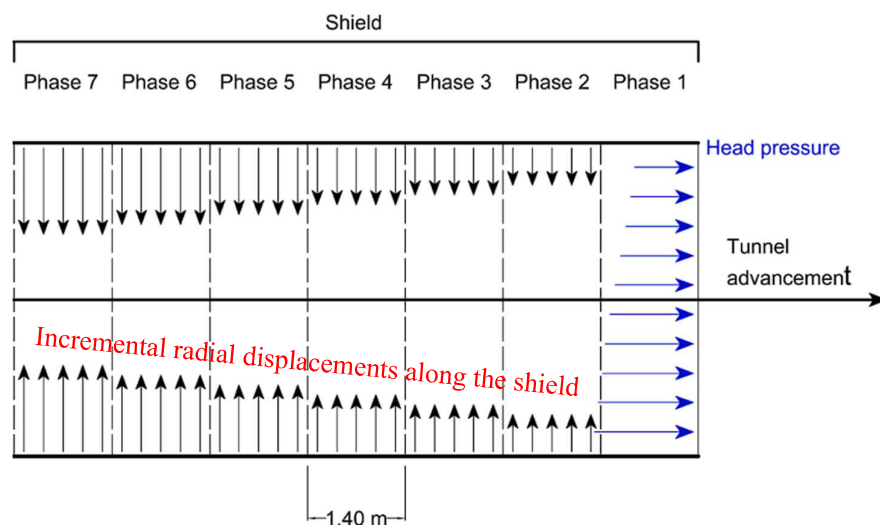


Figure 3.15. Forced soil displacement along the shield, modified from Amorosi & Sangirardi (2021)

Alternatively, instead of imposing the displacement of the soil around the excavation, an internal pressure can be enforced at the tunnel walls which can either aim to simulate a known or expected soil stress release (targeting, once again, a conservative or calibrated volume loss, as in Barla, Barla & Leuzzi (2012)), or can account for a ‘realistic’ pressure around the shield due to the intruding material inside the steering gap, that starts at the cutterhead equal to the face pressure and ends at the tail of the shield equal to the grout injection pressure (Mohammadzamani, Lavasan, & Wichtmann, 2023), or can be assumed to take a constant value in the longitudinal direction of the shield (Migliazza, Chiorboli, & Giani, 2009), only varying with depth due to the density of the material (Mooney, Grasmick, Kenneally, & Fang, 2016; Epel, Mooney, & Gutierrez, 2021), as shown in the next Figure 3.16 (notice the hint to the greater shield annulus pressure at the invert, compared to the crown). In all these cases, the model is simplified as the shield of the TBM does not need to be explicitly modelled; however, care must be taken to guarantee that these fictitious or ‘realistic’ radial pressures avoid the soil to converge a distance greater than the shield’s steering gap, as this would unrealistically assume that the soil can penetrate the shield.

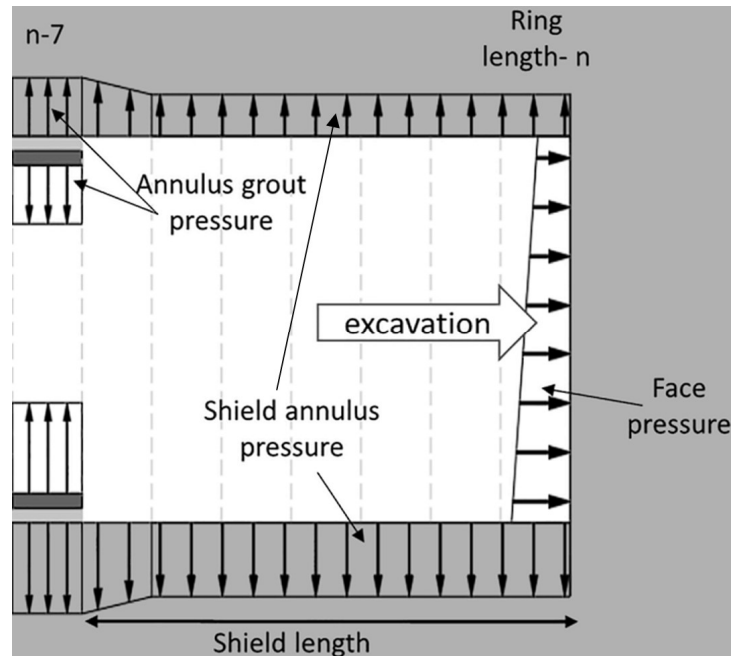


Figure 3.16. Enforced pressure at the tunnel excavation walls, around the shield, modified from Epel et al. (2021)

To deal with this past predicament, another approach, apparently closer to the actual tunnelling process, is to allow the excavation walls to converge freely after the excavation step is completed. This is, no forced displacements or pressures are imposed at the walls aiming to reproduce a given volume loss, but the soil can displace without constraint until it meets the shield (through contact interactions) or until it is stopped at a distance equal to the steering gap. To revise this latter case, Nemorini (2010) proposed a way to stop the convergence of the freely converging soil without the need for modelling the shield: by adding rings of springs at the nodes of the tunnel walls (see next Figure 3.17), with each spring having negligible stiffness while its relative

displacement, equal to the radial displacement of the node it is connected to (SPRING1 in ABAQUS/Standard and Spring-> Connect point to ground in ABAQUS/CAE), is lower than the shield's steering gap, and with a near infinite stiffness once the relative displacement is equal or greater than the gap, locking in place the node from displacing further into the excavation and only admitting its retreat. In the author's case, the shield gap was considered of a magnitude near 1.2 cm, concentric with the tunnel's axis (expectedly, the soil convergence will be more reminiscent of a uniform radial ground movement, as presented in Figure 3.11 a).

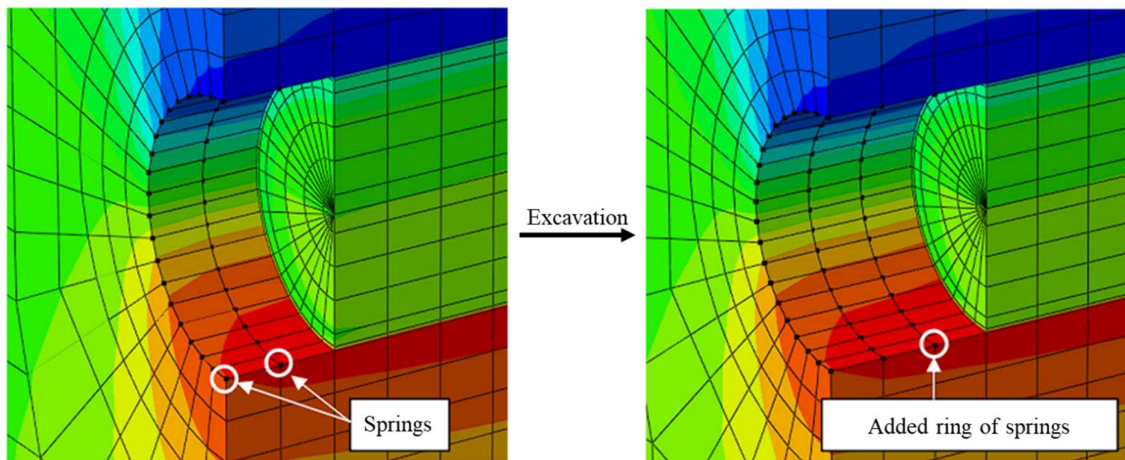


Figure 3.17. Spring rings to limit the soil's convergence around the shield, modified from Nemorini (2010)

The past method, nonetheless, has the difficulty that the mesh of the soil cuboid must be known and fixed from the beginning, as well as the labels of the nodes to apply the springs around the excavation. This, in some cases, is not ideal, especially when automatic mesh generators are used and so, the labels of the nodes are unknown and everchanging with every mesh regeneration, or when a re-meshing technique is to be used to automatically assess the areas where finer meshes are required and thus, in this case again, the numbers of the nodes change, and the spring conditions are lost.

The most practical alternative to surpass this, is to model the shield of the TBM, which may sound intricate because contact interactions must be simulated between the shield and the soil, but conceptually these do not deviate much from Nemorini's proposal.

In their most efficient configuration, contact interactions in ABAQUS are defined as a master-to-slave surface contact algorithm. In this way, two surfaces must be defined: the master surface, usually of a coarser mesh and stiffer material, and the slave surface, with a higher mesh density and softer underlying material. The differentiation between mesh densities should always predominate when selecting the type of surface since the segments of the master surface can penetrate the slave surface, as shown in Figure 3.18. This is particularly important when modelling tunnels since the excavation walls and the shield are circular and the position of their nodes may not coincide. When the excavation walls converge and meet the shield, their nodes may penetrate the shield if the discretization is not fine enough for the selected type of surface, and this penetration may become inadmissible or cause numerical convergence problems. It is usual to

assign the excavation walls the role of the master surface, for its coarser discretization, and the shield the role of the slave surface.

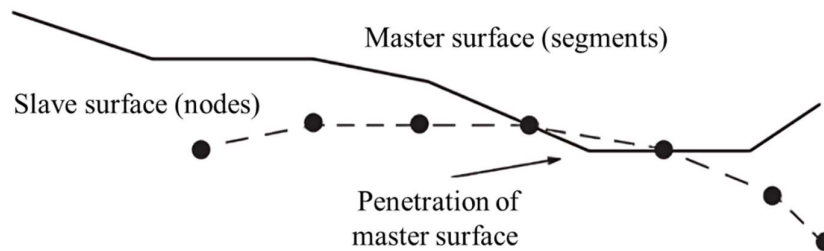


Figure 3.18. Master-to-slave surface interaction, adapted from Dassault Systemes (2024)

For the contact interaction of three-dimensional finite elements, it is recommended to use first-order elements, either of reduced integration or fully integrated, because if second-order elements are used their mid-nodes may bias the interpretation of the nodal forces generated during contact: given that they have parabolic interpolation functions between nodes, the mid-nodes may land in an area where the parabola predicts an opposite sign of the contact pressure or conversely, the nodes at the corners may exhibit zero loading when constant pressures are applied on an element face, misleading the calculation of the nodal forces.

For first-order elements, both master and slave surfaces enter into contact interaction when they are placed nearby, and a contact property model is activated between them. ABAQUS judges if the surfaces are in contact or not for each increment in the numerical computation process, depending on the *clearance* between them, and consequently activates or not the contact constraint, for an open-closed contact state. In this way, the program can keep the force equilibrium in the implicit numerical model.

When the surfaces are in a closed contact state, the contact property model governs the normal and tangential interaction between the surfaces. In the normal direction, it is common to define pressure-overclosure relationships (Kavvadas, Litsas, Vazaios, & Fortsakis, 2017; Boldini, Losacco, Bertolin, & Amorosi, 2018; Losacco & Viggiani, Class A prediction of mechanised tunnelling in Rome, 2019). An example of the “hard” contact is exhibited in the next Figure 3.19. This type of contact property is the strictest one, simulating a “perfect” contact by limiting the surface penetration and assigning infinite normal contact stiffness between them. In this way, it allows the precise transmission of any pressure between the contacting surfaces. This is similar to Nemorini’s (2010) spring method, which sees the nodal forces increase indefinitely when the contraction of each spring equals the distance between the excavation walls and the shield extrados. In the case of hard contact, when a node of the slave surface penetrates the master surface, the program provides an opposing nodal force that restitutes the node back to the target surface, nullifying the penetration. The precision of the hard contact can, however, generate numerical convergence problems.

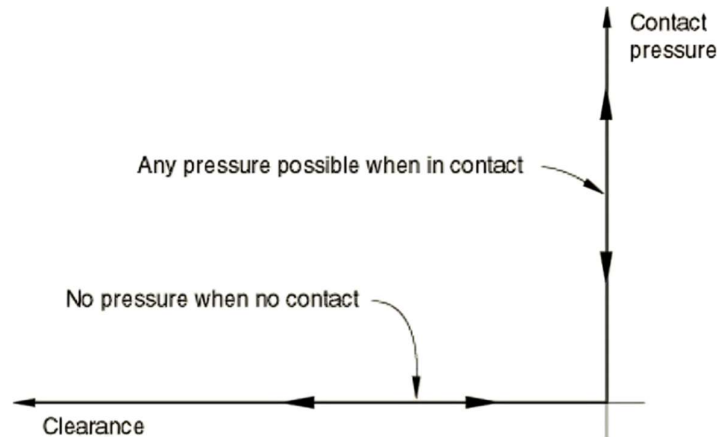


Figure 3.19. Hard contact pressure-overclosure property (Dassault Systemes, 2024)

An alternative is using the penalty method, which approximates the hard contact by setting the contact forces proportional to the penetration distance. In this way, the penalty allows a limited penetration between the surfaces by setting a finite normal contact stiffness (called *penalty stiffness*) and furthermore, it allows early pressure transmission if the user assigns a value for the *clearance* larger than zero. These two properties allow for the “numerical softening” of the contact problem, in most cases improving computational run-times and numerical convergence. For any of these formulations, the option to allow separation after contact can be selected to simulate a gap between both surfaces.

In the tangential direction, frictional behaviors are usually included which transmit shear forces between the contacting surfaces. The most used friction algorithm is the classical isotropic Coulomb friction model, which considers that two surfaces have no relative motion if the frictional strength  $\tau = \mu \cdot \sigma_n$  is not surpassed, where  $\mu$  is the friction coefficient defined by the user and  $\sigma_n$  is the normal contact pressure that comes from the pressure-overclosure relationships studied before.

With the definition of the contact in ABAQUS, the interaction between different parts of the model can be simulated, for example between the shield extrados and the converging tunnel excavation walls. As an example, Kavvadas et al. (2017) and then revised by Litsas et al. (2017), accounted for a variable steering gap for their parametric analyses, this only present at the crown of the excavation with the TBM resting at the bottom, as shown in the next Figure 3.20. The values for the gap were taken equal to 2 cm (1 cm for each the overcut and the conicity), 4 cm (1 cm of overcut and 3 cm of conicity) and 6 cm (2 cm of overcut and 4 cm of shield conicity). In their results, the authors witnessed the pronounced effect of increasing the steering gap in the surface settlements, in some cases almost doubling the value of the volume loss when expanding the gap from 2 to 6 cm.

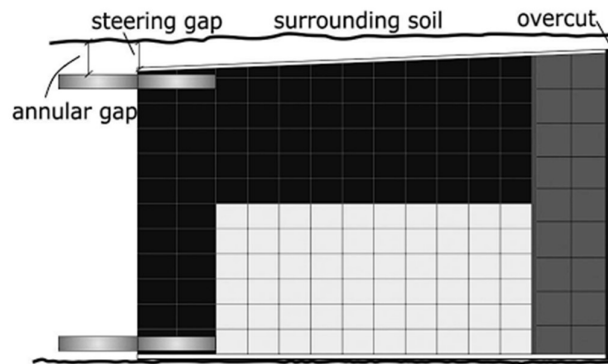


Figure 3.20. Scheme of the machine showing the overcut, steering and annular gap (Litsas, Sitarenios, & Kavvadas, 2017)

With this geometry or rather, assembly of distinct parts, namely the soil and the shield, the prominent form of ground movement is sure to resemble an oval-shaped tunnel contraction, such as the one depicted in Figure 3.11 b). This is to say, the uniform soil contraction considered by Rowe & Kack (1983) to happen at the initial stage of the excavation is disregarded (remembering Figure 2.14), to directly account for the formation of the oval-shaped contraction from the beginning of the excavation. This is explained mainly due to the TBM's self-weight, which allows for the machine to sit at the invert re-confining the soil below it after the material is loosened by the over-excavation, contrary to the soil at the crown, which is also affected by the overcut, but it is left to freely displace and never re-confined at the immediate excavation step. In this way, there is a homothetic contraction of the excavation walls with a downwards displacement of the cavity that produces zero displacements at the lowest point of the tunnel. Another cause, although minor, for the existence of the steering gap predominantly at the crown of the tunnel was before supported by the very detailed models developed by Kasper & Meschke (2004), who developed an algorithm to prescribe the non-uniform TBM jack thrust to counter the TBM's self-weight which tends, according to the authors, to vertically drift off course the machine, especially in soft soils. This is common in TBM steering practice, and in response the operators seek to correct the deviation of the machine's advancement from the designed tunnel axis, by adjusting the pitch of the cutterhead with the relocation of the center of truss of the jacks (Loganathan & Poulos, 1998; Park, et al., 2023). This minor (millimetric) pitch upwards to counter the self-weight can seemingly provide for slightly higher overcuts at the crown, in comparison to the invert.

Continuing with the investigations by Kavvadas et al. (2017), in terms of contact interactions it is disclosed that between the shield and the soil, a normal soft contact pressure-overclosure exponential relationship was defined, while frictionless contact was introduced in the tangential direction to account for a lubricated shield extrados. For the normal contact, the authors mention that parametric analyses were carried out to obtain reasonable stress transfer between the soil and the shield, given that the softened contact is not as precise as the hard contact, but it does provide higher numerical stability.



A similar contact property was defined by Losacco & Viggiani (2019), only replacing the soft exponential contact formulation with a hard penalty one, both behaving comparably, with the necessity once again to calibrate the contact interaction, in this case to minimize the overclosure while maintaining numerical convergence. To account for the shield gap, on the other hand, the authors selected the original TBM dimensions of the Line C of Rome project, having a cutting wheel diameter of 6.71 m, and a shield with a maximum diameter of 6.69 m behind the cutterhead, reduced to 6.67m at the tail due to the shield conicity. This results in a steering gap varying longitudinally from 2 cm at the cutterhead to 4 cm at the tail. This is true for their case, as they considered the shield to be concentric with the excavation, resulting in a uniform radial gap around the shield (also sketched in the next Figure 3.21), contrary to the assumptions of Kavvadas et al. and Litsas et al. revised above. This method is, however, in line with the initial observations of Rowe & Kack (1983), given that Losacco & Viggiani only fixed the shield and the first liner (closest to the TBM) concentrically with the excavation, while the rest of the liners were allowed to freely plunge due to their self-weight, reproducing faithfully Rowe & Kack's initial-to-final tunnel configurations, respectively shown in the past Figure 2.14 a) and b).

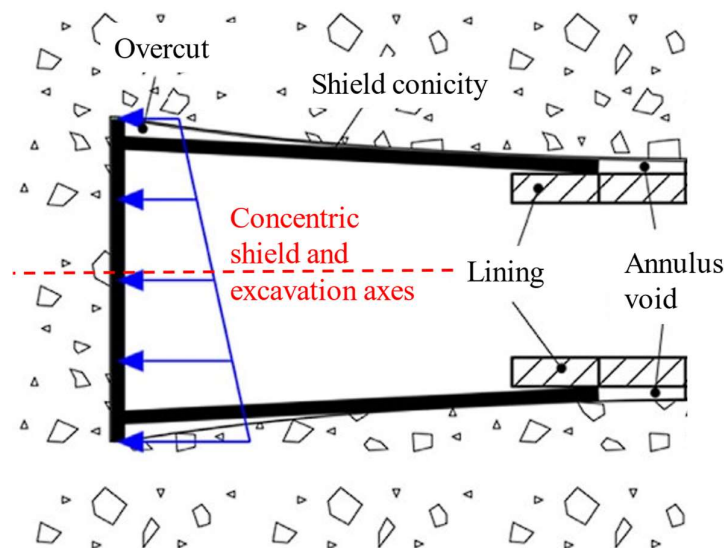


Figure 3.21. Scheme of the machine showing the overcut, steering and annular gap, modified from Losacco & Viggiani (2019)

The final consideration, although discussed briefly before, is the pressure induced by the intruding material in the shield gap. Earlier, seen as an alternative to simulate the convergence of the ground around the shield without explicitly modelling the TBM, this pressure can also be imposed in models that include the shield as a distinct part. As well illustrated by Epel et al. (2021) in the next Figure 3.22, even if mostly true for slurry shield TBMs more than EPBs, the material mix present in the machine's pressurized chamber can infiltrate inside the steering gap generating a radial pressure, and at the tail of the shield this same material is met by the annulus grout, which also exerts a radial pressure at the excavation walls.

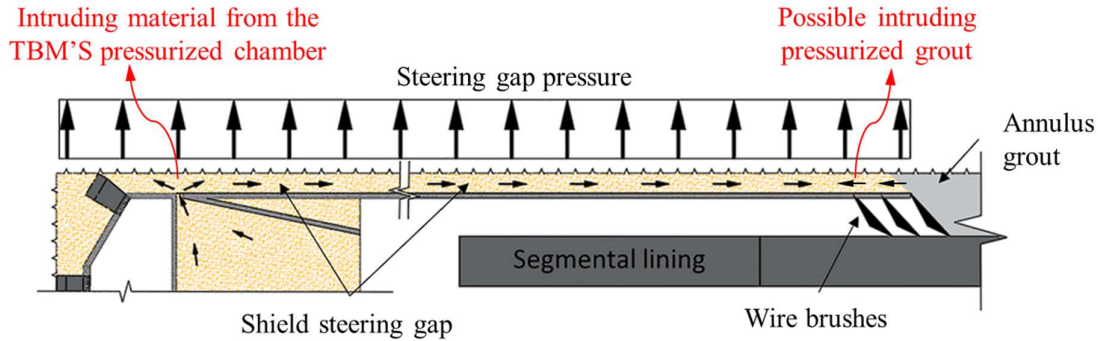


Figure 3.22. Causes of the steering gap pressure, modified from Epel et al. (2021)

Indeed, Litsas et al. (2017) concentrated their efforts on studying the impact of considering different shapes of the pressurized steering gap area to the surface settlements. By defining the Scenario A: trapezoidal total pressure that starts at the cutterhead equal to the face pressure and ends at the tail of the shield equal to the grout injection pressure; Scenario B: triangular total pressures only acting at the extremes of the shield and extending inwards for one-third of the shield's length, respectively equivalent to the face and grout injection pressures at their highest values; both these scenarios depicted in the next Figure 3.23, while a third no-pressure scenario was also considered to account for an absent intruding material. In their results, the authors showed that comparatively, considering the Scenario B and no-pressure configurations seldom differ in the values of the volume loss, while the Scenario A does have volume losses that can be as small as the half of those found for the no-pressure scenario.

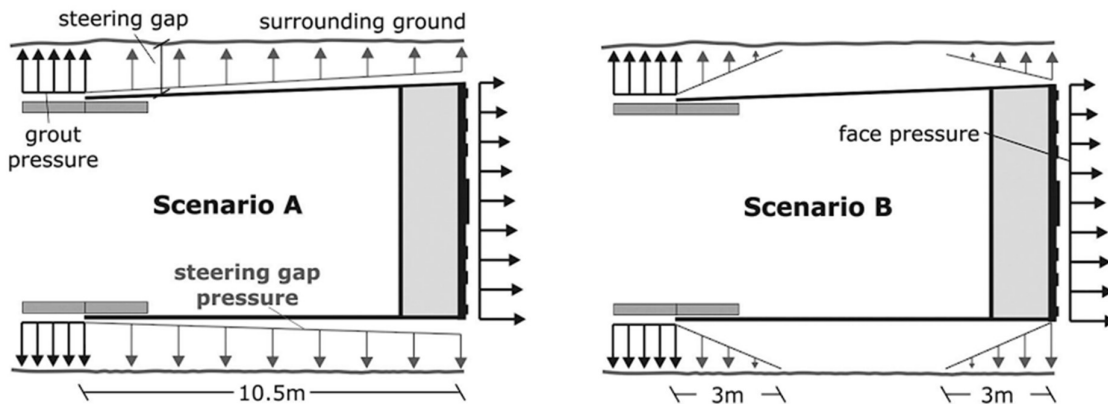


Figure 3.23. Steering gap pressure scenarios, as presented by Litsas et al. (2017)

### 3.1.5.3 Soil convergence around the liners and grout

On top of the convergence around the shield of the TBM, as also mentioned in Chapter 2, the surface settlements are likewise a product of the convergence of the ground around the liners. In this scenario, the soil may displace freely inside the annulus void until it meets the extrados of the liners (recalling Figure 2.9 from the same Chapter 2) if the void is not completely filled by a capable material: the two-component grout, among those discussed under the past heading 3.1.3.3. At the beginning of the injection

from the tail supply lines, the grout behaves as an incompressible and pressurized liquid, which is expected to show low contractions or even, due to its pressurization it might expand the cavity moving the soil outwards (Kasper & Meschke, 2004; Kavvadas, Litsas, Vazaios, & Fortsakis, 2017; Mollon, Dias, & Soubra, 2012). Still, even after the void is entirely filled with grout, as the material hardens in time it becomes compressible and depending on its elastic properties, under pressure it can further contract an additional distance.

In numerical modelling, the decision might be to not account for these intricate material behaviors. Without considering grout curing (time-dependent Young's modulus) or grout injection pressure, some authors have effectively modelled the influence of the annulus grout by providing it with a conservatively low Young's modulus (Migliazza, Chiorboli, & Giani, 2009; Nemorini, 2010), which is representative of its stiffness at early stages. The grout hardening, nonetheless, has already been proven to affect significantly the evolution of the surface settlements (bearing in mind section 3.1.3.3) and not including it may lead to overestimated volume losses.

For what concerns the grout injection pressure, already hinted in Figure 3.13 and Figure 3.23, Litsas et al. (2017) presented a noteworthy study on its influence on the basin of subsidence. Firstly, the authors modelled a crown annular gap of varying width between 11 to 15 cm, afterwards filled with grout solid elements which carried an inner isotropic stress equal to 200, 400 and 600 kPa, pressure only activated at the lining ring immediately after the shield's tail, and deactivated for the rest, to simulate different grout pressures in a series of parametric analyses. Their results showed, expectedly, that higher grout injection pressures do help in limiting the volume losses, although its effect is minor in comparison to other model parameters such as the shield steering gap and steering gap pressure.

Several more authors have also simulated annulus gaps and grout injection pressures: Losacco & Viggiani (2019) accounted for a uniform concentric tail void gap of 31 cm, applying a grout pressure only at the first liner ring behind the tail equal to 250 kPa, which sit within the targeted injection pressure of 400 kPa and an alarm trigger of 100 kPa set by the contractor; Mooney et al. (2016) modelled an uniform annulus concentric gap of 26 cm and they filled it with two-component grout elements, which were also only pressurized at the first liner ring behind the shield (considering that the two-component grout hardens rapidly and therefore, its pressurized liquid state is only preserved for a limited time), conducting parametric analyses with 276, 429 and 785 kPa of grout pressure at the tunnel springline, applied as distributed pressures at the excavation walls and varying in the vertical with the grout's unit weight, with their results supporting those of Litsas et al. indicating that the grout pressure, even if considered only for a limited length, is capable of controlling the surface subsidence; finally, Mollon et al. (2012) with an exercise model of excavation diameter and overburden equal to 10 m, reproduced an uniform concentric gap of 26 cm and applied an uniform grout pressure of 215 kPa (according to the authors equal to 1.20 times the overburden pressure) around the excavation walls, once again only for the first liner immediately behind the shield, and their results are best illustrated in the next Figure 3.24 in which they show how the soil can retract locally due to the applied pressure,

reducing the ground convergence at the crown of the tunnel even after the grout has solidified, in comparison to the accumulated settlement values obtained right after the shield conicity.

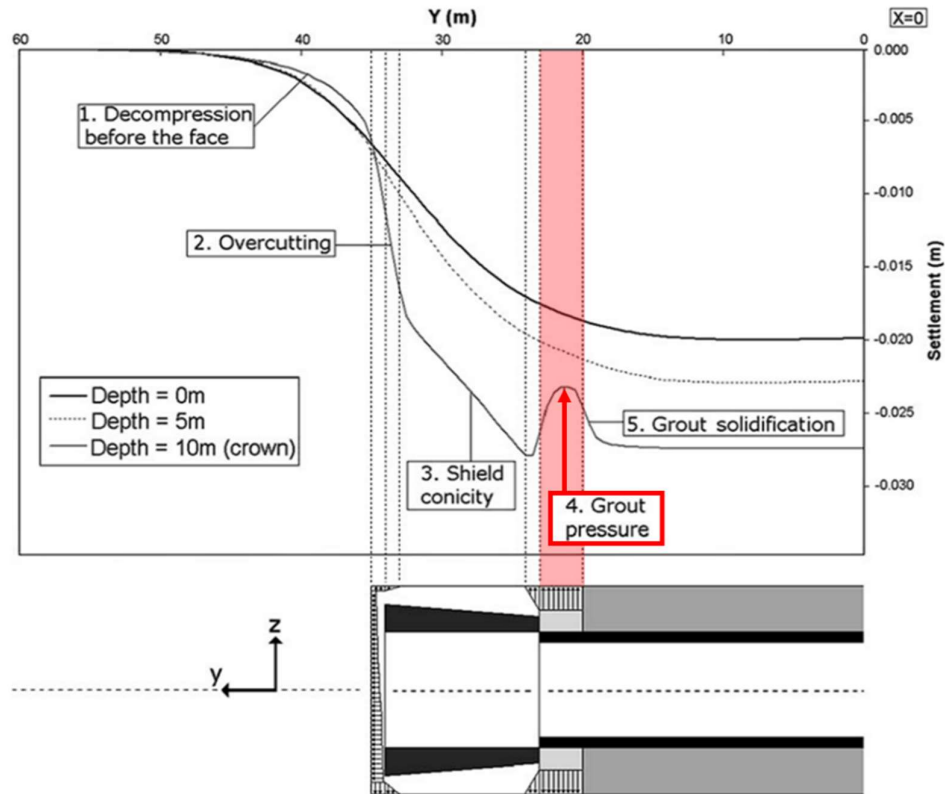


Figure 3.24. Results of ground settlements obtained by Mollon et al. (2012), modified to draw especial attention to the effect of the grout pressure

The last ingredient is the activation of the segmental lining and grout elements behind the shield. Particularly in ABAQUS (Dassault Systemes, 2024), it is possible to deactivate the soil elements to simulate the excavation and to activate them once more after the shield has passed, but this second time with different material properties representative of the liner's reinforced concrete and the grout (Nemorini, 2010). In ABAQUS CAE, on the other hand, this sudden material model change is not possible, and a workaround must be employed: defining the material parameters (i.e. the Young's modulus) in function of a field variable that at the beginning may represent the soil and, after a certain model step, changes to emulate the liner and grout properties, without changing the constitutive formulations of the original material. This last part, however, may present some difficulties when there is the need to model a completely different material behavior.

An alternative approach is to model both the soil and the liners plus grout as distinct parts, each with their respective material models, for then assigning a contact interaction between the grout extrados and the soil excavation walls once the lining rings are activated; in the same way as was performed for the soil and the shield interaction. Therefore, the same comments around the definition of the contact

discussed in the past heading 3.1.5.2 apply here, only this time the contact surfaces must not be allowed to freely separate, to account for the grout adhesively attaching to the surrounding soil.

#### *3.1.5.4 Consolidation*

In the case of fine grained stratigraphies, the consolidation settlements tend to be more significant than the immediate tunnelling settlements, extending in time for even decades and in some cases increasing the vertical displacements up to a factor of three (Burland, 2001). Quite a few authors have included the effects of the long-term settlements in their models, for a limited number of days after the passing of the TBM's cutterhead (Kasper & Meschke, 2004), for the time frame between the passing of two TBMs in twin tunnelling (Losacco & Viggiani, 2019) and for several years after the conclusion of the excavation (Yiu, 2018). In particular, this last study demonstrated the relevance of the segmental lining's permeability in the evolution of the consolidation settlements in London Clay, acting as a water siphon for fully permeable linings, leading to greater effective stresses around the tunnel when excess water pressure dissipated and thus, increasing the consolidation settlements in agreement with Mair & Taylor's (1997) statements.

## **3.2 The model of the building**

In this chapter, emphasis is made on three-dimensional numerical models from the literature following the finite element method, that simulate the interaction between a subsiding soil under the effects of a tunnel excavation, and a surface building affected by the produced settlements. Special attention is paid to the model of the building, since the model of the tunnel excavation was already described, while some comments are made on different forms to model the soil – structure interaction during shallow tunnelling.

### **3.2.1 Geometrical model, discretization and boundary conditions**

Trailing the scope of this effort, the interest is directed to the modelling of historical masonry buildings. In the same way as presented in a corresponding section above, here the geometry and the mesh of different masonry building models are described, for a list of relevant research articles that successfully simulated the soil – structure interaction in three dimensions during the tunnelling process. Contrary to the soil model, however, the model of a historical masonry building is of higher geometrical and constitutive complexity, that the engineers must be able to simplify to balance the computational costs with the accuracy of the solution. These simplifications are, commonly, not straightforward because of the numerous uncertainties regarding the types of materials used, their mechanical characteristics, the loading history, degree of

connectivity between structural elements and their internal morphology, added the transformation, repair and improvement interventions that the building may have experienced throughout the history, some of them not well documented or not easily identifiable in-situ (Ministero delle Infrastrutture e dei Trasporti, 2018).

Once these uncertainties are mitigated, the masonry in general can be numerically modelled following three approaches, according to Giordano, Mele & De Luca (2002), and still valid in this day and age. The first is the detailed micro-modelling with the finite element method with discontinuous elements (FEMDE), which accounts for the precise distribution of bricks and joints of the masonry, by modelling them as solid elements each with its own constitutive law and failure criteria and entering in frictional contact at their interfaces. This method is best employed when precise failure mechanisms are to be studied in limited portions of the building, yet it is both geometrically and computationally expensive when the entire structure is to be analyzed.

A simplified micro-modelling with the discrete element method (DEM) approach could be a better, less computationally expensive alternative to the FEMDE, because in this case the joint elements can be disregarded and instead, between the rigid or deformable masonry bricks a frictional contact formulation can be introduced to be equivalent to the action of the joint mortar, allowing the blocks to slip, rotate and impact each other once the shear stresses overcome the strength of the joints. This method is, nonetheless, better for the study of limited macro-elements and not entire structures as these block-to-block interactions can prove to be, once again, demanding.

The final method is a homogenized approach, with macro-modelling with the finite element method (FEM). In this case, which is widely used in the field of soil – structure interaction during shallow tunnelling, the masonry is modelled as a continuous equivalent material, that accounts for the properties of both the bricks and the mortar joints as a representative average that describes the behavior of the whole and, depending on the constitutive formulation employed, it can be either iso or anisotropic. This alternative is preferred when modelling the entirety of a masonry structure, as it allows to neglect the specificities of the brick-and-mortar arrangement, contributing to considerably fast model run-times and simplified geometrical modelling.

In literature, FEM is the preferred method to model soil – structure interaction due to shallow tunnelling. This is the case of Yiu (2018), who modelled in ABAQUS a generic masonry building with around 4 thousand shell second-order triangular elements of characteristic length equal to 0.5 m. The building and the soil were created as isolated parts. Particularly the building is modelled without considering the presence of inner walls nor slabs. For the simulation of the interaction, the foundation of the building was included in the same model of the soil and the building, using the embedment constraint in ABAQUS, was rigidly attached to the foundation. The model is displayed in Figure 3.25.

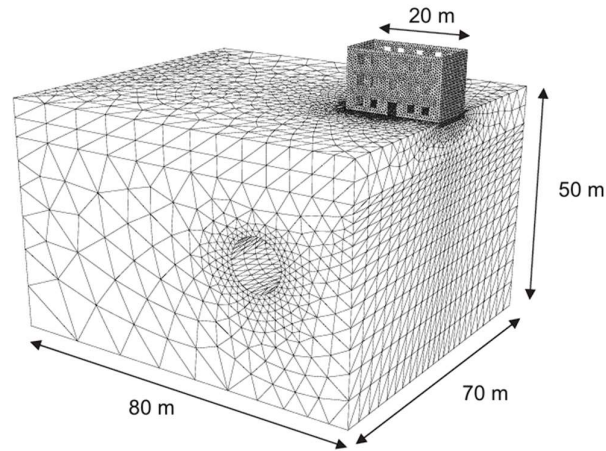


*Figure 3.25. Soil – structure interaction model mesh by Yiu (2018)*

Or the case of Losacco (2011) who included the building as a three-dimensional extension of the soil model with about 12 thousand solid hexahedral elements. The author also investigated two cases: a building with internal walls and another building without them (the latter is shown in Figure 3.26), showing that the presence of internal walls seldom affects the basin of subsidence. In none of the cases the presence of slabs was included.

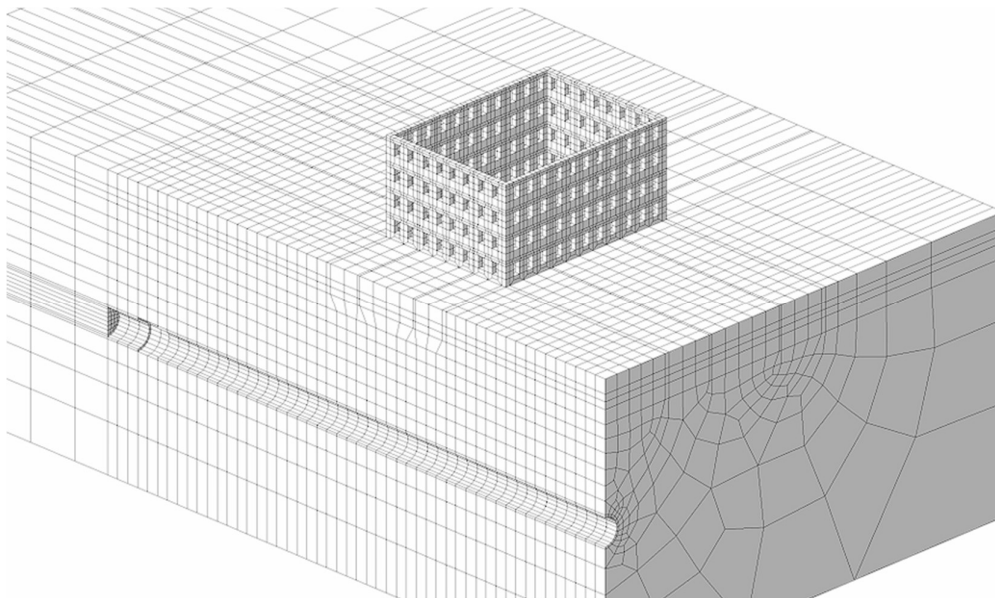


*Figure 3.26. Soil – structure interaction model mesh by Losacco (2011)*

Or finally the case of Rampello, Callisto, Viggiani & Soccodato (2012) who utilized two-dimensional shell elements for the building, of high degree of geometrical complexity as it considered inner bearing walls, yet again, disregarded the presence of slabs as noticeable in Figure 3.27 a). In Figure 3.27 b), the equivalent solid that represents the building with its stiffening contribution is also modelled, this one most definitely with three-dimensional solid hexahedral elements. This latter is a satisfactory alternative when complex structures must be modelled, but it is necessary to save

computational and geometrical modelling efforts. In this sense, an equivalent stiffness is found for the solid through an iterative procedure between the uncoupled models of the building and the soil, calibrated to best represent the building's stiffness which is known to reduce the surface settlements.

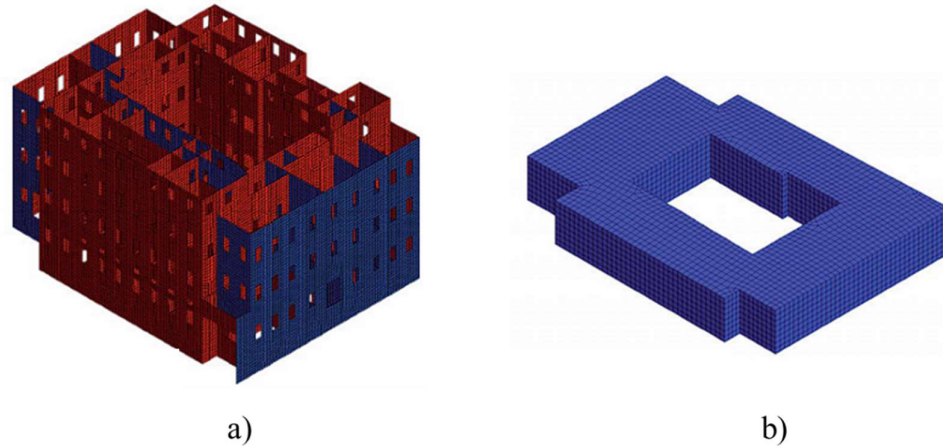


Figure 3.27. Soil – structure interaction model mesh of the a) building and b) equivalent solid by Rampello, Callisto, Viggiani & Soccodato (2012)

### 3.2.2 Material properties

Masonry is a characteristically heterogeneous construction material, especially when historical buildings are analyzed. Firstly, because the typology of the masonry can drastically change, not only from one building to another, but regarding the same building that may have been raised during multiple periods, using different types of materials according to their availability in the respective era, with different degrees of preservation. Consequently, for each material and each construction technique, the strength and elastic properties of the masonry macro-elements may change considerably (Aoki, Sabia, & Rovesti, 2022).

But, more importantly, it is heterogeneous because of the very same procedure followed to erect the masonry: walls made of ordinary masonry, for example, are typically built of clay bricks connected by mortar joints. Here already, the behaviors of two very different materials must be regarded in the analyses, creating a plethora of fragile failure mechanisms that are unique to each constitutive behavior and that propagate in the whole, differentiating it from modern reinforced structures. These two materials, on the other hand, in numerical modelling can be homogenized, as discussed in a previous section, to improve the model run-times and cut geometrical complexities, while still providing accurate results if the equivalent material is engineered to well represent the monolithic mechanisms of the brick-and-mortar unit.

An example of a homogenized anisotropic elastic-perfectly plastic constitutive model for masonry, close to the world of rock mechanics, is the *Jointed Masonry Model*



(JMM) formulated by Lasciarrea et al. (2019) based on the *Jointed Rock Model* (JRM) available in the numerical code PLAXIS. The novelty of the model is that it uses the theory of discontinuities in rock masses to describe the masonry as a rock-like material, due to its intact blocks, governed by discontinuities, which are its mortar joints, that change their frictional Mohr-Coulomb yielding behavior depending on the orientation of the joint planes and interlocking of the bricks.

Precisely taking advantage of this constitutive model, the authors simulated the excavation of a tunnel below a masonry building. The results of the comparison between the elastic and elasto-plastic JMM constitutive behaviors are shown in Figure 3.28, as presented by the authors (it is strongly recommended to consult the original paper to study the specificities of the model), in terms of the tensile total strains. In this case, it is clearly noticeable that the elastic behavior underestimates by almost 100 times the results provided by the JMM, in terms of the tensile strains. This is, nevertheless, not the first time it has been proven that elastic behaviors for masonry undervalue the real magnitude of the deformations. Before the authors, Losacco (2011) also demonstrated with a simplified numerical model of a masonry building that the tensile strains were underestimated by 5 to 10 times using the elastic constitutive formulations instead of elasto-plastic ones (in this case the author employed a modified version of Hoek & Brown's (1997) criterion). In the following years, Giardina et al. (2013) showed both from numerical results and laboratory tests that neglecting elasto-plasticity not only underestimates the magnitude of the tensile strains and extension of the deformations, but also disregards the real brittle failure kinematism of the masonry. Consistent results were obtained from large scale experiments by Dalgic et al. (2023).

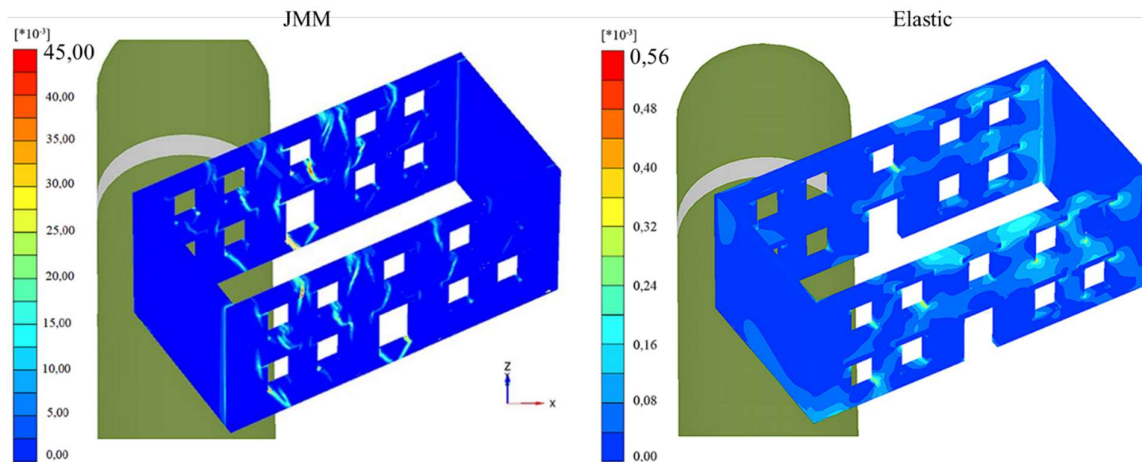


Figure 3.28. Results presented by Lasciarrea et al. (2019): comparison between tensile total strain in masonry provided by the elastic and JMM constitutive models

In literature, the importance of considering elasto-plasticity has been well proven. In ABAQUS, nevertheless, to employ a plastic model such as the JMM, an user material (UMAT) must be defined and this is not an easy task for the unexperienced. Instead, in this commercial software, engineers prefer using the *Concrete Damaged Plasticity* (CDP) model with isotropic damaged elasticity to emulate the behavior of masonry. Contrary to what its name suggests, the model is not only useful to describe the elasto-

plastic behavior of the concrete, but it has been widely used for other types of quasi-brittle materials, such as masonry (Anecchiarico, Portioli, & Landolfo, 2010; Acito, Bocciarelli, Chesi, & Milani, 2014; Tiberti, Acito, & Milani, 2016; Yiu, 2018; Acito, Magrinelli, Milani, & Tiberti, 2020; Zizi, Corlito, Lourenco, & De Matteis, 2021; Cattari, Camilletti, D'Altri, & Lagomarsino, 2021; Rainone, Tateo, Casolo, & Uva, 2023; Schiavoni, Giordano, Roscini, & Clementi, 2023; Aoki, Sabia, & Rovesti, 2022).

The model is isotropic and rate independent. If used to describe the masonry, it must be acknowledged that the model disregards the orthotropy of the material due to its joint planes. In elasticity, the formulation is described by the typical Hook's law  $\sigma = \mathbf{D} \cdot \boldsymbol{\varepsilon}$ . Once the material reaches its failure or yield stress (onset of micro-cracking) either in tension  $\sigma_{t0}$  or compression  $\sigma_{c0}$ , independently defined by the user for each branch, the material enters the post-peak behavior, which is also defined by the user in terms of compressive stresses and inelastic strains  $\tilde{\varepsilon}_c^{in}$ , and tensile stresses and cracking strains  $\tilde{\varepsilon}_t^{ck}$ . In compression, the behavior can be first characterized by a hardening curve followed by a softening end, while in tension it is limited to the constitutive softening. In this way, the model can predict crushing in compression and cracking in tension (Dassault Systemes, 2024), by outputting the results in terms of elastic  $\varepsilon^{el}$  and equivalent plastic  $\tilde{\varepsilon}^{pl}$  strains both in tension and compression.

The novelty of the model is that it allows to account for the progressive damage or fracturing of the material with an irreversible loss of stiffness, reducing its original (undamaged) elastic Young's modulus  $E_0$ . In the next Figure 3.29 and Figure 3.30 showing the uniaxial tension and compression stress behaviors, a damage parameter represented by  $d_c$  in compression or  $d_t$  in tension is configured by the user to decrease the value of the elastic modulus with the increase of the inelastic or cracking strains, respectively. The values of the Young's modulus for each strain are  $E_c = (1 - d_c) \cdot E_0$  and  $E_t = (1 - d_t) \cdot E_0$ .

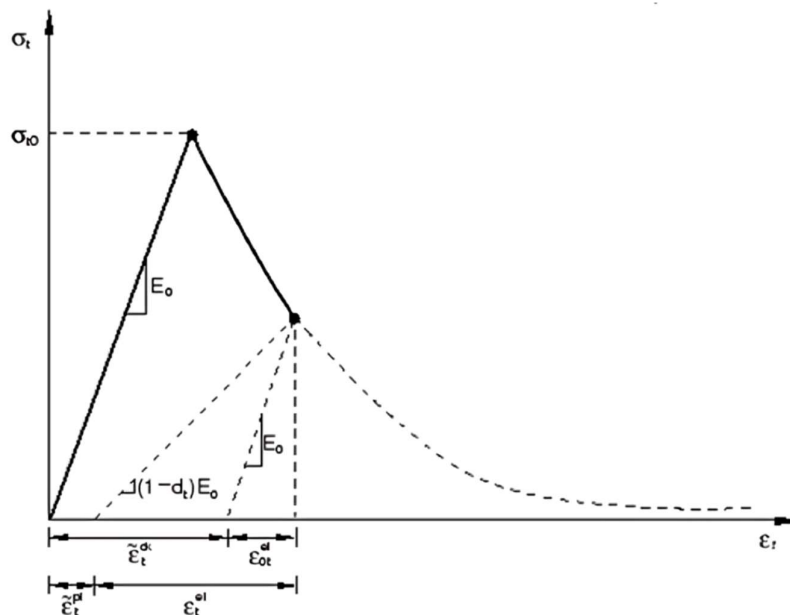


Figure 3.29. Typical CDP model response for uniaxial tensile loading (Dassault Systemes, 2024)

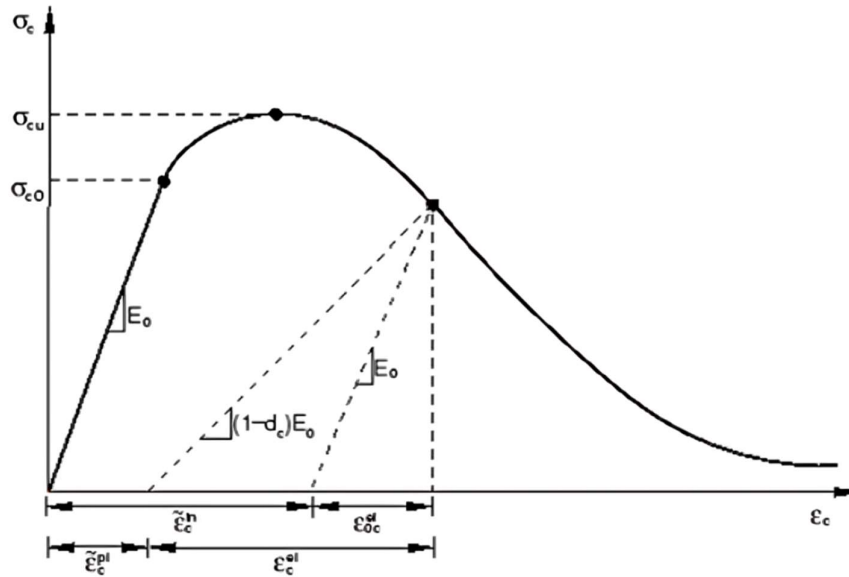


Figure 3.30. Typical CDP model response for uniaxial compression loading (Dassault Systemes, 2024)

In this way, once the material is unloaded, it does not follow the initial slope  $E_0$  but that of the damaged elastic modulus. This damaged state is very important to consider, especially in seismic analysis and by extension in tunnelling – masonry structure interaction step-by-step models, as the building will suffer both loading and unloading cycles as the excavation advances below it.

A dilation angle  $\psi$  must also be included to define the non-associate flow potential, formulated with Drucker-Prager's hyperbolic function. This, in turn, considers a regularization of the tensile regime by cutting the linear trend of the function and replacing it with a hyperbole, reducing slightly the tensile strength with a correction parameter known as the eccentricity, taken usually equal to  $\varepsilon = 0.1$ . The effect of the dilatancy is well studied by Rainone et al. (2023), who proves that this parameter in reality does not affect the elastic limit, leaving the yield surface untouched, but only modifies the post-elastic strength proportionally.

The yield function is that proposed by Lubliner, Oliver, Oller & Oñate (1989) and Lee & Fenves (1998) (Dassault Systemes, 2024), which modifies the Drucker-Prager strength domain with a  $K_c$  parameter equal to 0.667 to approximate it to Mohr-Coulomb's domain. The formulation also asks for the ratio between the mono-axial and biaxial compressive strengths, by default set at 1.16. Once again, Rainone et al. (2023) studied the effect of varying this latter ratio, which showed negligible influence in the constitutive behavior of the modelled masonry walls. According to the authors, the parameters that affect the most the CDP are the tensile failure strength and the size of the model mesh.

The final parameter, allegedly one of the most important as it can completely bias the output of the model, is the viscosity parameter  $\mu$ . This parameter is merely included in the CDP to counter possible convergence issues in implicit models while simulating the

constitutive softening; this by allowing the stress state to be fictitiously outside the yield surface. The values used by several researchers in the literature range from 0.00005 to 0.01, as presented in the subsequent Table 3.2, being 0.00005 the value that provides the most accurate results yet higher probability of incurring in numerical instability, and 0.01 the value that can alter the most the output with surely more stable simulations. Most of the authors that have worked with masonry buildings appear to use the value of 0.002. This is a good alternative if first it is verified in ABAQUS that the magnitude of the viscosity parameter remains small in comparison to the characteristic model time increment (Dassault Systemes, 2024).

To provide the model with the required parameters, according to the Eurocode EN 1991-1 (CEN, 2005), the compressive strength and elastic modulus of new masonry constructions must be determined from test results, either available from the construction site or from databases. In all cases, the code indicates that the tensile strength of the masonry must be disregarded. This is also true for existing buildings, following the Italian NTC 2018 Chapter 8 (Ministero delle Infrastrutture e dei Trasporti, 2018). In this case, nonetheless, no mention is made to databases, and it is explicitly required to perform at least a limited number of in-situ tests and investigations, from visual to geophysical and compulsory destructive tests, to assess the properties of the existing material.

In the literature it is noticed that, at the level of research, the constitutive parameters of the materials for the CDP model are mainly acquired from non-destructive tests, especially in constructions protected by the UNESCO, with many parameters still being obtained through databases of old destructive investigations on the same structure or on structures nearby, with a selected few then calibrated to fit a certain dynamic behavior recorded in-situ. An important number of studies also derive the parameters from national construction codes, such as the NTC Chapter 8 and its annexes, arguing that the lack of specific experimental tests can be countered by obeying the norm.

The next Table 3.2 presents a collection of different research articles, many of which successfully dealt with the CDP model for masonry structures, concerning the characteristics of a heterogeneous variety of Italian historical constructions and controlled numerical and laboratory studies on masonry, to grasp a probable range for the elasto-plastic properties that the material exhibits in-situ. The table is precisely that, a *collection of different* studies for exhibition, and should not be approached as a comparative unit. In the same table, the particularities of each masonry building or sample, such as the type of masonry and year of construction, are exposed to highlight the heterogeneity of the investigations.

It is also imperative to remark that most of these examples emerge from seismic analyses of existing masonry buildings. Still, since these types of analyses are the golden banner of structural engineering, the models are considered well-suited to reproduce more ‘modest’ engineering problems, such as the soil – structure interaction in urban tunnelling.

Table 3.2 Elastic and CDP properties of different masonry buildings and samples in the literature

	Acito et al. (2020)	Acito et al. (2020)	Schiavoni et al. (2023)	Aoki, Sabia & Rovesty (2024)	Tiberti et al. (2016)	Tiberti et al. (2016)
Type of building	Residential	Residential	Church	Cathedral	Castle	Castle
Location	Amatrice, Italy	Amatrice, Italy	Camerino, Italy	Modena, Italy	Finale Emilia, Italy	Finale Emilia, Italy
End of construction	1900	1900	1800-1835	1319	1401	1401
Materials	Low quality masonry. Disordered stone masonry walls (irregular)	High quality masonry. Cut stone masonry walls (irregular)	Regular clay masonry facades	External dry cut stone masonry with internal regular clay masonry	Non-restored regular clay masonry with poor mortar	Restored regular clay masonry with poor mortar
Elasticity						
Young's [MPa]	690	1980	2250	2500	900	1500
Poisson's	0.15	0.15	0.25	0.20	NR	NR
Concrete damaged plasticity						
Plasticity						
Dilation angle [°]	10.0	10.0	10.0	30.0	10.0	10.0
Eccentricity	0.10	0.10	0.10	0.10	0.10	0.10
$\sigma_b/\sigma_c$	1.16	1.16	1.16	1.16	1.16	1.16
K	0.667	0.667	0.667	0.667	0.667	0.667
Viscosity parameter	0.002	0.002	0.01	0.0005	0.002	0.002
Compressive behavior						
Yield stress 1 [MPa]	1.22	3.80	6.50	3.00	1.22	2.40
Yield stress 2	0.95	3.40	0.70	3.00	0.95	1.90
Yield stress 3	0.95	3.40	0.70	0.03	0.95	1.90
Yield stress 4	0.80	2.80	NR	NR	0.8	1.80
Inelastic strain 1	0	0	0	0	0	0
Inelastic strain 2	0.005	0.005	0.0075	0.002	0.005	0.005
Inelastic strain 3	0.01	0.01	0.1	0.005	0.01	0.01
Inelastic strain 4	0.10	0.10	NR	NR	0.10	0.10
Tensile behavior						
Yield stress 1 [MPa]	0.04	0.12	0.65	0.08	0.04	0.08
Yield stress 2	0.0005	0.0005	0.0005	0.007	0.0005	0.0005
Yield stress 3	0.0005	0.0005	NR	0.003	0.0005	0.0005
Cracking strain 1	0	0	0	0	0	0
Cracking strain 2	0.003	0.007	0.001	0.00025	0.003	0.005
Cracking strain 3	0.10	0.10	NR	0.001	0.10	0.10
Tension damage						
Damage parameter 1	0	0	NR	NR	0	0
Damage parameter 2	0.95	0.95	NR	NR	0.95	0.95
Cracking strain 1	0	0	NR	NR	0	0
Cracking strain 2	0.003	0.007	NR	NR	0.003	0.005

*Table (Continuation) Elastic and CDP properties of different masonry buildings and samples in the literature*

	Acito et al. (2014)	Zizi (2021)	Annechiarico (2009)	Cattari (2021)	Giardina (2013)	Rainone et al. (2023)
Type of building	Clock tower	Medieval churches	Numerical masonry wall	Numerical masonry wall	Physical and numerical models	Numerical masonry wall
Location	Finale Emilia, Italy	Abruzzi region, Italy	2D micro- and macro-	2D macro-modelling in FEM and	Experimental tests and 2D FEM	Extensive parametrical analyses
End of construction	1401	1000-1700	modelling of panels with	macro-elements of panels with CDP	models, using the Sequentially	on micro- and macro-models of
Materials	Poor clay masonry	Regular clay masonry	CDP		linear analysis (SLA), not CDP	masonry panels. Best fit
Elasticity						
Young's [MPa]	1200 - 1800	1800	3000	1800	3000	3128
Poisson's	NR	0.25	0.15	0.20	0.20	0.15
Concrete damaged plasticity						
Plasticity						
Dilation angle [°]	10.0	10.0	20.0	20.0	NR	36.9
Eccentricity	0.10	0.10	NR	0.10	NR	0.10
$\sigma_b/\sigma_c$	1.16	1.16	NR	1.20	NR	1.16
K	0.667	0.667	NR	0.667	NR	0.667
Viscosity parameter	NR	0.00005	NR	0.0001	NR	0.0001
Compressive behavior						
Yield stress 1 [MPa]	2.4	4.0	7.0	5.5	Used failure energy	13.0
Yield stress 2	1.9	NR	NR	6.2	NR	17.5
Yield stress 3	1.9	NR	NR	0.7	NR	0
Yield stress 4	1.8	NR	NR	NR	NR	NR
Inelastic strain 1	0	Used failure energy	0	0	Used failure energy	0
Inelastic strain 2	0.005	NR	NR	0.002	NR	0.004
Inelastic strain 3	0.01	NR	NR	0.009	NR	0.01
Inelastic strain 4	0.10	NR	NR	NR	NR	NR
Tensile behavior						
Yield stress 1 [MPa]	0.17	0.2	0.35	0.22	Used failure energy	0.35
Yield stress 2	0.0005	NR	NR	0.02	NR	0
Yield stress 3	0.0005	NR	NR	NR	NR	NR
Cracking strain 1	0	Used failure energy	0	0	Used failure energy	0
Cracking strain 2	0.003	NR	NR	0.001	NR	0.0001028m*
Cracking strain 3	0.003	NR	NR	NR	NR	NR
Tension damage						
Damage parameter 1	0	NR	NR	0	NR	0
Damage parameter 2	0.95	NR	NR	0.90	NR	0.10
Cracking strain 1	0	NR	NR	0	NR	0.004m*
Cracking strain 2	0.003	NR	NR	0.001	NR	0.01m*

NR= Not reported by the authors

\* In terms of displacement

## Chapter 4

### The Metro-Line 2 of Torino project

#### 4.1 General information

The Metro-Line 2 of Torino project represents the next milestone in transportation, engineering and socio-economic development for the City of Torino, Italy. With a configuration in Y that encompasses zones towards the north and south-west of the city before not reached by the Metro-Line 1, connecting three university campuses, two hospital districts, two train stations and several cultural centers, the entire line (seen in the Figure 4.2) is projected to move around 280 thousand citizens every day (Infratrasporti.To S.r.l., 2024), aiming for the title of “15-minute metropolitan city”.

The first phase of the project is focused on the north and central quarters of the city, from the stations of Rebaudengo to Politecnico as depicted in Figure 4.1. This decision, taken by the City of Torino and its society Infratrasporti.To S.r.l. (also referred to as Infra.To, main actor behind the preliminary designs and contract administration of the project), was motivated by the possibility of reactivating the north pole of the city.

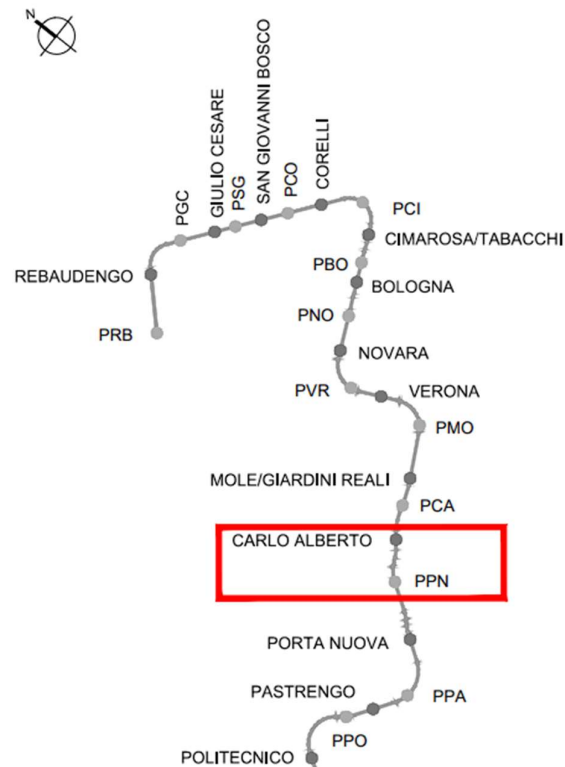


Figure 4.1. First phase of the Metro-Line 2 project (Infratrasporti.To S.r.l., 2024)

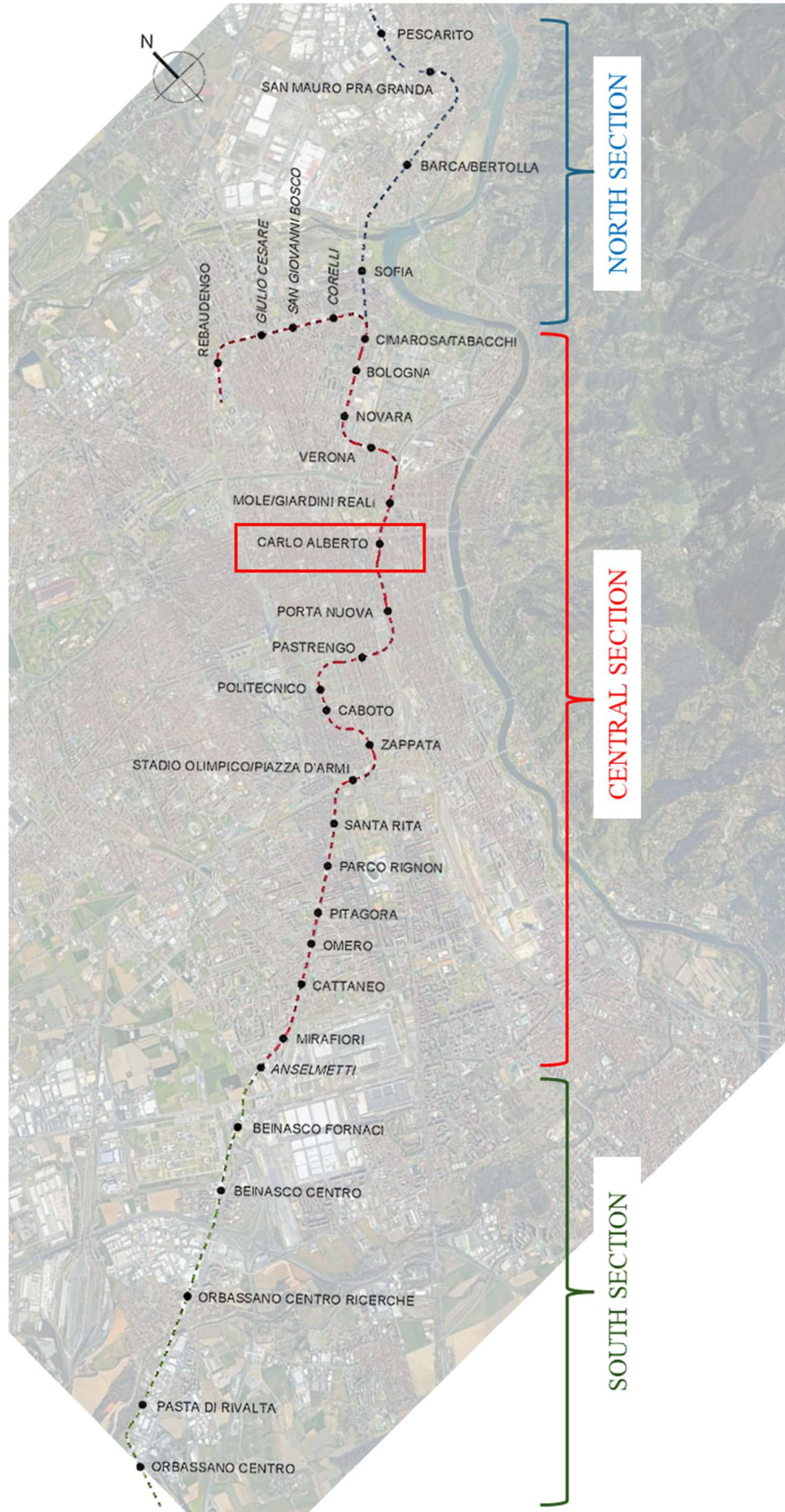


Figure 4.2. Metro-Line 2 of Torino complete development



Truly, the north quarters reunite some of the highest population densities and public transportation usages of the entire city, as shown in Figure 4.3.

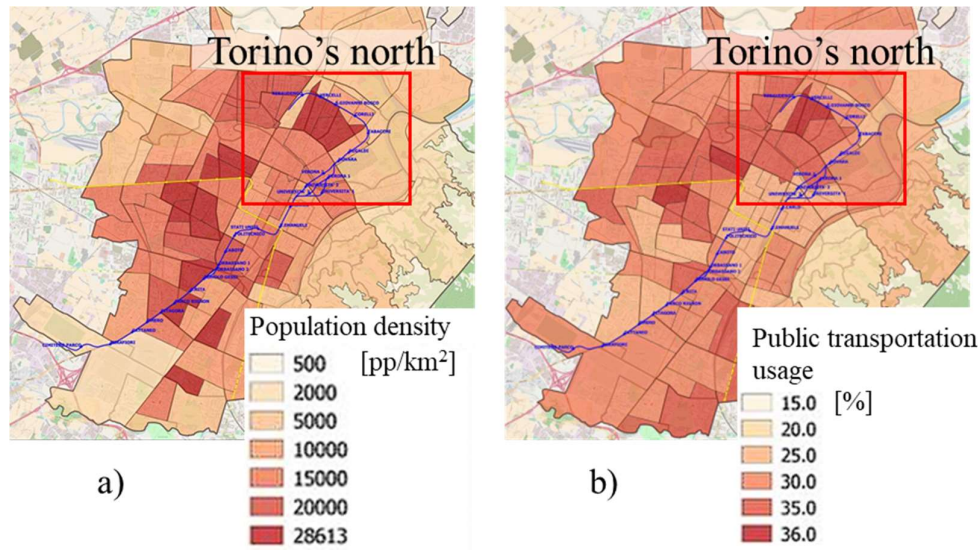


Figure 4.3. From left to right: a) population density and b) public transport usage in the City of Torino, modified from Infratrasporti.To S.r.l. (2024)

However, these zones are characterized by not being commercially active and aesthetically unattractive for new citizens to inhabit the areas or start new activities. By connecting the center of the city and the most important academic and cultural poles to the north, and providing the vicinities with visually appealing architecture and abundant vegetation (see Figure 4.4) as a part of the Metro-Line 2 project, the hope is to revitalize the zones from the inauguration of the Metro and for years to come.



Figure 4.4. Revitalization of Torino's north, driver of the Metro-Line 2 project (Infratrasporti.To S.r.l., 2024)



## 4.2 The soil of Torino

### 4.2.1 Geology

The host of the next Metro-Line 2 of Torino is the Torino subsoil. This particular soil, known by Italian geotechnical engineers of every corner of the nation, is characterized by its coarse fluvio-glacial and fluvial deposits, as better depicted in the geological map of Figure 4.6. The top layers of the geology that extend in depth from 25 to 50 m, horizons 1 to 3 shown in the section cut “A-A” (subsequent Figure 4.7), are defined as gravels and pebbles in a silty-sand matrix, with an inherently variable degree of cementation that grants it notable mechanical properties: see the face of the excavation in Figure 4.8, about six meters tall is either unsupported or minimally restrained and even so, it maintains its stability.

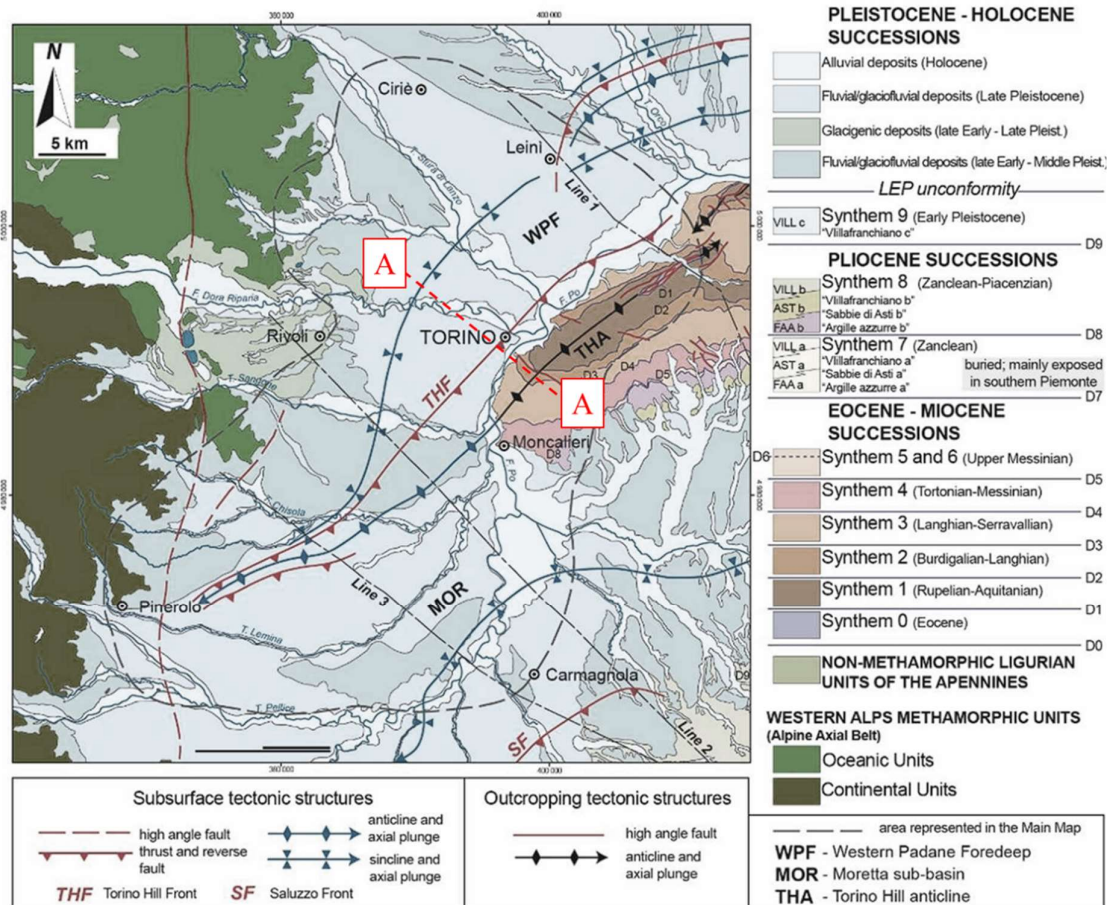


Figure 4.6. Geology of western Piemonte, modified from Irace et al. (2024)

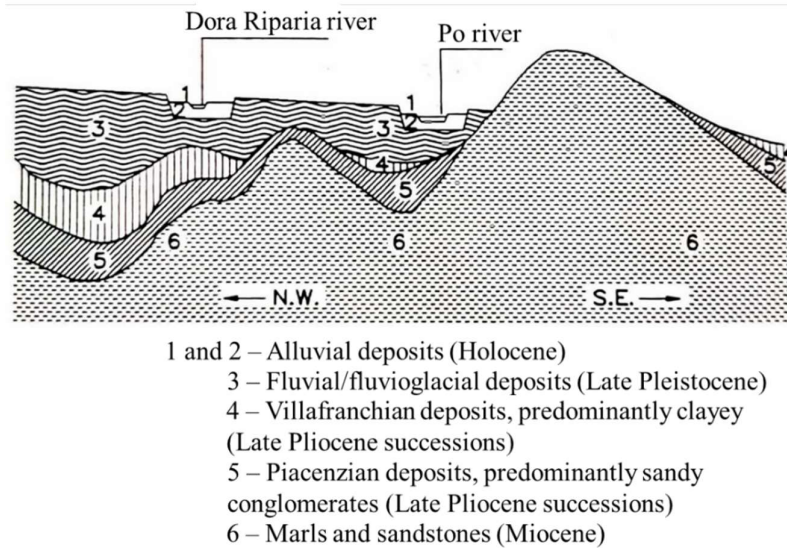


Figure 4.7. Elevation scheme of the A-A section of the geological map, modified from Bottino & Civita (1986)

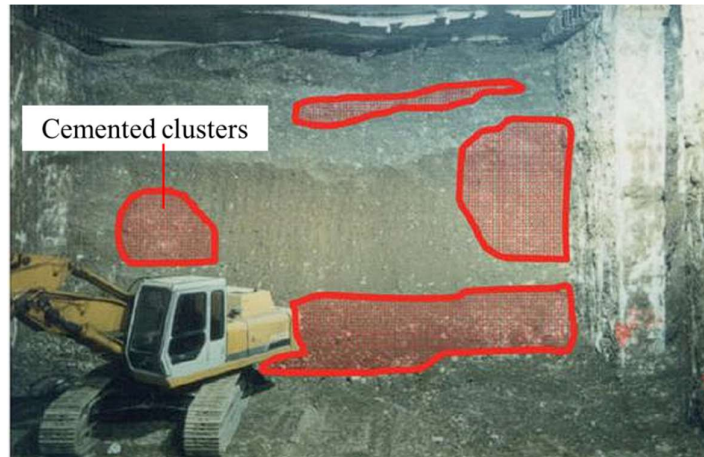


Figure 4.8. Bare excavation front of the Underground Railway Link of Torino (Barla & Barla, 2012)

This is a “block-in-matrix” soil, in which the blocks are conglomerates locally called “puddinga” that can vary in size from a few centimeters to various meters and have an arbitrary distribution within the matrix, as clearly shown in the figure above. The genesis of these cemented clusters is still under debate, with some researchers (Bottino & Civita, 1986) believing that it occurs mainly due to the overlapping of waters of different pH and temperature descending from the Alps, promoting the deposition of calcium carbonate and with it, the formation of the material clusters; while others (De Rienzo & Oreste, 2011) arguing that it is because of slightly acidic meteoric waters permeating into the subsoil’s vadose zone. Whichever is the reason for the cementation, this process is not homogeneous, as has been proven by De Rienzo & Oreste (2011), who studied the spatial variability of the conglomerates and produced planimetries for different depths as shown in the next Figure 4.9. In these planimetries, the contours indicate the probability of meeting one of three different cementitious densities of the subsoil: C1 indicates that the soil is mainly loose or has weak localized cementation, C2 that there are important cemented levels and C3 that the matrix is predominantly

cemented. In the figure, the Piazza Carlo Alberto zone is enclosed and a stratigraphic section of this zone, near the building Palazzo Campana, is below in the Figure 4.10.

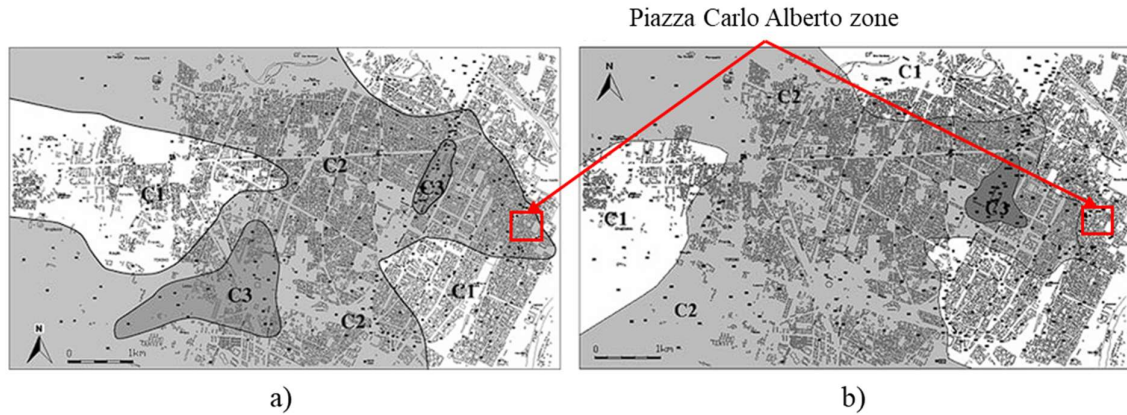


Figure 4.9. Degrees of cementation in the Torino subsoil at: a) 15 m below the ground surface and b) 20 m, after De Rienzo & Oreste (2011)

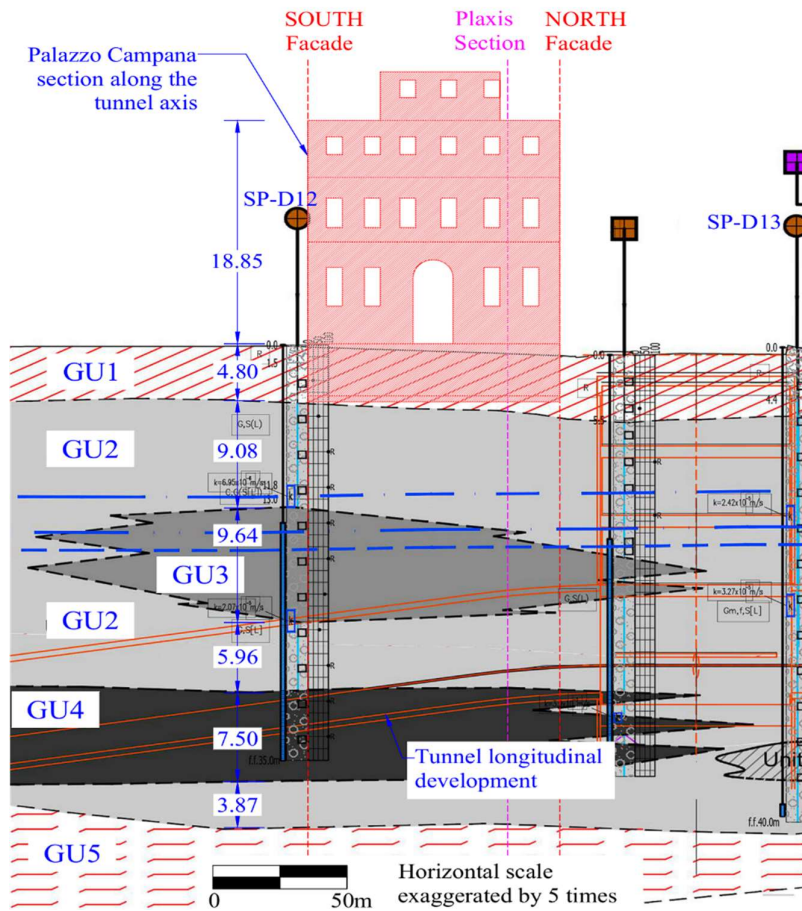


Figure 4.10. Stratigraphy in the Piazza Carlo Alberto zone, below Palazzo Campana (Infra.To S.r.l., 2024)

The stratigraphy provided above is mainly derived from two survey boreholes, SP-D12 and SP-D13 (the complete logs can be consulted in Appendices A.1 and A.4, in Italian). In this representation, four geotechnical units (GU1 to GU4) were identified, all of them

formed by gravels and pebbles in a silty-sand matrix, mainly varying in their degrees of cementation. There is also a bottom layer GU5 composed of blue clays, which are a mix of highly consolidated plastic silts and clays. In gradual order and supported on Barla & Barla's (2005) classification, GU1 corresponds to an anthropic fill with little to no cementation, GU2 to a weakly cemented layer with degree of cementation  $C = 0\sim 25$  [%], GU3 with  $C = 25\sim 50$  [%] and GU4 a strongly cemented layer with  $C = 50\sim 75$  [%]. Then, the stratigraphy is in agreement with De Rienzo & Oreste's studies, given that in the Piazza Carlo Alberto zone the GU2 predominates over the rest or the geotechnical units (confirmed also from a transversal section of the Carlo Albert station) as well as the contour C1 in the authors' planimetry is predominant at a depth of 20 m, and the contour C2 at a depth of 15 m, coinciding with the GU3 in the stratigraphic cut.

#### 4.2.2 Hydrology

The City of Torino has a slight inclination starting from the direction of the Alps at the west with 280 m.a.s.l. and ending at the Torino Hill at the east with 230 m.a.s.l. (Bottino & Civita, 1986; De Rienzo & Oreste, 2011; Barla & Barla, 2012), resting inside the Dora Riparia river fan. This location, its proximity to the Po and Stura di Lazo rivers and the coarse alluvial genesis of the soil make the city have a fairly superficial water table, with the water flow complying with the city's dip, running from the west to the east and finishing in the Po river as presented in Figure 4.11.

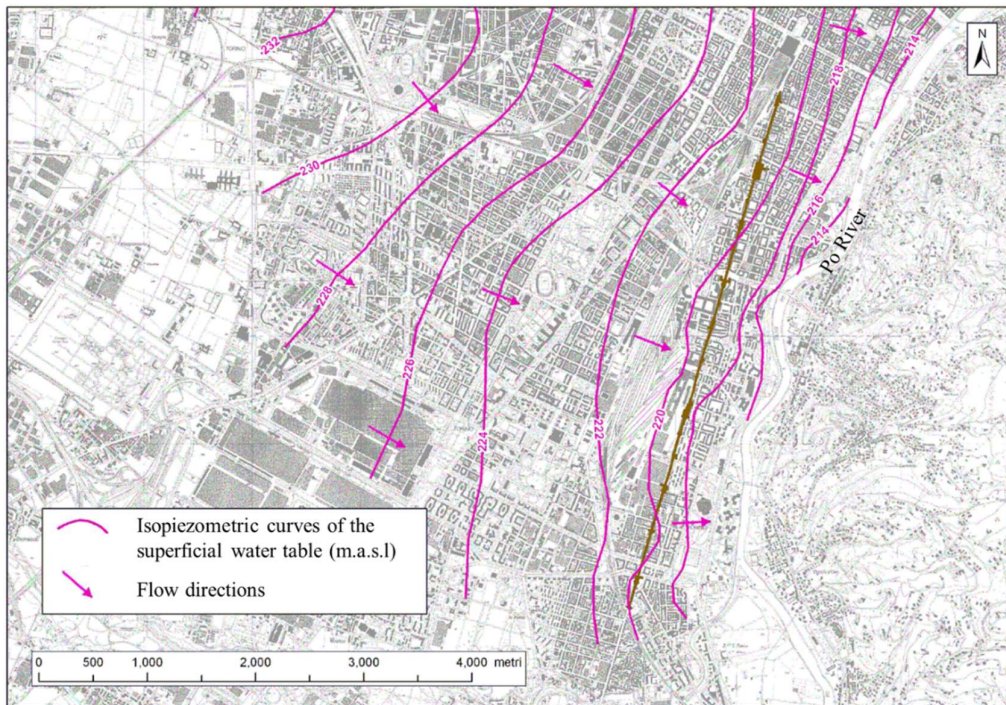


Figure 4.11. Flow direction and isopiezometric curves of the superficial water table of Torino, as seen in *Infratrasporti.To S.r.l. (2024)*

The water table depth is then displayed in Figure 4.12 enclosing once again the Carlo Alberto zone which allocates it ranging from 10 to 20 meters. From piezometric measurements obtained in collaboration with ARPA Piemonte, Infra.To reports water table depths from 15.5 to 18.4 m in the same zone, with an average of 17 meters. Consistent data was then verified with stratigraphic boreholes near Piazza Carlo Alberto.

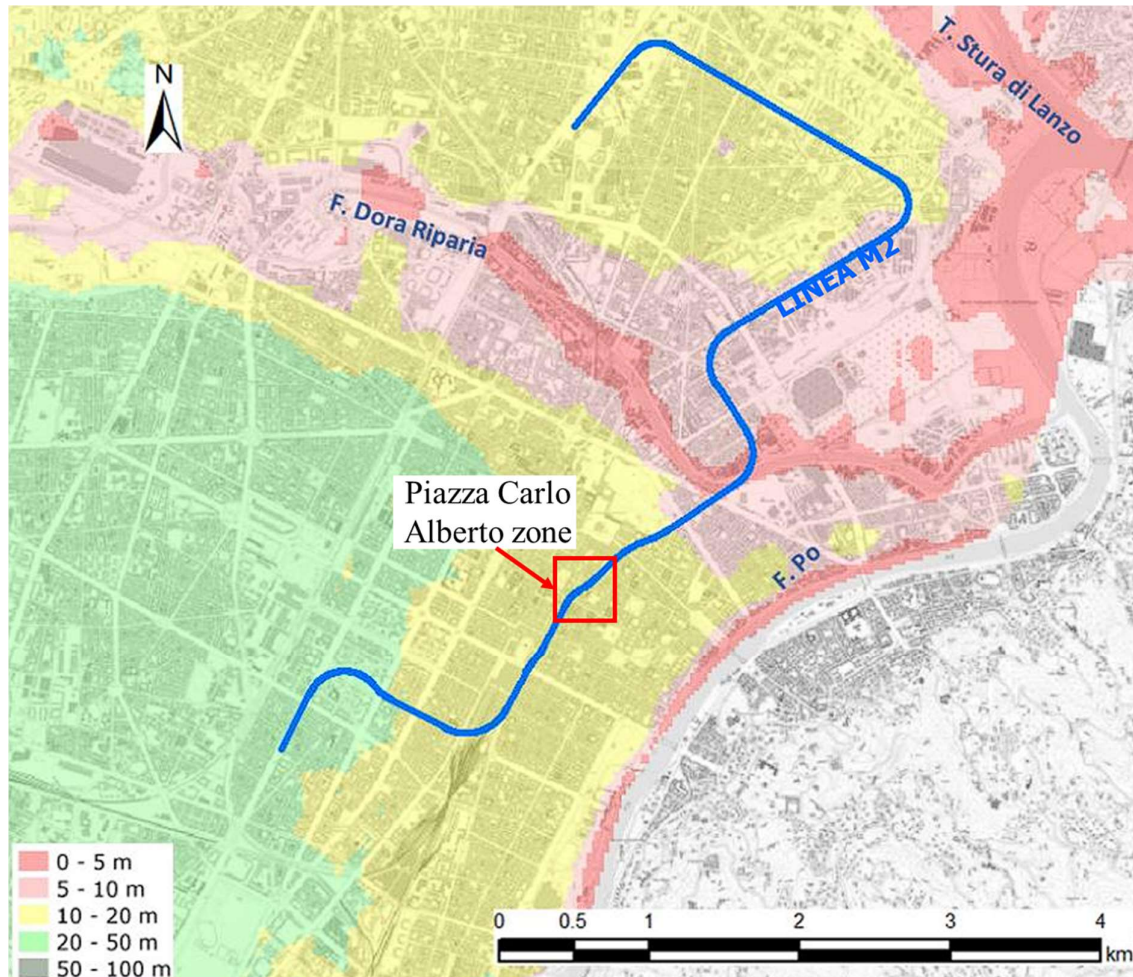


Figure 4.12. Superficial water table depth in the City of Torino (Infratrasporti.To S.r.l., 2024)

The soil, being of coarse alluvial origin, presents a good to moderate permeability ranging around  $k = 2.50 \cdot 10^{-5} \text{ m/s}$ . This was identified from LeFranc permeability tests in the same SP-D12 and SP-D13 boreholes drilled for the stratigraphic logs (the complete permeability reports in Italian are annexed in A.3 and A.6).

### 4.2.3 Geotechnical investigations

From even before the site investigations performed for the Metro-Line 2 project, the Torino soil had already been reasonably well defined from numerous geotechnical investigations (around 400 according to De Rienzo & Oreste (2011)), from previous underground works such as the Metro-Line 1 or the Underground Railway Link, and

from water research wells, given that Torino's clean water comes from an aquifer that runs through the sandy conglomerates of the Piacenzian deposits (layer 5 of the geological section shown before). These investigations are, nonetheless, either in-situ tests such as the standard penetration test (SPT) or plate loading test, or geophysical tests such as the cross-hole or MASW for the entire block-in-matrix (BIM) soil, or laboratory tests for the separate coarse matrix and separate conglomerate blocks. The possibility of doing laboratory tests for the entire BIM soil is null, given the metric size of some cemented clusters. The laboratory testing of the coarse matrix is also difficult, since unaltered samples cannot be obtained from these soils unless freezing or gel techniques are employed. Laboratory testing of conglomerates is also not an easy feat, realizing that these clusters are, for the most part, uneven and produce irregular samples when prepared for the tests. In short, testing the Torino soil in the laboratory is a nuisance.

For the Metro-Line 2 project, Infratrasporti.To S.r.l. (2023) reports in their document "MTL2T1A0DINDGENR002: RELAZIONE TECNICA DESCRITTIVA DELLE INDAGINI GEOGNOSTICHE ESEGUITE" that 82 geotechnical investigation points were located along the tunnel layout, in which 396 SPT tests were executed, 51 boreholes were drilled to obtain 367 disturbed (from coarse grained layers) and 15 undisturbed (all from fine grained layers) soil samples, and to perform 97 LeFranc tests, in some of them installing piezometers, also performing 3 cross-hole and 6 down-hole geophysical tests, and 18 MASW tests. In the vicinities of Piazza Carlo Alberto there were 7 SPT tests, 2 LeFranc and 2 borehole drillings (SP-D12 and SP-D13 from annexes A.1 and A.4, some images of the drillings follow, noticing the pebbly cemented nature of the soil) to obtain mainly disturbed samples from coarse grained layers. The disturbed laboratory samples were mainly to ascertain the granulometry of the coarse soil, water content and unit weight. No geomechanical tests were performed in these, recalling the difficulties that the Torino soil represent for laboratory testing.



Figure 4.13. From left to right: inside of a borehole drilling and the survey activity (Infratrasporti.To S.r.l, 2023)

Keeping this predicament in mind, the mechanical parameters of the soil for the numerical models designed by Infra.To (and by extension, performed in this thesis as will be discussed in Chapter 5) are still, in any case, related to those defined by Barla



& Barla (2005) and Barla & Barla (2012), and it would seem that the bulk of geotechnical investigations performed served mainly to confirm the authors' original proposal, correlating the Young's modulus obtained from MASW geophysical tests to stratigraphic logs.

#### 4.2.4 Geomechanical characteristics

Seeing the prominence of Barla & Barla's work in the modelling assumptions of both Infra.To and the current thesis, their investigations are here further explained. It is exhorted, in any case, to consult the original articles (Barla & Barla, 2005; Barla & Barla, 2012) as many details here will be omitted. The researchers also started with the results of in-situ tests in the BIM soil ranging from plate loading to geophysical tests, and laboratory tests only on cemented clusters. From these, they derived the parameters necessary to model in numerical software, such as FLAC and PFC, laboratory tests of large-scale samples (1 by 2 meters in size). The parameters still did not concern the entirety of the BIM soil but its separate components, the coarse matrix (0% degree of cementation) and the cemented clusters (100% degree of cementation). With the objective of estimating via numerical modelling the mechanical characteristics of the BIM soil with an intermediate degree of cementation, the authors configured different numerical models as shown in Figure 4.14 precisely varying the cementation by including more horizontal bands with the characteristics of the conglomerates (blue zones in the figure), and then tested them in simulated unconfined compression tests.

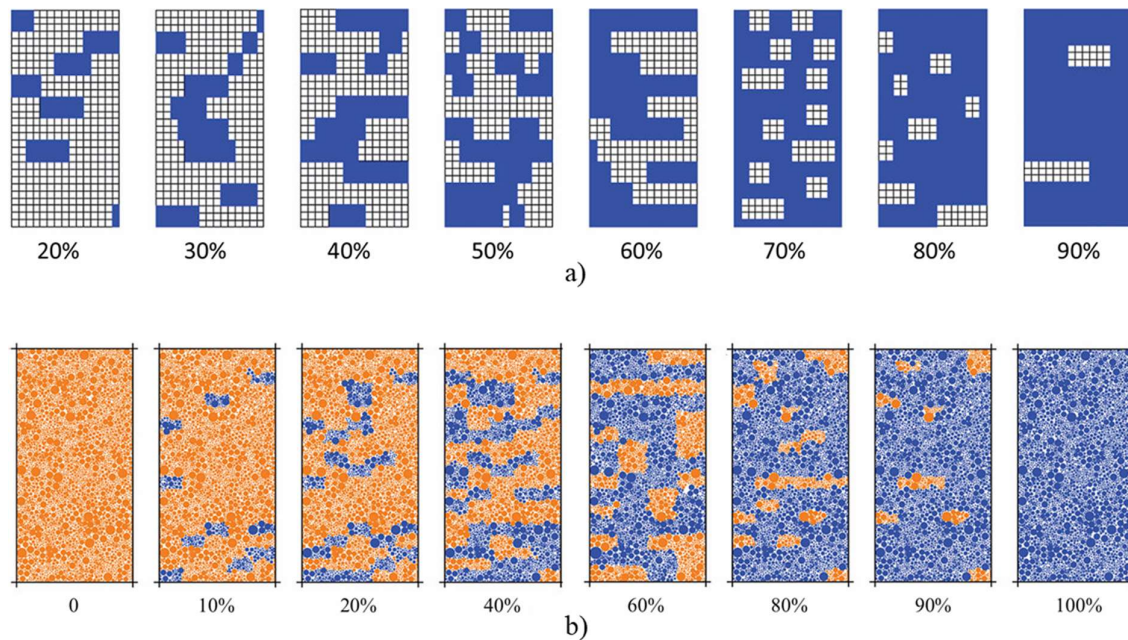


Figure 4.14. a) FLAC and b) PFC numerical models configured by Barla & Barla (2012) to numerically estimate the characteristics of the Torino soil with a given degree of cementation (percentage)

Results were obtained by the authors for both the deformation elastic moduli and compression strengths of the samples; here only the former is shown in Figure 4.15, noticing that for an entirely loose sample (degree of cementation equal to zero) and for

a fully cemented one (degree of cementation equal to 100%) the results resemble those obtained in real life laboratory test, with the deformation moduli of intermediate degrees of cementation also being similar to those of in-situ tests. The values of the elastic moduli obtained numerically were, nevertheless, initially much lower and had to be increased as the parameter was calibrated to reproduce realistic surface settlements recorded during the excavation of the Metro-Line 1 of Torino (Barla & Barla, 2005; Barla G. , Barla, Bonini, & Crova, 2005).

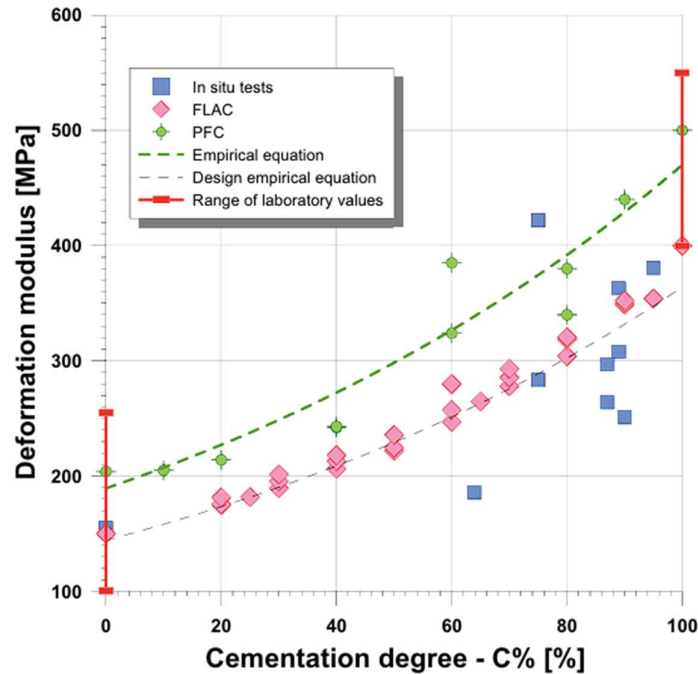


Figure 4.15. Results presented by Barla & Barla (2012): deformation modulus of the numerical Torino soil samples in FLAC and PFC

Here is where Papantonopoulos & Atmatzidis (1993) failure criterion comes into play, detailedly explained under the heading 3.1.3.1, that varies between the Mohr-Coulomb and Hoek & Brown constitutive models. Based on the Equation (3.5) of  $m_b$ , if the disturbance factor is taken  $D = 0$  for null rock disturbance during TBM excavation (Hoek, Carranza-Torres, & Corkum, 2002), and the degree of cementation of the soil  $C\%$  is treated analogously to the GSI, Barla & Barla (2012) suggest to use the relationship:

$$m = 20 \cdot e^{\frac{C\% - 100}{53}} \quad (4.1)$$

By varying  $C\%$  and using Equation (3.11) that relates the Mohr-Coulomb and the Hoek & Brown criterion through the degree of cementation of the material, the authors found the next yield criterion curves, from which the immediate cohesion and friction angles of the BIM soil can be obtained.

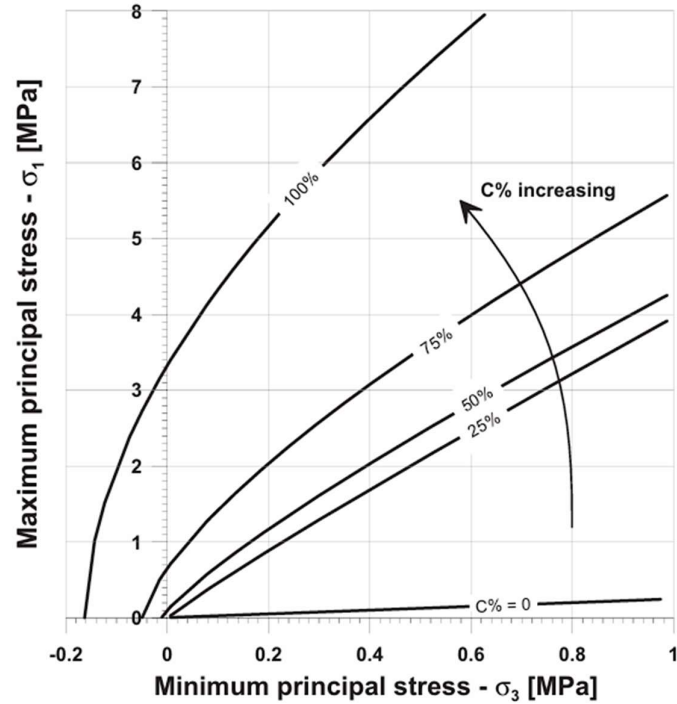


Figure 4.16. Results presented by Barla & Barla (2012): yield criteria in function of the degree of cementation of the Torino soil

With this output, Barla & Barla recommended the next deformability and strength parameters for the Torino soil (here only the Mohr-Coulomb parameters are presented) and according to the authors, these are especially useful in shallow tunnelling applications as the range of minimum principal stresses from 0.1 to 0.3 MPa, representative of these civil works, was used to obtain the values in Table 4.1.

Table 4.1. Mohr-Coulomb elasto-plastic parameters for the Torino cemented soil, after Barla & Barla (2012)

Geotech. unit	Degree of cementation [%]	Natural unit weight [kN/m <sup>3</sup> ]	Effective friction angle [°]	Effective cohesion [kPa]	Elastic modulus [MPa]	Poisson's ratio [-]
GU1	-	17 - 19	36 - 37	-	10 - 20	0.35
GU2	0 - 25	18 - 21	37 - 39	0 - 30	190 - 240	0.30
GU3	25 - 50	19 - 22	37 - 42	15 - 80	240 - 300	0.30
GU4	50 - 75	19 - 22	39 - 48	50 - 200	300 - 370	0.30

As a quick note, the entirety of the Torino soil does not include only the geotechnical units from 1 to 4 that regard the cemented layers. As illustrated in the stratigraphy in the Piazza Carlo Alberto zone, below Palazzo Campana (Figure 4.10) there could be the presence of fine-grained layers of silts and clays. These, in any case, are not predominant in the zone of interest and thus, will not be studied in this essay.

### **4.3 Prediction of the basin of subsidence and building damage risk**

Both the City of Torino and its society Infratrasporti.To S.r.l., in charge of the preliminary designs of the works, supervision, in-situ surveys, feasibility studies and contract administration of the Metro-Line 2 of Torino, are rightfully interested in guaranteeing the successful completion of the tunnelling works with negligible effects on the surface structures. For this purpose, in the design stage the society studied the interaction between the excavation and the buildings on top of the tunnel path, and through simplified empirical and two-dimensional numerical alternatives, they identified 11 buildings at risk of experiencing moderate to severe damage, from which only one building, Palazzo Campana, fell in the highest degree of severity.

Here, therefore, the building Palazzo Campana, the results obtained by Infratrasporti.To on the prediction of the basin of subsidence and potential building damage are examined.

#### **4.3.1 Palazzo Campana**

The Palazzo Campana is one of those buildings that in the everyday rush would pass unobserved, blending in perfectly with the characteristic baroque Torinese of the structures in the city center. And even still, after stepping inside from the grand doorway, abandoning via Carlo Alberto and witnessing the brimming youth that presently occupies its cavernous halls, one would not imagine the depth of its historical awareness and lingering hold on Torino's past, present and future.

In the past, the building was conceived as a mere part of the cloister of the San Filippo Neri church, with its first foundation being laid in 1675 for its completion about 80 years later. The building has seen the passing of masses and rulers alike, hosting most of them in its premises, starting from the Oratorians, then sheltering Napoleonic troops during the French occupation of Piemonte in the XIX century, for afterwards fifty years later being repurposed by the Italian government as a public building to serve as the premises of the Ministry of Public Works and the Central Post Office, that had the opportunity to function as a hub for incoming mail of Friedrich Nietzsche during the last quarter of the century, and for the second quarter of the XX century becoming the headquarters of the Provincial Federation of the Fascist Party and that would operate, from its balconies pointing towards Piazza Carlo Alberto, as a podium for political divulgation, only to be partially burned in 1943 by a group of protesters passing through the city center in the morning, fire that could only be extinguished in the late afternoon by the city's fire department (Designers Riuniti, 1983; ISTORETO, 2002; Università di Torino, 2017). This event, shown in Figure 4.17, is crucial to this thesis as it may suggest that the materials of some zones of the building are degraded due to the fires.



Figure 4.17. Fires of 1943 in Palazzo Campana (Designers Riuniti, 1983; ISTORETO, 2002)

In the present, Palazzo Campana accommodates the Faculty of Mathematics of the Università degli Studi di Torino. The current holders of the building do ensure that the structure has been granted a Fire Prevention Certificate after the completion of refurbishment works; nonetheless, no mention is made about structural improvements or changes apart from the installation of an internal elevator and two staircases. Some additional work has been performed on the building but merely concerning the esthetic aspects of the two main facades. It is therefore assumed that the principal structure of the building, with its bearing walls and vaulted floors, remains original.

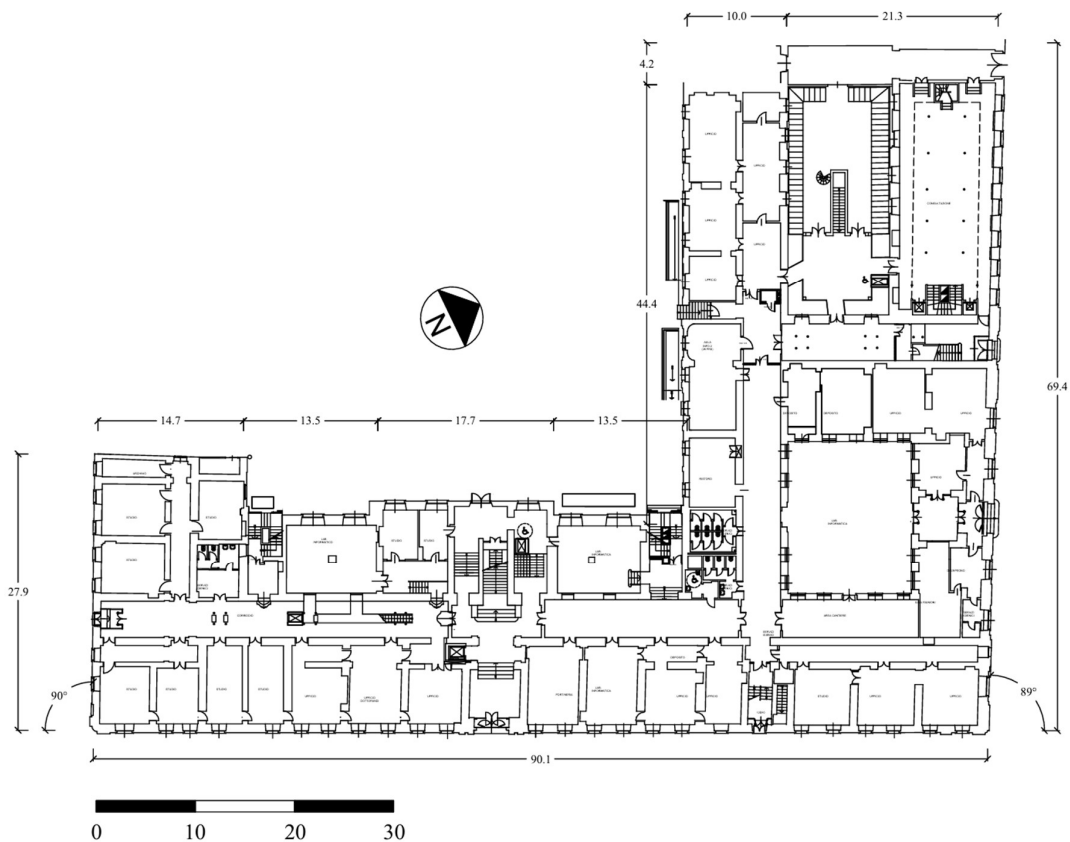


Figure 4.18. Blueprint of the first floor of Palazzo Campana

The planimetry of the first floor of Palazzo Campana is depicted in Figure 4.18 above, while the rest of the blueprints are annexed in the Appendix B (all courtesy of the Building and Sustainability Directorate of the Università degli Studi di Torino). In general, the building has four floors above the ground level with a total height of 21.5 meters, and one underground cellar with a foundation depth of 4.80 meters.

From in-situ visual surveys the principal accessible areas of the building were recognized; still, due to the nature of the thesis and cultural value of the Palazzo, in-situ tests on the materials were not possible, as well as the detailed investigation of structural members, i.e. voids inside the walls, was not allowed. Some figures of the facades and internal halls follow, as well as a localized damaged zone below a slab which helps to confirm that these are indeed built with solid brick masonry and mortar bond.



Figure 4.19. From left to right: Palazzo Campana's NORTH, SOUTH and EAST facades

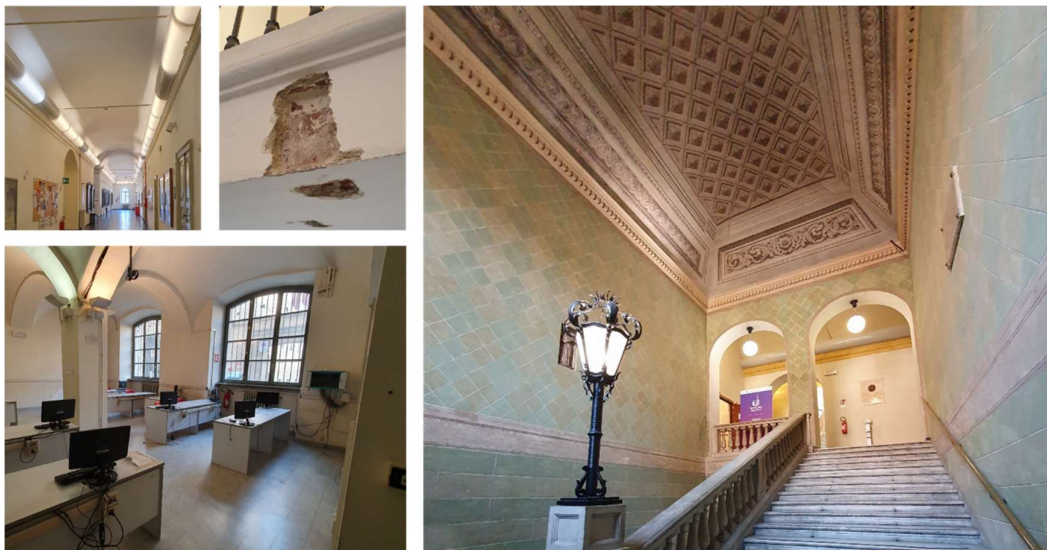


Figure 4.20. Internal halls of Palazzo Campana and localized damage below a slab

In the future, Palazzo Campana still lingers with its hunger for making the headlines as the Metro-Line 2 of Torino digs below its premises. Indeed, the Palazzo did not have enough with the fires of 1943 and now, more than 80 years later, has resurfaced again as the only building in the 8.3 Km of development of the metro project that presents a very severe risk of damage owing to the excavation effects, according to Infratrasporti.To's preliminary predictions, which are further detailed next.

### 4.3.2 Damage risk assessment

Infratrasporti.To conducted a series of empirical analyses to ascertain the extension of the basin of subsidence and maximum settlement along the tunnel alignment in greenfield conditions (neglects the presence of buildings on the surface), varying the value of the volume loss from 0.5 to 1.0% as they considered these values to be conservative for EPB TBM tunnelling. The results of the analyses are in Figure 4.21.

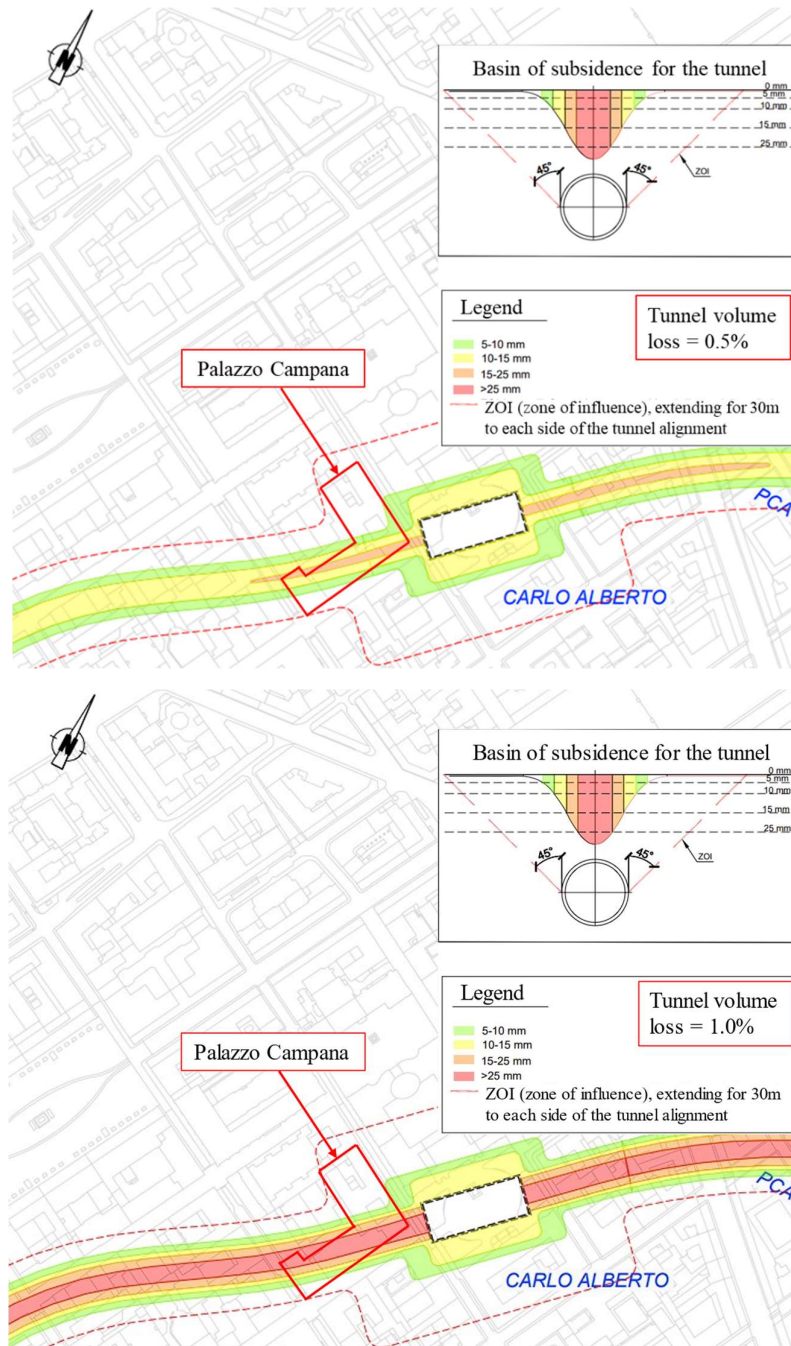


Figure 4.21. Development of the basin of subsidence for  $V_L^T = 0.5$  and  $1.0$ , according to Infratrasporti.To (2024) based on empirical methods

As displayed in the figure above, Palazzo Campana consistently lands in the zones with the highest greenfield settlements, since the tunnel alignment crosses directly below its premises. In the figure it is only shown that the building may experience settlements of 15 to 25 mm for a volume loss of 0.5% and higher than 25 mm for a volume loss of 1.0%, but from the full report sheet included in the Appendix C.1 (in Italian) it can be concluded that Palazzo Campana can suffer settlements up to 65 mm (Infratrasporti.To S.r.l., 2024). At this point, the 1) *Preliminary assessment* of the framework for the building risk of damage assessment of Figure 2.19, as detailed at the beginning of the document, is surpassed because the maximum settlement remains higher than the threshold proposed by Rankin (1988) of 10 mm to obtain negligible building damage.

The next step 2) *Second-stage assessment* of the framework is to be performed consequently. Infra.To, analyzing in detail the transversal greenfield trough with the EBA method following Burland & Wroth (1974), found that the building presented severe to very severe risk of damage, as shown in comparison to other nearby structures in Figure 4.22.

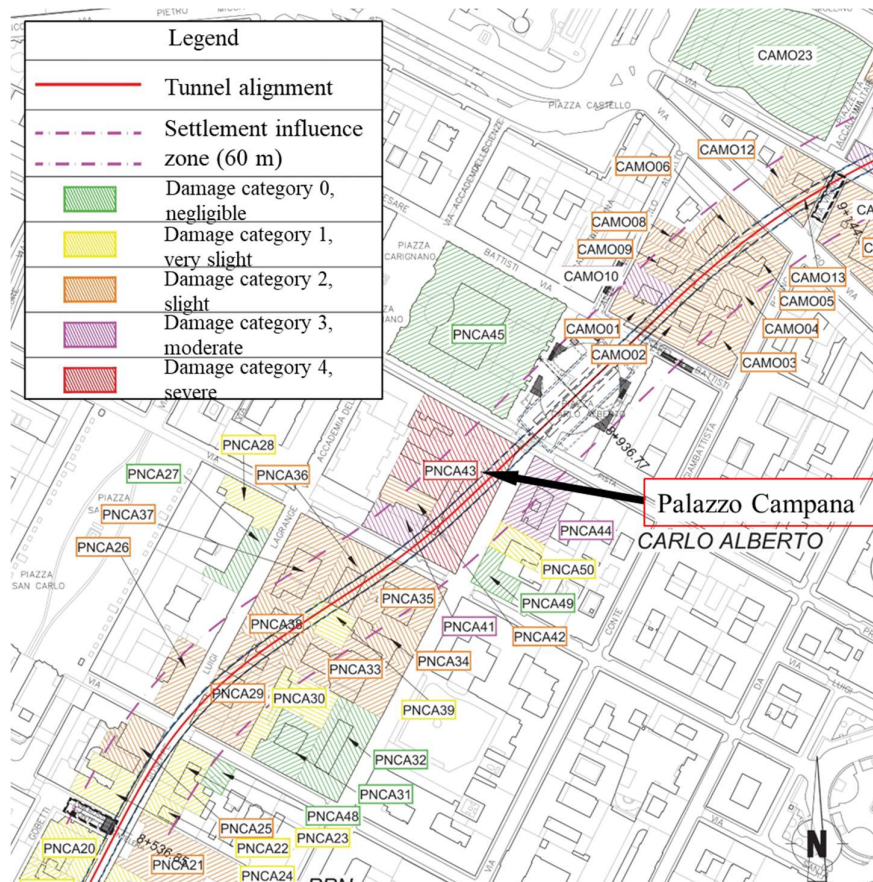


Figure 4.22. Risk of building damage assessment, with minor modifications as seen in Infratrasporti.To (2024)

It is at this point that Infratrasporti.To decides to provide jet grouting (or permeation grouting) injections below Palazzo Campana, on top of the crown of the tunnel, to reduce the settlements as better explained in the next section 4.3.3, to then reevaluate



the effects of the excavation, this time with a two-dimensional numerical approach revised in the following heading 4.3.4.

### 4.3.3 Soil improvement, jet grouting or permeation grouting umbrella

To counter the effects of the subsiding soil below Palazzo Campana, Infra.To projected the injection of grouting material in the configuration presented in from a top view in Figure 4.23 and in profile in Figure 4.24. It must be noticed that from both sections B-B and C-C of the injections, illustrated in Figure 4.25, the B-B holds the longest development below the building.

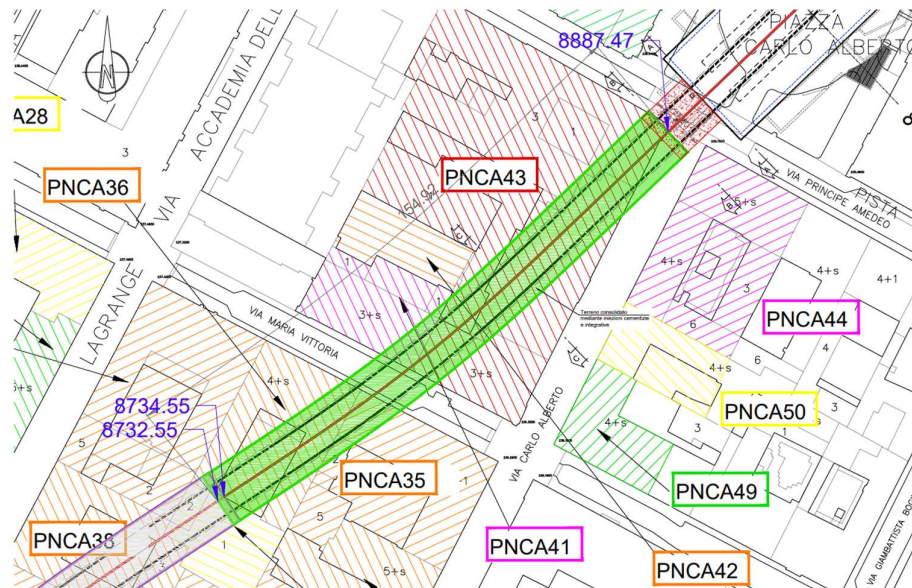


Figure 4.23. Planimetry of the jet grouting injections (Infratrasporti.To S.r.l., 2024)

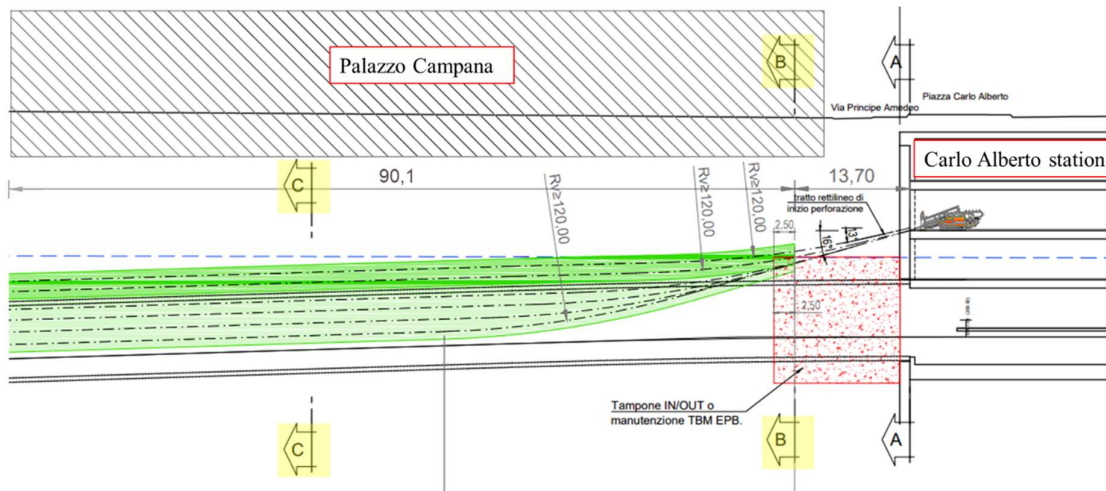


Figure 4.24. Profile view of the jet grouting injections below Palazzo Campana, modified from (Infratrasporti.To S.r.l., 2024)

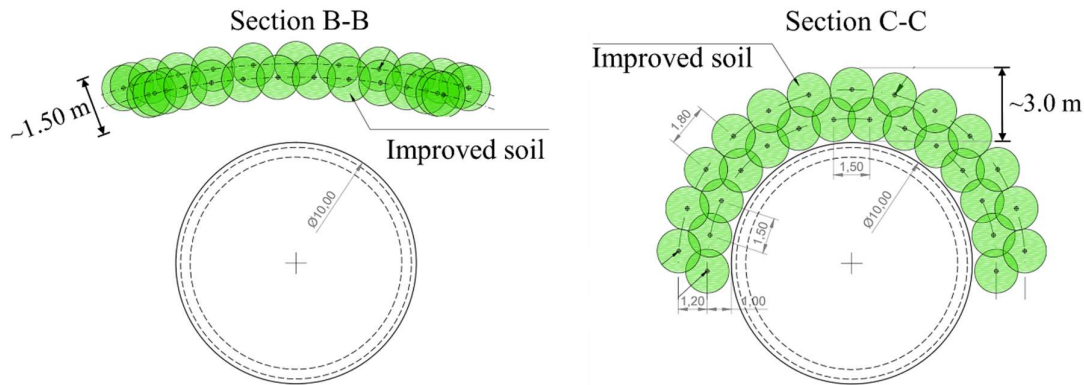


Figure 4.25. Detailed configurations of the jet grouting umbrella in sections B-B and C-C of the profile view, modified from (Infratrasporti.To S.r.l., 2024)

The final requirements for the jet grouting umbrella (or permeation grouting) material are set by Infratrasporti.To as to those in Table 4.2.

Table 4.2. Minimum requirements for the improved soil (Infratrasporti.To S.r.l., 2024)

Natural unit weight [kN/m <sup>3</sup> ]	Effective friction angle [°]	Effective cohesion [kPa]	Young's modulus [MPa]	Poisson's ratio [-]
19.0	>36	≥150	≥450	0.3

#### 4.3.4 A 2D numerical approach for the subsidence and building risk of damage prediction

Continuing with the framework of the building risk of damage estimation, after the 2) *Second-stage assessment* was concluded and it was predicted that Palazzo Campana would still experience severe risk of damage, Infra.To reevaluated the problem in the numerical software PLAXIS2D as part of the stage 3) *Detailed evaluation*, in hopes to obtain a lower risk of damage prediction as usually happens when more complex methods are used. The numerical models are shown in Figure 4.26 for the soil in natural conditions and Figure 4.27 with the improved soil at the crown of the excavation. For a volume loss of 1.0%, the results are respectively for the first model a maximum settlement of 32.6 mm and a major tensile strain of 0.052% (landing in the category of *slight* damage for vulnerable and public buildings, and *very slight* for common structures following Boscardin & Cording (1989)) and for the second model a maximum settlement of 16.9 mm and a major tensile strain of 0.017% (landing in the category of *very slight* damage for both vulnerable and public buildings, and common structures following Boscardin & Cording (1989)). Even though the settlement is still higher than 10 mm, the evaluated tensile strains of the building according to Infra.To are small and therefore, the building is expected to not suffer significant damage during the excavation.

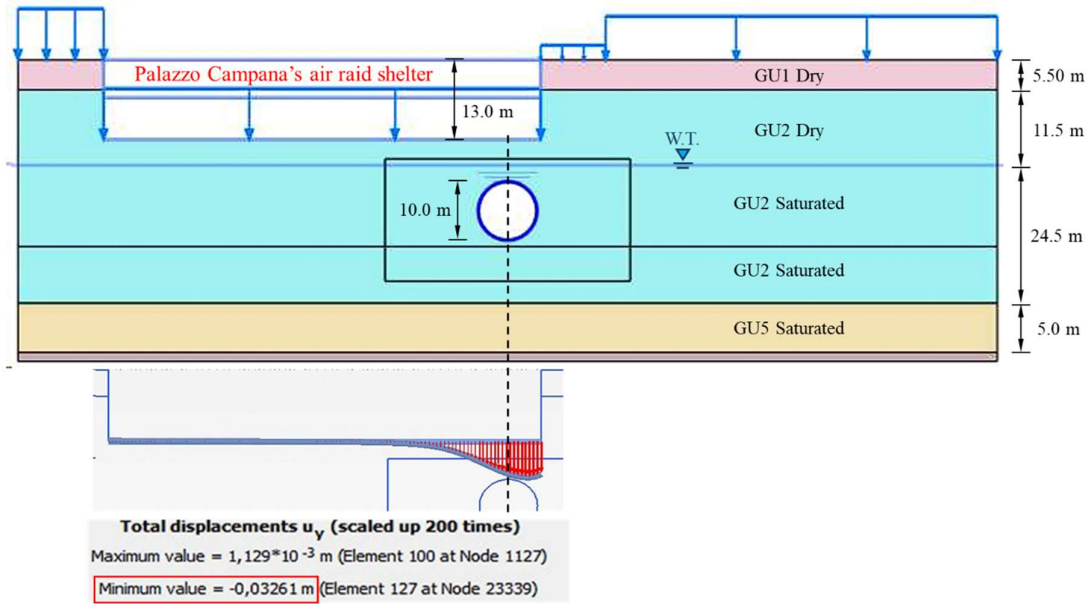


Figure 4.26. 2D numerical model in natural conditions and transversal subsidence results, modified from Infratrasporti.To S.r.l. (2024)

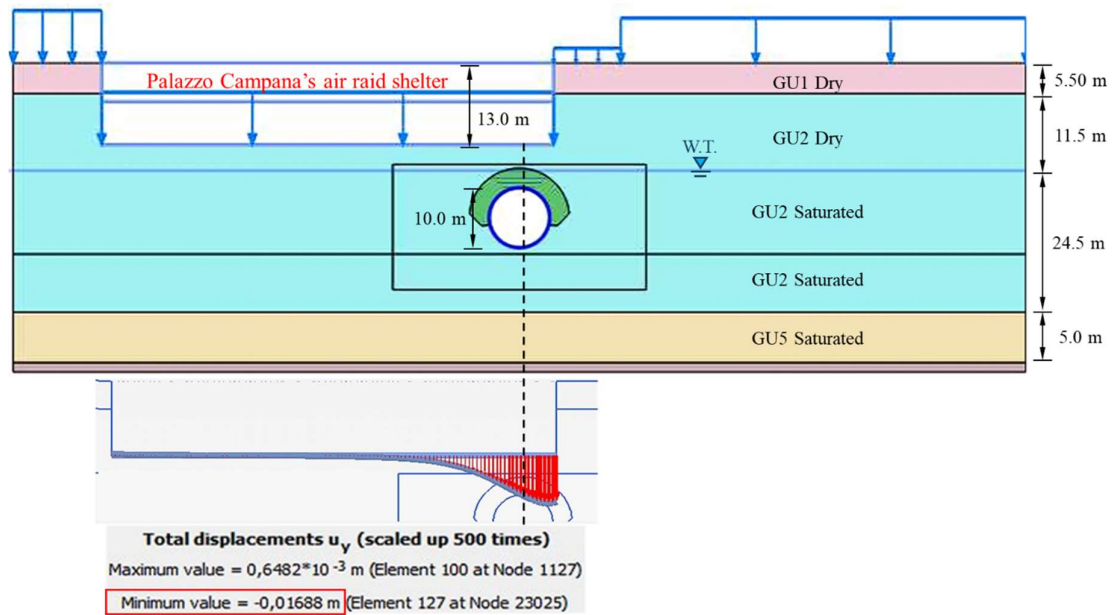


Figure 4.27. 2D numerical model in natural conditions and transversal subsidence results, modified from Infratrasporti.To S.r.l. (2024)

A note here is that, against the work of the current thesis which will be more detailedly explained in Chapter 5, but that from now it can be anticipated that the subsidence was evaluated at the level of the foundation at 4.80 meters below the ground surface corresponding to the lowest elevation of the main structure, Infra.To evaluated the subsidence acting on the building at a depth of 13 m under the ground surface.

This is justified because they considered the presence of an underground air raid shelter that extends in depth up to 13 m below the surface and is connected to Palazzo Campana. The image of the plan of the shelter is included in Figure 4.28 a), and a picture of its insides in b). The first thing to notice is from b), that the air raid shelter was constructed in concrete and therefore, it cannot be regarded as inherent to the structure. This is to say, the shelter was built afterwards in a different material and consequently, no structural continuity can be guaranteed between the Palazzo Campana and this underground structure. In fact, the most probable case scenario is that there is a joint separating both materials, either intended from its genesis or that the induced subsidence will naturally help create. It must be clarified that access to the air raid shelter was not allowed for the present effort, the information presented here was derived from in-situ investigations of a third party working with Infratrasporti.To.

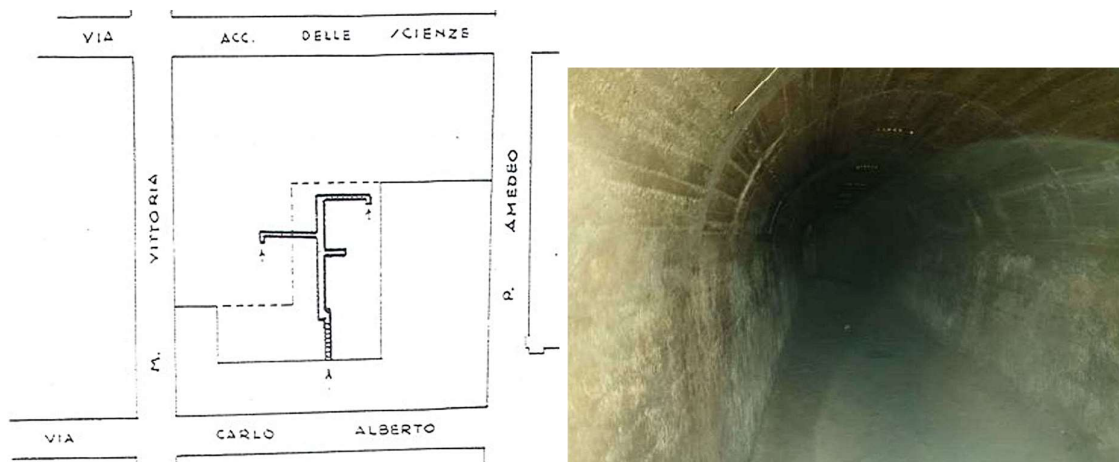


Figure 4.28. From left to right: a) plan view of the air raid shelter in the courtyard of Palazzo Campana and b) insides of the shelter

From Figure 4.28 a) the second important thing to notice emerges, and it is that the air raid shelter is only connected to the wing of the building in front of via Carlo Alberto, and the rest of its development occurs outside the Palazzo Campana, below the internal courtyard. Here it is argued, therefore, that it is overly conservative to evaluate the damage risk of Palazzo Campana at the bottom level of the air raid shelter, 13 m below the ground surface, seeing that both structures are barely interfering with each other.

In this outline, the next Chapter 5 will study the same case of the subsidence below Palazzo Campana but with a three-dimensional numerical soil – structure interaction model, that considers the building's foundation resting at a depth of 4.80 m.

## Chapter 5

# A 3D numerical model for the subsidence and building risk of damage prediction in the Metro-Line 2 of Torino project

### 5.1 Greenfield models

The numerical models here examined, developed in ABAQUS (Dassault Systemes, 2024), concern the simulation of the tunnel excavation neglecting surface structures, in a framework known as greenfield conditions. The entire assembly of the model is next reviewed, as well as different models are projected for further parametric analyses.

#### 5.1.1 Geometrical model and discretization

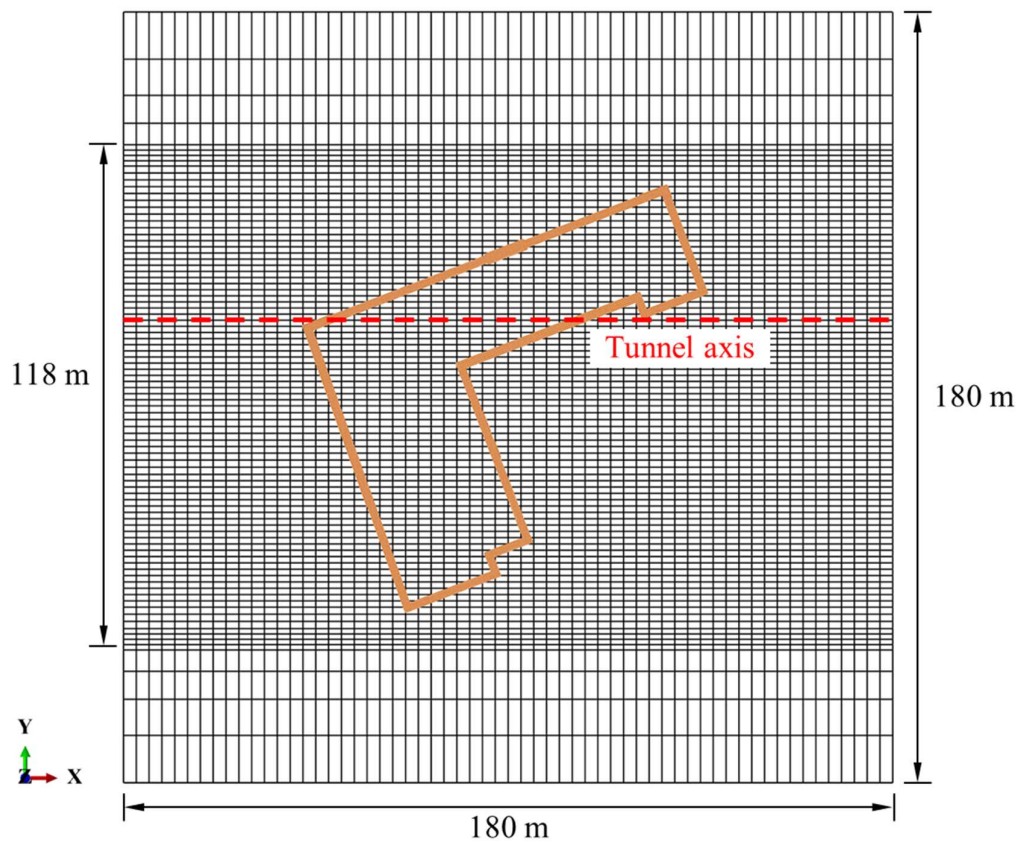


Figure 5.1. Top view of the excavation model and recommended size based on the extension of Palazzo Campana

Based on the model sizes from the literature review of heading 3.1.1, and aiming to create a model prepared to receive a building of the dimensions of Palazzo Campana, the geometry of the soil is shown in Figure 5.1 from a top view.

To host the stratigraphy of the Torino soil, the soil cuboid fully formed of hexahedral solid elements was made of a depth of 38.5 m as presented in the following Figure 5.2. The relatively limited distance between the bottom of the soil cuboid and the invert of the tunnel excavation, equal to 7.5 m ( $0.75D$  with  $D$  being 10 m equal to the tunnel diameter), is justified to reduce unrealistic heave at the invert (Boldini, Losacco, Bertolin, & Amorosi, 2018) and to save computational time by reducing the number of elements in the model, given that the surface settlements are marginally affected by this assumption (Barla, Barla, & Leuzzi, 2012). In any case, in preliminary models this supposition was tested by varying the distance between 7.5 and 19 meters (maximum distance below the invert for which invasive in-situ investigations exist), noticing affirmatively that it does not affect in a significant manner the settlement trough.

The depth of each layer and of the water table is based on the stratigraphic profile before presented when introducing the Torino soil in section 4.2.1. The configuration here shown could be considered a simplification of the real stratigraphy as it does not include the geotechnical units 3 and 4 seen in the longitudinal profile of Figure 4.1; however, from a transversal profile of Carlo Alberto station (near Palazzo Campana, our subject of interest) it was verified that these layers do not consistently extend in the horizontal plane, transversal to the tunnel axis and therefore, it is instead realistic to not include them in the geometrical model.

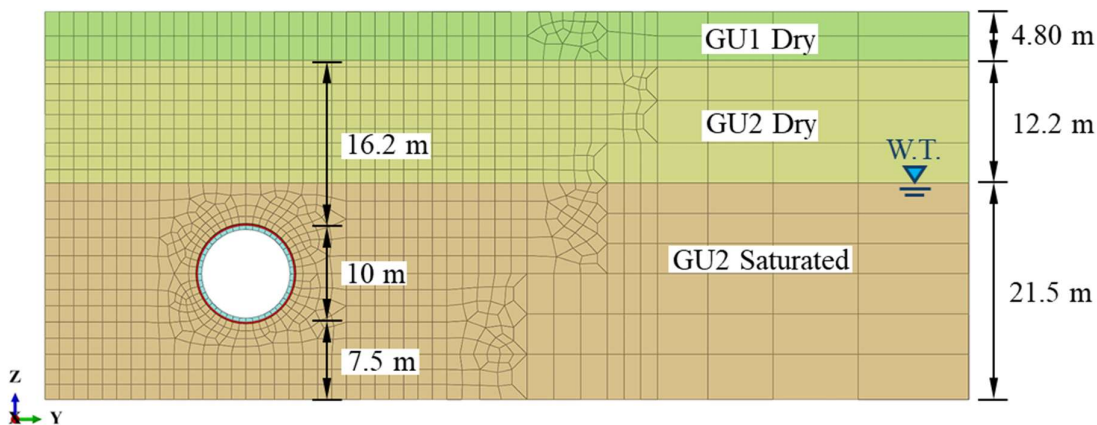
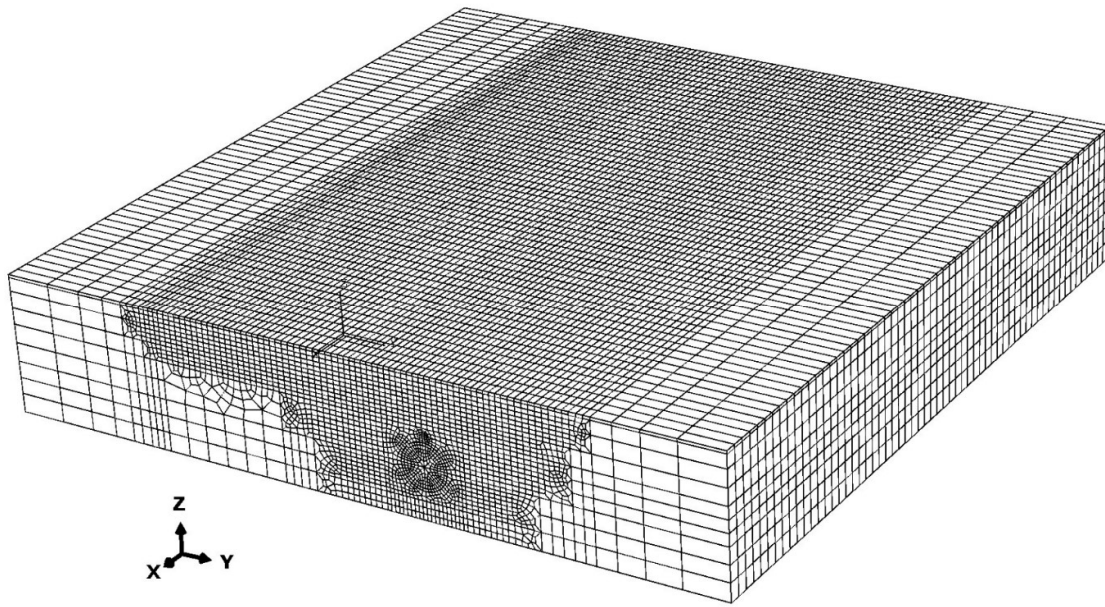
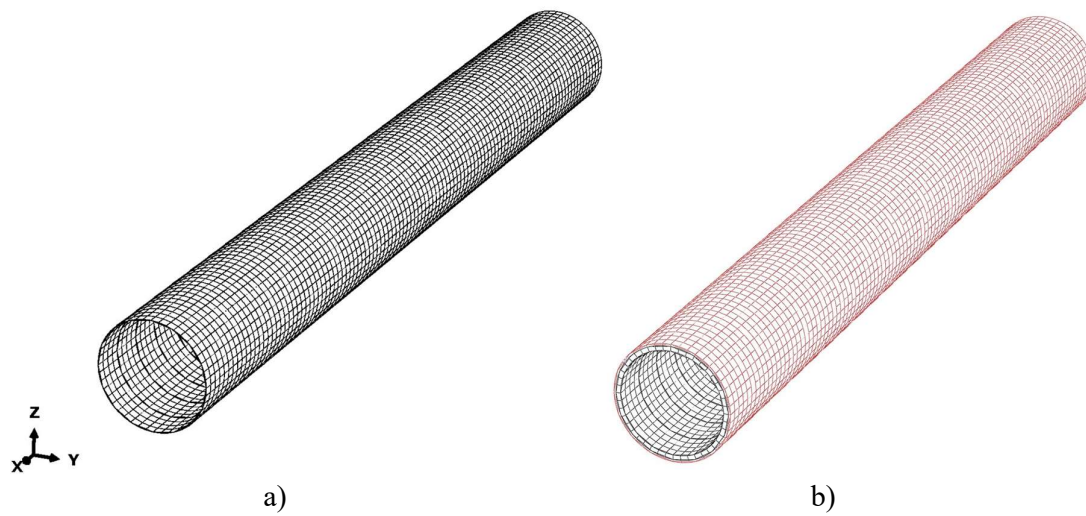


Figure 5.2. Elevation of the different layers of the soil model

On the other hand, because the model was conceived from the beginning to receive the building, the decision was taken to deactivate the first 4.80 m of soil, from the ground surface to the foundation level of the building, and to account for its weight in the form of a distributed load. In this way, the next figures show the model mesh without the superficial soil elements. The model meshes of the TBM shield (assumed to have nine meters in length) made of shell elements and the liners and grout formed with hexahedral solid elements, are also presented below.



*Figure 5.3. Model mesh of the soil*



*Figure 5.4. From left to right: a) model mesh of the shield, b) model mesh of the lining segments (black) and the grout (red)*

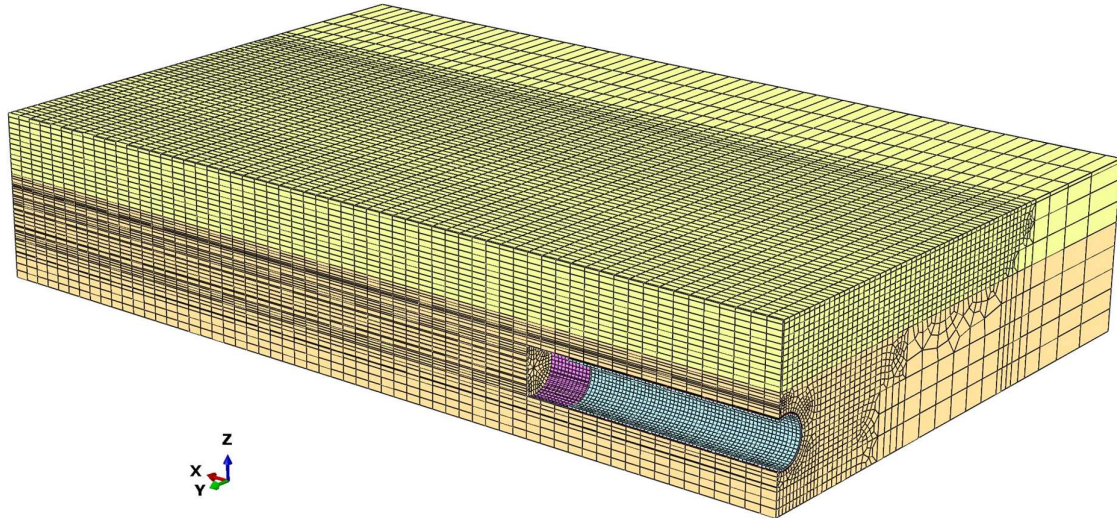


Figure 5.5. Jointed model of the excavation (assembly), featuring the parts of the soil, shield and liners plus grout in interaction

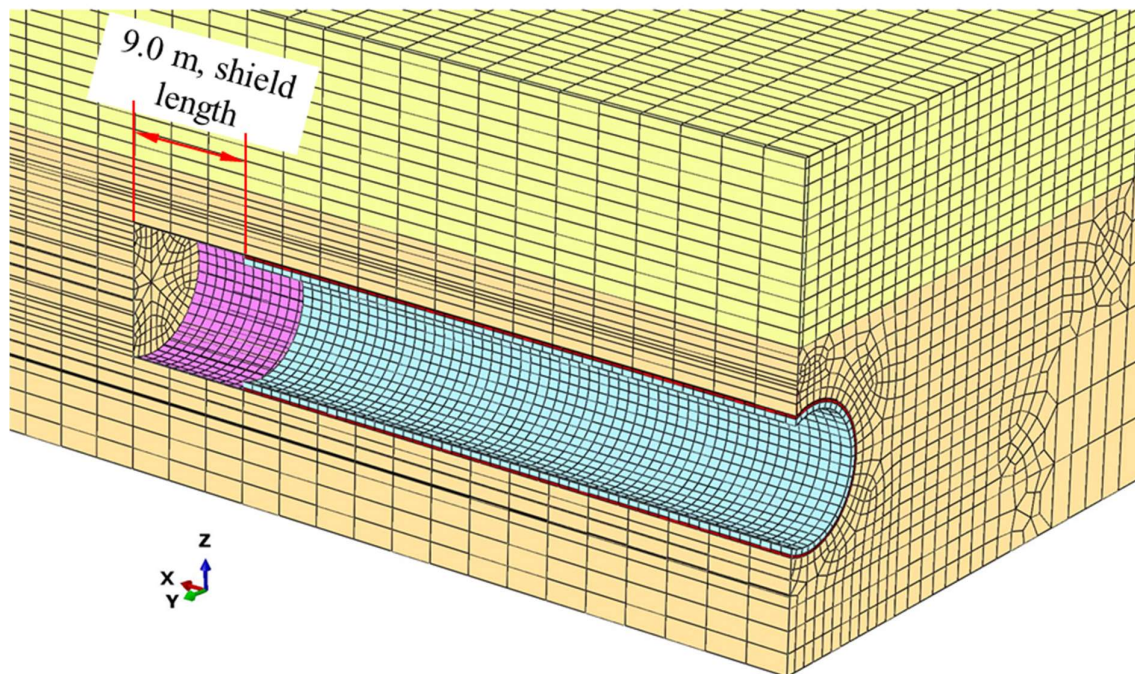


Figure 5.6. Detail of the model of the excavation

For the mesh of the soil, higher densification of hexahedral elements was conceived in a transversal radius of 30 meters about the tunnel axis, since in preliminary models it was identified that the extension of the most significant stresses and vertical displacements was completely developed in this area. A higher density can also be noticed at the top face in the surface-most layers, in a rectangular area that well encloses the future location of the model of the building. In the vicinities of the excavation boundaries, an even higher densification was produced to detail the circular shape of



the tunnel, mainly to avoid spurious overlaps between the contacting nodes of the tunnel walls, the TBM shield and the grout's extrados. With the same purpose of generating an effective contact interaction, the meshes of the shield and of the liners plus grout parts were densified even more than the soil excavation walls, optimizing the slave – master surfaces' penetration.

For the current purpose, noticing that Infratrasporti.To (2024) envisioned a jet grouting umbrella for the improvement of the soil properties below Palazzo Campana, as before stated in section 4.3.3, a greenfield model with the improved soil on the crown of the excavation was also produced and is shown in the next Figure 5.7. The thickness of the improved zone was modelled equal to 1.50 m, conservatively seeing that the injections below the building Palazzo Campana for the most part follow the Section B-B configuration of Figure 4.25, which is a slab-like soil improved zone of about 1.50 m of thickness. Nevertheless, the slab geometry is not adopted, but a radially concentric area of improved soil around the tunnel is modelled to compare against Infra.To's two-dimensional numerical model, where the improved zone was also conceived in this way.

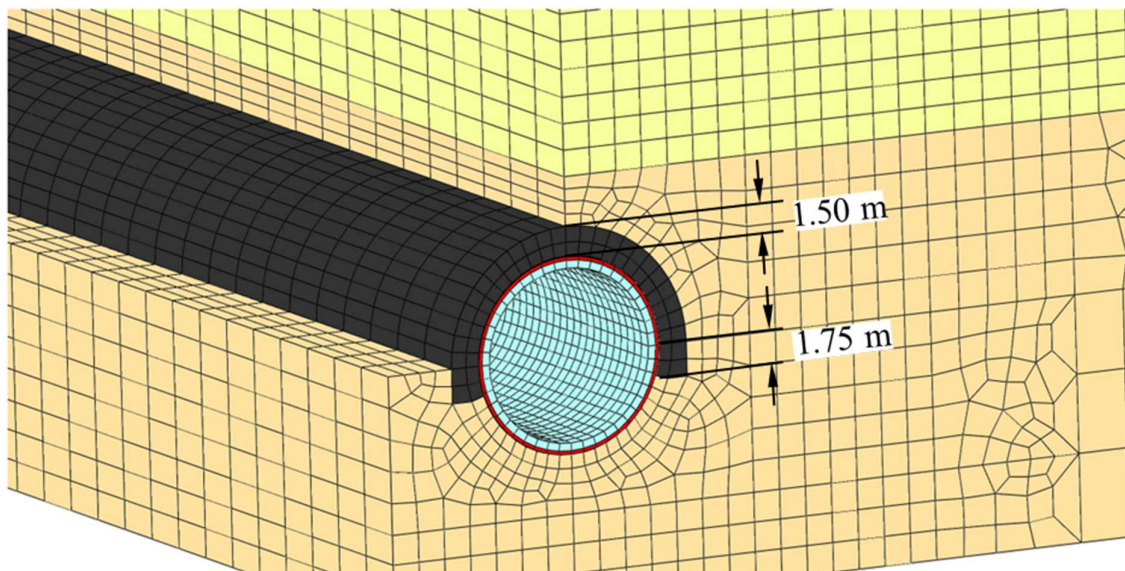


Figure 5.7. Detail of the model of the excavation with the jet grouting umbrella

In an undeformed condition, the parts of the assembly are arranged in the configuration illustrated in Figure 5.8 (the sketch is not to scale). As can be noticed, the shield was positioned with its bottom lying at the invert to reproduce the oval-shaped tunnel contraction as accomplished by other researchers (Rampello, Callisto, Viggiani, & Soccodato, 2012; Litsas, Sitarenios, & Kavvadas, 2017; Boldini, Losacco, Bertolin, & Amorosi, 2018; Yiu, 2018), leaving a steering gap at the crown whose dimension was varied between 2, 4 and 6 cm (more on this in the next heading 5.1.5.2).

If complete convergence of the soil around the shield is achieved (true in most cases for excavations in soil), the difference between the diameter of the extrados of the shield and of the lining becomes the annulus gap, assumed to be completely filled with two-component grout. Given that parametric analyses were performed varying the dimension of the steering gap, the annulus gap was then also a function of this variation,

to maintain fixed the excavation diameter equal to 10 m and the liner intrados equal to 8.8 m, with the thickness of the liners being 40 cm in all cases, as stated by Infratrasporti.To (2024).

The annulus gap was here assumed concentric with the shield and radially uniform. This decision accounts for the realistic in-situ installation of the lining rings, which are concentrically assembled inside the shield and while the TBM pushes forward, the liners are exposed to the naked soil and to the two-component grout being simultaneously injected behind the tail of the shield. Because this material gelifies in a little more than 10 seconds (Peila, et al., 2015; Todaro, Saltarin, & Cardu, 2022), and due to its early incompressibility, the lining rings are locked in place (summed their frictional resistance mobilized by the thrust of the jacks), maintaining their original alignment with the shield (Pelizza, Peila, Sorge, & Cignitti, 2012) and rendering the annulus void radially uniform.

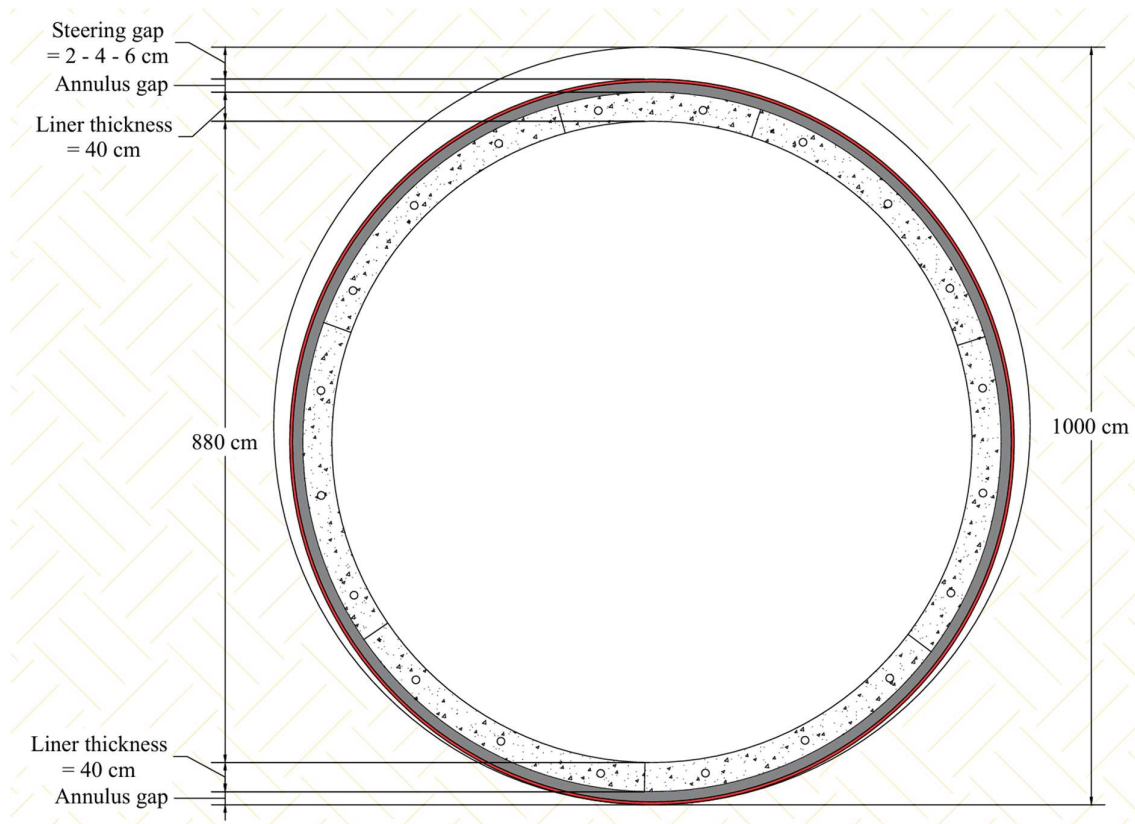


Figure 5.8. Transversal section of the tunnel assembly

## 5.1.2 Boundary conditions

### 5.1.2.1 Soil external constraints

The same configuration discussed in heading 3.1.2.1 is adopted here, where the nodes at the Top face are left free to displace, the nodes at the Lateral faces are restricted to

move in Y direction ( $U_2=0$ ), those at the Front and Rear faces are restricted to move in X direction ( $U_1=0$ ) and those at the Bottom face are pinned ( $U_1, U_2$  and  $U_3=0$ ).

### 5.1.2.2 *The shield and the lining segments*

Both the shield and the liner rings, not the grout, are permanently fixed (restricted displacements in all directions) in the position shown in Figure 5.8, this from the beginning of the step-by-step advancement until the very last step. In this framework, the assumption is that the TBM perfectly follows the design alignment, and that the rings are perfectly locked in place by the grout once installed, as explained previously. With this, the shield and the lining, respectively to the space, remain in an immovable position, while the soil has a relative movement around them, in the same way that the observer remains motionless inside a running train while the world moves around him.

### 5.1.2.3 *Applied pressures*

Since the top soil layer until the mark of 4.8 m below the ground surface was not explicitly modeled to position the foundation of the building in a future coupled interaction model, from the greenfield models still a vertical confining pressure equivalent to the removed soil's weight was introduced at the model's Top face, equal to 91.2 kPa.

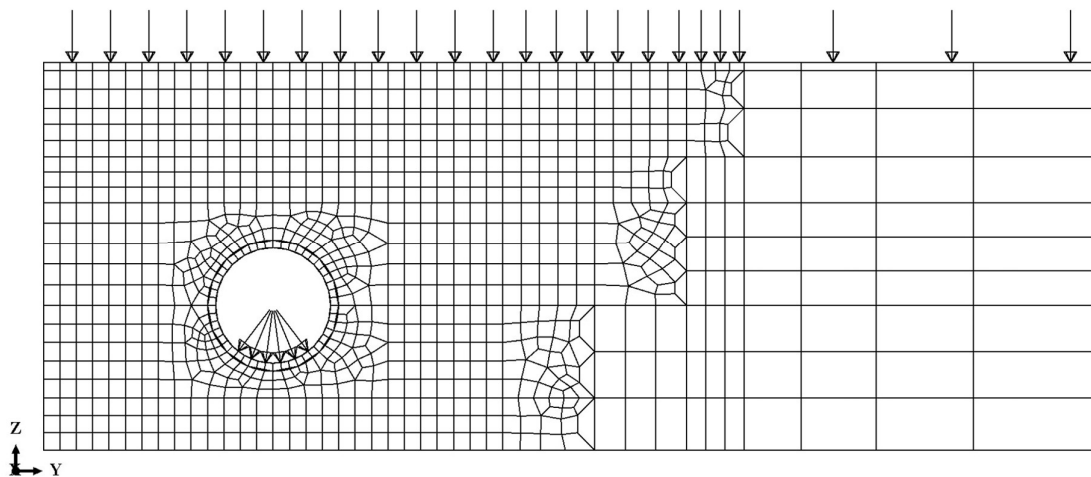


Figure 5.9. *Applied topsoil and shield/liner pressures to account for their weights*

In a zone comprising one-fourth of the tunnel perimeter at the invert of the excavation, a distributed pressure was also included regarding the weight of the cutterhead and shield of the TBM, and of the segmental lining with the grout. This is because, as described above, these parts are fixed in the space and do not interact with the soil through gravity loading. A pressure of 60 kPa is activated below the advancing shield and another of 47 kPa below the installed lining; the former obtained from a literature study on the weight of tunnel boring machines, and the latter from the weight of the reinforced concrete and grout.

An additional applied pressure is that of the conditioned soil that provides support at the excavation front. This will be more detailly explained when describing the excavation advancement in 5.1.5.1.

#### 5.1.2.4 Additional boundary conditions

Other boundary conditions, such as those concerning the convergence of the tunnel walls, the application of the face pressure, the contact interactions, and so on; are closely related to the excavation stages and therefore, will be later discussed under the heading 5.1.5.

### 5.1.3 Material properties

#### 5.1.3.1 Soil properties

Following the mechanical characterization of the Torino subsoil by both Barla & Barla (2012) and Infratrasporti.To (2024), revised before under the heading 4.2.4, the next drained parameters are chosen to perform parametrical analyses, enclosing the expected behavior of the soil in-situ with the elasto-plastic Mohr-Coulomb constitutive formulation. In this case, the ITO model refers to the properties adopted by Infra.To to conduct the two-dimensional numerical studies to assess the surface settlements, while the BARMIN and BARMAX parameters are obtained from Barla & Barla's 2012 article on the characterization of the Torino soil by means of experimental and numerical investigations.

Table 5.1. Parameters selected for the model of the Torino soil

Model	Geotech. unit	Natural unit weight [kN/m <sup>3</sup> ]	Effective friction angle [°]	Effective cohesion [kPa]	Young's modulus [MPa]	Poisson's ratio [-]
ITO	GU1	19.0	29.0	0.1	15.0	0.30
	GU2	19.0	36.0	10.0	150.0	0.30
BARMIN	GU1	19.0	36.0	0.1	10.0	0.40
	GU2	19.0	37.0	5.0	190.0	0.30
BARMAX	GU1	19.0	37.0	0.1	20.0	0.40
	GU2	19.0	39.0	30.0	240.0	0.30

#### 5.1.3.2 The shield and the lining segments

The shield of the machine is assumed to behave elastically, assigning it the isotropic Young's modulus of the steel equal to 200 GPa and Poisson's ratio of 0.3. The prefabricated lining segments are regarded to be continuous (no joints between segments are simulated), also considered to behave in elasticity with the concrete's elastic modulus of 30 GPa and Poisson's ratio of 0.2. These values are, in any case, formalities as these parts are rigidly fixed in space as commented before and thus, the deformability characteristics are of no use.

5.1.3.3 *Annulus grout*

Based on the literature review submitted under the heading 3.1.3.3, the next Table 5.2 proposes a range of values for the prediction of the time-dependent elastic modulus of the two-component grout in the Metro-Line 2 project, the curve GSMIN referring to the most pessimistic and the curve GSMAX referring to the most optimistic expected behaviors of the material, with an artificial GSMEAN curve created from the arithmetic average of the two extremes, which are in turn obtained as explained in the following paragraphs. It must be highlighted that the elastic parameters from the work by Oreste et al. (2021), before listed in the Table 3.1, were not included in the present analysis, as their values appear significantly higher than their counterparts, even from an early age. It is not the goal of the present effort to discuss the reasons for this superior behavior; nonetheless, it can be hinted that this study was the only one to mix the components A and B with a “[...] device engineered for the continuous mixing of two-component fluid materials (developed by GEEG and available in the geotechnical laboratory of Sapienza University of Rome [...])” instead of using high-speed rotating mixers or manually mixing the ingredients as usually performed, and because the mechanical properties of the samples are greatly affected by the mixing methods (Oggeri, Oreste, & Spagnoli, 2021; Di Giulio, Bavasso, Di Felice, & Sebastiani, 2020), it is hypothesized that this could have provided the remarkably high elastic properties.

Table 5.2 Proposed Metro-Line 2 of Torino’s two-component grout elastic parameters

	GSMIN	GSMAX	GSMEAN
Young's modulus [MPa]			
1 [hr]	1.30	2.50	1.90
8 [hrs]	11.0	25.0	18.0
16 [hrs]	21.0	45.0	33.0
1 [day]	26.1	82.3	54.2
7 [days]	35.9	172.0	104.0
28 [days]	64.3	172.0	118.2
Poisson's ratio [-]			
	0.45	0.45	0.45

The next Figure 5.10 and Figure 5.11, in spite of presenting the results of the literature review simultaneously, it does not pretend to compare them. Due to their heterogeneity, regarding the unstandardized experimental methods, correlations and constitutive models employed to determine the values of the time-dependent elastic properties of the two-component grout; these investigations serve merely to fulfill the necessities of the current project: finding a reasonable range of behaviors for the grout in the construction site. This range, from the curve GSMIN to GSMAX, is designed to enclose the results of the studies, following the criteria:

- 1) The early hardening rate  $E_{gel}/E_{solid}$  is expected to be of the same order of magnitude of that introduced by Nikakhtar et al. (2020), while the late hardening

rate  $E_1/E_{28}$  is required to be near or higher than 0.50, as discussed under the heading 3.1.3.3 when commenting on the investigations by Mohammadzamani et al. (2023). Respectively so, the values obtained for these rates with the curves GSMIN and GSMAX are, for the early hardening rate about 0.10 while for the late hardening rate around 0.45.

- 2) Closely related to the previous remark, the values of  $E_{get}$  and  $E_{solid}$  are respectively chosen to be the elastic moduli of the grout at 1 and 8 hours of curing. Then, the values of  $E_1$  and  $E_{28}$  are respectively chosen to be the elastic moduli of the grout at 1 and 28 days of hardening. It is then required for these two latter to belong to the same study. For example, for the curve GSMIN the values of  $E_1 = 26.1$  MPa and  $E_{28} = 64.3$  MPa come from the same investigation performed by Oggeri et al. (2021).
- 3) Related to the elastic modulus of GSMAX at 28 days, seeing that the majority of the studies show that the modulus increases from 7 to 28 days, in a conservative effort the modulus is kept constant at 172 MPa, derived from the investigations of Rahmati et al. (2022).
- 4) In response to the limitations imposed by the scarcity of research on the topic and lack of standardized regulations, the knowledge gaps that may remain in the values of the elastic modulus (for example, the value of 45 MPa for the elastic modulus at 16 hours in GSMAX being selected to approximate the value from the study of Epel et al. (2021) due to the lack of this information in Rahmati et al. (2022)) and Poisson's ratio (assumed equal to 0.45, constant for all ages) are selected to be representative of the expected behavior of the material, based on the experience collected from the literature.

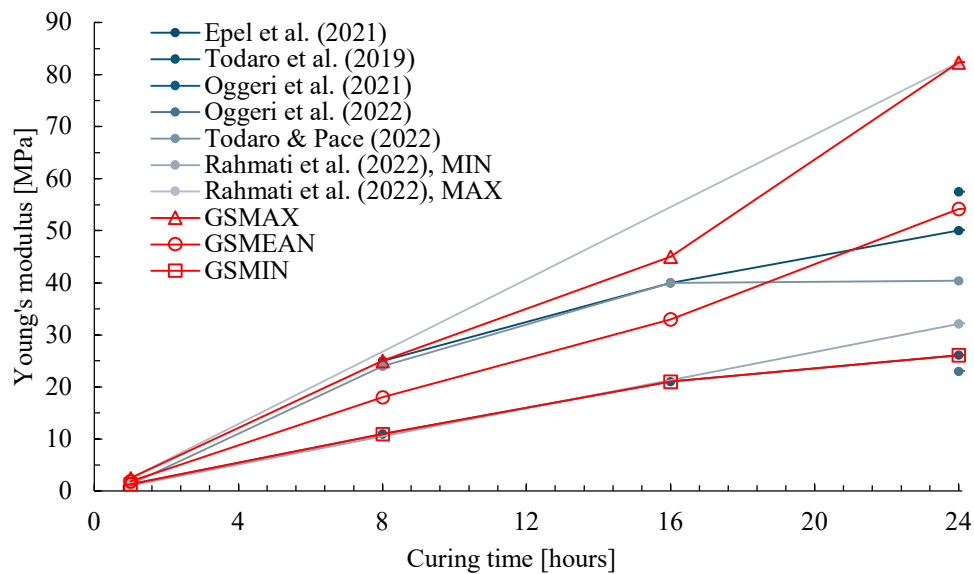


Figure 5.10 Young's modulus of the two-component grout at an early curing time frame

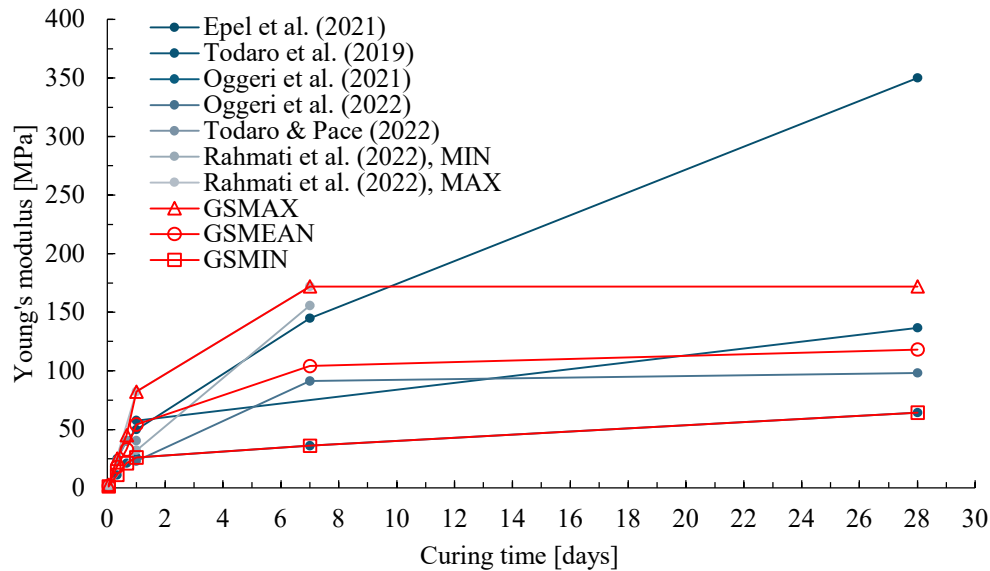


Figure 5.11. Young's modulus of the two-component grout in time

It is then that these three curves are used in the numerical model to define the time-dependent Young's modulus of the two-component grout, keeping the Poisson's ratio fixed at 0.45. Since the excavation steps are simulated every three meters (two lining rings installed), as discussed in a prior opportunity, and regarding the advancement rate of the TBM near 9 meters per day (in the past heading 4.1.1 it was declared that the expected advancement rate of the machine was of 10 m/day, here this rate is lowered for simplicity); the grout hardening is consequently modelled by following the next steps and Figure 5.12

- 1) At the first step, two liners  $i$ -th are instantaneously installed behind the shield, and the grout takes its stiffness constant and equal to the Young's modulus at 1 hour of hardening.
- 2) At the second step, when 8 hours have passed, a new pair of liners  $i$ -th+1 is installed after the shield's tail, once again with stiffness equal to the Young's modulus at 1 hour of hardening. The elastic modulus of the older  $i$ -th pair is then increased to its value at eight hours and it is kept constant.
- 3) At the third step, when 16 hours have passed, a new pair of liners  $i$ -th+2 is installed after the shield's tail, once again with stiffness equal to the Young's modulus at 1 hour of hardening. The elastic modulus of the older  $i$ -th+1 pair is then increased to its value at eight hours, and that of the  $i$ -th pair is increased to its value at 16 hours.
- 4) The process is repeated until the 20<sup>th</sup> day, noticing that each pair of new liners is installed every eight hours.

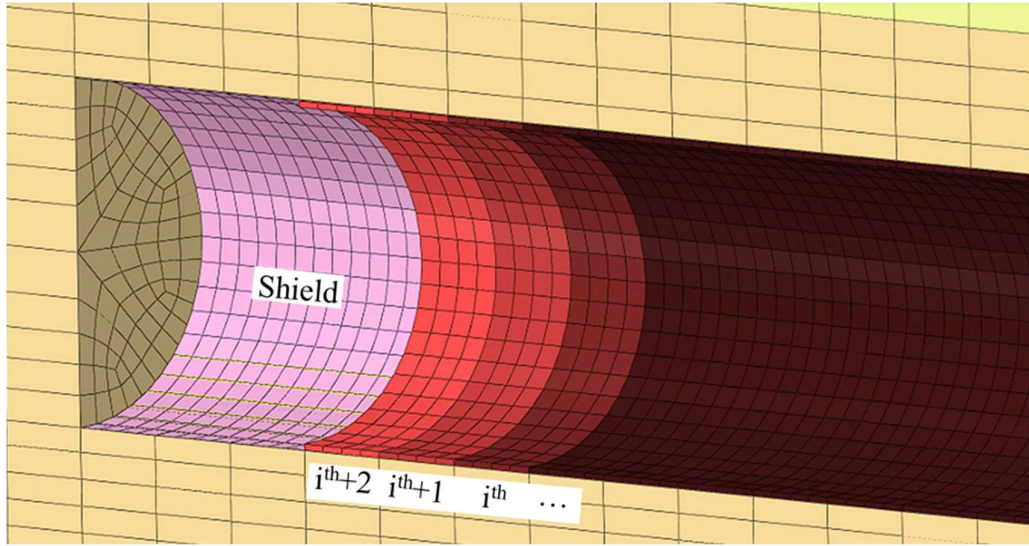


Figure 5.12. Modelling the time-dependent Young's modulus of the grout

As readily apparent, this is a step-function that goes along with the steps of the excavation and can be seen applied for the  $i$ -th liner pair with the three different GS curves in the next Figure 5.13. This function, nonetheless, only reaches the 20<sup>th</sup> day given that the total excavation length of 180 m can be completed in this time frame with the advancement rate of 9 m/day.

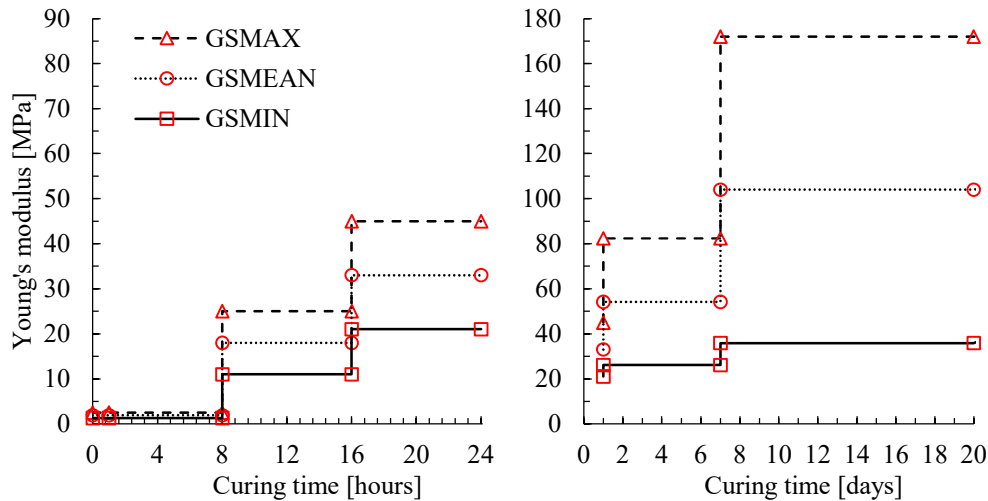


Figure 5.13. Step-function representing the stiffening of the two-component grout in the model, function of time

It must be remarked that, even though here time is repeatedly mentioned, the model does not depend on time as it remains an implicit numerical simulation and thus, the time of hardening of the material can only be related to the model through the length of the excavation steps and TBM advancement rate. In response to this, the same time-dependent Young's modulus is plotted in the following Figure 5.14 against the distance from the tail of the shield, which can also be interpreted as the length of advancement of the excavation with respect to a fixed section of the alignment.



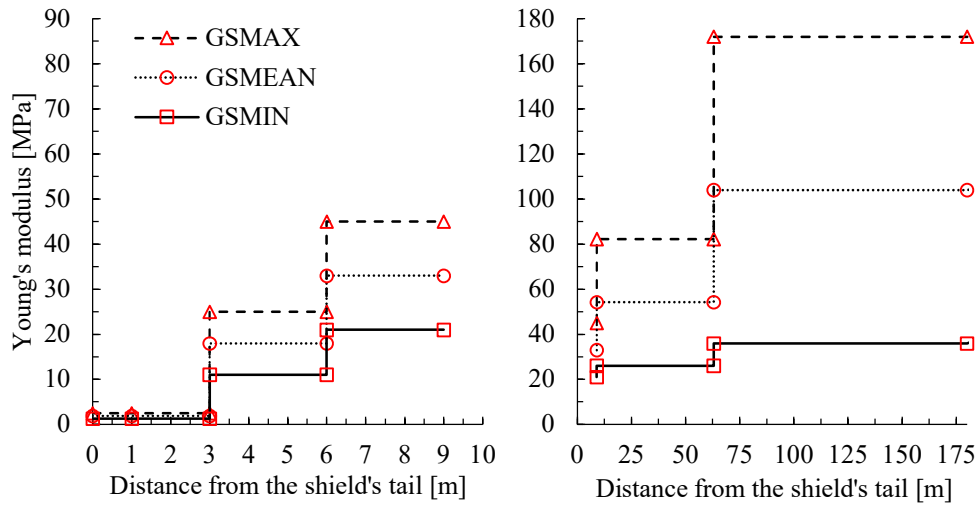


Figure 5.14. Step-function representing the stiffening of the two-component grout in the model, function of the distance from the tail of the shield

#### 5.1.3.4 Jet grouting umbrella for the soil improvement

Following the minimum requirements imposed by Infra.To for the mechanical characteristics of the improved soil, before revised under the section 4.3.3, the next parameters are employed to model the jet grouting umbrella.

Table 5.3. Parameters selected for the model of the jet grouting umbrella

Natural unit weight [kN/m <sup>3</sup> ]	Effective friction angle [°]	Effective cohesion [kPa]	Young's modulus [Mpa]	Poisson's ratio [-]
19.0	36.0	150.0	450.0	0.3

#### 5.1.4 Initial state of stress and geostatic step

In ABAQUS, the geostatic state of stress is initiated preceding all static computational steps. This is achieved by assigning body forces in the direction of the gravity (-Z) to each one of the geotechnical units (GU) in function of their unit density, and predefined geostress fields in function of both their vertical and horizontal effective stresses. Following previous scientific publications on the numerical modelling of the Metro-Line 1 of Torino (Barla G. , Barla, Bonini, & Gamba, 2005; Barla, Barla, & Leuzzi, 2012), to obtain the horizontal ground pressure, the earth pressure coefficient at rest is selected as  $K_0 = 0.50$ . The result is presented in the figure below.

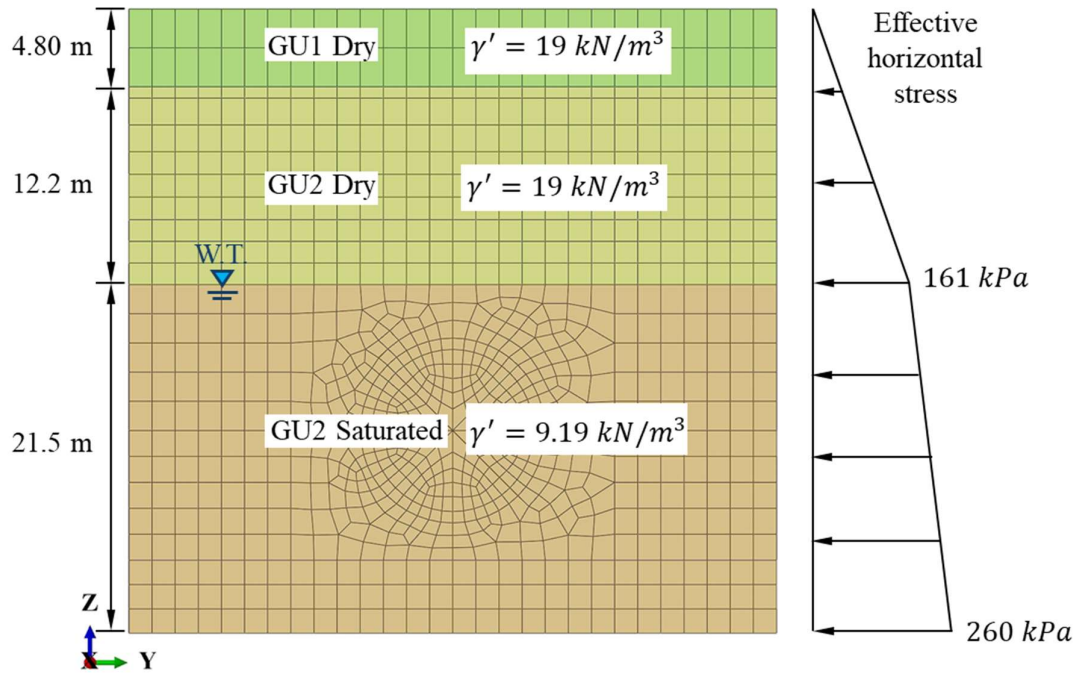


Figure 5.15. Effective horizontal stresses and unit weights assumed for the simulation of the geostatic stress

### 5.1.5 Stages

The step-by-step excavation procedure is executed for all models, with the objective of simulating a ‘near realistic’ mechanized excavation: emulating the advancement of the TBM’s shield, the formation of the steering gap and consequent ground convergence, the installation of the segmental liners, grout injection pressure, grout shrinkage due to the surrounding soil convergence and stiffening of the material, application of the supporting face pressure and also, the pressures at the invert derived from the weights of the TBM and the lining rings. No consolidation stage is considered after the excavation anticipating a drained behavior of the ground from initial stages, owing to the coarse granulometry of the soil. These steps are run as Static, General steps in ABAQUS (Dassault Systemes, 2024) with iterative full Newton equation solvers and unsymmetric matrix storage in a non-linear geometric scheme to account for the effects of large deformations; all these after the completion of the geostatic stress equilibrium step at the beginning of the computations.

#### 5.1.5.1 Excavation advancement

The excavation advancement is performed inspired by previous successful cases in literature that simulated the step-by-step procedure, as better explained under the heading 3.1.5. In detail:

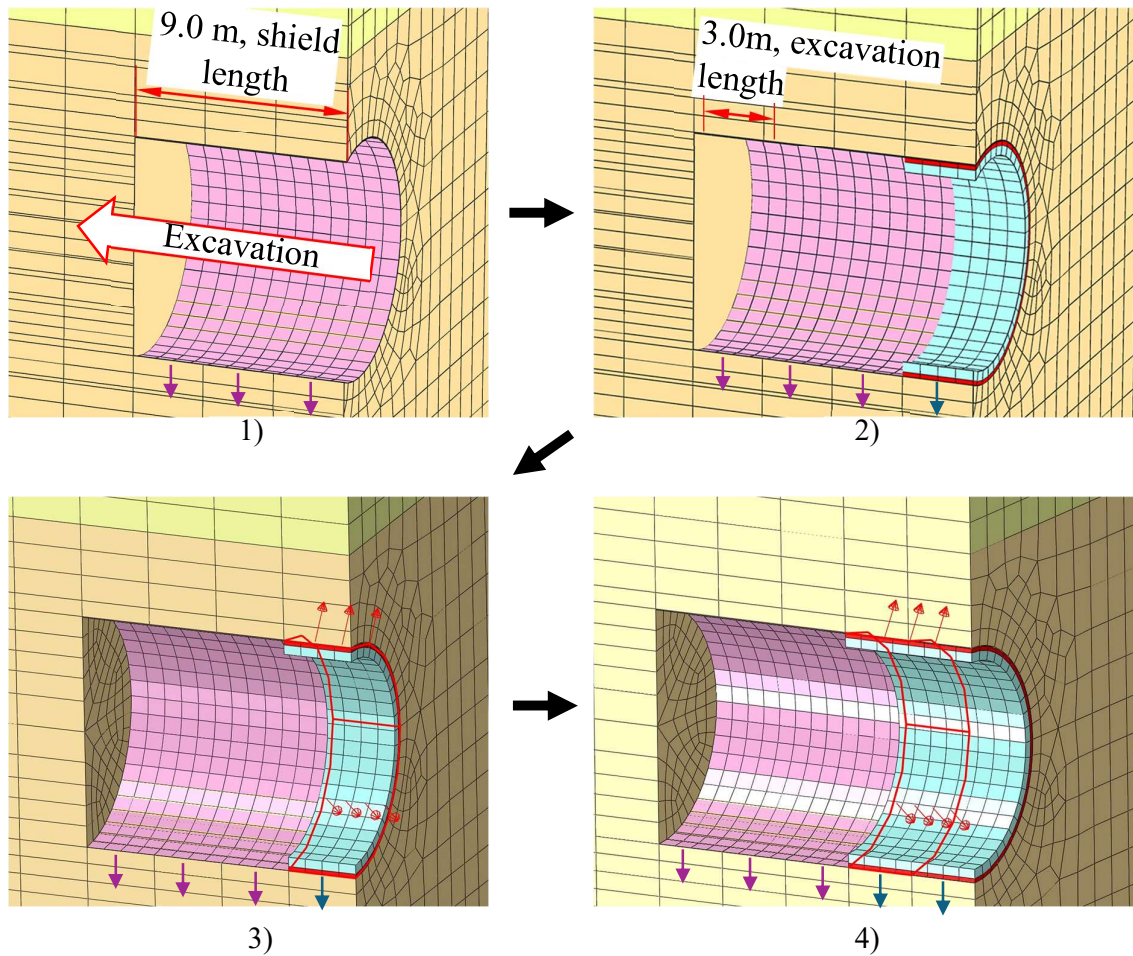


Figure 5.16. Step-by-step excavation process

- 5) Previous to this step where the shield is completely present, the shield had to be advanced in three excavation steps of three meters by activating its corresponding shell elements and deleting the relative solid elements of the ground. At all times the contact interaction between the shield and the converging ground is active. The applied pressure of the weight of the TBM is also included at one-fourth of the tunnel perimeter at the invert of the excavation.
- 6) The shield is advanced once again by one excavation length and immediately behind the tail of the shield, a pair of liner rings (each of 1.5 m) and solid grout elements are activated, with the applied pressure due to the concrete and grout weight at one-fourth of the tunnel perimeter at the invert of the excavation. At all times the contact interaction between the grout extrados and the converging ground is active.
- 7) The grout injection pressure is included as an outwards pointing distributed load acting on the grout extrados, only in the first two segmental rings behind the tail.
- 8) The process is repeated by activating the shield and liner plus grout elements, and their respective pressures, while deactivating the corresponding ground elements at the front of the tunnel.

In every step, a horizontal and trapezoidal pressure is activated at the front face of the tunnel as depicted in Figure 5.17, to simulate the supporting pressure exerted by the conditioned soil in the excavation chamber of the EPB-TBM. In the figure below, this pressure is perfectly balancing the effective geostatic stress initiated at the beginning of the computations; however, with the purpose of performing parametrical analyses, the pressure is later multiplied by 0, 25, 50, 100 and 150%, simulating different pressurizations at the front and the extreme case of null pressure.

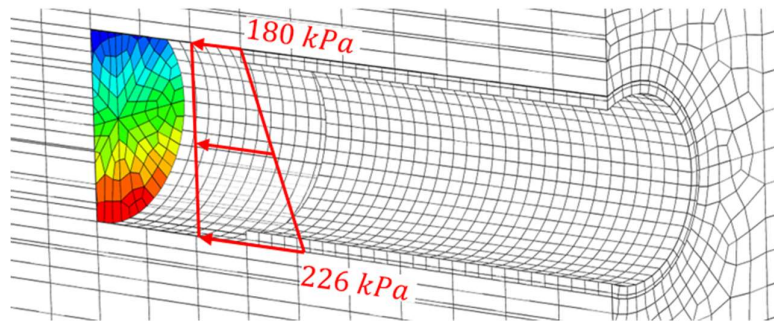


Figure 5.17. Simulation of the EPB-TBM face pressure

#### 5.1.5.2 Soil convergence around the shield

Based on the section 3.1.5.2, it is chosen to explicitly model the TBM's shield with its bottom lying at the invert of the excavation (as shown in Figure 5.8), featuring a steering gap solely at the crown but not at the invert (for contact compliancy, a small gap of 2 mm is left at the invert). This crown gap is then varied to perform parametric analyses, taking from Litsas et al. (2017) investigations the values of 2, 4 and 6 cm, which are well within the shield gap values considered by other authors (Migliazza, Chiorboli, & Giani, 2009; Mooney, Grasmick, Kenneally, & Fang, 2016; Kavvadas, Litsas, Vazaios, & Fortsakis, 2017; Losacco & Viggiani, 2019).

Given that the soil and the shield are modelled as two different parts, as explained under the same heading 3.1.5.2, these two must enter in contact as the ground converges. The contact interaction is here configured with penalties both in the tangential and normal directions. For the first, a friction coefficient equal to 0.30 is defined (Working Groups 2 & 14 SIG, 2014) to consider a constant dynamic soil-shield friction during the TBM advancement. For the second, a "hard" contact pressure-overclosure relation with a penalty constraint enforcement method is adopted, allowing for separation after contact and setting a default contact stiffness with an unitary scale factor, to allow ABAQUS to calculate the *penalty stiffness* as 10 times a representative underlying element stiffness (Dassault Systemes, 2024), while the *clearance at which the contact pressure is zero* is defined equal to 0.1 mm, meaning that a fictitious penetration of 0.1 millimeters is allowed to soften the contact interaction and promote easier numerical convergence. The accuracy of the model was not sacrificed with these simplifying assumptions, as different comparisons were performed with preliminary models having a perfect "hard" contact pressure-overclosure relation, and the results showed that with the softened penalty relations the penetration was negligible, and the surface settlements remained equal for both cases.

No steering gap pressure is specified at the excavation walls, conservatively assuming that the conditioned Torino soil, due to its predominantly coarse characteristics, cannot escape the TBM's pressured chamber to fully permeate the gap. A possible scenario can be imposing triangular pressures acting near the head and the tail of the shield due to the respective face and grout injection pressures (replicating the Scenario B from Figure 3.23), nonetheless, the same Litsas et al. (2017) showed that, if this scenario helps to reduce the volume loss, it is a marginal reduction and therefore, the inclusion of this additional boundary condition complexifying the model is here discarded.

#### *5.1.5.3 Soil convergence around the liners and the grout*

Based on the section 3.1.5.3, it is decided to model the soil as a separate part from the liners and the grout, as exhibited previously in Figure 5.4. Then in the assembly, both the soil excavation walls and the grout extrados enter in contact as the ground contracts towards the cavity. The contact interaction is here configured both in the tangential and normal directions. For the first, a 'rough' frictional formulation (Dassault Systemes, 2024) is used to impede all relative slipping between the two contacting surfaces, in line with the expected grout adhesion to the surrounding soil. For the second, a "hard" contact pressure-overclosure relation with a penalty constraint enforcement method is adopted, inhibiting separation after contact and setting a default contact stiffness with an unitary scale factor, to allow ABAQUS to calculate the *penalty stiffness* as 10 times a representative underlying element stiffness (Dassault Systemes, 2024), while the *clearance at which the contact pressure is zero* is defined equal to 0.1 mm. Analogously to the previous section, preliminary models were reviewed to guarantee the validity of the softened penalty alternative.

Additionally, the annulus gap results in a variable dimension in function of the modification of the steering gap, taking values from 34 to 38 cm, in line with the annulus gap values assumed by other authors introduced under the section 3.1.5.3. As also performed by the listed researchers, a grout injection pressure is imposed only at the first lining ring advancement behind the shield, in this case as a distributed stress on the grout extrados radially pointing outwards, towards the excavation walls. The values assumed for the grout pressure are also intended for parametric analyses, given that this information is unknown as the second line of the Torino Metro is yet to be constructed. The chosen values are 200, 400 and 600 kPa, which are within the ranges of the examples of section 3.1.5.3.

#### **5.1.6 Parametrical analyses**

Since the construction phase of the project of the Metro-Line 2 of Torino, now when this essay is being written has not started, no official date has been given for its onset and, furthermore, the construction bidding process has yet to take place; many characteristics of the tunnel excavation are uncertain. To name a few, the detailed dimensions of the cutterhead and the shield, from which the overcut and conicity can

be determined, or the material selected for the backfilling with its target injection pressure, are unknowns. Uncertainties also exist while the works are active: the ground conditions may differ from those predicted through geological profiles, the TBM may come to a complete stop losing progressively the applied face pressure, the steering of the machine could be imprecise increasing the overcut, among other unknowns that render impossible to create a deterministic excavation model. To consider this variability that the real excavation process will hold, greenfield parametric analyses are formulated following the next Figure 5.18, starting with a Reference model (REF) regarded as representative of the average conditions of the tunnel excavation, and then changing only one of its modelling assumptions, highlighted in red, while keeping fixed the rest.

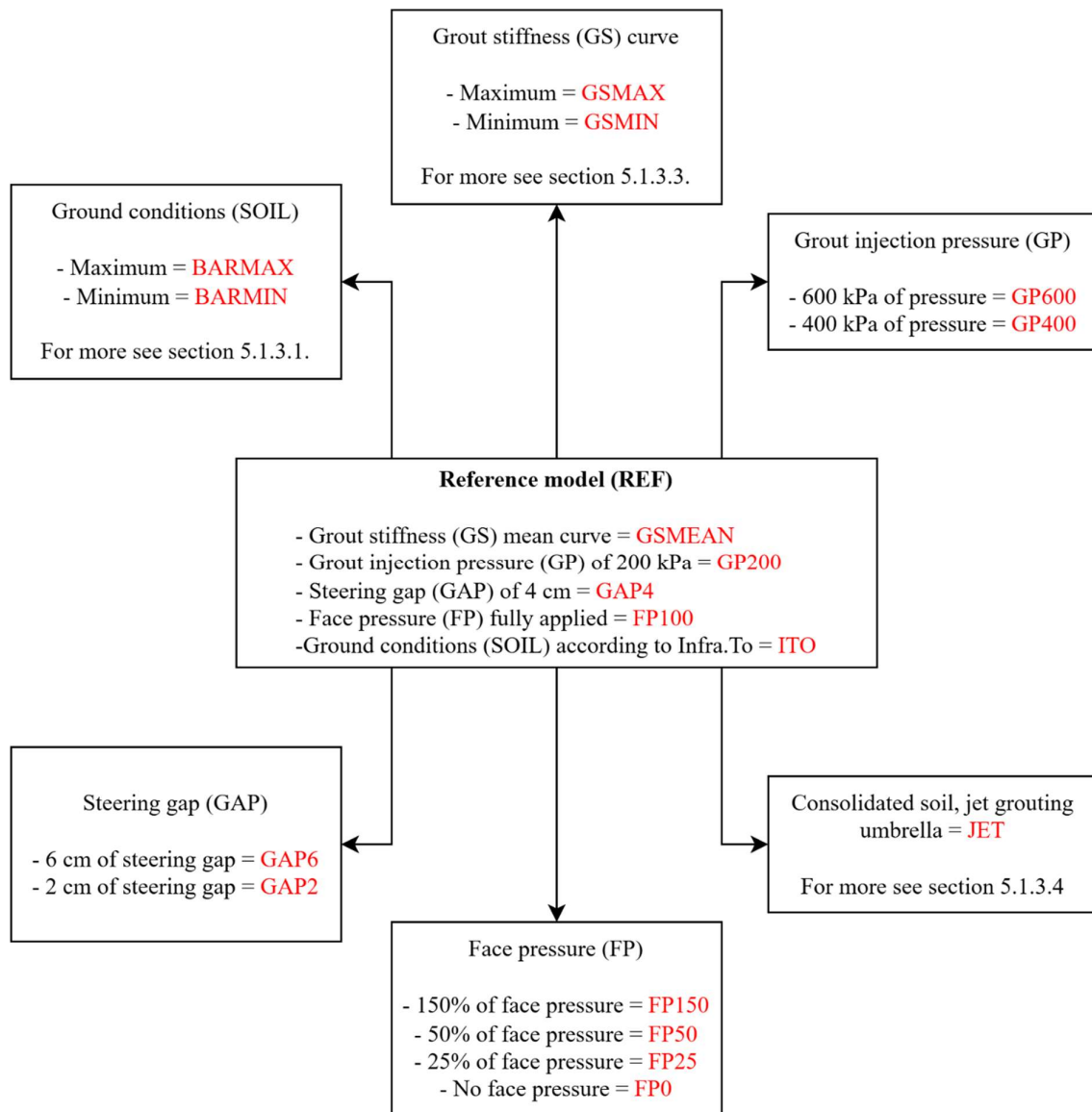


Figure 5.18. Workflow of the greenfield parametrical analyses

From these models, the so-called greenfield volume loss models are defined as VLMAX, VLMEAN and VLMIN, respectively representing the highest (most pessimistic), average and lowest (most optimistic) settlement volume losses witnessed from the parametric analyses. The nomenclature is further detailed in Table 5.4.

*Table 5.4. Nomenclature for the greenfield models*

Model	Description
VLMAX	The subsidence is the most pessimistic (highest settlement volume loss) found from the greenfield parametric analyses.
VLMEAN	The subsidence is the average case scenario found from the greenfield parametric analyses (settlement volume loss of the reference REF model).
VLMIN	The subsidence is representative of one of the most optimistic scenarios found from the greenfield parametric analyses (settlement volume loss of the model with the jet grouting umbrella).
GSMAX	The grout elements are ruled by the GSMAX constitutive behavior of Table 5.2, which has a Young's modulus of 2.50 MPa for the first hour of curing and 25.0 MPa at the next eight hours of hardening.
GSMEAN	The grout elements are ruled by the GSMEAN constitutive behavior of Table 5.2, which has a Young's modulus of 1.90 MPa for the first hour of curing and 18.0 MPa at the next eight hours of hardening.
GSMIN	The grout elements are ruled by the GSMIN constitutive behavior of Table 5.2, which has a Young's modulus of 1.30 MPa for the first hour of curing and 11.0 MPa at the next eight hours of hardening.
GP600	Only in the liner ring immediately behind the face, a distributed pressure of 600 kPa is applied at the grout extrados pointing outwards, radially facing the tunnel excavation boundary.
GP400	Only in the liner ring immediately behind the face, a distributed pressure of 400 kPa is applied at the grout extrados pointing outwards, radially facing the tunnel excavation boundary.
GP200	Only in the liner ring immediately behind the face, a distributed pressure of 200 kPa is applied at the grout extrados pointing outwards, radially facing the tunnel excavation boundary.
BARMAX	The soil adopts the elasto-plastic Mohr-Coulomb constitutive behavior BARMAX of Table 5.1 based on Barla & Barla's (2012) studies, which in the ground unit 2 (GU2) has an effective friction angle of 39°, effective cohesion of 30 kPa and a Young's modulus of 240 MPa.
BARMIN	The soil adopts the elasto-plastic Mohr-Coulomb constitutive behavior BARMIN of Table 5.1 based on Barla & Barla's (2012) studies, which in the ground unit 2 (GU2) has an effective friction angle of 37°, effective cohesion of 5 kPa and a Young's modulus of 190 MPa.
ITO	The soil adopts the elasto-plastic Mohr-Coulomb constitutive behavior ITO of Table 5.1 based on Infratrasporti.To's proposal, which in the ground unit 2 (GU2) has an effective friction angle of 36°, effective cohesion of 10 kPa and a Young's modulus of 150 MPa.
GAP6	The steering gap product of the TBM's over excavation and the shield conicity is assumed to be equal to 6 cm. This case can also be representative of a poor steering of the machine, leading to high overcuts.
GAP4	The steering gap product of the TBM's over-excavation and the shield conicity is assumed to be equal to 4 cm.

---

GA2	The steering gap product of the TBM's over-excavation and the shield conicity is assumed to be equal to 2 cm.
FP150	The pressure applied by the EPB TBM at the face of the excavation is equal to 150% the geostatic horizontal earth pressure (which assumes a triangular distribution).
FP100	The pressure applied by the EPB TBM at the face of the excavation is equal to the geostatic horizontal earth pressure (which assumes a triangular distribution).
FP50	The pressure applied by the EPB TBM at the face of the excavation is equal to 50% of the geostatic horizontal earth pressure (which assumes a triangular distribution).
FP25	The pressure applied by the EPB TBM at the face of the excavation is equal to 25% of the geostatic horizontal earth pressure (which assumes a triangular distribution).
FP0	The EPB TBM is assumed to apply no pressure on the face of the excavation. This case can be representative of situations in which the EPB stops advancing for relatively long periods, the conditioned soil loses its fluid properties and therefore, it cannot be used to apply the pressure at the front.
JET	A soil of improved characteristics is modelled around the crown towards the springline of the tunnel to simulate the projected jet grouting umbrella under Palazzo Campana, as presented in Figure 5.7.

---

## 5.2 Uncoupled building models

In an uncoupled framework, it is of interest seeing the behavior of the isolated building subjected to the greenfield settlement trough, frequently deemed as the worst-case scenario because the building's stiffness is neglected at the same time as the foundation is forced to follow the subsidence basin. Here, however, a new proposal is made to include the building's stiffness even from the uncoupled model, while the greenfield subsidence is still applied.

### 5.2.1 Geometrical model and discretization

Based on the models studied under the heading 3.2.1, the next model meshes are proposed, simplifying the geometry of the building presented before in section 4.3.1: for example, the CEAST facade in the next Figure 5.19 is shaped with a single horizontal wall, ignoring the various indentations of the real facade (recalling Figure 4.18) that render it inconveniently jaggy and unnecessarily complex for the current purpose. The figure below presents the nomenclature that hereafter will be used to refer to each facade. The subsequent Figure 5.20 and Figure 5.21 show instead the elevations adopted for the EAST and NORTH facades respectively, with vertical measures that are maintained constant throughout the entirety of the facades. For detailed elevations, the blueprints of the building are annexed in Appendix B.



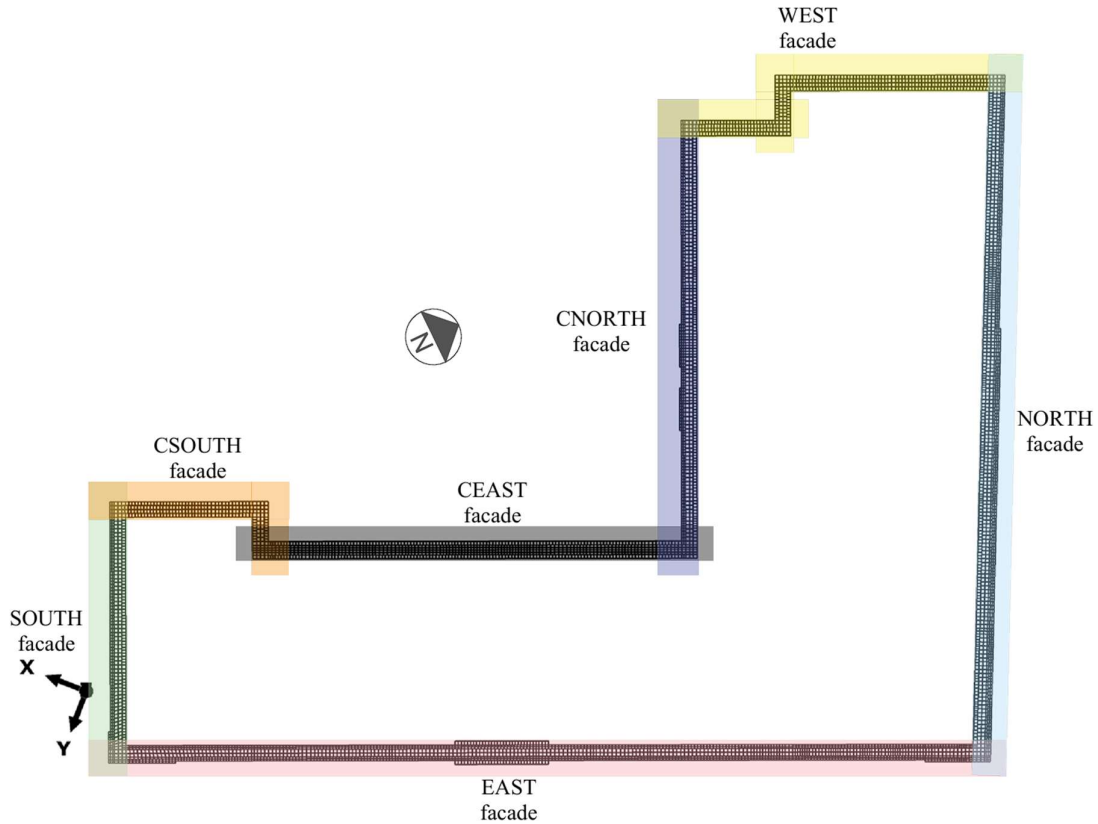


Figure 5.19. Model mesh of Palazzo Campana's perimetral facades, top view and facade nomenclature

For all the facades, the thicknesses of the walls range between 0.80 and 1.00 m, obtained from the dimensions observed in the top and elevation views in the Appendix B, subtracting 0.20 m to account for possible plaster coating or internal voids. The foundation, located at a depth of 4.80 m below the ground surface, is modelled as a strip footing of 0.50 m thickness and variable width, equal to the thickness of the respective facade summed an enlargement of 0.40 m to each side of the wall. In this sense, the foundations represent a widening of 0.80 m of each facade, typical in historical masonry buildings.

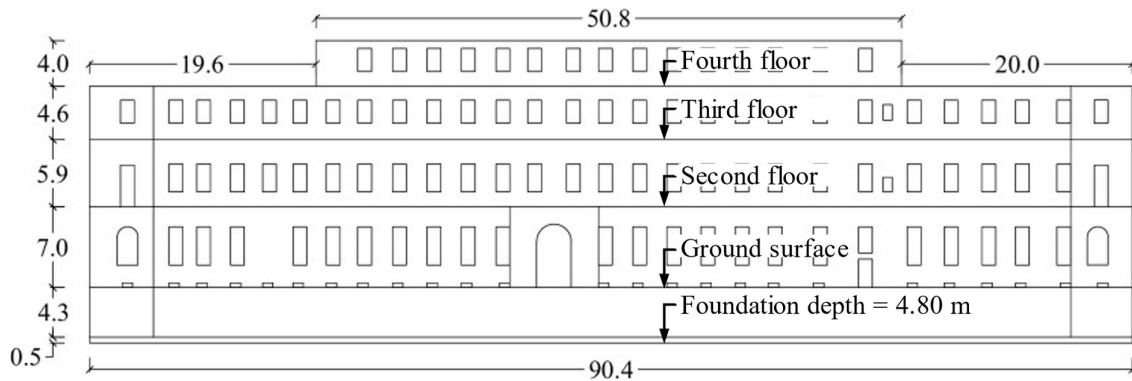


Figure 5.20. EAST facade. Simplified exterior elevation, Via Carlo Alberto wing

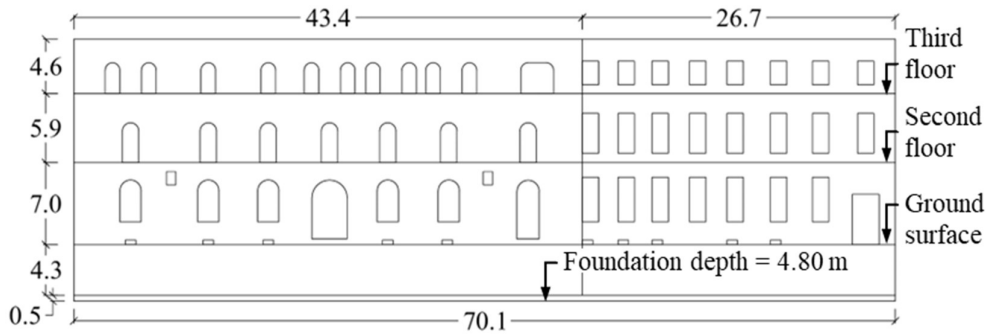


Figure 5.21. NORTH facade. Simplified exterior elevation, Via Principe Amedeo wing

The model meshes are presented next, for the perimetral facades in conjunction and for each one separately, to showcase the density of the mesh: for the NORTH facade, for instance, element sizes varied around 0.40 meters of length while in critical areas, identified with preliminary numerical analyses to have higher stresses-strains, their sizes reduced to 0.20 meters to better capture the stress concentrations and induced elastic and cracking strains. In general, for all the facades, the element sizes were reduced to 0.30 meters around the openings, where it is common to find high strains.

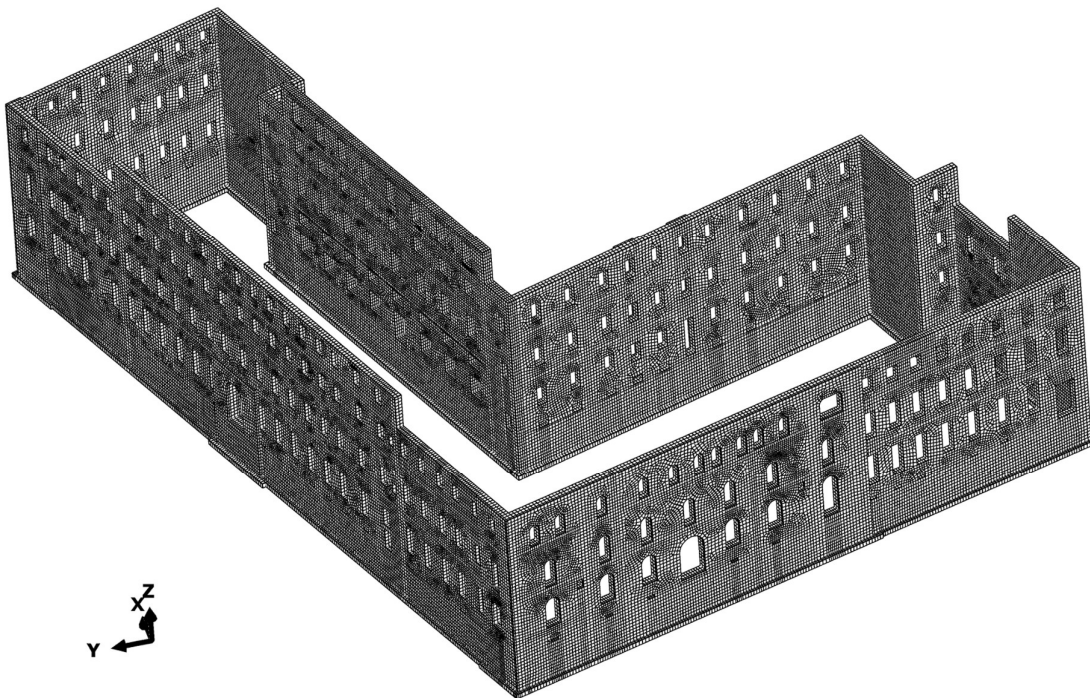
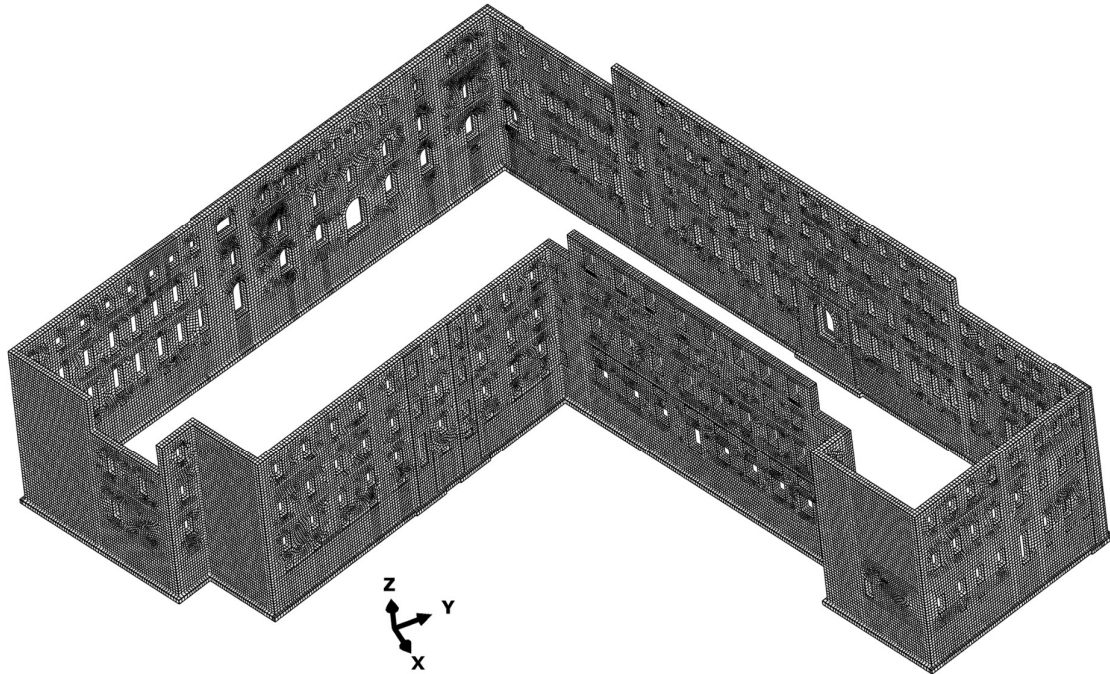
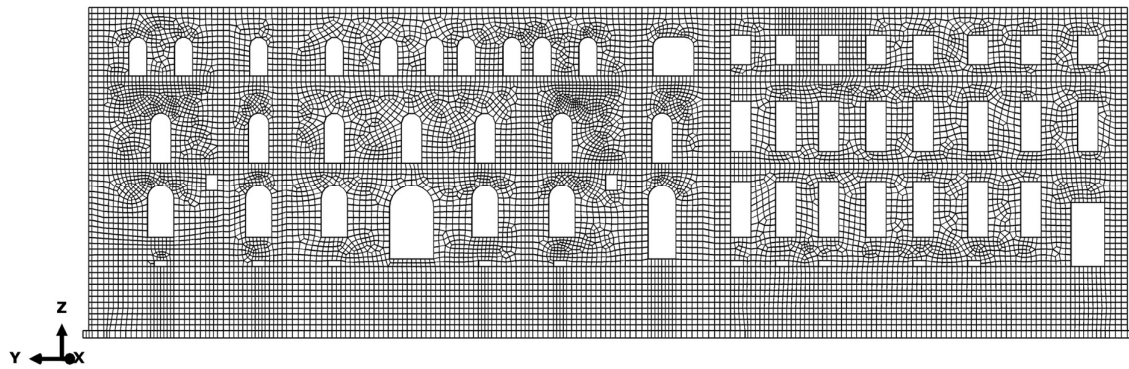


Figure 5.22. Model mesh of Palazzo Campana's perimetral facades, front view from Via Principe Amedeo



*Figure 5.23. Model mesh of Palazzo Campana's perimetral facades, rear view from Via Maria Vittoria*



*Figure 5.24. Model mesh of the NORTH facade*

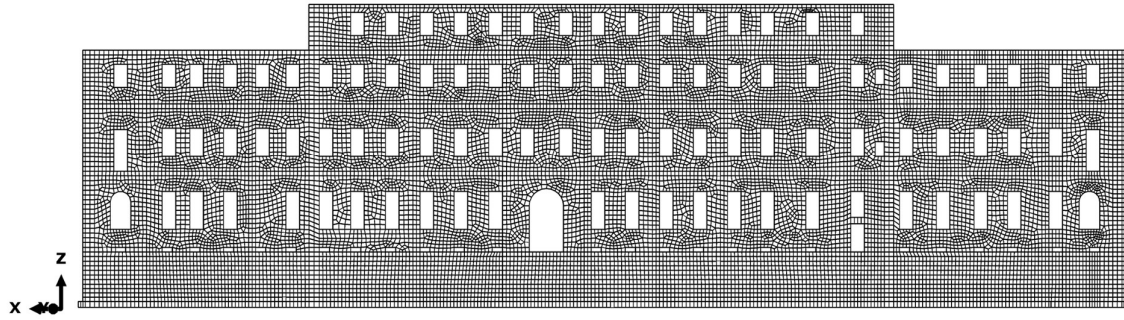


Figure 5.25. Model mesh of the EAST facade

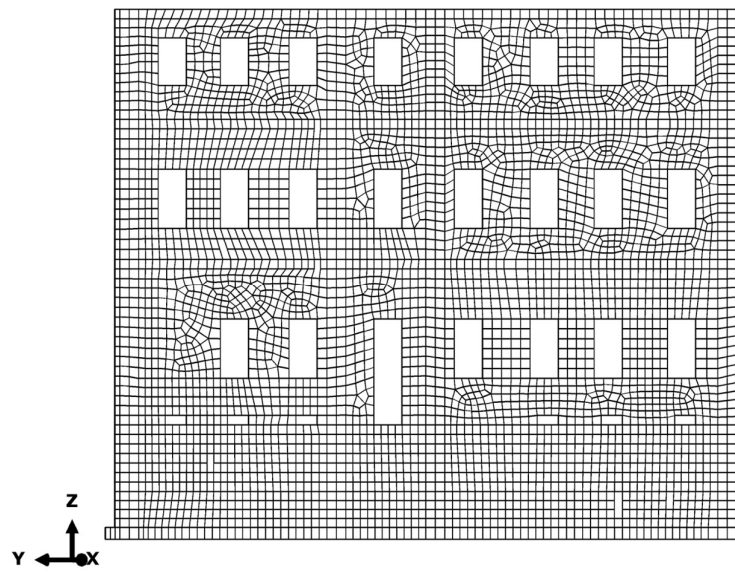
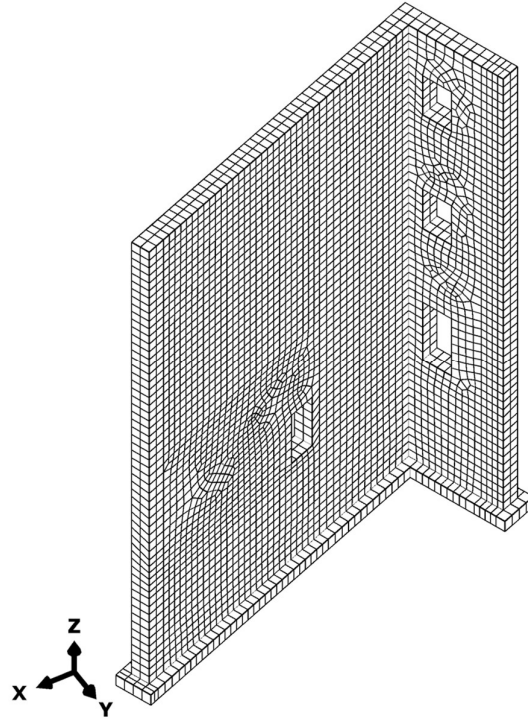
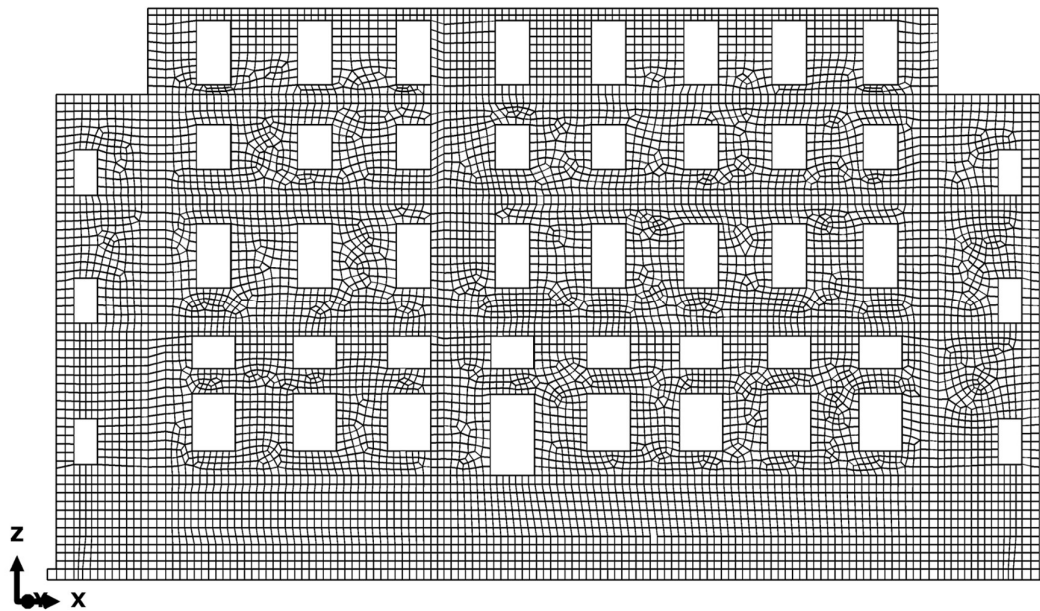


Figure 5.26. Model mesh of the SOUTH facade



*Figure 5.27. Model mesh of the CSOUTH facade*



*Figure 5.28. Model mesh of the CEAST facade*

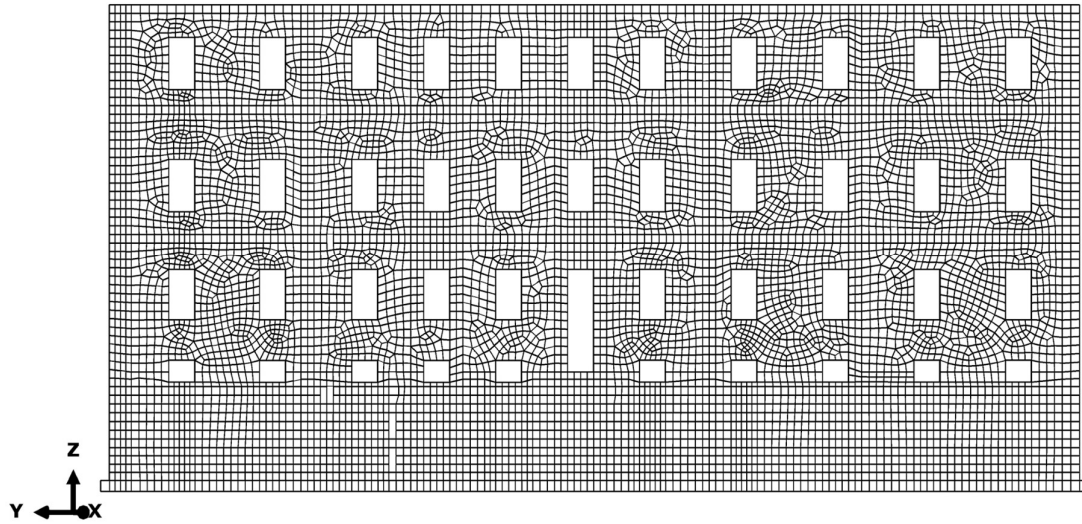


*Figure 5.29. Model mesh of the CNORTH facade*

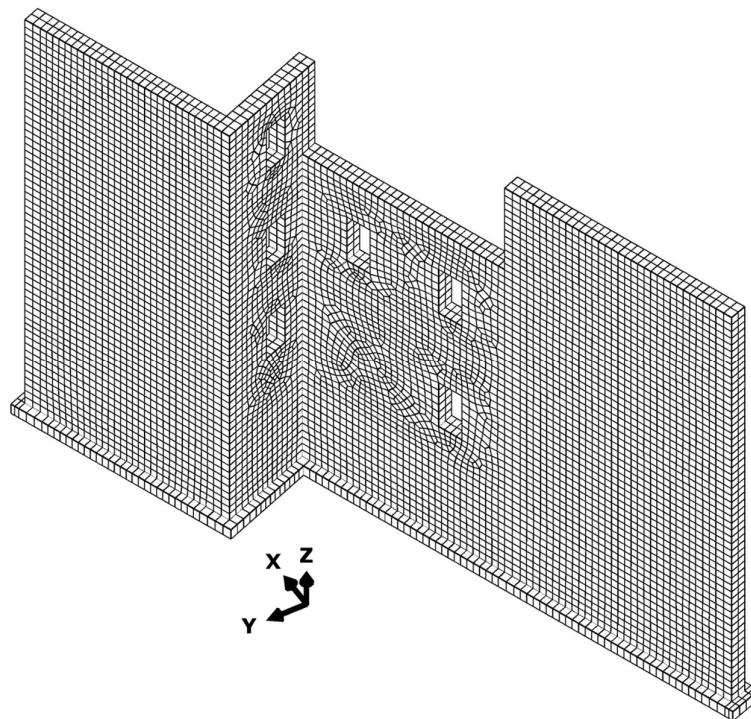


*Figure 5.30. Model mesh of the WEST facade*

## 5.2.2 Boundary conditions

### 5.2.2.1 Slab constraints

As readily apparent, in contrast to the original planimetry of the building, the model geometry does not consider explicitly internal walls, roofs or slabs. This decision was taken to reduce computational costs, geometrical modelling time and to simplify the overall building model, avoiding the adoption of uninformed or baseless assumptions: for example, as no experimental tests on the materials were performed, it is difficult to establish the out-of-plane stiffness of the slabs to avoid having unrealistic bending in the model.

As also seen in the literature review of section 3.2, the presence of roofs or internal slabs and walls is seldom considered, in most cases conservatively assuming that these elements provide no stiffness to the structure, which is realistic if the slabs or roofs are built of wood and internal bearing walls are not present. And while in Palazzo Campana the roofs are indeed wooden, on the other hand, from in-situ inspections and the next Figure 5.31 it is verified that the slabs are assembled as masonry vaults with metal tendons, that connect the walls and limit the out-of-plane displacements of the facades.



Figure 5.31. Halls of Palazzo Campana, showing vaulted slabs with metal tendons

With this information, a rigid floor behavior for the slabs can be reasonably assumed. The rigid floor in numerical modelling, especially in seismic analyses, is commonly integrated with a diaphragm constraint between the nodes of the perimetral elements to the slab. In this case, these elements are highlighted in red in the next Figure 5.32, corresponding to the portions of the facades at the level of the slabs. To model the diaphragm constraint in ABAQUS several alternatives are available: from *kinematic coupling* to *multi-point coupling* and *equation* constraints.

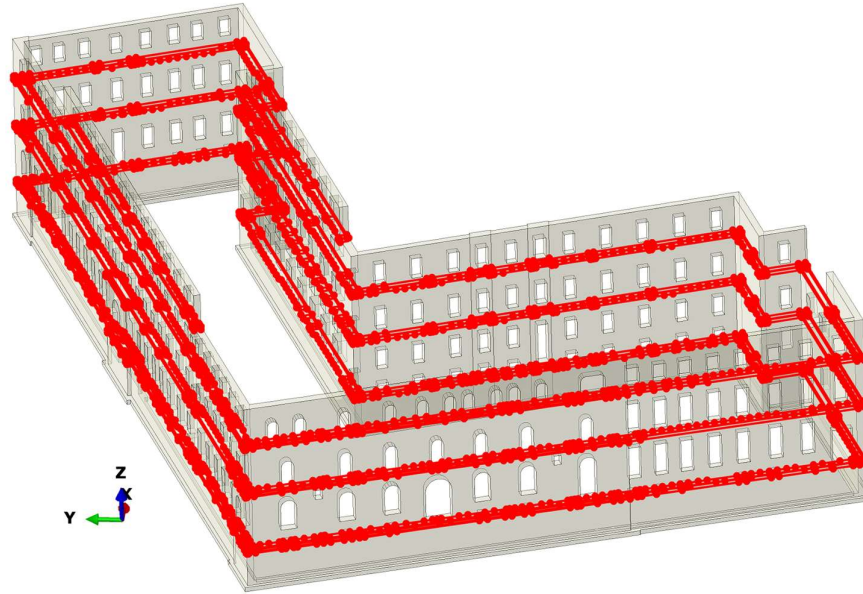


Figure 5.32. Portion of the facades at the level of the slabs

As an example, a *kinematic coupling* constraint of the nodes at the level of the last floor slab is displayed in the figure below, in which ABAQUS shows yellow lines to indicate that the nodes are connected by means of the constraint. Nevertheless, after running a preliminary model with this type of coupling it was verified that the alternative was computationally heavy.

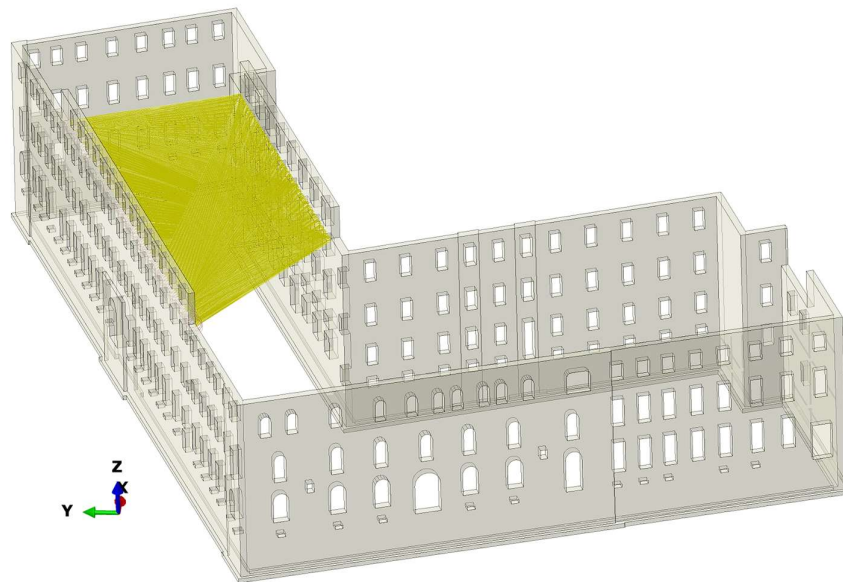


Figure 5.33. Diaphragm constraint for the last floor of the building model

The second alternative is analogous, yet instead of coupling two node sets simultaneously, it couples one node set with one reference point. This is the *equation* constraint, which equals the displacements of these two actors by configuring a simple equation on the degrees of freedom of the nodes. The concept is to equal the in-plane



displacements of the nodes to simulate the rigid action of the slab. The alternative proved to be faster than the *kinematic coupling*, but still computationally expensive. In this case, it was witnessed that the out-of-plane displacements of the facades at the level of the slabs were slight, in the U1 direction (X in the previous figures) lower than the millimeter and in the U2 direction (Y in the previous figures) in the order of one millimeter. Seeing the trivial nature of these out-of-plane displacements, a further simplifying assumption was adopted to improve the run-times of the models, especially the CDP elasto-plastic ones which have the longest computational times: pinned constraints in U1 and U2 were imposed for the facades only at the level of the slabs. The roof, being built with wooden materials, was left unpinned on the model to ignore its contribution to the lateral stiffness. For all the facades, the vertical displacements (in the U3 direction, Z in the previous figures) were never constrained, to allow for the building to deform with the settlement trough. This may seem contradictory, because it is implied that the rigid slabs have no contribution to the vertical stiffness. In the reality, it is expected that the slabs do help the building oppose the settlements, however, the magnitude of this contribution is difficult to assert without complete material and structural in-situ investigations and therefore, it is disregarded.

#### 5.2.2.2 *Subsidence simulation*

Inspired by the conditions of the isolated facade laboratory tests conducted by Giardina et al. (2013), and half-scale building models tested by Dalgic et al. (2023), while scaling up the scope to include the entire Palazzo Campana building, the greenfield steady state settlement trough is applied to the top face of a supporting layer, visible in the next Figure 5.34 as an extended rectangular mat of negligible stiffness on top of which the building rests, that acts analogous to the “settlement apparatus” of Dalgic et al. or the “steel profile for the settlement application” of Giardina et al., by simply providing a surface on top of which the facades are built and remain independent, unattached from said surface; for then the support to be deformed to fit the imposed settlement trough. In the laboratory tests the facades are able to separate from the supporting element, especially if they have a near elastic behavior (in Dalgic et al.’s studies witnessed in facades with relatively light loads, few openings or with rigid floors) as Giardina et al. and Dalgic et al. show with their results in Figure 5.35 a) and b), respectively; while they are more prone to follow compliantly the settlement trough when cracking models are considered (in Dalgic et al.’s studies, severe cracking was noticed for buildings with relatively high loads, high area of voids or with flexible joist floors) as the authors show with their results in Figure 5.35 c) and d), respectively.

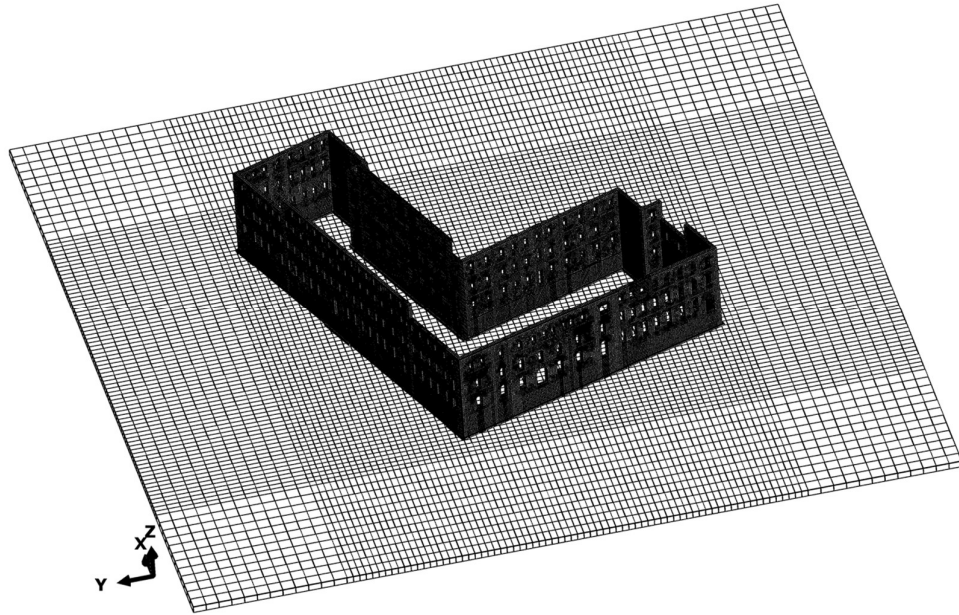


Figure 5.34. Mesh model of the facades on top of a supporting layer for the subsidence application

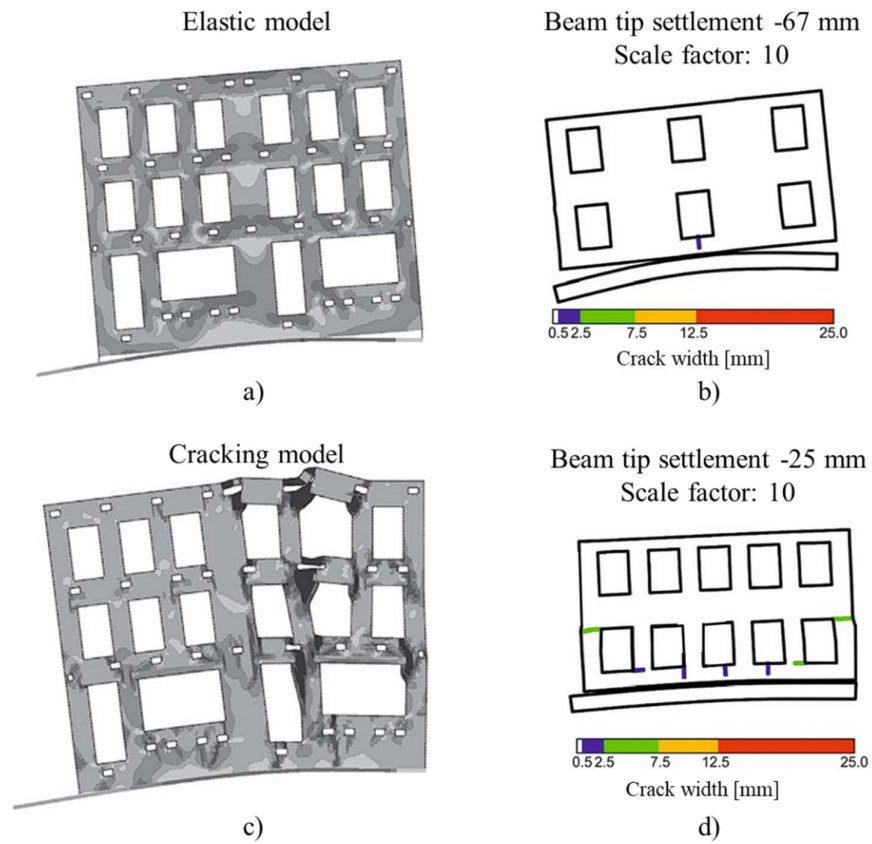


Figure 5.35. Side by side numerical and laboratory masonry facade models from: Giardina et al. (2013) a) elastic and c) cracking models; and Dalgic et al. (2023) b) lower versus d) higher area of openings

In the current thesis, given that the supporting layer and the building are modelled in ABAQUS as two different parts, these two must enter in contact from the activation of the building to the onset and termination of the settlement application. The contact interaction is here configured with penalties both in the tangential and normal directions. For the first, a friction coefficient of 0.50 is defined, equal to 2/3 the friction angle of the soil (typical value for soil – concrete friction). For the second, a “hard” contact pressure-overclosure relation with a penalty constraint enforcement method is adopted, allowing for separation after contact and setting a default contact stiffness with an unitary scale factor, to allow ABAQUS to calculate the *penalty stiffness* as 10 times a representative underlying element stiffness (Dassault Systemes, 2024), while the *clearance at which the contact pressure is zero* is defined equal to 0.1 mm, meaning that a fictitious penetration of 0.1 millimeters is allowed to soften the contact interaction and promote easier numerical convergence. The accuracy of the model was not sacrificed with these simplifying assumptions, as different comparisons were performed with preliminary models having a perfect “hard” contact pressure-overclosure relation, and the results showed that with the softened penalty relations the penetration was negligible, and the building damage risk remained equal for both cases.

With this methodology, the facades’ foundation is not forced to comply with the greenfield settlement trough, and the stiffness of the structure can act opposing the subsidence, obtaining more applicable damage risk estimates from the same uncoupled models.

### 5.2.3 Material properties

Realizing the importance of modelling the building with an elasto-plastic constitutive behavior from the literature cases discussed in Chapter 3.2 and in response to the lack of experimental investigations in Palazzo Campana (PNCA43), based on the literature review submitted under the heading 3.2.2 and closely regarding the Italian NTC 2018 Chapter 8, Table C8.5.I (Ministero delle Infrastrutture e dei Trasporti, 2018), the next Table 5.5 and Figure 5.36 present the proposed range of values for the estimation of the elasto-plastic parameters of the building in accordance with the *Concrete Damaged Plasticity* (CDP) model, the curve CDP MIN referring to the most pessimistic and the curve CDP MAX referring to the most optimistic expected behaviors of the material, with an artificial CDP MEAN curve created as follows:

- 1) For the elastic regime, the arithmetic average of the extreme yield strengths (mean of MIN, MAX values of both  $\sigma_c$  and  $\sigma_t$ ) is obtained, as well as the mean value of the elastic moduli (MIN, MAX). With these values, the inelastic crushing strain  $\varepsilon_c^{in}$  and the direct cracking strain  $\varepsilon_t^{ck}$  are simply obtained by computing:

$$\varepsilon_c^{in} = \sigma_{c,avg}/E_{0,avg} \quad (5.1)$$

$$\varepsilon_t^{ck} = \sigma_{t,avg}/E_{0,avg} \quad (5.2)$$

- 2) In the plastic regime, since the data is generally given in terms of total strains ( $\varepsilon_c$  and  $\varepsilon_t$  must be known); first, the elastic strains corresponding to the undamaged material must be calculated as:

$$\varepsilon^{el} = \sigma/E_{0,avg} \quad (5.3)$$

With  $\sigma < \sigma_{t,avg}$  or  $\sigma > \sigma_{c,avg}$ . Then, the inelastic and the cracking strains to input in the CDP model are the total strains minus the elastic strains calculated above:

$$\varepsilon_c^{in} = \varepsilon_c - \varepsilon_c^{el} \quad (5.4)$$

$$\varepsilon_t^{ck} = \varepsilon_t - \varepsilon_t^{el} \quad (5.5)$$

This results in:

Table 5.5. Proposed elasto-plastic parameters for the Palazzo Campana masonry building

	CDP MIN	CDP MAX	CDP MEAN
Elasticity			
Young's [MPa]	1500	2500	2000
Poisson's ratio	0.20	0.20	0.20
Concrete damaged plasticity			
Plasticity			
Dilation angle [°]	10.0	20.0	15.0
Eccentricity	0.10	0.10	0.10
$\sigma_{b0}/\sigma_{c0}$	1.16	1.16	1.16
K	0.667	0.667	0.667
Viscosity parameter	0.002	0.002	0.002
Compressive behavior			
Yield stress 1 [MPa]	2.40	3.80	3.10
Yield stress 2	1.90	3.40	2.65
Yield stress 3	1.90	3.40	2.65
Yield stress 4	1.80	2.80	2.30
Inelastic strain 1	0	0	0
Inelastic strain 2	0.005	0.005	0.005
Inelastic strain 3	0.01	0.01	0.01
Inelastic strain 4	0.10	0.10	0.10

	CDP MIN	CDP MAX	CDP MEAN
<b>Tensile behavior</b>			
Yield stress 1 [MPa]	0.08	0.17	0.13
Yield stress 2	0.0005	0.0005	0.0005
Yield stress 3	0.0005	0.0005	0.0005
Cracking strain 1	0	0	0
Cracking strain 2	0.005	0.007	0.006
Cracking strain 3	0.10	0.10	0.10
<b>Tension damage</b>			
Damage parameter 1	0	0	0
Damage parameter 2	0.95	0.95	0.95
Cracking strain 1	0	0	0
Cracking strain 2	0.005	0.007	0.006

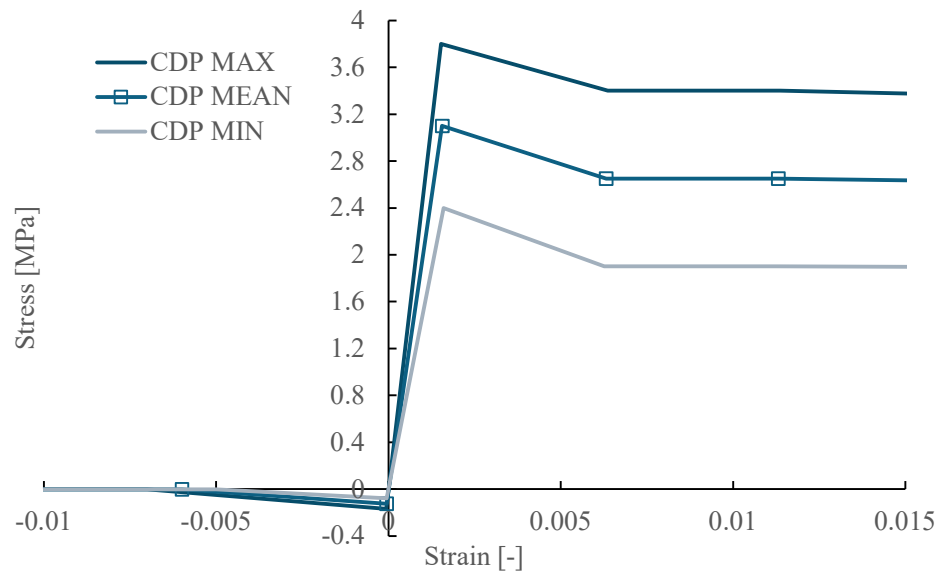


Figure 5.36. Stress-strain proposed curves for the Palazzo Campana masonry building

It must be remarked that here, however, the partial coefficients mandated by the Italian construction code NTC Chapter 8 are not applied, since the interest of the present effort is neither the design of a structural intervention nor the safety assessment of the building. The objective is to estimate the building damage risk due to tunnelling, defining a range of possible characteristic behaviors that the structure may reveal during the tunnel excavation. For this, the unaffected characteristic parameters are used. Once the decision is made to reinforce any part of the building, more specific, local analyses must be carried out on structural macro-elements (Ministero delle Infrastrutture e dei Trasporti, 2018), using the respective partial coefficients for the actions, materials, and resistances, accordingly with the Knowledge Level of the existing structure.

### 5.2.4 Stages

The model stages start with the building's immediate activation on top of the supporting layer (that remains fixed), not considering construction stages. With it, the initiation of the structure's body forces takes place, applying the acceleration of gravity in Z direction, computed with the density of the material equal to  $2375 \text{ kg/m}^3$  (resultant of increasing the original density of  $1900 \text{ kg/m}^3$  by 25% to indirectly account for the dead weight of the floors, possible inner partitions, fixtures, fittings and the roof (Yiu, 2018; Amorosi & Sangirardi, 2021), neglecting live loads) to obtain the weight of the perimetral facades. The successive and final stage is the application of the greenfield steady state settlement trough on top of the supporting layer. These settlements are varied in correspondence to the greenfield volume loss models VLMAX, VLMEAN and VLMIN, previously obtained from the parametric analyses in free field conditions (see 5.1.6 for more information).

### 5.2.5 Parametric analyses

Uncertainties once again plague the prediction of the real behavior of Palazzo Campana once it is subjected to the settlements induced by the Metro-Line 2 of Torino tunnel excavation. Many of these uncertainties were tackled before deterministically, including the geometrical properties of the model, the contribution of the internal slabs and walls, for all making reasonably conservative decisions. The constitutive properties of the masonry, however, in response to the lack of in-situ experimental tests here are evaluated through parametric analyses based on the CDP models proposed before in Table 5.5. Starting from the greenfield volume loss models, 18 permutations are generated between these three models and six different constitutive behaviors, as illustrated in Figure 5.37.

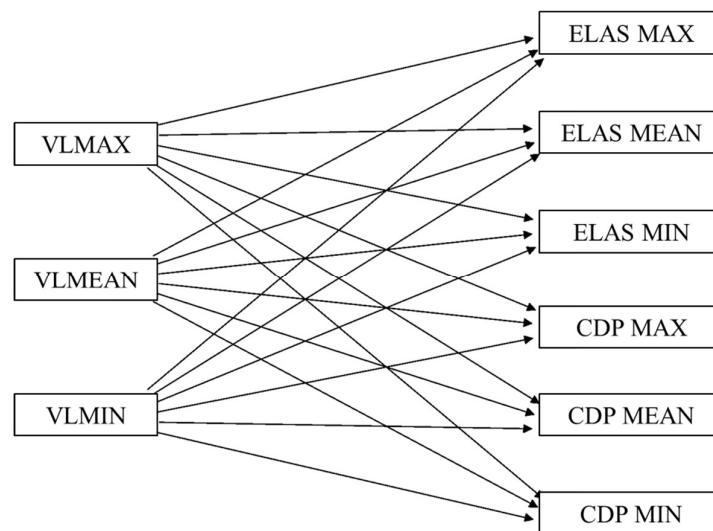


Figure 5.37. Workflow of the parametrical analyses for the uncoupled building model

The nomenclature is further detailed in Table 5.6. As an example, a model could be named VLMAX\_ELAS\_MIN, meaning that the building is subjected to the worst subsidence found in greenfield conditions (VLMAX) and it has a masonry constitutive model corresponding to the softest elastic model (ELAS\_MIN, with Young’s modulus of 1500 MPa).

*Table 5.6. Nomenclature for the uncoupled building models*

Model	Description
VLMAX	The subsidence is the most pessimistic (highest settlement volume loss) found from the greenfield parametric analyses.
VLMEAN	The subsidence is the average case scenario found from the greenfield parametric analyses (settlement volume loss of the reference REF model).
VLMIN	The subsidence is representative of one of the most optimistic scenarios found from the greenfield parametric analyses (settlement volume loss of the model with the jet grouting umbrella).
ELAS MAX	The building adopts the stiffest elastic masonry constitutive model (from Table 5.5), with a Young’s modulus of 2500 MPa.
ELAS MEAN	The building adopts an average elastic masonry constitutive model (from Table 5.5), with a Young’s modulus of 2000 MPa.
ELAS MIN	The building adopts the softest elastic masonry constitutive model (from Table 5.5), with a Young’s modulus of 1500 MPa.
CDP MAX	The building adopts the strongest and stiffest CDP masonry constitutive model from Table 5.5.
CDP MEAN	The building adopts the average CDP masonry constitutive model from Table 5.5.
CDP MIN	The building adopts the weakest and softest CDP masonry constitutive model from Table 5.5.

### 5.3 Coupled models: soil – structure interaction

#### 5.3.1 Geometrical model, discretization

Acknowledging the initial requirements of Infratrasporti.To S.r.l., which constrain the contractors to provide a jet grouting umbrella to minimize the settlements induced by the tunnelling activities below Palazzo Campana, and also keeping in mind that the interaction models are significantly more demanding in computational terms than previous models, both increasing the run time and absorbing more CPU and RAM resources, the decision is made to compute only the combined VLMIN with ELAS MAX and CDP MAX models. The VLMIN, in greenfield called JET model, precisely corresponds to the situation in which the jet grouting umbrella is present within the soil, being this the most realistic representation of the real tunnelling problem once the civil work starts. The elastic ELAS MAX and elasto-plastic CDP MAX constitutive behaviors are solely for the building model, before detailed under heading 5.2.3. The assembly of the model is displayed in the Figure 5.38 and Figure 5.39 below.

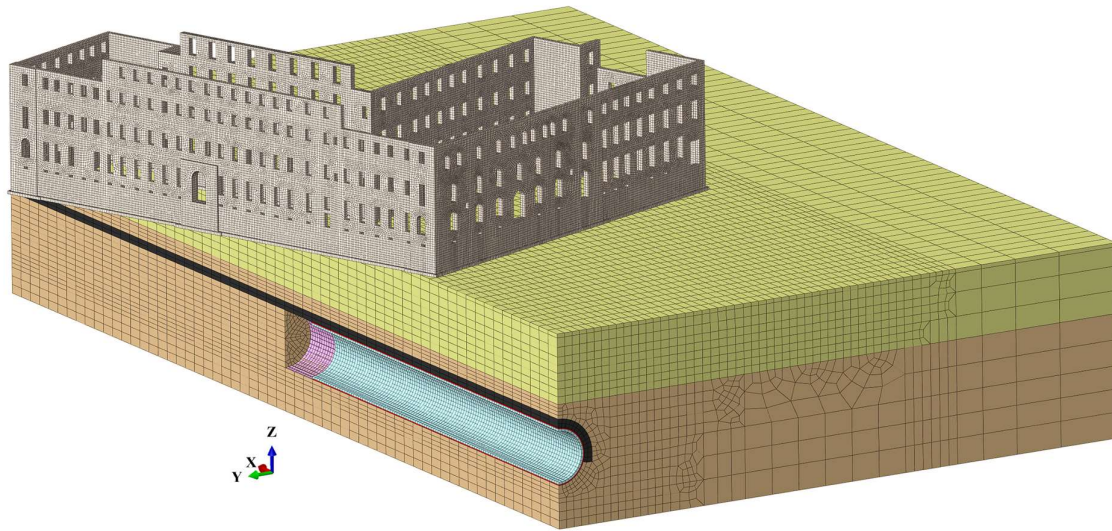


Figure 5.38. Jointed coupled model (assembly), featuring the parts of the soil with the jet grouting improved zone, shield, liners plus grout and the building in interaction

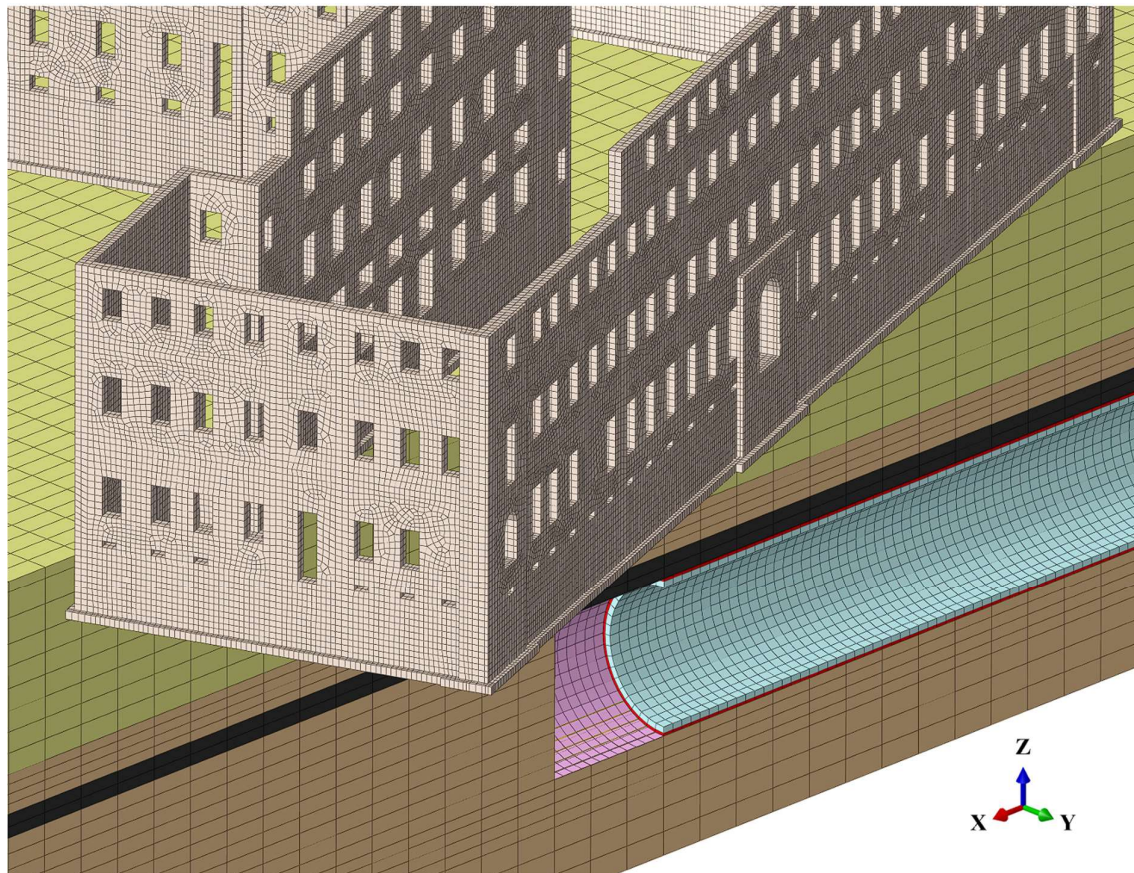


Figure 5.39. Detail of the coupled model



### 5.3.2 Boundary conditions

Apart from the boundary conditions detailed for the model of the excavation in section 5.1.2 and for the model of the building in section 5.2.2, a contact interaction is activated between the Top face of the soil cuboid and the bottom face of the building's foundation, configured with penalties both in the tangential and normal directions. For the first, a friction coefficient of 0.50 is defined, equal to  $2/3$  the friction angle of the soil (typical value for soil – concrete friction). For the second, a “hard” contact pressure-overclosure relation with a penalty constraint enforcement method is adopted, allowing for separation after contact and setting a default contact stiffness with an unitary scale factor, to allow ABAQUS to calculate the penalty stiffness as 10 times a representative underlying element stiffness (Dassault Systemes, 2024), while the clearance at which the contact pressure is zero is defined equal to 0.1 mm, meaning that a fictitious penetration of 0.1 millimeters is allowed to soften the contact interaction and promote easier numerical convergence. The accuracy of the model was not sacrificed with these simplifying assumptions, as different comparisons were performed with preliminary models having a perfect “hard” contact pressure-overclosure relation, and the results showed that with the softened penalty relations the penetration was negligible, and the building damage risk remained equal for both cases.

### 5.3.3 Material properties

The material properties of the soil correspond to those of the JET model, which combines the ITO constitutive parameters for the natural stratigraphy (see 5.1.3.1) and the consolidated jet grouting umbrella on top of the crown of the tunnel (see 5.1.3.4). For the building, the ELAS MAX and CDP MAX constitutive behaviors are utilized, before detailed under heading 5.2.3.

### 5.3.4 Stages

After the geostatic step, that has the same characteristics listed in section 5.1.4, the immediate activation of the building on top of the soil is performed, not considering construction stages. With it, the initiation of the structure's body forces takes place, applying the acceleration of gravity in  $-Z$  direction, computed with the density of the material equal to 2375 kg/m<sup>3</sup> (resultant of increasing the original density of 1900 kg/m<sup>3</sup> by 25% to indirectly account for the dead weight of the floors, possible inner partitions, fixtures, fittings and the roof (Yiu, 2018; Amorosi & Sangirardi, 2021), neglecting live loads) to obtain the weight of the perimetral facades. Simultaneously, the top layer of the soil until 4.8 m depth is removed and a pressure equal to 60 kPa is activated on the new Top face. This pressure represents the weight of the surrounding buildings (10 kPa per floor of buildings with six floors, including the underground cellars), all assumed to have foundations at the 4.8 m mark and to occupy this entire plane, disregarding conservatively the lower loads of roads and open spaces in the vicinities. After these two steps and considering the JET greenfield model is the base of the coupled interaction scheme, the step-by-step excavation procedure described in 5.1.5 is here also simulated.

## Chapter 6

### Results

#### 6.1 Greenfield models

In this chapter the greenfield steady-state results of the numerical simulations are revealed, with the aim of estimating the effects of the tunnel advancement in free field conditions (surface structures are disregarded), comparing them alongside analytical and empirical formulae to validate their reliability. Afterwards, the goal is to conduct parametrical analyses to observe the change in the surface settlements induced by the excavation, according to the variation of different model parameters. With these parametric results, three curves called greenfield volume loss curves are chosen based on the most positive, average, and most negative observed scenarios (in function of the settlement volume loss); and these will be later used for the building uncoupled and soil – structure interaction models. The transversal and longitudinal troughs, as well as the transversal horizontal displacements and strains, are given at the depth of the building's foundation equal to 4.8 m, consistently with the model definition in which the soil elements above this depth were removed and replaced with an equivalent distributed load. For the longitudinal trough, two transversal section cuts are positioned and named “Cutterhead passes the section” and “Tail passes the section.” By section it refers to the plane A-A of the next Figure 6.1, that records in every excavation step the positions of the nodes, stresses, strains, and so forth, while the TBM is cruising through.

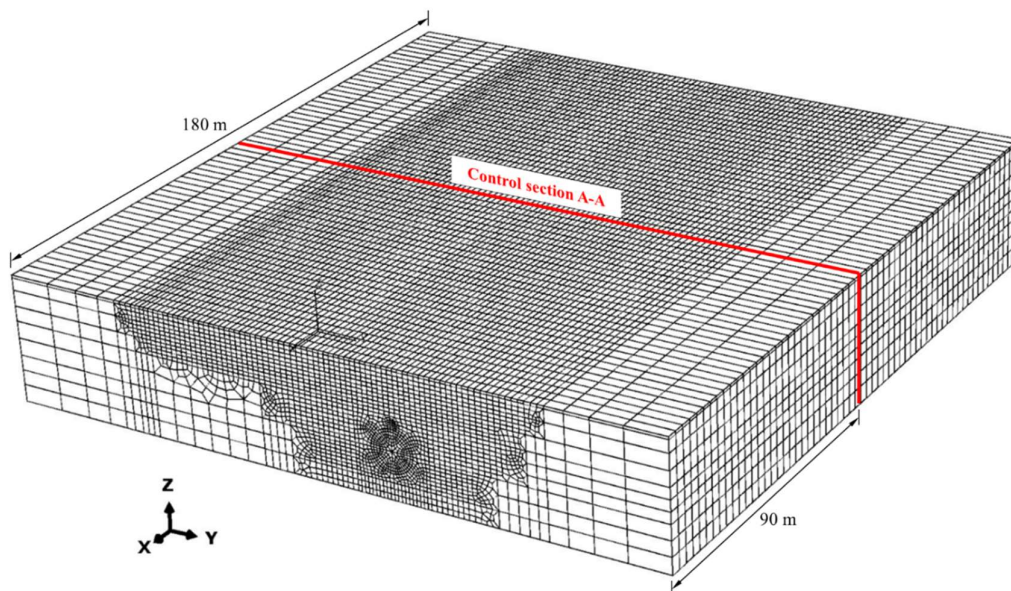


Figure 6.1. Control section A-A for the longitudinal troughs

### 6.1.1 The Reference (REF) model and related closed-form solutions

As a reminder of Figure 5.18, the Reference model is formulated under the following assumptions:

- 1) Grout stiffness (GS) taken after the mean curve (GSMEAN) from Figure 5.11 that assigns the grout average stiffness parameters in time.
- 2) Grout injection pressure (GP) of 200 kPa (GP200).
- 3) Steering gap (GAP) of 4 cm (GAP4).
- 4) Face pressure (FP) fully applied (FP100)
- 5) Ground conditions (SOIL) according to Infra.To (ITO), registered in the past Table 5.2.

The FEM results for the longitudinal subsidence are presented in the next Figure 6.2, as well as the cumulative probability function, with a inflection distance  $i_x$ , defined equal to  $i_y = 12.5$  m (the value it takes in the transversal trough, seen further below). Yet, it is verified that the best fit occurs for  $i_x = 10.0$  m, confirming what authors Uriel & Sagaseta (1989) declared about inflection distances being different in the longitudinal and transversal directions, especially for granular soils.

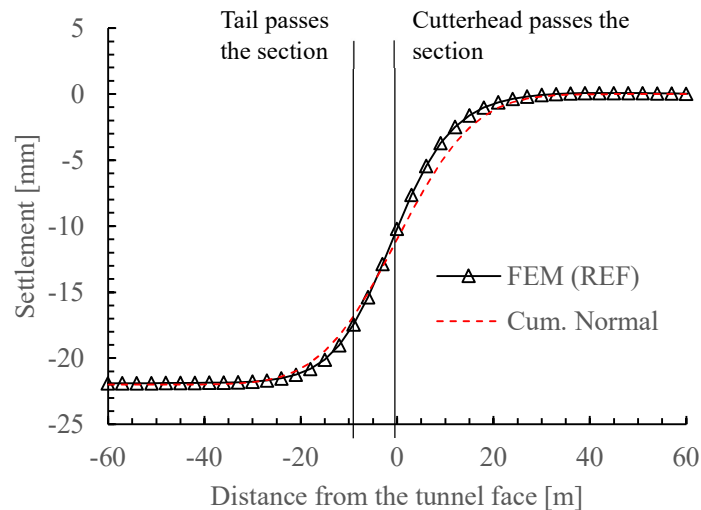


Figure 6.2. REF model. Longitudinal trough for FEM results and with the cumulative distribution

The curve above only presents the vertical displacements for nodes at the level of the foundation. For nodes at the crown and invert, highlighted in Figure 6.3, the curves of Figure 6.4 show the displacements as the TBM advances across section A-A. In general, it is observed that the behavior of these nodes is in agreement, both in terms of order of magnitude and shape of the curves, with previous numerical studies performed by Kasper & Meschke (2004), Kavvadas et al. (2017), and Epel et al. (2021).

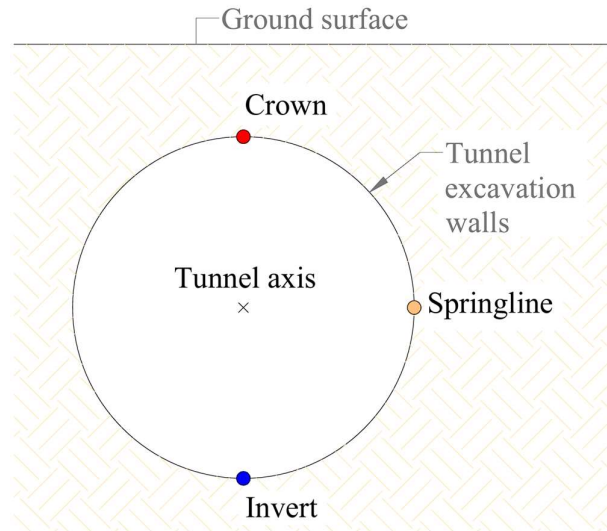


Figure 6.3. Location of the nodes for the plot of the longitudinal trough

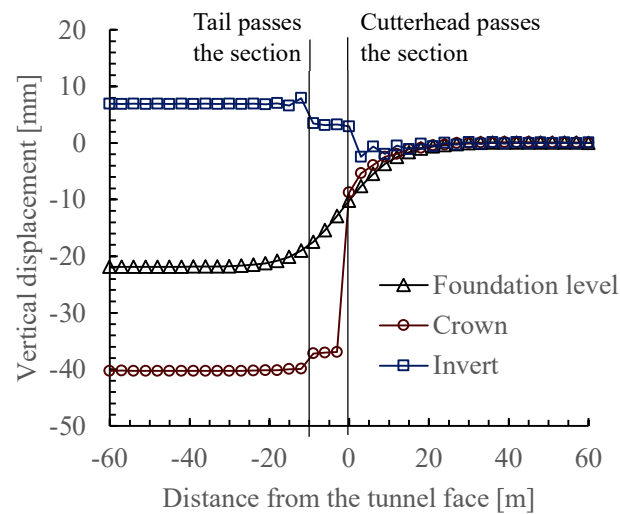


Figure 6.4. REF model. Longitudinal trough for the nodes at the surface, crown and invert

The curves in Figure 6.5 below are companion of the longitudinal profile at the level of the foundation, displaying the transversal troughs at the different moments of the excavation. The most prominent curve with 22 mm of maximum settlement represents the steady state after the excavation. It is reminded that here no consolidation process was considered due to the drained characteristics assumed for the coarse stratigraphy and therefore, the permanent deformations correspond to those immediately after the excavation is completed and the two-component grout has reached its highest stiffness.

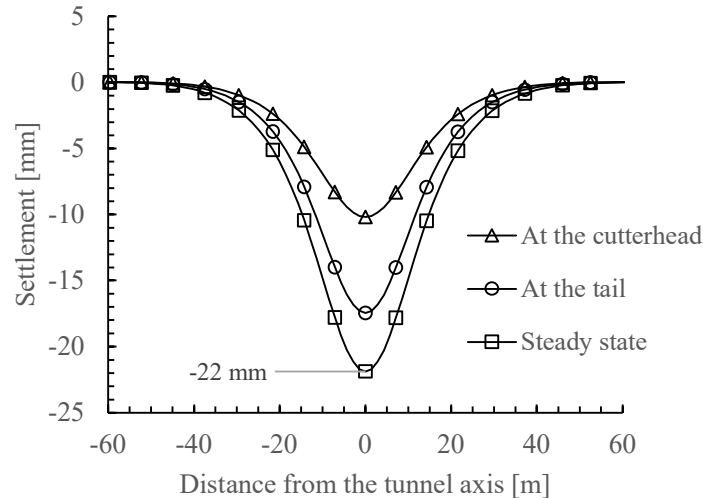


Figure 6.5. REF model. Transversal trough in FEM for different moments of the excavation

With the goal of validating the reliability of the numerical results, at a minimum in their order of magnitude, comparisons are pursued against the empirical and analytical methods described at the beginning of the document, under the section 2.3. It is strongly recommended to revise the equations posed in that section as here they will be merely cited. The results are shown in Figure 6.64. For simplicity for all the formulations, except for the one of Loganathan & Poulos that will be analyzed with higher detail, the depth of the tunnel  $z_0$  is set equal to 21.2 m subtracting the level of the foundation. This is still a conservative assumption since for low overburdens higher surface displacements (and strains) are generated. Furthermore, because most of these methods are projected for isotropic, homogeneous materials, the characteristics of the entire soil are regarded to be those of the dry Geotechnical Unit 2 (ITO GU2 of Table 5.1), which represents a soil of variable degree of cementation between 0 to 25% and Poisson's ratio of 0.30. Even still, the purpose of the comparison is not breached as the order of magnitude of the settlements is not expected to change with these simplifications.

For the normal distribution (Gaussian curve) the value of the trough half-width parameter  $i_y$  is equal to 12.5 m, calculated with Equation (2.5) knowing the area of the settlement trough is  $A_s = 0.69 \text{ m}^2$  (and so, the volume of the settlement trough per meter of advancement is  $V_s = 0.69 \text{ m}^3/\text{m}$ ) and the maximum settlement  $s_{v,max}$  is 22 mm. The empirical Gaussian curve obtained with Equation (2.2) is in good agreement with the numerical results, if only at the hogging zones the settlements seem to be slightly underestimated by the empirical formula.

Passing to Loganathan and Poulos' semi-empirical proposal, the Equation (2.10) for the subsurface settlements, at a depth  $z$  and with a tunnel axis at  $z_0 = 26 \text{ m}$ , is employed to obtain an accurate curve at the level of the foundation ( $z = 4.80 \text{ m}$  below the ground surface), not readily noticeable in the figure below as it almost perfectly overlaps with the numerical results. This ideal overlap is, nevertheless, product of the calibration of the GAP parameter. First, it is assumed that the soil extrusion at the front of the excavation  $U_{3D}^*$  is null because the EPB-TBM can maintain the supporting pressure at

the face of the tunnel. Second, the value of the overcut (or workmanship)  $w$  is set equal to 37 mm in correspondence with the behavior of the node at the crown, between the cutterhead and the tail of the shield in the past Figure 6.4, and the physical *gap* is set equal to the annulus gap of 36 cm (recall Figure 5.8 of the transversal section of the tunnel assembly). It is reminded that Lee, Rowe & Lo (1992) suggested reducing this value to its 7~10% fraction if mono-component grout backfilling was present. However, since in the numerical models the properties of the two-component grout were emulated, including its high early stiffnesses and near incompressible behavior, the reduction proposed by the authors could be an underestimation. It is in this way that the GAP parameter is calibrated in function of the *gap* distance that depends on the two-component grout limited shrinkage, setting the final value of  $GAP = 0.75\% \cdot gap + w = 40 \text{ mm}$  to provide the best fit. Notice here the reduction of 0.75% is almost ten times lower than the inferior bound proposed by Lee, Rowe & Lo, in line with the much stiffer displacement-locking action of the modelled grout.

Starting with the analytical methods, Equation (2.13) regarding Sagaseta's (1987) method for the transversal settlement estimation is used. For this, the volume of the settlement trough per meter of advancement is once again  $V_s = 0.69 \text{ m}^3/\text{m}$ . In agreement with another study carried out in a neighboring city to Torino, Milan (Migliazza, Chiorboli, & Giani, 2009) for one of the extensions of the Metro-Line 1, this method underestimates the maximum settlement of the predicted trough with numerical modelling. In this case also, it shows an overall wider trough in comparison with the rest of the predicted curves.

Lastly, the settlements are also predicted with Verruijt & Booker's (1996) method. Here, to feed Equation (2.14) the relative uniform convergence  $\varepsilon$  is calculated with Equation (2.17) and is equal to 0.31% while the ovalization is equal to 0.80%, calculated as the ratio between the maximum value of the radial displacement of the tunnel walls and the radius of the tunnel (González & Sagaseta, 2001). Here the authors' curve overestimates the maximum settlement, also in agreement with Migliazza's et al. (2009) previous observations.

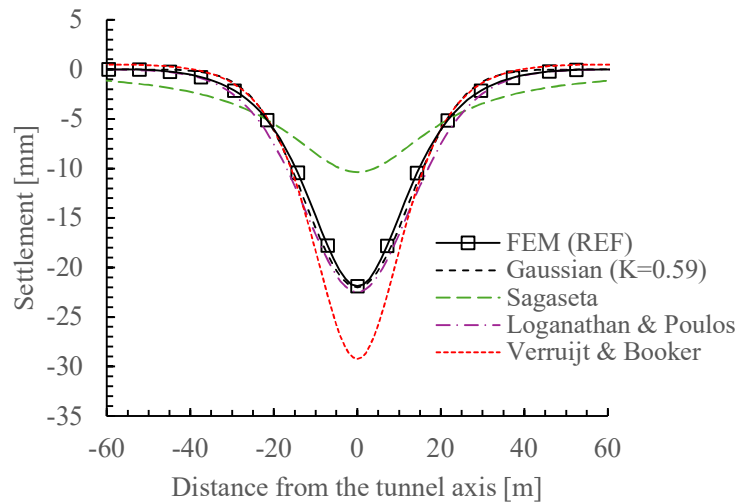


Figure 6.6. REF model. Transversal trough with FEM and empirical and analytical formulations

The horizontal displacements and strains are plotted in the next two figures, both for the numerical outputs and the empirical approximation proposed by O'Reilly & New (1982) with Equations (2.11) and (2.12). In these  $i_y = 12.5$  m and it is verified that the best fit for the curves is obtained when considering the depth of the tunnel  $z_0$  as 21.2 m subtracting the level of the foundation, consistently with the former assumptions.

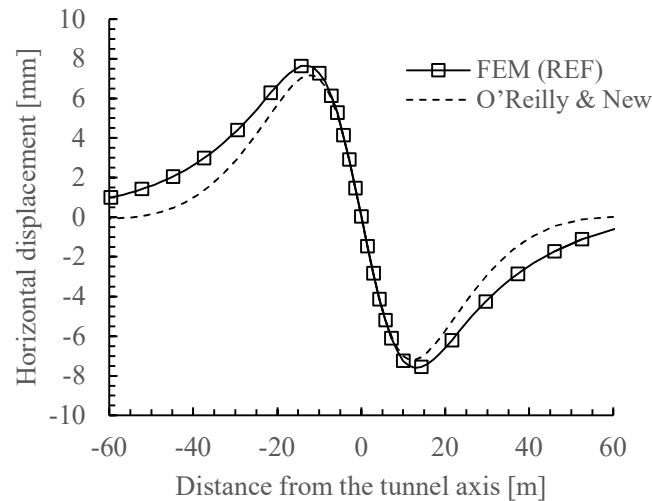


Figure 6.7. REF model. Horizontal displacements with FEM and O'Reilly & New's formulation

Specifically in this next Figure 6.8, if O'Reilly & New's method is used, compared against the numerical results the value of the strains appears heavily overestimated in the hogging zones. This is of paramount importance if local strains are used when evaluating masonry building damage risk with Burland's (1995) damage category charts because in these, for high values of the horizontal strains, high damage categories are predicted. In this case, therefore, O'Reilly & New's method proves to be conservative if not overly conservative.

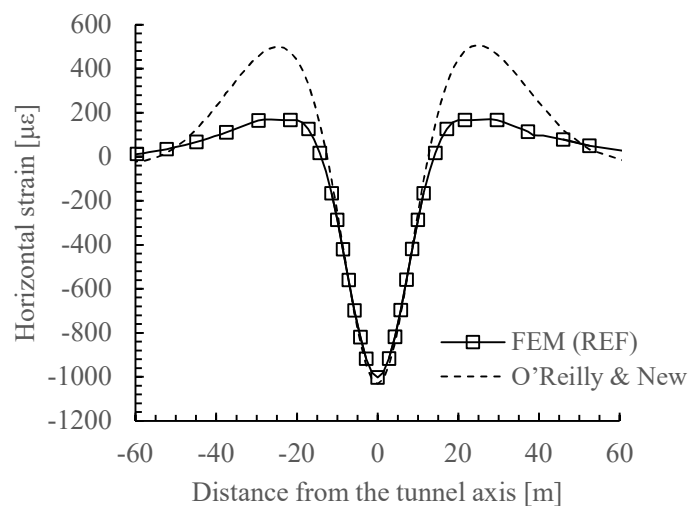


Figure 6.8. REF model. Horizontal strains with FEM and O'Reilly & New's formulation

### 6.1.2 Parametric analyses

As a response to the uncertainties surrounding the Metro-Line 2 of Torino project, parametric analyses focused on the excavation process and ground conditions were performed in the framework described in the past 5.1.6 section.

#### 6.1.2.1 Grout stiffnesses (GS)

First, the grout stiffnesses were varied according to the GS<sub>MAX</sub>, GS<sub>MEAN</sub> and GS<sub>MIN</sub> grout time-dependent curves studied under section 5.1.3.3, for which the GS<sub>MAX</sub> represents the stiffer and GS<sub>MIN</sub> the softer type of two-component grout; maintaining all the other parameters equal to those of the REF model. After a swift revision of the next figures, the change from one two-component grout constitutive behavior to the other yields negligible differences in the settlements.

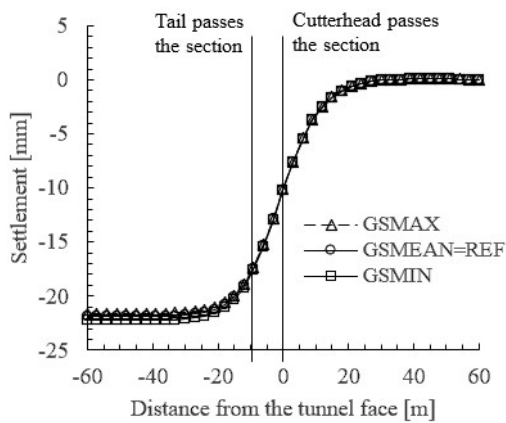


Figure 6.9. GS models. Longitudinal trough

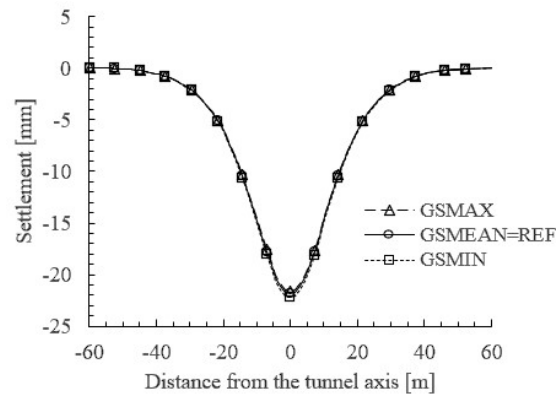


Figure 6.10. GS models. Transversal trough

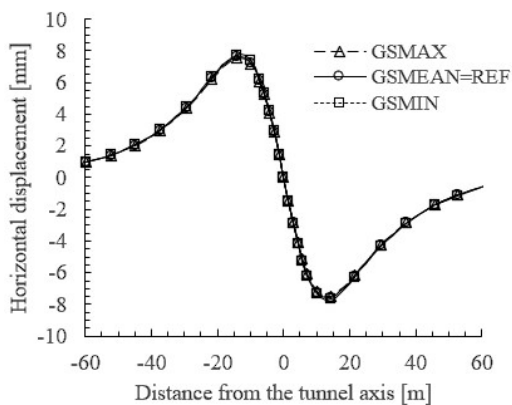


Figure 6.11. GS models. Horizontal displacements

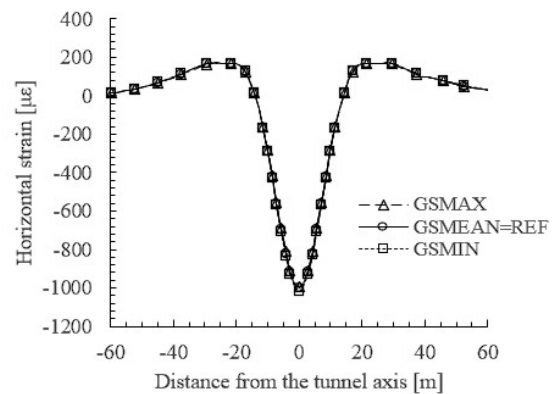


Figure 6.12. GS models. Horizontal strains

These results, in comparison to those of Nikakhtar et al. (2020) who did reported changes in the maximum settlements when varying the grout stiffnesses in time, from softer to stiffer types of grouts, could have two possible justifications: first, the range of grout constitutive models used by the authors is more varied than the one used here,



in their case ranging from 2.5 to 15 MPa for the Young’s modulus at early time of hardening and 10 to 60 MPa for the Young’s modulus after eight hours of curing; while in the present project the values were varied from 1.3 to 2.5 MPa at early hardening and 11 to 25 MPa after eight hours of curing. These shorter ranges may impede witnessing changes from one constitutive model to another; it is here argued, however, that these shorter ranges could be regarded as realistic since they are the product of an in-depth literature study on the real behavior of the two-component grout during laboratory experimental campaigns (see section 3.1.3.3 for the detailed information). The second reason is the inherently different characteristics of both studies. For Nikakhtar’s, the overburden and mechanical properties of the soil were decisively inferior to those of the present thesis, allowing for the immediate changes around the excavation, like the grout stiffening, to more prominently impact the surface settlements.

6.1.2.2 Grout injection pressure (GP)

On top of changing the grout constitutive properties, the injection pressure of the material behind the tail of the TBM’s shield was also varied between 200, 400 and 600 kPa corresponding respectively to the REF, GP400 and GP600 models. In this case again, negligible (or inexistent) changes were witnessed from one model to another.

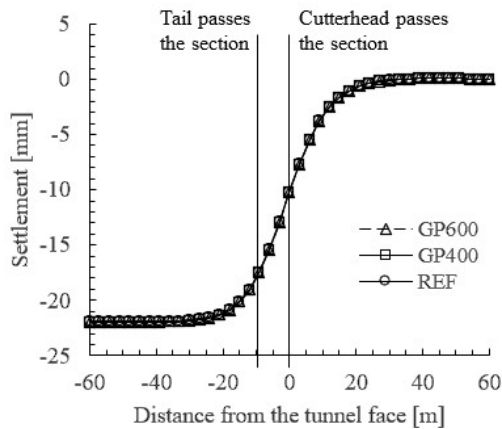


Figure 6.13. GS models. Longitudinal trough

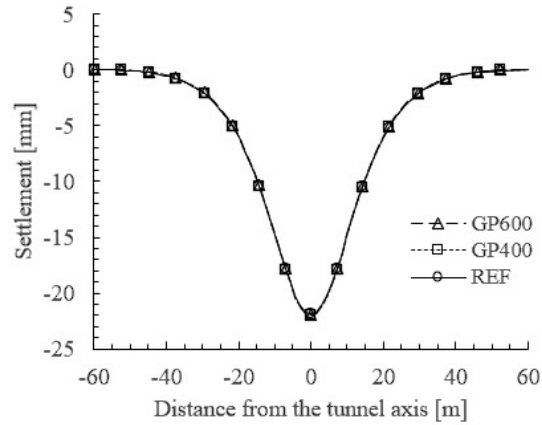


Figure 6.14. GS models. Transversal trough

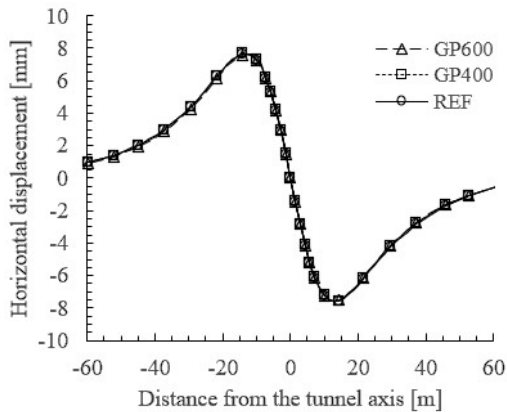


Figure 6.15. GS models. Horizontal displacements

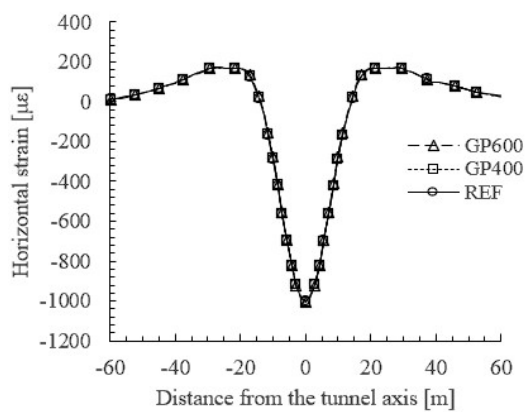


Figure 6.16. GS models. Horizontal strains

These results are, in this case, in agreement with evidence found in the literature. Losacco & Viggiani (2019) reported marginal differences in surface settlements when changing the applied grout pressures from 250 to 400 kPa, as well as Litsas, Sitarenios & Kavvadas (2017) found slight differences when varying the pressures between 200, 400 and 600 kPa. It is here hypothesized that this occurs owing to the limited area in which the grout pressure acts, only the first liner behind the tail, and to the high early stiffness of the grout that by itself counters the enlargement induced by the expanding pressure.

### 6.1.2.3 Steering gaps (GAP)

The next parametric variations were operated for the shield steering gaps, with gaps of 2, 4 and 6 centimeters corresponding to the respective GAP2, REF and GAP6 models. These parametrical analyses were, by far, the most impactful for the basin of subsidence, as clearly apparent from the next figures.

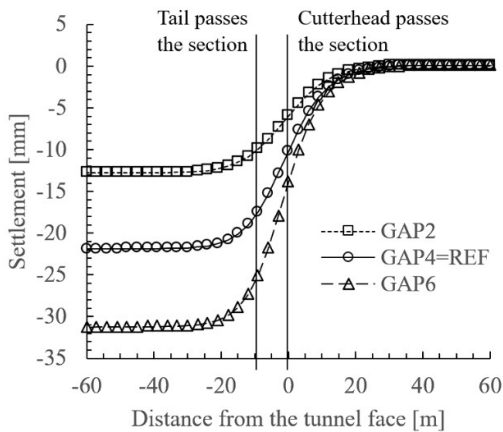


Figure 6.17. GAP models. Longitudinal trough

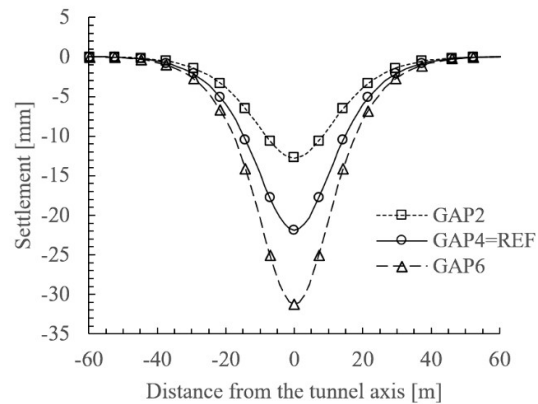


Figure 6.18. GAP models. Transversal trough

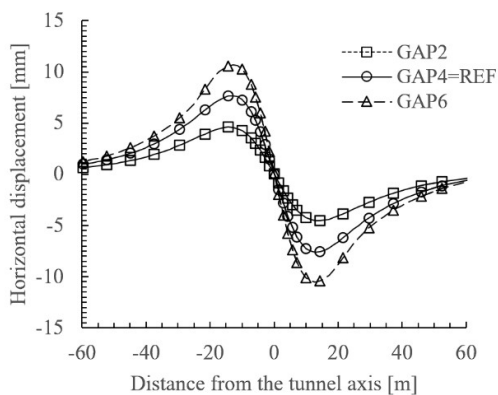


Figure 6.19. GAP models. Horizontal displacements

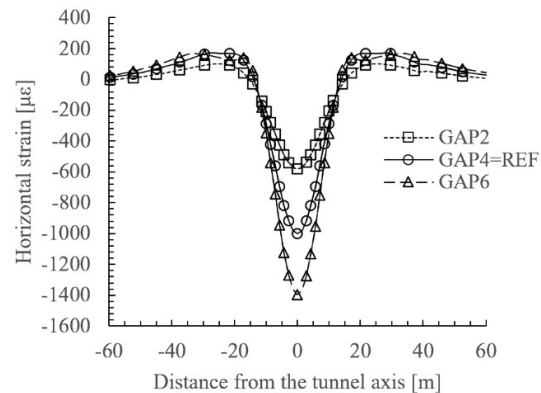


Figure 6.20. GAP models. Horizontal strains

The results are also in agreement with the literature, especially with those of Litsas et al. (2017) that observed a variation of the settlement volume loss from 0.4 to 0.6% respectively when changing the steering gap from 2 to 4 cm, and from 4 to 6 cm. In the

present thesis, the settlement volume loss varied consistently around 0.33% when the same changes to the steering gap were implemented.

Analogously to the results reported for the REF model alone, here the displacements of the nodes at the crown and invert of the tunnel are displayed for the GAP models. The most relevant comment to come from these results is that the soil at the crown and invert of the tunnel fully converges in the shield length until stopped by the same rigid body of the shield, and then fully converges a small distance around the grout until reaching an equilibrium in the length of the segmental lining, after the tail of the shield passes. This is to say, the modelled soil is soft enough to compliantly displace around the TBM and the liners until it meets a stiffer body that stops it. The modelled soil in this case, even though it shows capable characteristics from its cementitious genesis that grants it an exceptionally high Young's modulus (in GU2 equal to 150 MPa) with an equally capable friction angle and cohesion, it is not able to support itself around the walls of the excavation.

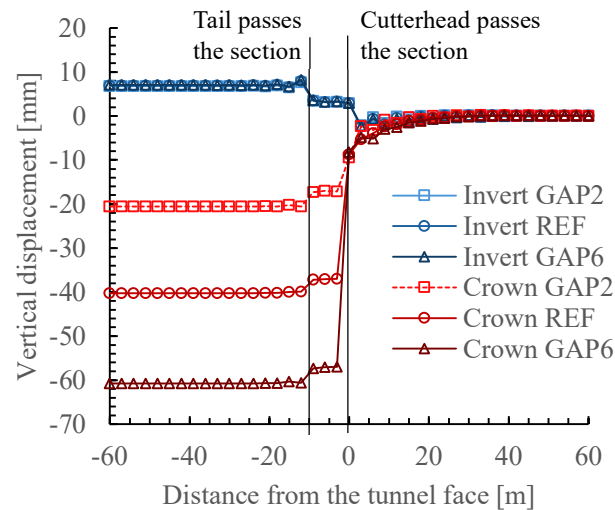


Figure 6.21. GAP models. Longitudinal trough for the nodes at the crown and invert

Another relevant comment regards the remarkably steady deformation state of the soil after the tail of the shield passes. In practice, the model was configured to apply an outwards grout pressure around the first pair of liners after the tail, and to assign a gradual stiffening of the grout along the lining development. These effects, even from the nearness of the invert and the crown, are not visible in the past figure. It is here postulated, therefore, that the high early stiffness of the two-component grout counters the enlargement induced by the expanding pressure and locks in place the displacements of the converging ground, in line with the comments made for the results of the GS and GP models and moreover, in agreement with the experience from eminent researches (Pelizza, Peila, Sorge, & Cignitti, 2012) who confirm that the two-component grout, with its near incompressible early behavior and fast hardening, can thwart the convergence of the soil from the first moments of the excavation.

#### 6.1.2.4 Face pressures (FP)

This body of parametric analyses changes the applied supporting pressure at the front of the excavation in function of a percentage of the horizontal geostatic stress. In this way, FP100 means that the earth pressure is perfectly balanced (100% of counter pressure is being applied) while FP0 indicates that no face pressure is active.

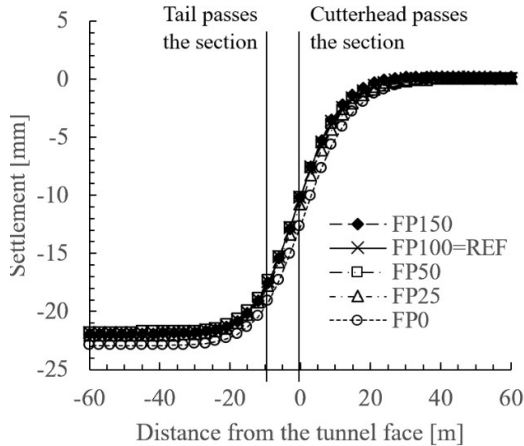


Figure 6.22. FP models. Longitudinal trough

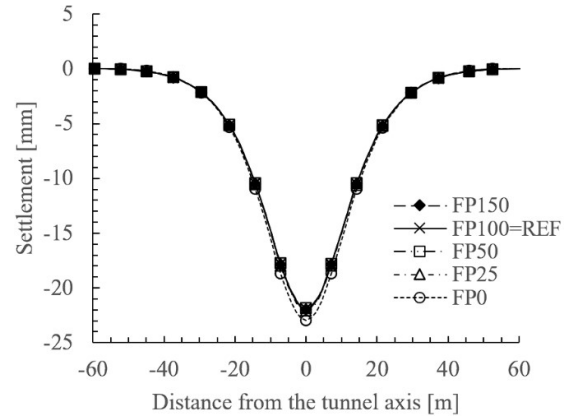


Figure 6.23. FP models. Transversal trough

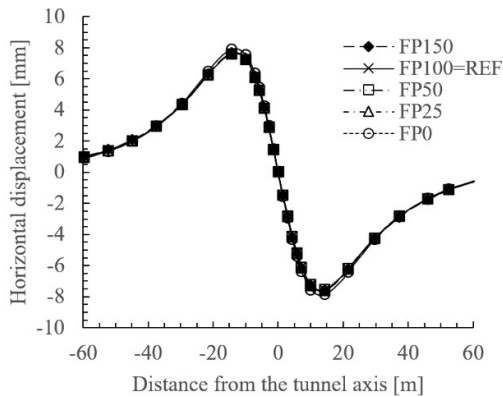


Figure 6.24. FP models. Horizontal displacements

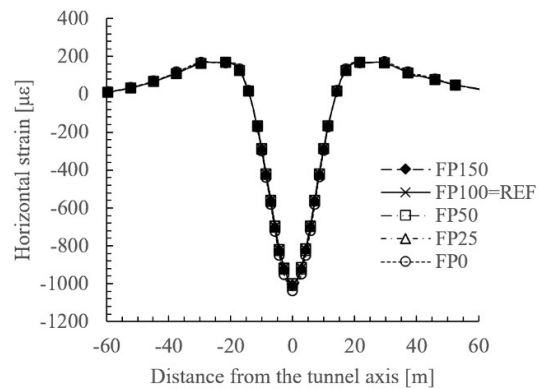


Figure 6.25. FP models. Horizontal strains

In agreement with the literature, especially the investigations of Nemorini (2010), the modification of the face pressure barely affects the basin of subsidence. In real life, this could prove true if no plastic bands develop from the tunnel front towards the surface due to poor support, because on the contrary the formation of sinkholes is inevitable. In any case, for the null face pressure FP0 the FEM model may be underestimating the real effects of removing the TBM's face pressure in a soil with a coarse and loose matrix: the continuous elements in FEM modelling are not able to capture the granularity of coarse soils.

In this framework, an alternative to estimate the face stability is researched and found with Prountzopoulos' (2012) meta-model. To adopt this method, first the face extrusion of the excavation front, parallel to the tunnel axis, is obtained and plotted in Figure 6.26. It is recommended to consult section 3.1.5.1 for the formulations as here they will be only cited.

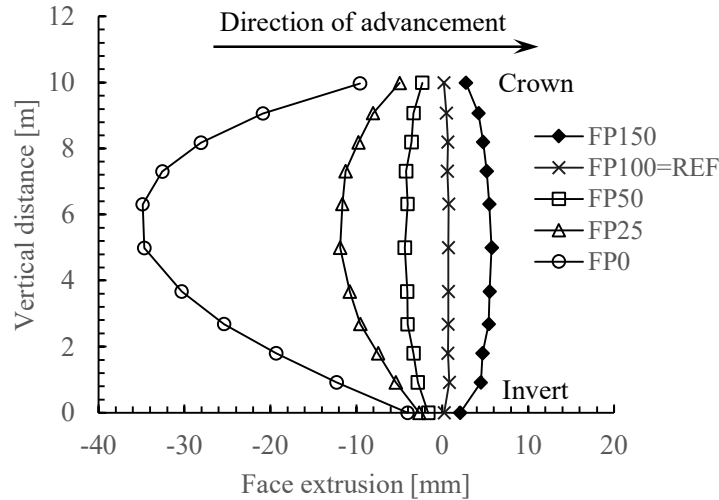


Figure 6.26. Tunnel face extrusion results with the parametrical variations. Tunnel face centered at zero

For each model, employing Equation (3.13) with the respective face extrusions  $U$ , tunnel diameter of 10 meters, average geostatic effective stress  $P_0 = 304$  kPa at the tunnel axis, and the Young's modulus of the geotechnical unit 2 equal to  $E = 150$  MPa; the normalized face extrusion  $\Omega_F$  can be obtained, and with the best fit curve in the next Figure 6.27 (also Equation (3.14)) the first Tunnel Stability Parameter  $\Lambda_{FP}$  is obtained.

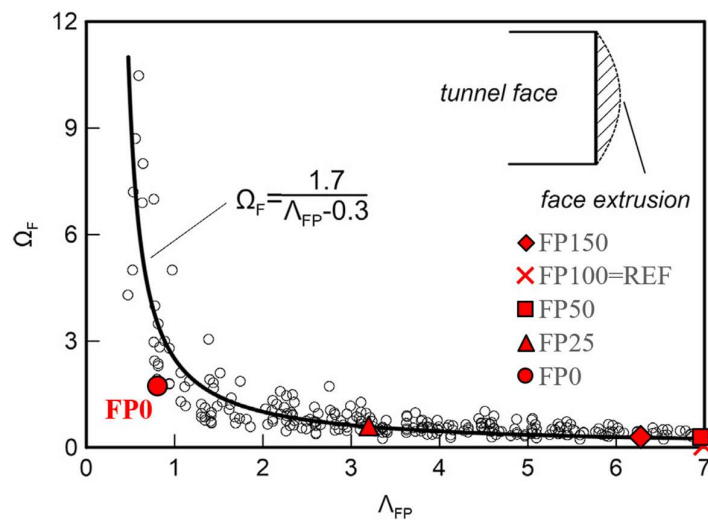


Figure 6.27. Results of the parametric analyses against Proutzopoulos' (2012)  $\Omega_F - \Lambda_{FP}$  curve

The second  $\Lambda_{FP}$  can be obtained from the alternative procedure described in 3.1.5.1, for which the original Stability Factor  $\Lambda_F$  (Equation (3.15)) is calculated knowing that the tunnel is at a depth  $H = 26$  m, and the soil has an unit weight of  $19$  kN/m<sup>3</sup>, cohesion of  $10$  kPa and friction angle of  $36^\circ$ . The value of  $\Lambda_F$  is then corrected to account for the horizontal effective stress at the tunnel axis  $P_{h0} = 203$  kPa and the applied face pressure  $P_F$  which depends on the FP model. With the correction, the second  $\Lambda_{FP}$  is calculated as per Equation (3.17).

In the past Figure 6.27 the most conservative (lower) value between both  $\Lambda_{FP}$  is selected, remembering that if  $\Lambda_{FP} < 1$  the model indicates face instability. After analyzing the figure, it can be noticed that only the case for which the face pressure is null, FP0, results in an unstable excavation face. To validate this result, the maximum principal absolute plastic strains are plotted in Figure 6.28 below, where the plastic zone is shown to cover only a limited area in the vicinities of the excavation walls, supported by the shield and liner, and at the front of the excavation in a much more reduced magnitude. No plastic strain propagation is witnessed from the face of the excavation towards the surface. Therefore, if the method by Prountzopoulos' (2012) indicates face instability for the FP0 condition, it may only be locally.

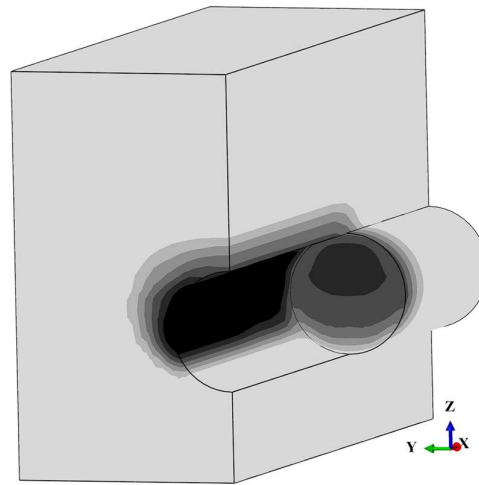


Figure 6.28. Maximum absolute plastic strains for the FP0 face pressure model

If the face pressure is reduced to the 25 or 50% of the horizontal geostatic stress, in correspondence with the FP25 and FP50 models, according to Prountzopoulos' (2012)  $\Omega_F - \Lambda_{FP}$  curve, the face is not instable. This is in good agreement with experiences in underground excavation in the Torino subsoil which, as described before when introducing the material in Chapter 4, has an inherently variable degree of cementation that grants it notable mechanical properties (remember the face of the excavation in Figure 4.8, about six meters tall was either unsupported or minimally restrained and even so, it maintained its stability). This is by no means supporting the use of open-faced TBMs during the Metro-Line 2 works, but rather it provides a sense of tranquility if the worst-case scenario happens during the excavations: the EPB TBM is jammed and the conditioned soil loses its pressurized properties with the degradation of the foam, leading to a drop in the face pressure. In this case, at least the soil is known to be capable of providing some limited self-support while the problem is solved.

#### 6.1.2.5 Ground conditions (SOIL: ITO and BAR)

Seeing that previous three-dimensional numerical models were built to analyze the excavation of the first Metro-Line of Torino using the elasto-plastic Mohr-Coulomb soil parameters proposed by Profs. Barla & Barla (2012), here the parametric analyses were performed with three constitutive models, BARMAX and BARMIN for the maximum

and minimum soil parameters in the ranges of Barla & Barla (2012), and ITO with the deterministic values provided in the project documentation of the Metro-Line 2, by Infratrasporti.To S.r.l. (2024). All the other parameters were maintained equal to those of the REF model.

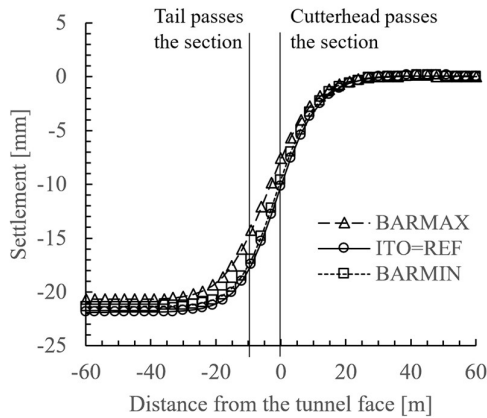


Figure 6.29. SOIL models. Longitudinal trough

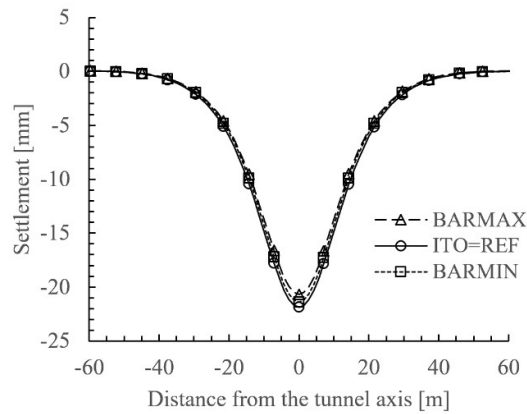


Figure 6.30. SOIL models. Transversal trough

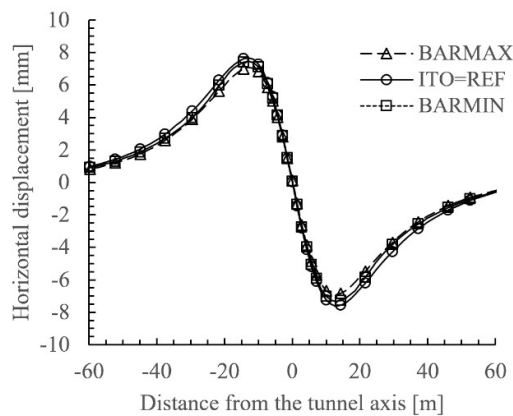


Figure 6.31. SOIL models. Horizontal displacement

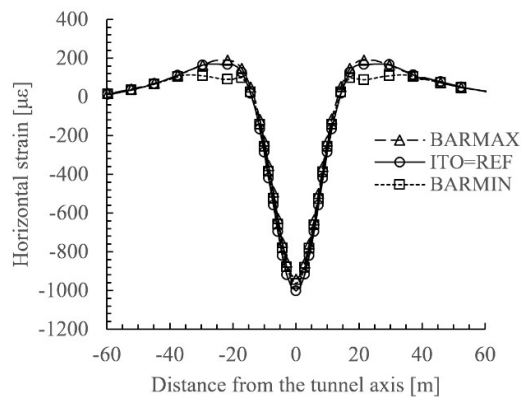


Figure 6.32. SOIL models. Horizontal strains

Here again, the parametrical variations seem to provide little change to the overall settlement trough, surely because the ITO parameters employed by Infra.To (the same used for the REF model) seem to be strongly influenced by the original ranges proposed by Barla & Barla (2012), if only adopting the most conservative values in those ranges.

#### 6.1.2.6 Soil improvement, jet grouting umbrella (JET)

The final set of parametric analyses concerns the modelling of an improved soil via the jet grouting technique, positioned on the crown of the tunnel as better described in sections 4.3.3 and 5.1.3.4. Analogously to the GAP models, the JET model does have a strong impact on the subsidence basin, expectedly with the stiffening of the involved soil area from 150 to 450 MPa of Young's modulus, and with the strengthening from 10 to 150 kPa of cohesion, in comparison against the REF model.

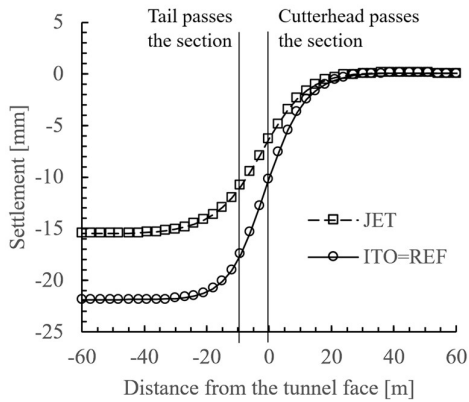


Figure 6.33. JET model. Longitudinal trough

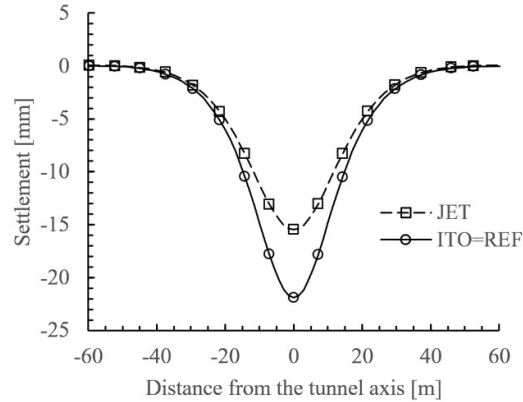


Figure 6.34. JET model. Transversal trough

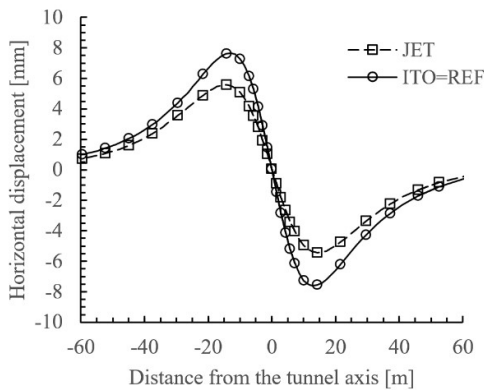


Figure 6.35. JET model. Horizontal displacement

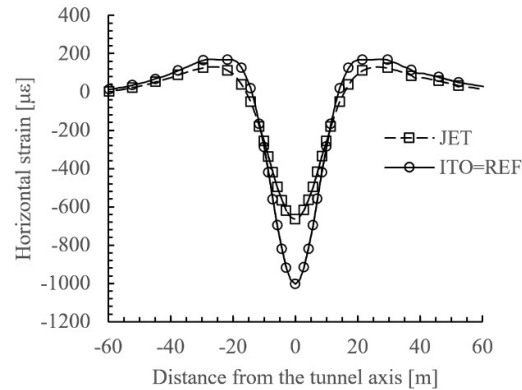


Figure 6.36. JET model. Horizontal strains

The main take away would be the expected realization that the jet grouting technique is effective in lowering the surface settlements. Surprisingly, not even the soil improvement measures are as effective in reducing the basin of subsidence as delivering a correct steering of the TBM while trying to provide the smallest steering gap possible, in comparison to the GAP2 model, reminding the project managers and contractors alike of the importance of involving cautious and experienced operators in the excavation.

### 6.1.3 Greenfield volume loss models

From the past parametrical analyses, the settlement volume losses ( $V_L^S$ , as defined in Chapter 2) are calculated and presented in the next Table 6.1. From these results, it is evident that the lowest settlement volume losses are produced in the GAP2 model, while the largest are present in the model GAP6, once again highlighting the impact of the steering gap on the basin of subsidence, in agreement with the literature which shows that the largest settlements are always produced during the passing of the shield of the machine (except in the cases where long-term consolidation is also modelled).



Furthermore, with the current modelling assumptions, most of the settlement volume losses sit around 0.88%, clearly reflecting the dominance of the parameters assumed for the REF model, especially the steering gap of 4 cm seeing that the GAP models are among the most impactful. If the reader can agree that the steering gap equal to 4 cm represents a reasonably average condition in tunnelling, then it is rational to conclude that the volume losses adopted by Infratrasporti.To (2024) during their empirical and two-dimensional numerical modelling assessments equal to 0.5 and 1.0% are not entirely conservative. In fact, the value of 0.5% would appear to underestimate the settlement trough while the 1.0% would only sit above the average condition by a little.

Table 6.1. Settlement volume losses calculated for each model of the greenfield parametric analysis

Group	Model	$V_L^S$
Reference	REF	0.88%
Grout stiffness (GS)	GSMIN	0.89%
	GSMAX	0.87%
Grout injection pressure (GP)	GP400	0.88%
	GP600	0.87%
Steering gap (GAP)	GAP2	0.54%
	GAP6	1.21%
	FP0	0.91%
Face pressure (FP)	FP25	0.88%
	FP50	0.88%
	FP150	0.88%
Ground conditions (SOIL)	BARMIN	0.84%
	BARMAX	0.81%
Jet grouting umbrella	JET	0.66%

For further analyses, it is convenient to define three curves: VL MAX, VL MEAN and VL MIN, that are representative, respectively, of the most negative, average and positive scenarios that are here predicted to occur during the excavation. The models related to these curves are called the greenfield volume loss models and will be used to analyze consequently the soil – structure interaction. As expected, the VL MAX and VL MEAN models will be given the same characteristics of the GAP6 and REF models used before for the parametric analyses. However, instead of assigning to the VL MIN model the GAP2 properties, which produced the lowest settlement volume losses, it is more interesting to analyze the case in which the soil is improved by means of jet grouting and thus, the JET parametric model is selected. The conversions are as follows:

GAP6 → VL MAX

REF → VL MEAN

JET → VL MIN

In the next Figure 6.37 to Figure 6.40, the results of the greenfield volume loss models are displayed.

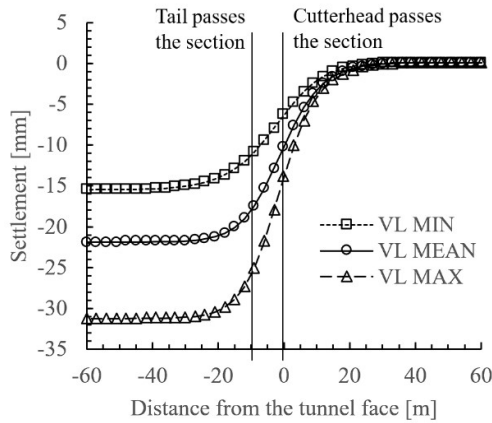


Figure 6.37. VL models. Longitudinal trough

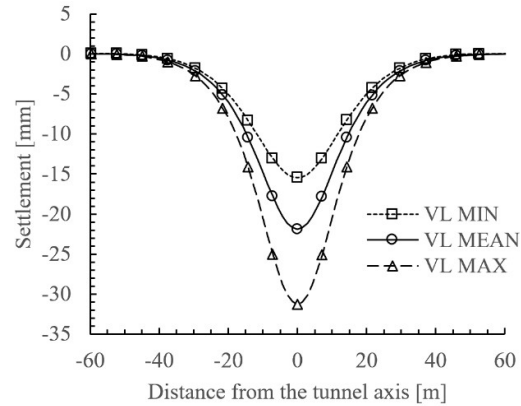


Figure 6.38. VL models. Transversal trough

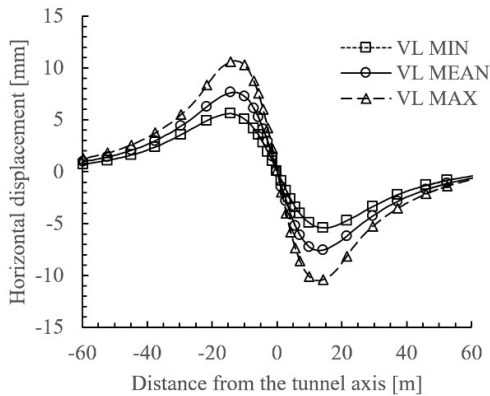


Figure 6.39. VL models. Horizontal displacements

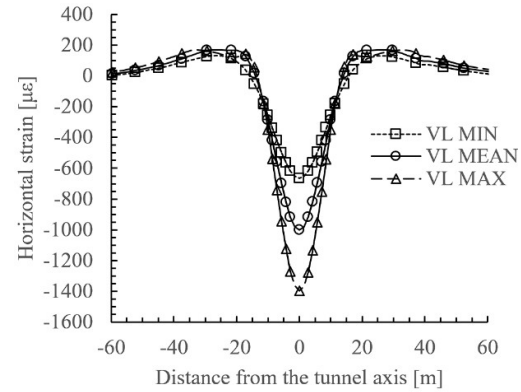


Figure 6.40. VL models. Horizontal strains

## 6.2 Uncoupled building models

The results of the uncoupled building model and the parametric analyses described in section 5.2.5 are here presented. It is reminded that the displacements are not forced at the foundation of the building, but in an effort to scale up typical laboratory tests on facades subjected to subsidence phenomena (i.e. Giardina et al. (2013)) now applied for the entire building, a displacement field replicating the steady-state greenfield surface settlements is applied on top of a supporting layer of negligible stiffness, and the building is positioned on top of said layer entering in a contact interaction, characterized by penalty normal and tangential constraints that resemble the natural building – soil contact (near “hard” normal contact and tangential contact with a friction coefficient equal to 0.5). This allows the building to separate from the supporting layer if the structure is rigid enough to oppose the greenfield subsidence, which is typically seen for isolated facades in experimental tests. This information was more detailly reviewed under heading 5.2.

The different subsidence fields applied below the building's foundation (on top of the supporting layer) are displayed in Figure 6.41. These correspond to the so-called greenfield volume loss models defined as VLMAX, VLMEAN and VLMIN, respectively representing the highest (most pessimistic equal to 1.21%, with a maximum settlement of 32 mm), average (equal to 0.88% with a maximum settlement of 22 mm) and lowest (most optimistic equal to 0.66%, with a maximum settlement of 15 mm) settlement volume losses witnessed from the greenfield parametric analyses. The nomenclature of the most relevant facades, as will be seen subsequently, is also emphasized in the figure.

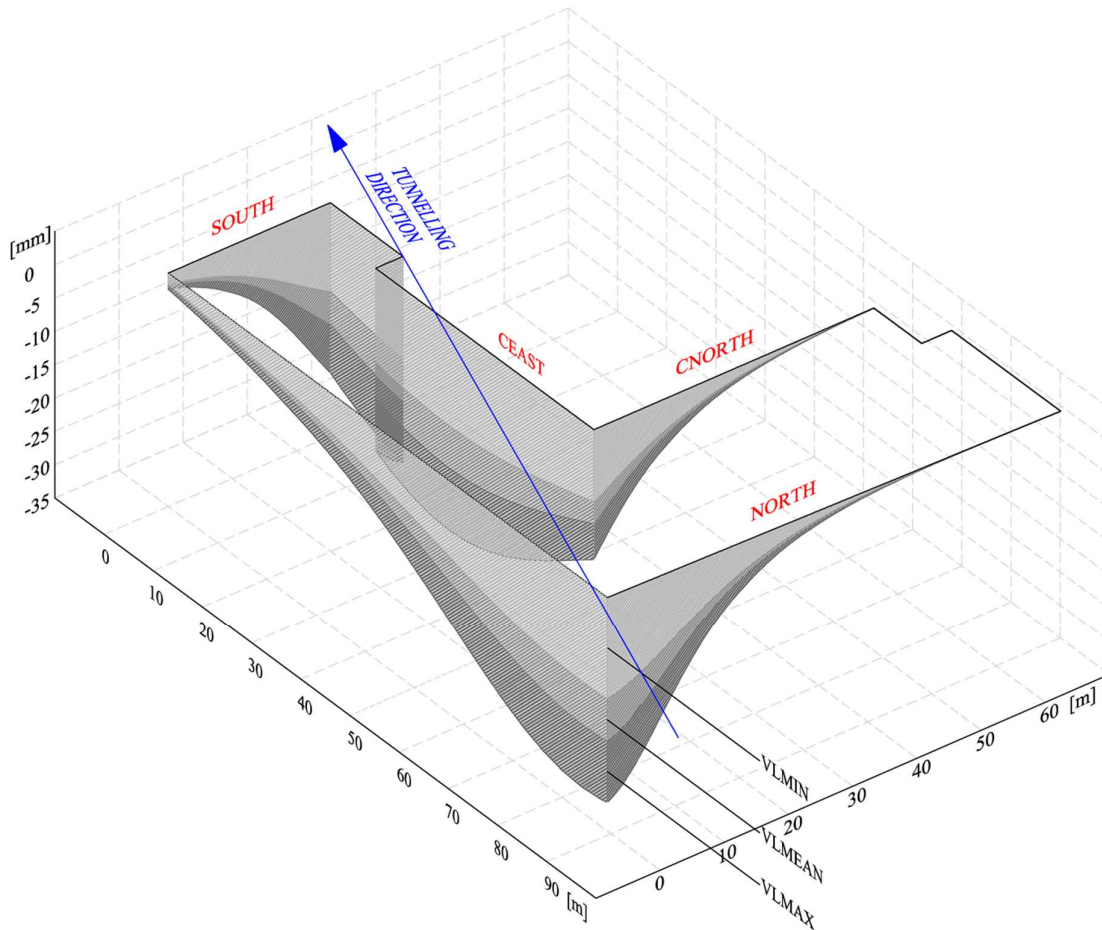


Figure 6.41. Subsidence fields applied below the facades of Palazzo Campana

For the building risk of damage assessment, here the original ranges of the limiting tensile strain proposed by Boscardin & Cording (1989), listed at the beginning of the document in Table 2.1, are analyzed to provide a more general overview of the output. In any case, if the more specific ranges for vulnerable and public buildings are to be used, it must be noticed that the range of limiting tensile strains from 0.075 to 0.15%, originally considered of a *slight* degree of severity, now passes to be *moderate*, and the range from 0.15% to 0.30% before considered *moderate* now passes to be *severe to very severe*. In short, the top degrees of severity are increased in criticality by one damage category. Below 0.075% the strains would represent from *negligible* to *slight* degrees of severity, which is more reminiscent of the natural cracking of the building due to

seasonal changes and thus, the masonry walls can be regarded to be at “low risk” of damage, meaning that structural integrity is not compromised and repair works can be performed easily and economically (Mair, Taylor, & Burland, 1996).

Therefore, for the original Boscardin & Cording (1989) limiting tensile strain ranges, it is also valuable to comment that a threshold has been set for the next figures that show the building risk of damage in function of the total tensile strain. The threshold is equal to 0.15%, being the borderline between the *slight* and *moderate* degrees of severity, or categories of damage 2 and 3 respectively (recalling Table 2.1). According to Burland et al. (1996, p. 715), “The division between damage categories 2 and 3 is particularly important. Case records show that risk of damage up to category 2 can result from a variety of causes, often in combination, either from within the building itself (e.g. shrinkage or thermal effects) or associated with ground movement”. In this sense, in the next figures particular attention will be redirected to the strains with values equal to or greater than 0.15% by coloring them with a distinct shade.

### 6.2.1 VLMAX subsidence

#### 6.2.1.1 Entire building

The tensile strains experienced by the model of the building when the VLMAX subsidence is applied are shown in the next Figure 6.42. As a reminder, the VLMAX model is the same GAP6 model in the greenfield analyses (refer to 6.1.3) in which the highest steering gap of 6 cm is included, and the maximum volume loss is observed. Attention is also driven towards the facades that manifest the most propagated, higher major principal strains. These will be individually studied in more detail in the next subsection.

From the next Figure 6.42 it results that the tensile strains vary negligibly from one elastic model (ELAS) to the other, suggesting that independently of the facades’ stiffnesses, in the chosen range of elastic properties the facades are flexible enough to follow thoroughly the greenfield subsidence applied on the supporting layer. Because in FEM the strains are first calculated in function of the nodal displacements, if the nodal displacements of all the elastic models are similar, indicating equivalent deformation modes, then the strains will be comparable from one model to the other. For all the ELAS models, the maximum elastic strain is lower than the upper threshold of the limiting tensile strain for *slight damage risk* suggested by Boscardin and Cording (1989) equal to 0.15%.

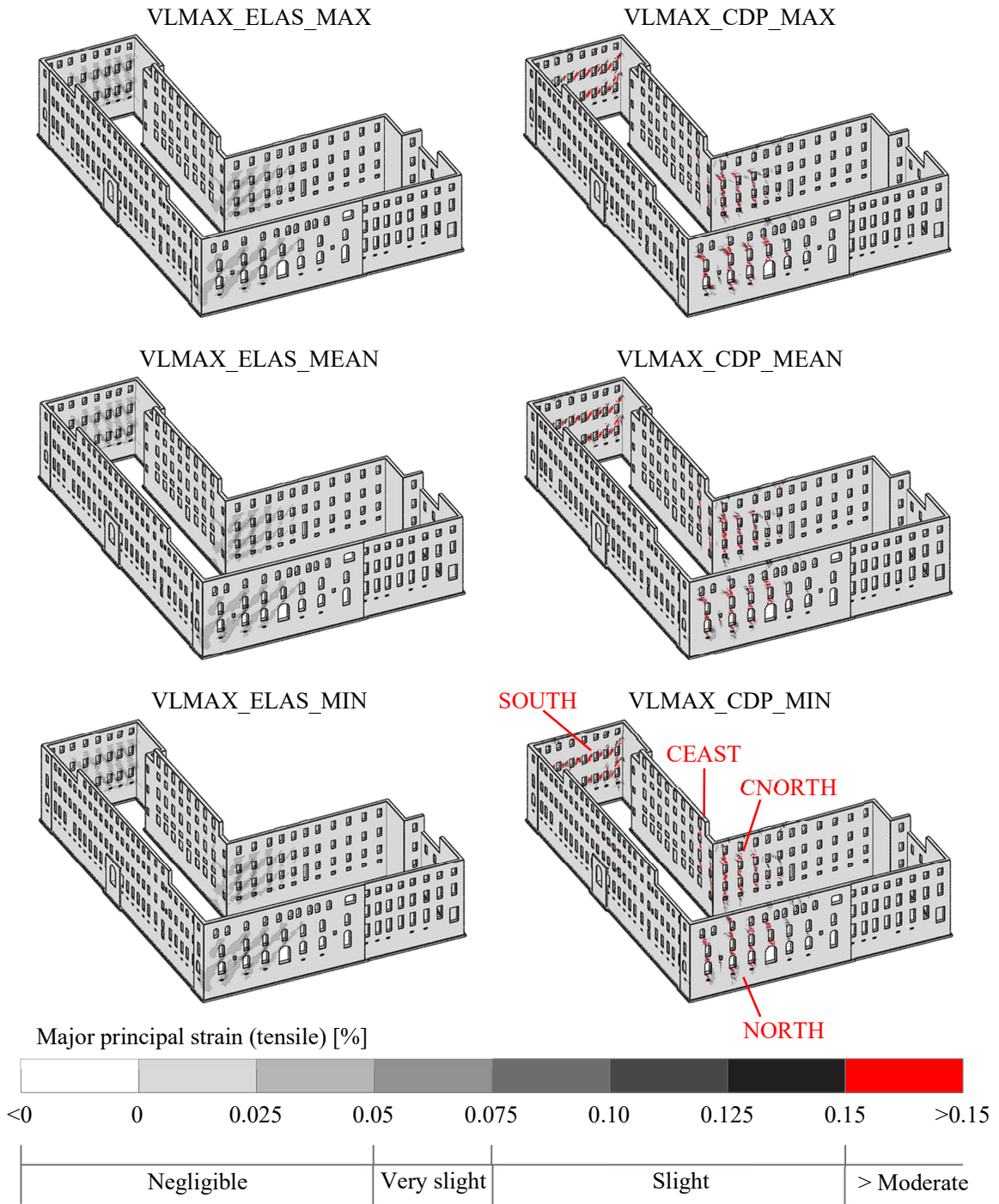


Figure 6.42. Uncoupled model: Major principal strains of the facades for the VLMAX models with both ELAS and CDP masonry constitutive behaviors

Based on Table 2.1 related to the damage categories suggested by Burland et al. (1996) and Boscardin and Cording (1989), the next Figure 6.43 shows that the tensile strains experienced by the perimetral facades of the ELAS models fall mainly (99.1% to 99.2%) in the damage category 0 for negligible severity, while a 0.7 to 0.8% enter in category 1 for very slight severity of damage and a 0.1% concern the category 2 for

slight severity. These percentages are obtained by calculating the portion of finite elements that enter each category, from a total of 141350 elements that compose the building model.

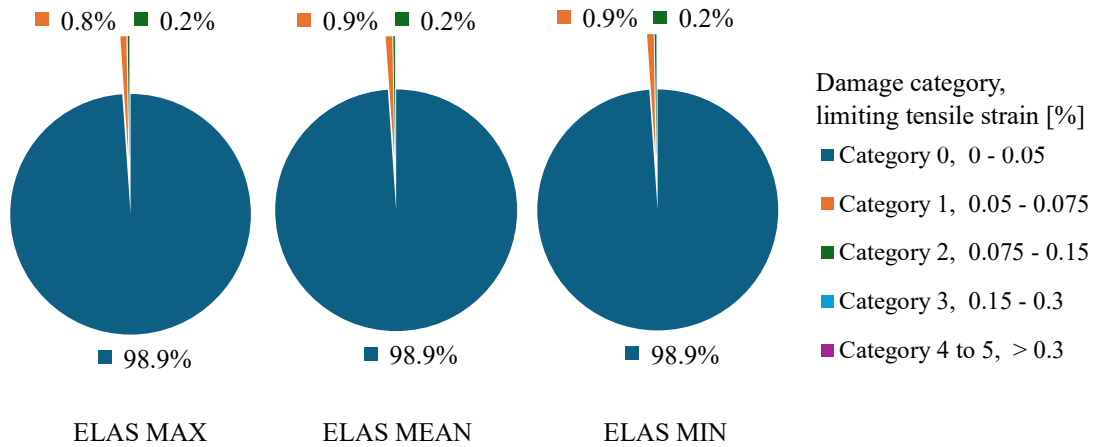


Figure 6.43. Uncoupled model: Cumulative portions of the facades belonging to the damage categories based on the limiting tensile strain, for the VLMAX models with the ELAS masonry constitutive behavior

For the elastoplastic models the effect of changing the CDP constitutive behavior is slightly noticeable. In the next section where the individual facades are analyzed it is somewhat visible how some portions of the walls enter into more severe damage categories, the weaker the constitutive model becomes; nevertheless, the variations from one CDP model to the other appear trivial in the long run. For all, the elastoplastic models (CDP) always predict higher severity of damage in more extent areas of the facades than the elastic models (ELAS), supporting the findings of other authors reviewed in the past heading 3.2.2. In particular, based on Table 2.1 related to the damage categories suggested by Burland et al. (1996) and Boscardin and Cording (1989), according to Figure 6.44 below the tensile strains experienced by the perimetral facades of the CDP models fall mainly (98.0% to 98.2%) in the damage category 0 for negligible severity, while a 0.6% enters in category 1 for very slight severity of damage, a 0.6% in the category 2 for slight severity, .03 to 0.4% in category 3 for moderate severity and a 0.3% concern the categories 4 and 5 for severe to very severe level. These percentages are obtained by calculating the portion of finite elements that enter each category, from a total of 141350 elements that compose the building model.

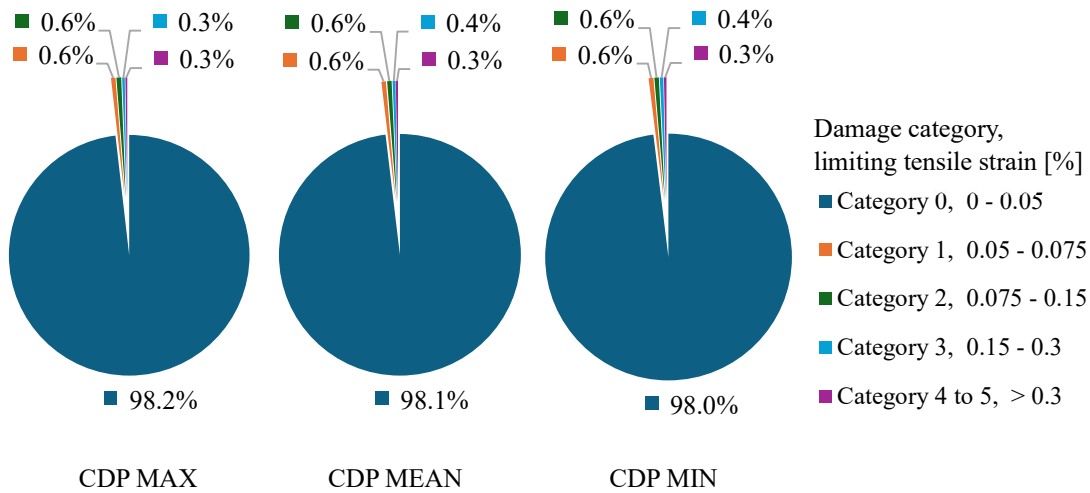


Figure 6.44. Uncoupled model: Cumulative portions of the facades belonging to the damage categories based on the limiting tensile strain, for the VLMAX models with the CDP masonry constitutive behavior

These past figures, however, are too coarse as they account for large volumes of facades that are far from entering into interaction with the basin of subsidence. For example, the volume of the WEST facade (refer to Figure 5.19) is still included in the pie charts from before summing entirely for the percentage of category 0 of damage, given that it is relatively far from the tunnel axis and thus, it is seldom affected by the excavation. In this way, in the next section the facades that present the most propagated, higher major principal strains are individually analyzed to determine how affected they are by the excavation.

#### 6.2.1.1 Individual facades

For all the models, the facades that present the most propagated, higher strains are those with a near orthogonal orientation to the tunnel axis, directly the NORTH, CNORTH and SOUTH facades. The CEAST facade also shows high strains but only at the corner where it enters in interaction with the CNORTH facade. The next Figure 6.45, Figure 6.46 and Figure 6.47 show in detail the results of the parametric analyses for these facades.

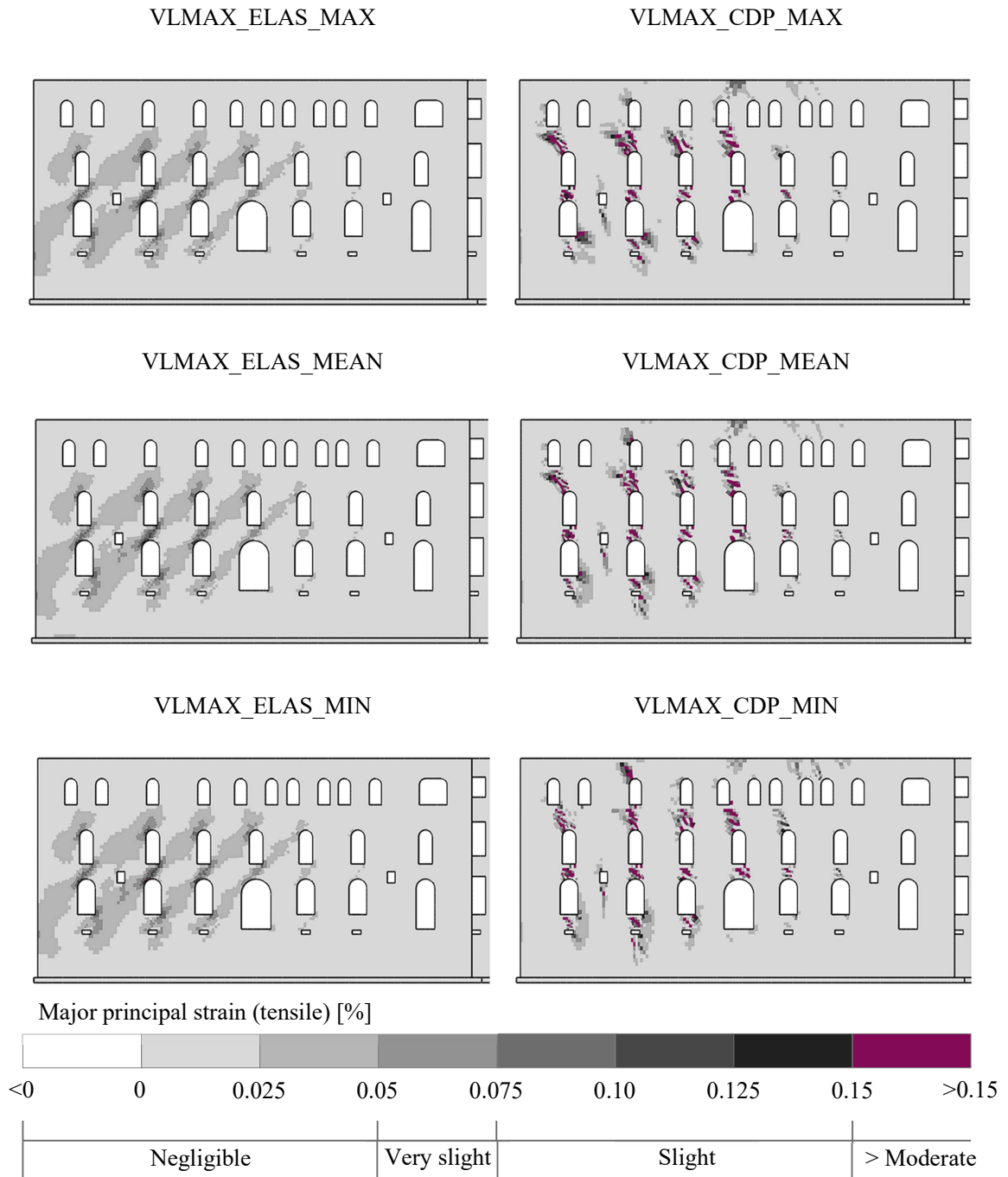


Figure 6.45. Uncoupled model: Major principal strains of the NORTH facade for the VLMAX models with both ELAS and CDP masonry constitutive behaviors



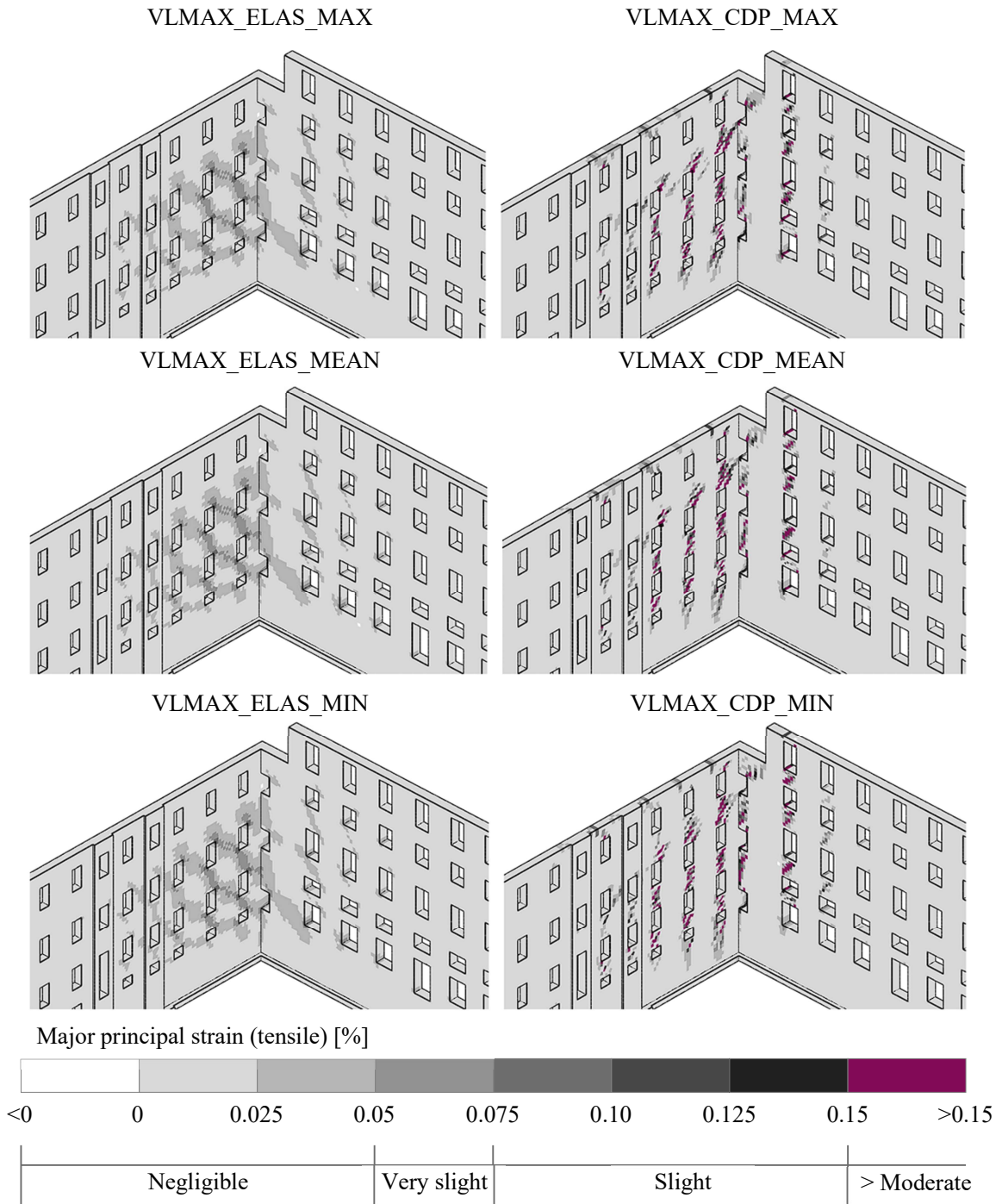


Figure 6.46. Uncoupled model: Major principal strains of the CNORTH and CEAST facades for the VLMAX models with both ELAS and CDP masonry constitutive behaviors

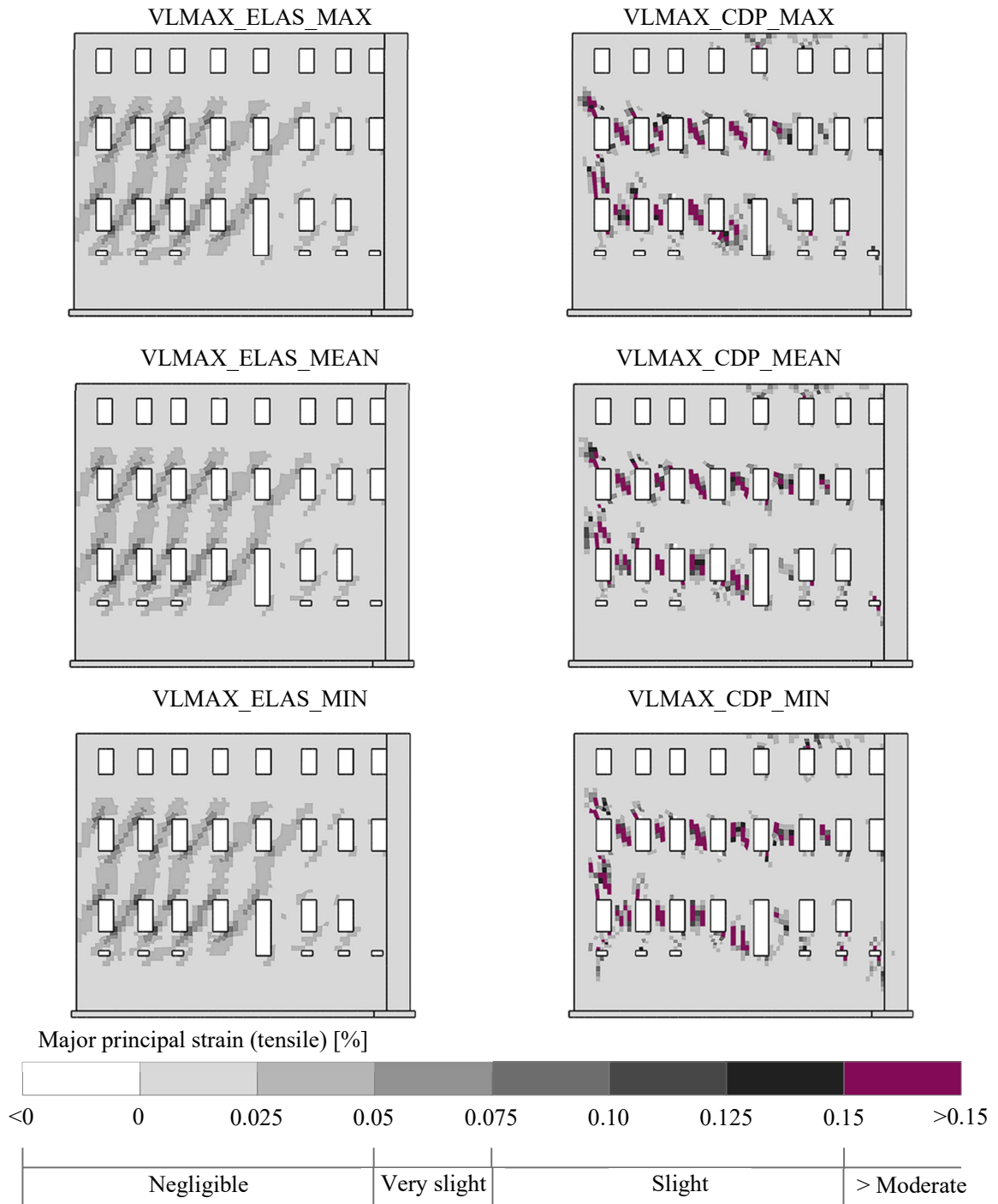


Figure 6.47. Uncoupled model: Major principal strains of the SOUTH facade for the VLMAX models with both ELAS and CDP masonry constitutive behaviors

Once again, based on Table 2.1 related to the damage categories suggested by Burland et al. (1996) and Boscardin and Cording (1989), the next figures show the proportion of risk of damage experienced by each individual facade.

For the NORTH facade the results of the ELAS and CDP models show respectively:

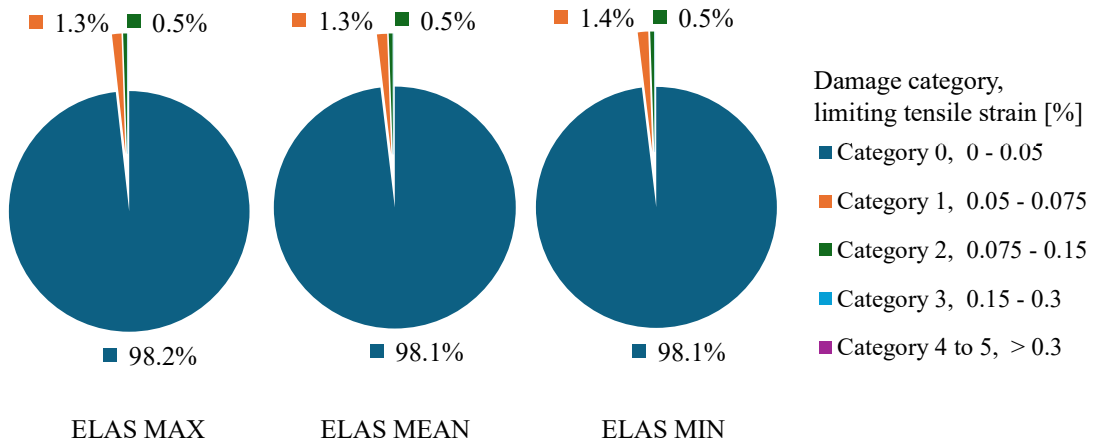


Figure 6.48. Uncoupled model: Cumulative portions of the NORTH facade belonging to the damage categories based on the limiting tensile strain, for the VLMAX models with the ELAS masonry constitutive behavior

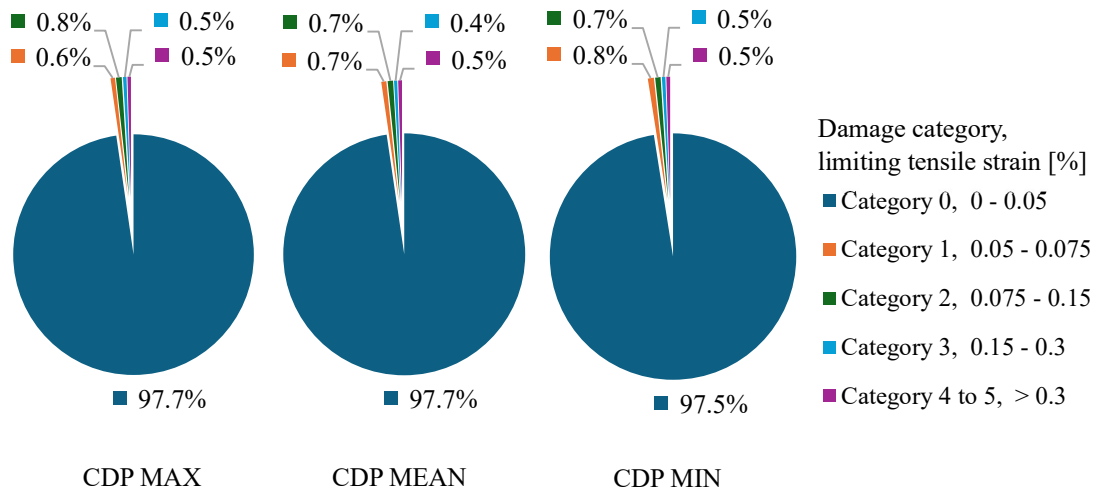


Figure 6.49. Uncoupled model: Cumulative portions of the NORTH facade belonging to the damage categories based on the limiting tensile strain, for the VLMAX models with the CDP masonry constitutive behavior

These percentages are obtained by calculating the portion of finite elements that enter each category, from a total of 41563 elements that compose the NORTH facade model. Particularly, for the CDP MAX model the detailed damage category map shows:



Figure 6.50. Uncoupled model: Damage category map of the NORTH facade for the VLMAX models with the CDP MAX masonry constitutive behavior

For the SOUTH facade the results of the ELAS and CDP models show respectively:

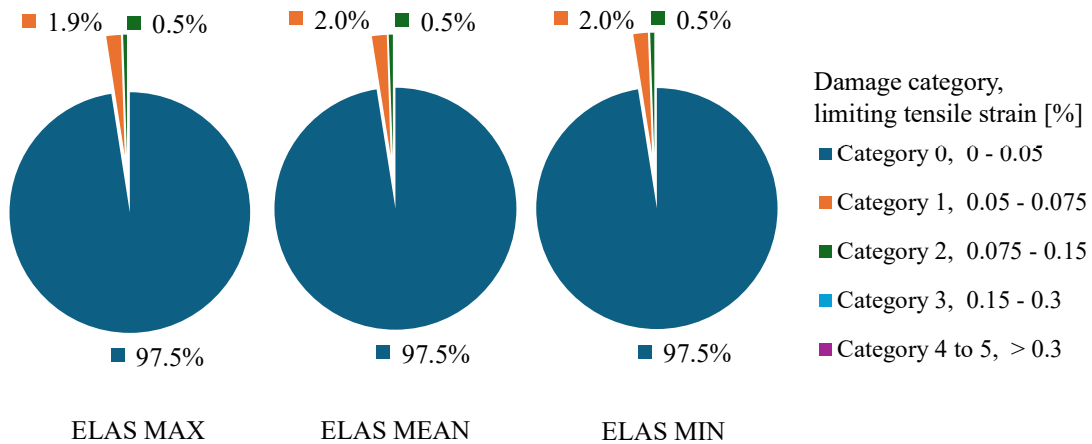


Figure 6.51. Uncoupled model: Cumulative portions of the SOUTH facade belonging to the damage categories based on the limiting tensile strain, for the VLMAX models with the ELAS masonry constitutive behavior

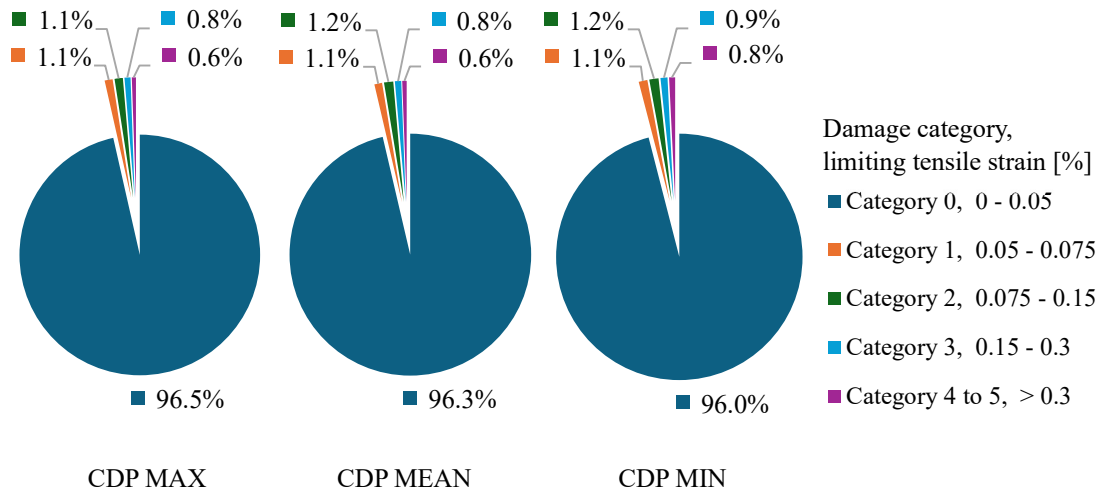


Figure 6.52. Uncoupled model: Cumulative portions of the SOUTH facade belonging to the damage categories based on the limiting tensile strain, for the VLMAX models with the CDP masonry constitutive behavior

These percentages are obtained by calculating the portion of finite elements that enter each category, from a total of 12014 elements that compose the SOUTH facade model. Particularly, for the CDP MAX model the detailed damage category map shows:

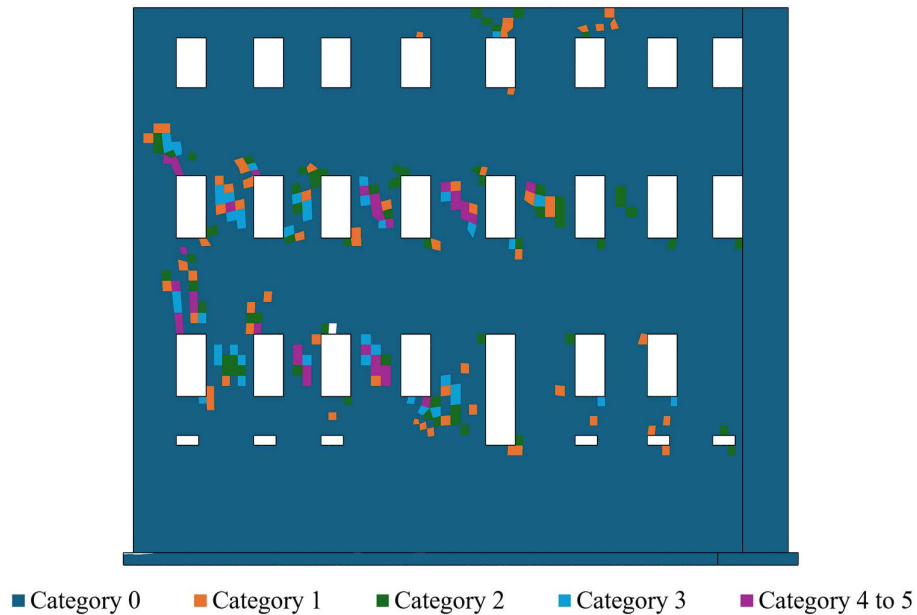


Figure 6.53. Uncoupled model: Damage category map of the SOUTH facade for the VLMAX models with the CDP MAX masonry constitutive behavior

For the CEAST and CNORTH facades the results of the ELAS and CDP models show respectively:

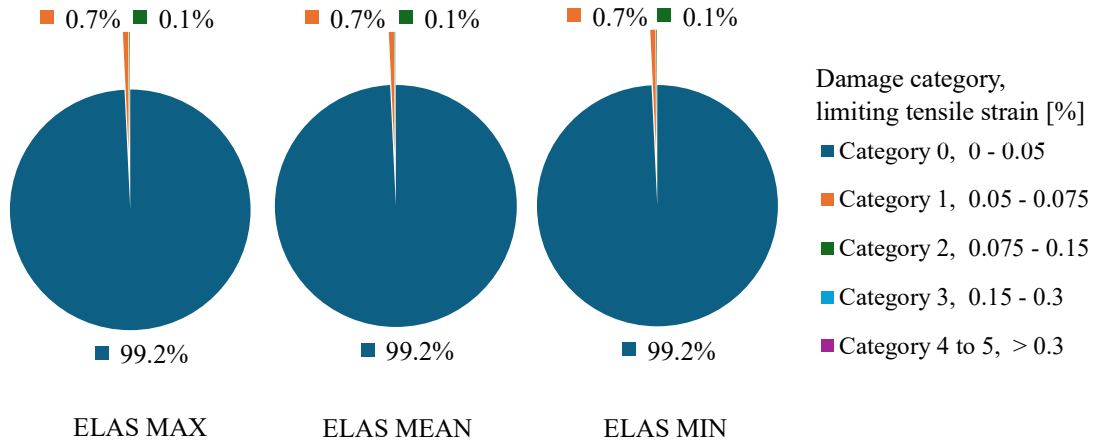


Figure 6.54. Uncoupled model: Cumulative portions of the CEAST and CNORTH facades belonging to the damage categories based on the limiting tensile strain, for the VLMAX models with the ELAS masonry constitutive behavior

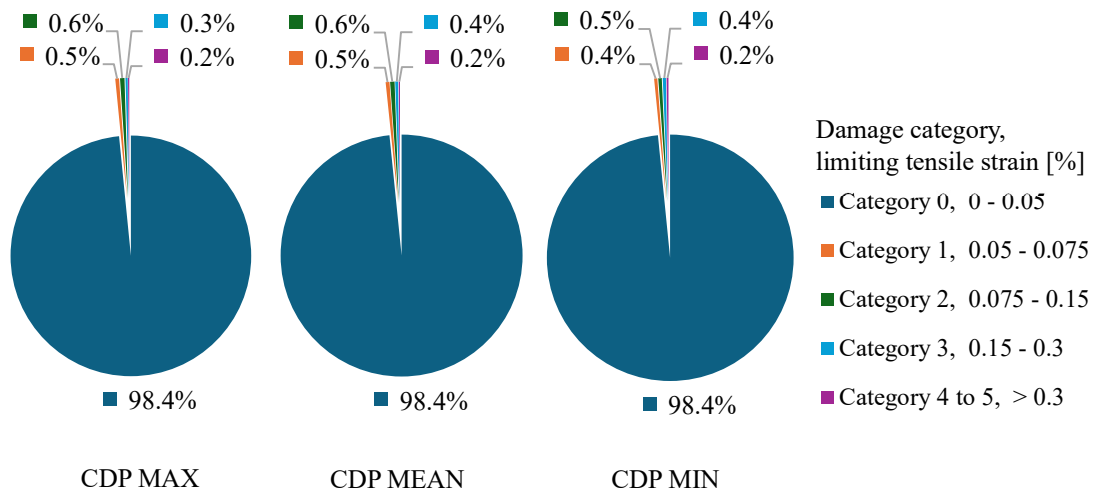


Figure 6.55. Uncoupled model: Cumulative portions of the CEAST and CNORTH facades belonging to the damage categories based on the limiting tensile strain, for the VLMAX models with the CDP masonry constitutive behavior

These percentages are obtained by calculating the portion of finite elements that enter each category, from a total of 61233 elements that compose the CEAST and CNORTH facade models. Particularly, for the CDP MAX model the detailed damage category map shows:

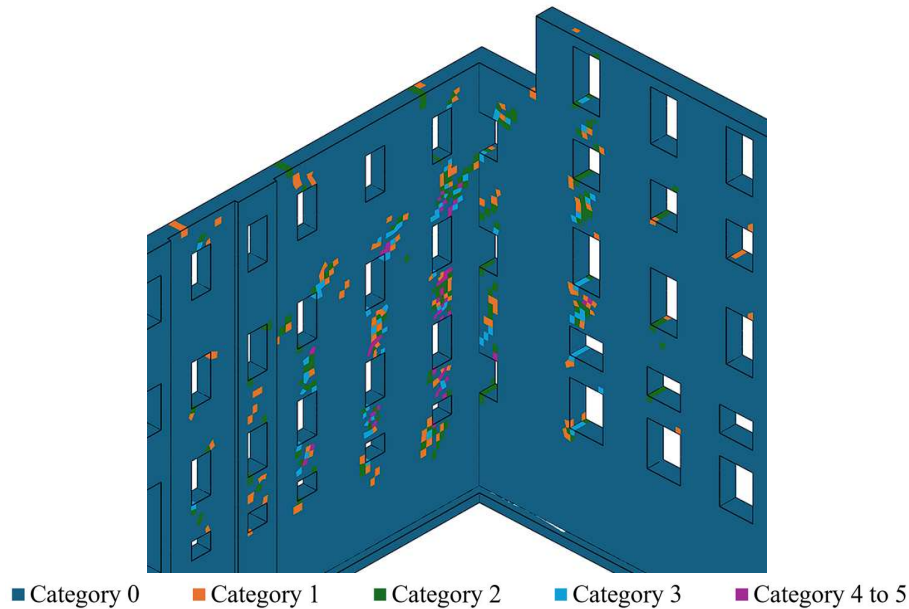


Figure 6.56. Uncoupled model: Damage category map of the CEAST and CNORTH facades for the VLMAX models with the CDP MAX masonry constitutive behavior

From all these graphs, the facade that shows the most concentrated damage risk is the SOUTH facade, only because it has the lowest amount of elements of the four. In elasticity, the NORTH facade is the one showing the highest amount of elements entering categories of damage 1 and 2 with 775 elements out of 41563. In elasto-plasticity, the same NORTH facade shows the highest amount of elements surpassing category of damage 0 (negligible) with 986 elements out of 41563, and it also has the largest number of elements entering categories of damage 3 to 5, above the threshold of 0.15% for the limiting tensile strain, with 400 elements out of 41563. This information is presented here both in terms of percentage (from past pie charts) and number of elements because none of these results by themselves serve to identify the most critical facade, but at most they can be paired with Figure 6.45 to Figure 6.47 to focus accordingly the monitoring of the facades during the tunnelling works.

## 6.2.2 VLMEAN subsidence

### 6.2.2.1 Entire building

The tensile strains experienced by the model of the building when the VLMEAN subsidence is applied are shown in the next Figure 6.57. As a reminder, the VLMEAN model is the same REF model in the greenfield analyses (refer to 6.1.3), selected to be the reference model with the ‘average’ behavior. Attention is also driven towards the

facades that manifest the most propagated, higher major principal strains. These will be individually studied in more detail in the next subsection.

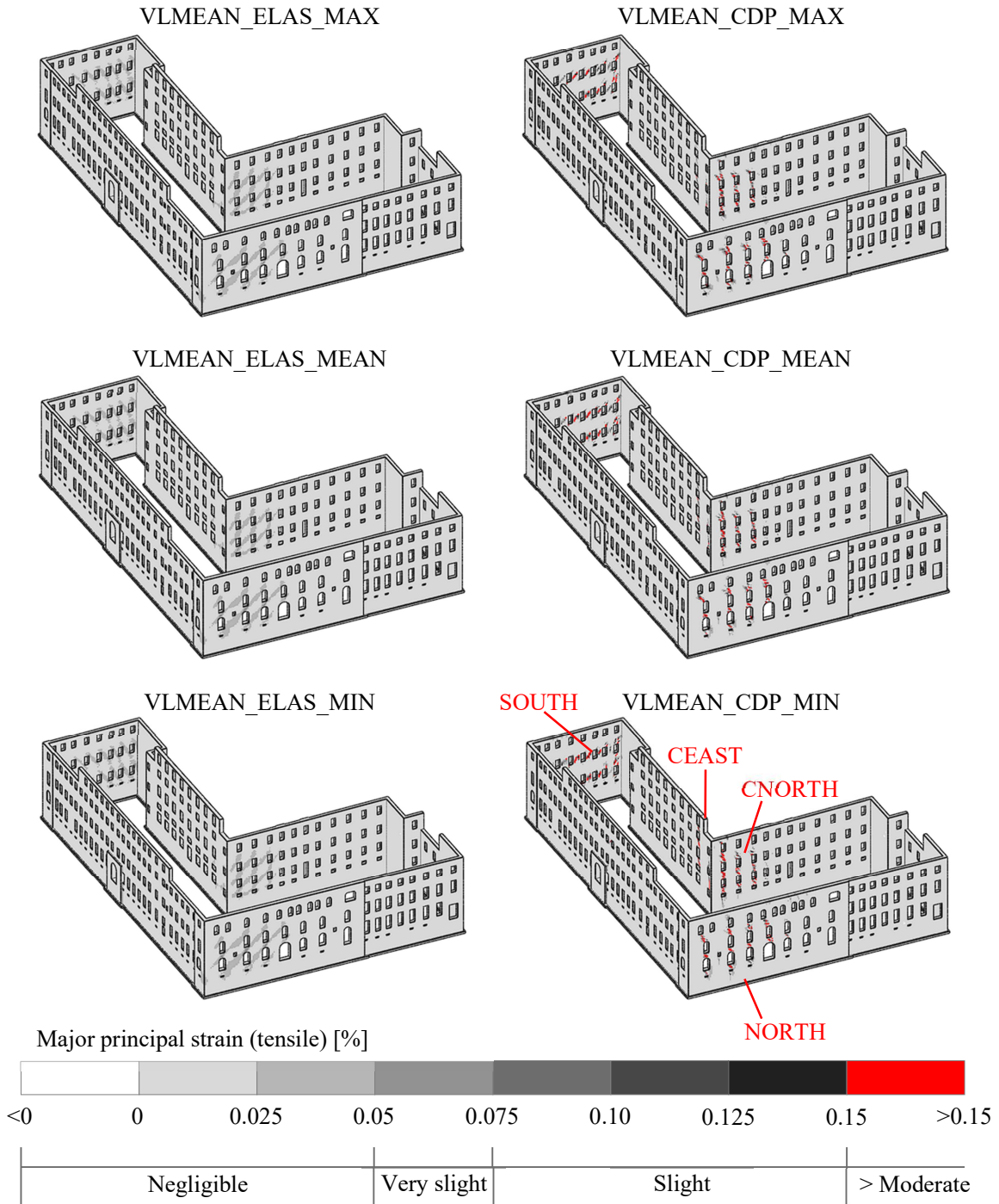


Figure 6.57. Uncoupled model: Major principal strains of the facades for the VLMEAN models with both ELAS and CDP masonry constitutive behaviors

From the figure above it results that the tensile strains vary negligibly from one elastic model (ELAS) to the other, suggesting that independently of the facades' stiffnesses, in the chosen range of elastic properties the facades are flexible enough to follow



thoroughly the greenfield subsidence applied on the supporting layer. Because in FEM the strains are first calculated in function of the nodal displacements, if the nodal displacements of all the elastic models are similar, indicating equivalent deformation modes, then the strains will be comparable from one model to the other. For all the ELAS models, the maximum elastic strain is lower than the upper threshold of the limiting tensile strain for *slight damage risk* suggested by Boscardin and Cording (1989) equal to 0.15%. Based on Table 2.1 related to the damage categories suggested by Burland et al. (1996) and Boscardin and Cording (1989), the next Figure 6.58 shows that the tensile strains experienced by the perimetral facades of the ELAS models fall mainly (99.7%) in the damage category 0 for negligible severity, while a 0.3% enter in category 1 for very slight severity of damage. These percentages are obtained by calculating the portion of finite elements that enter each category, from a total of 141350 elements that compose the building model.

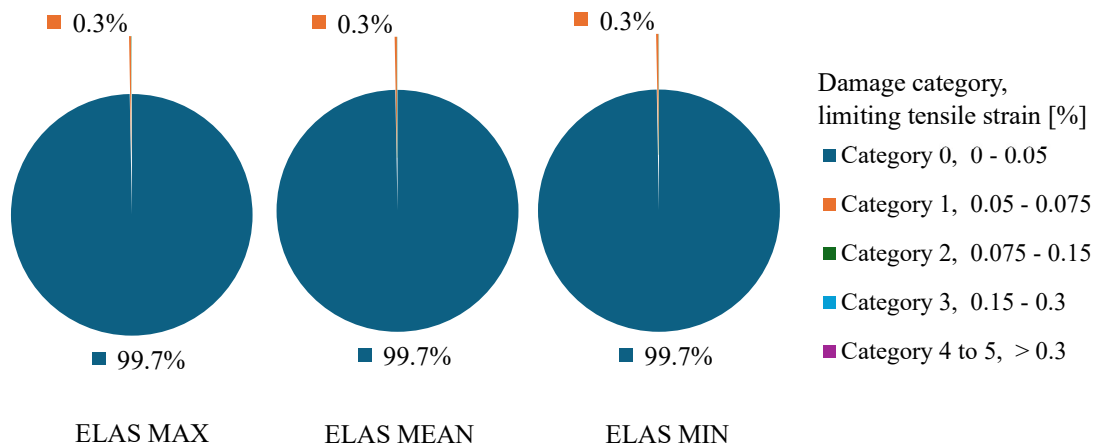


Figure 6.58. Uncoupled model: Cumulative portions of the facades belonging to the damage categories based on the limiting tensile strain, for the VLMEAN models with the ELAS masonry constitutive behavior

For the elastoplastic models the effect of changing the CDP constitutive behavior is slightly noticeable. In the next section where the individual facades are analyzed it is somewhat visible how some portions of the walls enter into more severe damage categories, the weaker the constitutive model becomes; nevertheless, the variations from one CDP model to the other appear trivial in the long run. For all, the elastoplastic models (CDP) always predict higher severity of damage in more extent areas of the facades than the elastic models (ELAS), supporting the findings of other authors reviewed in the past heading 3.2.2. In particular, based on Table 2.1 related to the damage categories suggested by Burland et al. (1996) and Boscardin and Cording (1989), according to Figure 6.44 below the tensile strains experienced by the perimetral facades of the CDP models fall mainly (98.8% to 98.9%) in the damage category 0 for negligible severity, while a 0.4% enters in category 1 for very slight severity of damage,

a 0.4% in the category 2 for slight severity, .0.2 to 0.3% in category 3 for moderate severity and a 0.1 to 0.2% concern the categories 4 and 5 for severe to very severe level. These percentages are obtained by calculating the portion of finite elements that enter each category, from a total of 141350 elements that compose the building model.

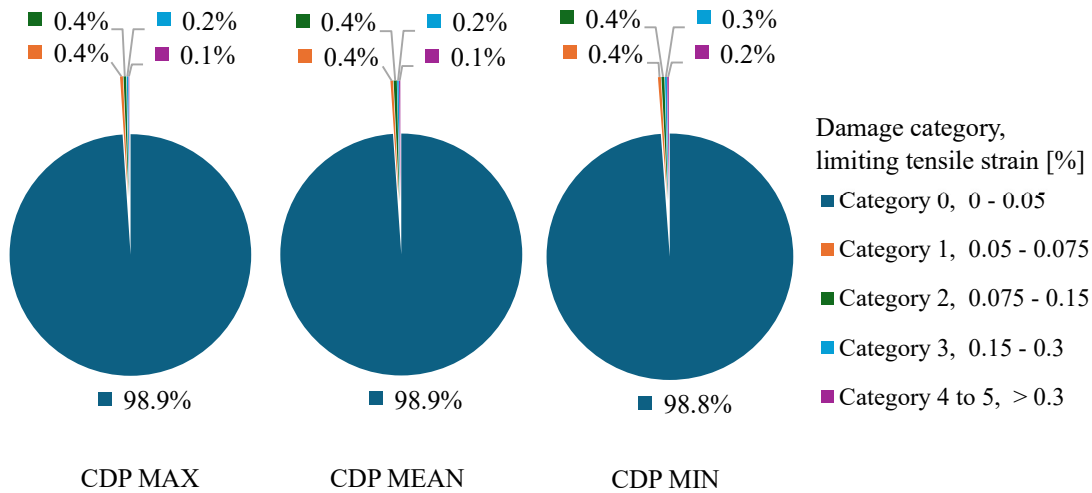


Figure 6.59. Uncoupled model: Cumulative portions of the facades belonging to the damage categories based on the limiting tensile strain, for the VLMEAN models with the CDP masonry constitutive behavior

These past figures, however, are too coarse as they account for large volumes of facades that are far from entering into interaction with the basin of subsidence. For example, the volume of the WEST facade (refer to Figure 5.19) is still included in the pie charts from before summing entirely for the percentage of category 0 of damage, given that it is relatively far from the tunnel axis and thus, it is seldom affected by the excavation. In this way, in the next section the facades that present the most propagated, higher major principal strains are individually analyzed to determine how affected they are by the excavation.

#### 6.2.2.2 Individual facades

For all the models, the facades that present the most propagated, higher strains are those with a near orthogonal orientation to the tunnel axis, directly the NORTH, CNORTH and SOUTH facades. The CEAST facade also shows high strains but only at the corner where it enters in interaction with the CNORTH facade. The next Figure 6.60, Figure 6.61 and Figure 6.62 show in detail the results of the parametric analyses for these facades.

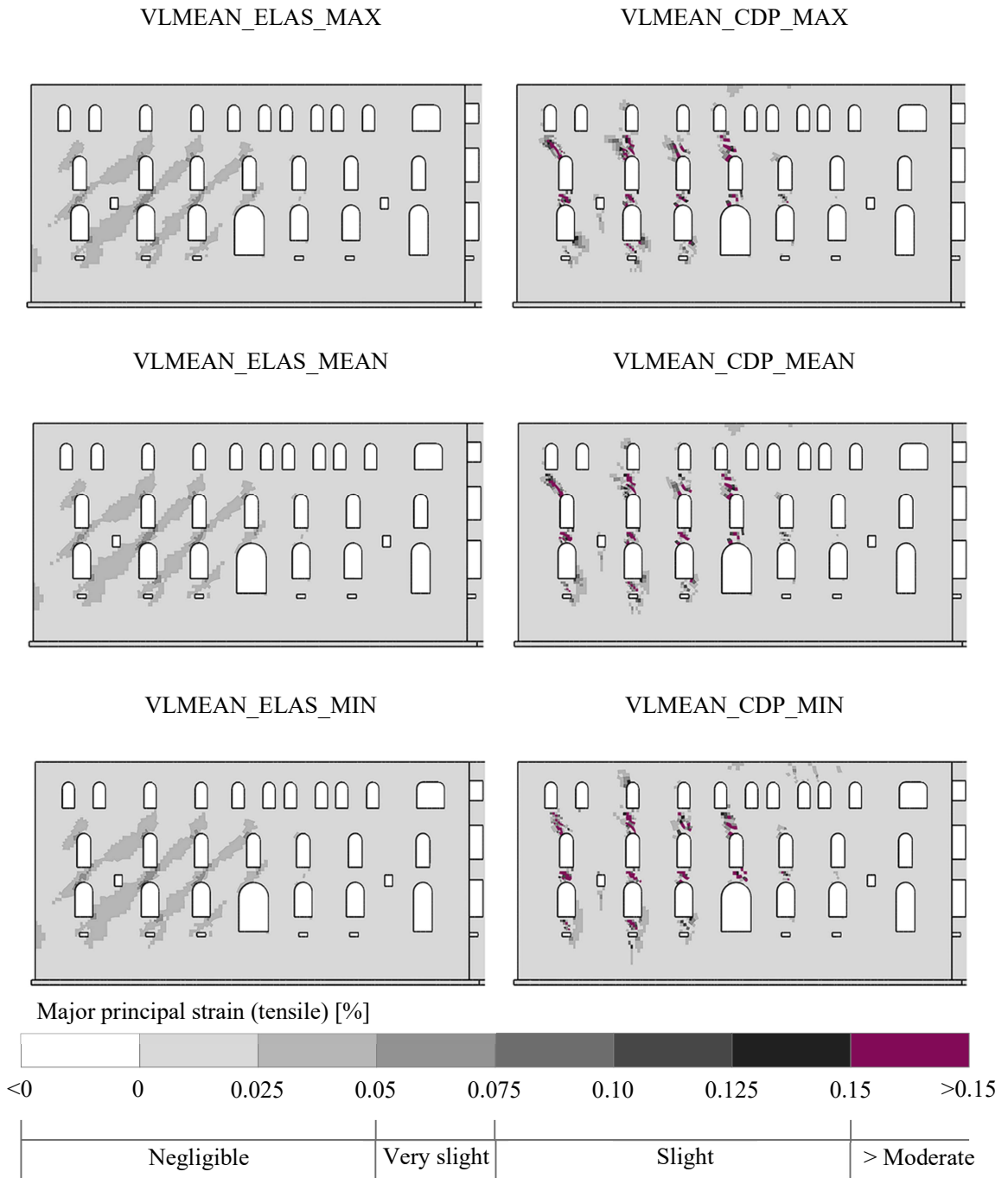


Figure 6.60. Uncoupled model: Major principal strains of the NORTH facade for the VLMEAN models with both ELAS and CDP masonry constitutive behaviors

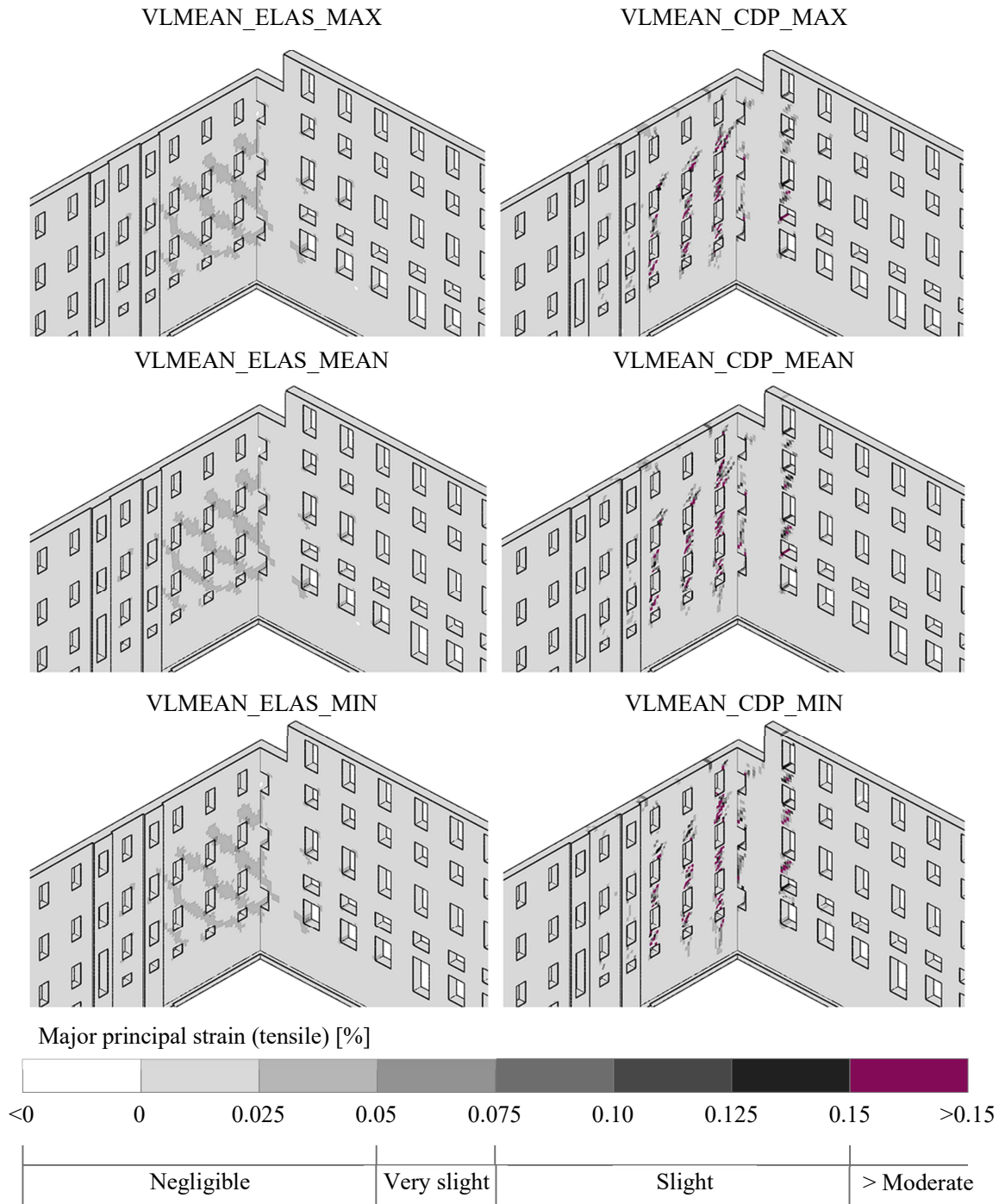


Figure 6.61. Uncoupled model: Major principal strains of the CNORTH and CEAST facades for the VLMEAN models with both ELAS and CDP masonry constitutive behaviors

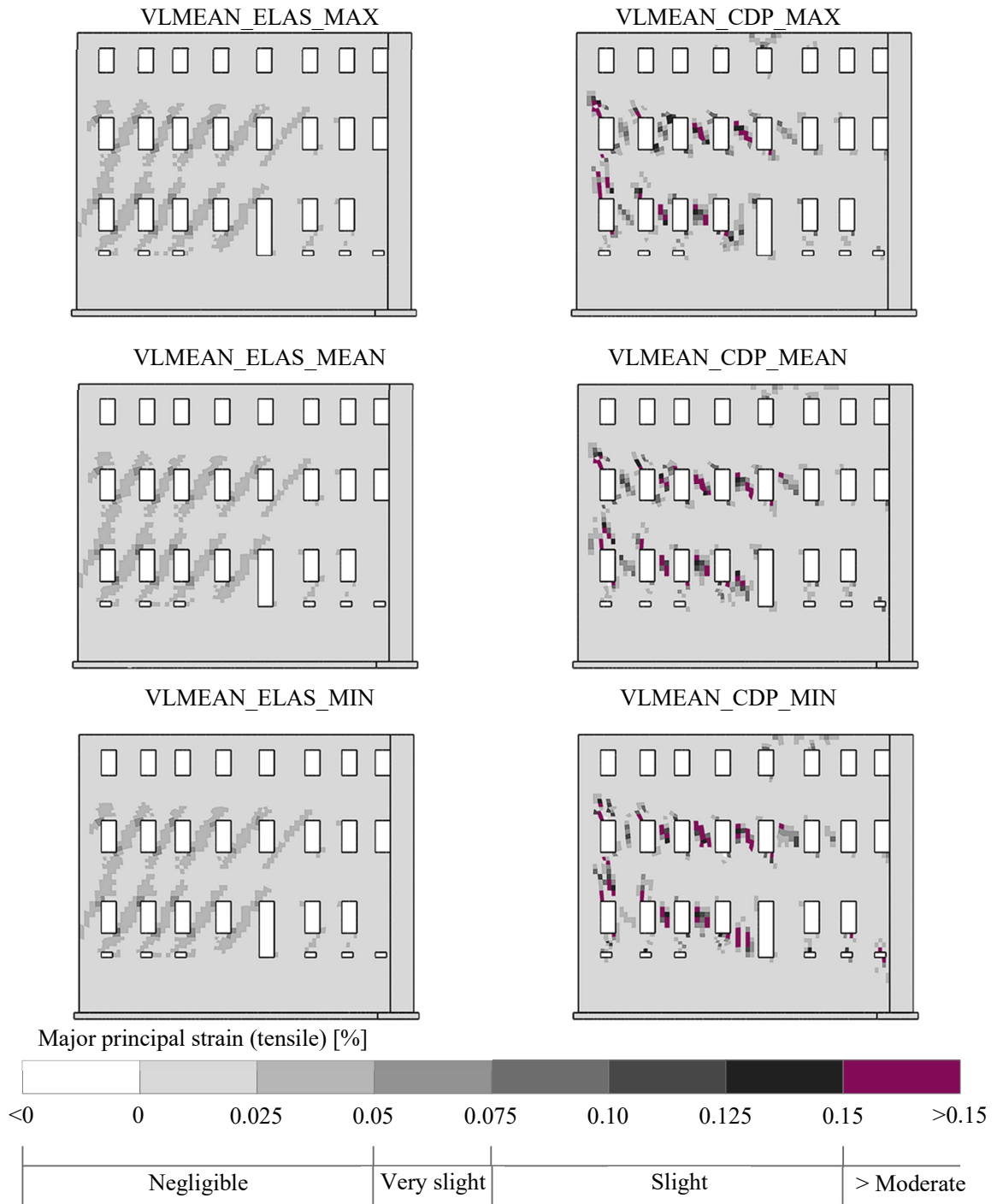


Figure 6.62. Uncoupled model: Major principal strains of the SOUTH facade for the VLMEAN models with both ELAS and CDP masonry constitutive behaviors

Once again, based on Table 2.1 related to the damage categories suggested by Burland et al. (1996) and Boscardin and Cording (1989), the next figures show the proportion of risk of damage experienced by each individual facade.

For the NORTH facade the results of the ELAS and CDP models show respectively:

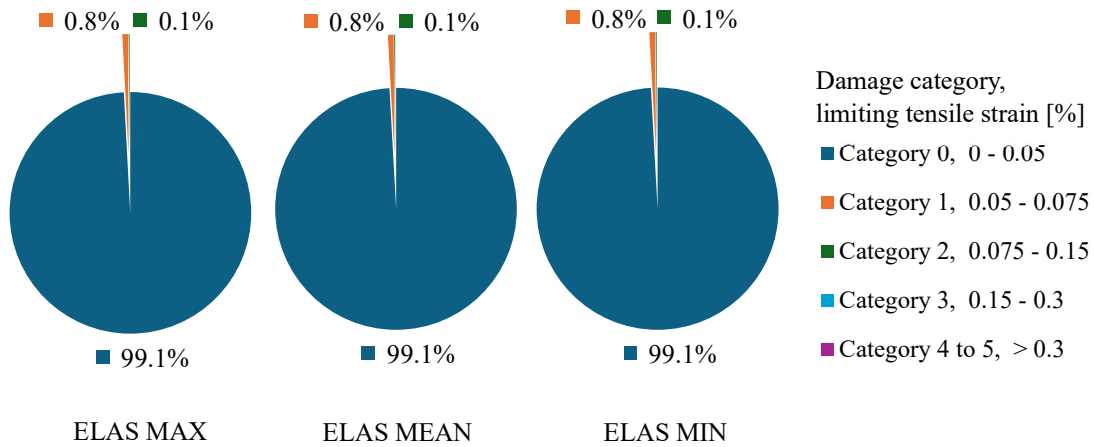


Figure 6.63. Uncoupled model: Cumulative portions of the NORTH facade belonging to the damage categories based on the limiting tensile strain, for the VLMEAN models with the ELAS masonry constitutive behavior

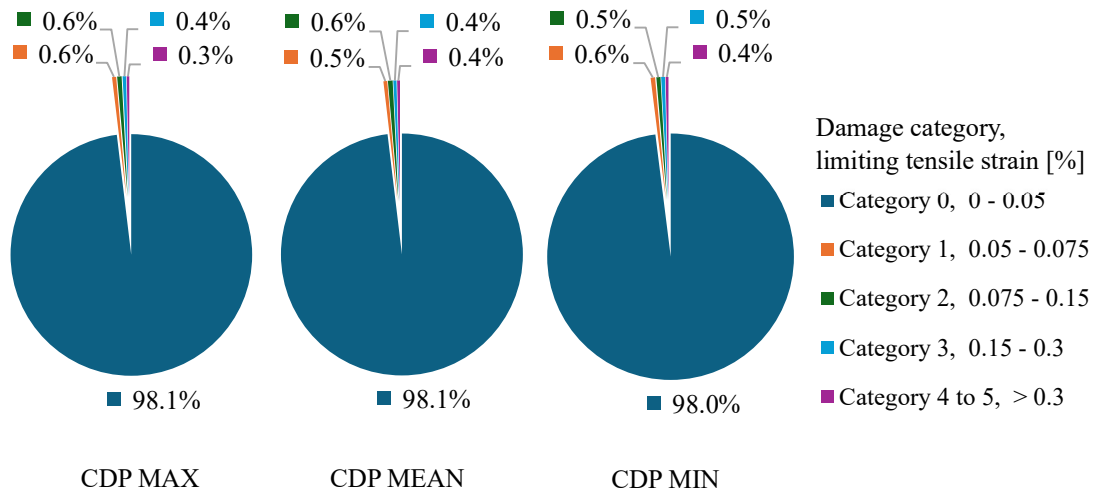


Figure 6.64. Uncoupled model: Cumulative portions of the NORTH facade belonging to the damage categories based on the limiting tensile strain, for the VLMEAN models with the CDP masonry constitutive behavior

These percentages are obtained by calculating the portion of finite elements that enter each category, from a total of 41563 elements that compose the NORTH facade model. Particularly, for the CDP MAX model the detailed damage category map shows:

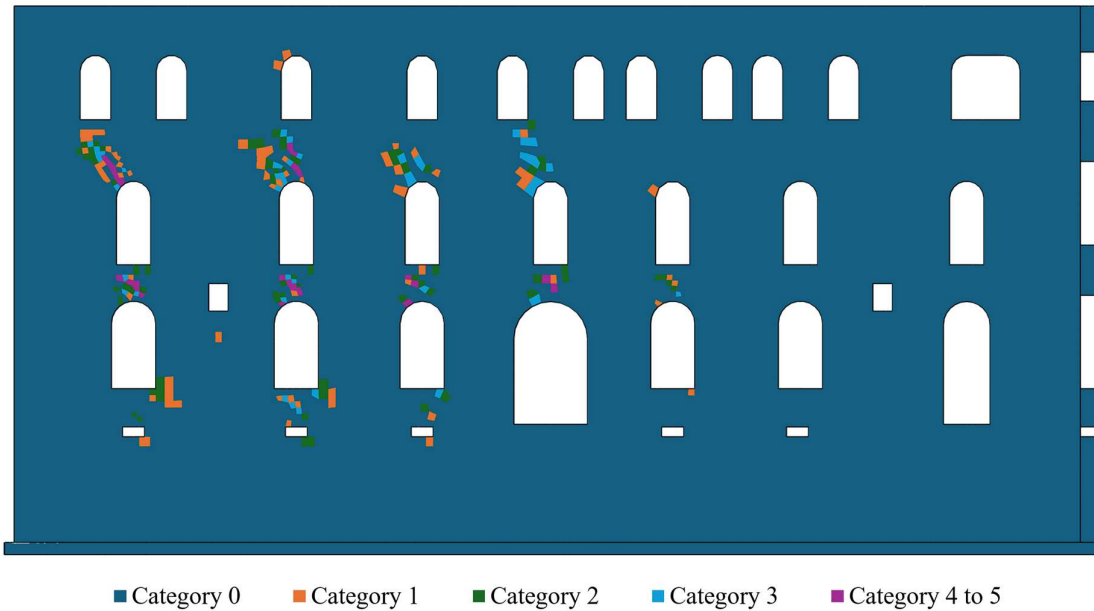


Figure 6.65. Uncoupled model: Damage category map of the NORTH facade for the VLMEAN models with the CDP MAX masonry constitutive behavior

For the SOUTH facade the results of the ELAS and CDP models show respectively:

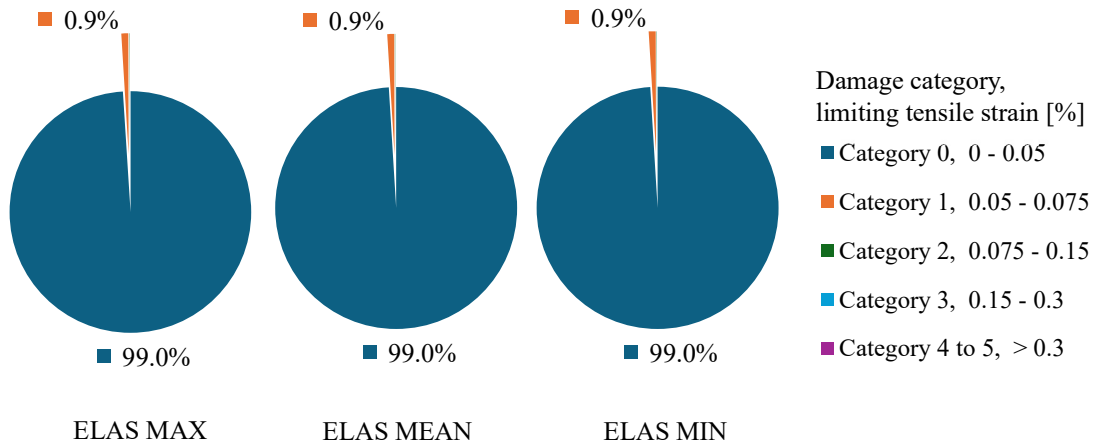


Figure 6.66. Uncoupled model: Cumulative portions of the SOUTH facade belonging to the damage categories based on the limiting tensile strain, for the VLMEAN models with the ELAS masonry constitutive behavior

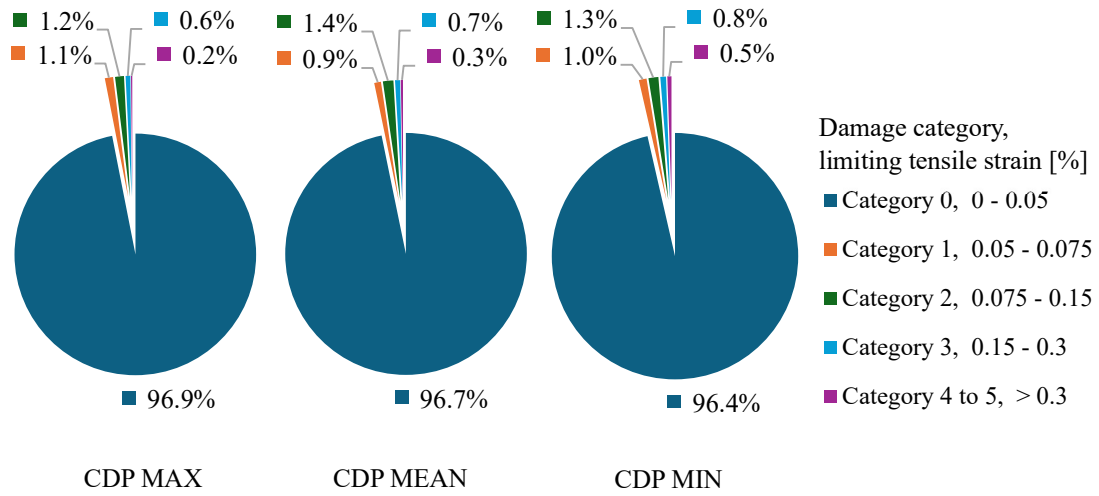


Figure 6.67. Uncoupled model: Cumulative portions of the SOUTH facade belonging to the damage categories based on the limiting tensile strain, for the VLMEAN models with the CDP masonry constitutive behavior

These percentages are obtained by calculating the portion of finite elements that enter each category, from a total of 12014 elements that compose the SOUTH facade model. Particularly, for the CDP MAX model the detailed damage category map shows:

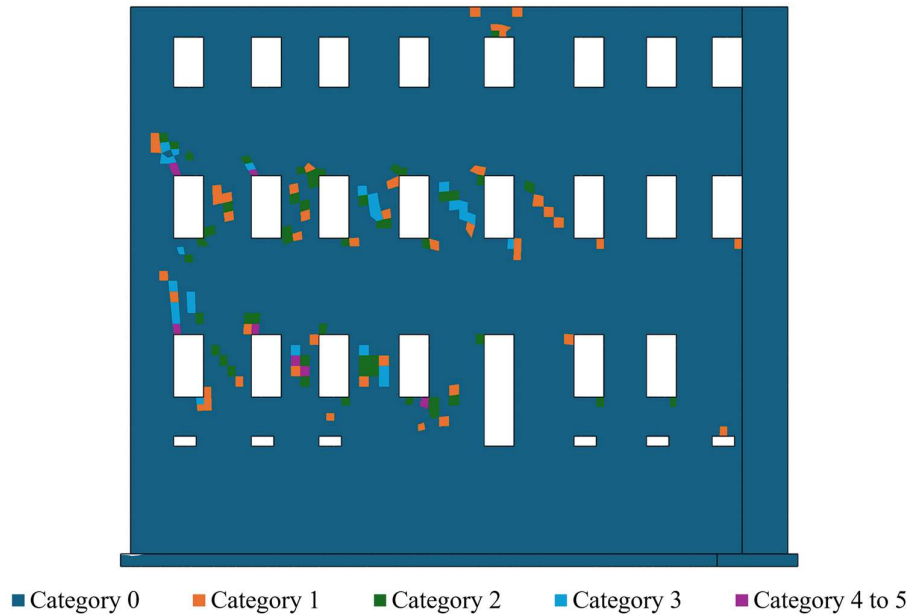


Figure 6.68. Uncoupled model: Damage category map of the SOUTH facade for the VLMEAN models with the CDP MAX masonry constitutive behavior



For the CEAST and CNORTH facades the results of the ELAS and CDP models show respectively:

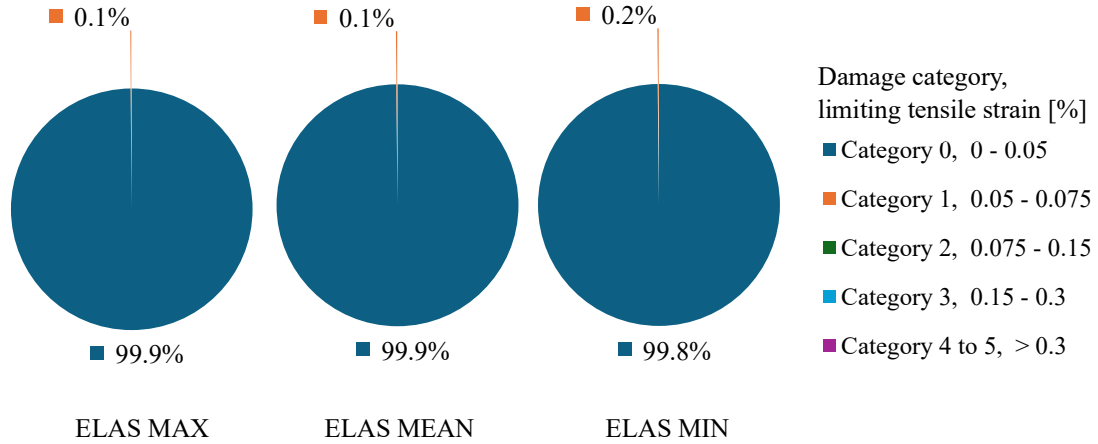


Figure 6.69. Uncoupled model: Cumulative portions of the CEAST and CNORTH facades belonging to the damage categories based on the limiting tensile strain, for the VLMEAN models with the ELAS masonry constitutive behavior

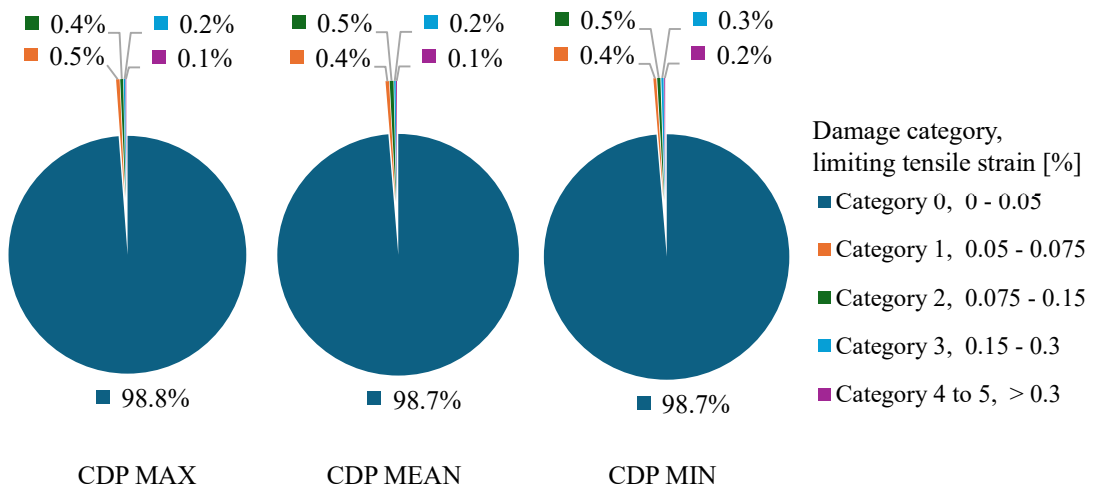


Figure 6.70. Uncoupled model: Cumulative portions of the CEAST and CNORTH facades belonging to the damage categories based on the limiting tensile strain, for the VLMEAN models with the CDP masonry constitutive behavior

These percentages are obtained by calculating the portion of finite elements that enter each category, from a total of 61233 elements that compose the CEAST and CNORTH facade models. Particularly, for the CDP MAX model the detailed damage category map shows:

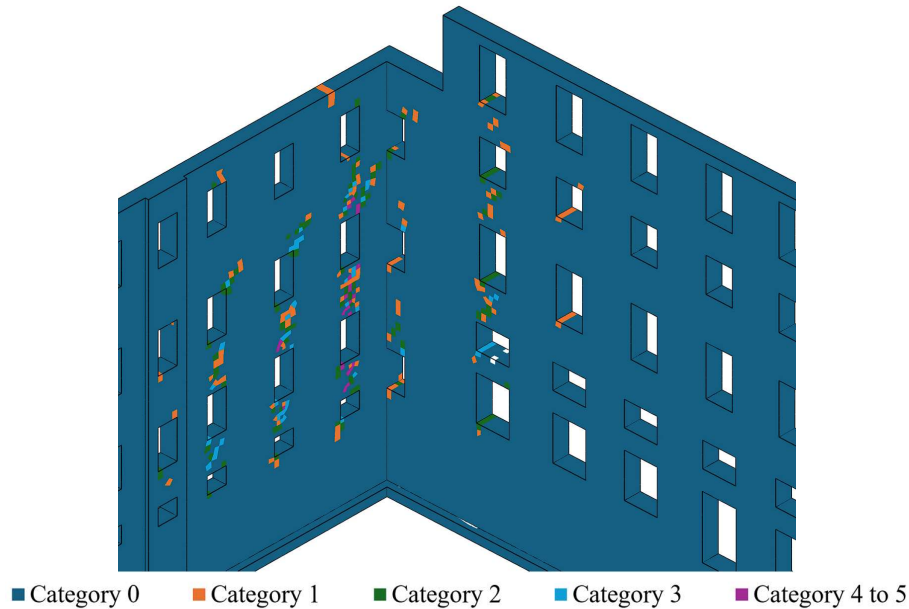


Figure 6.71. Uncoupled model: Damage category map of the CEAST and CNORTH facades for the VLMEAN models with the CDP MAX masonry constitutive behavior

From all these graphs, the facade that shows the most concentrated risk of damage is the SOUTH facade, only because it has the lowest amount of elements of the four. In elasticity, the NORTH facade is the one showing the highest amount of elements entering categories of damage 1 and 2 with 272 elements out of 41563. In elastoplasticity, the same NORTH facade shows the highest amount of elements surpassing category of damage 0 (negligible) with 607 elements out of 41563, and it also has the largest number of elements entering categories of damage 3 to 5, above the threshold of 0.15% for the limiting tensile strain, with 251 elements out of 41563. This information is presented here both in terms of percentage (from past pie charts) and number of elements because none of these results by themselves serve to identify the most critical facade, but at most they can be paired with Figure 6.60 to Figure 6.62 to focus accordingly the monitoring of the facades during the tunnelling works.

## 6.2.3 VLMIN subsidence

### 6.2.3.1 Entire building

The tensile strains experienced by the model of the building when the VLMIN subsidence is applied are shown in the next Figure 6.72. As a reminder, the VLMIN model is the same JET model in the greenfield analyses (refer to 6.1.3) in which the improved soil with the jet grouting umbrella is included and the minimum volume loss

is observed. Attention is also driven towards the facades that manifest the most propagated, higher major principal strains. These will be individually studied in more detail in the next subsection.

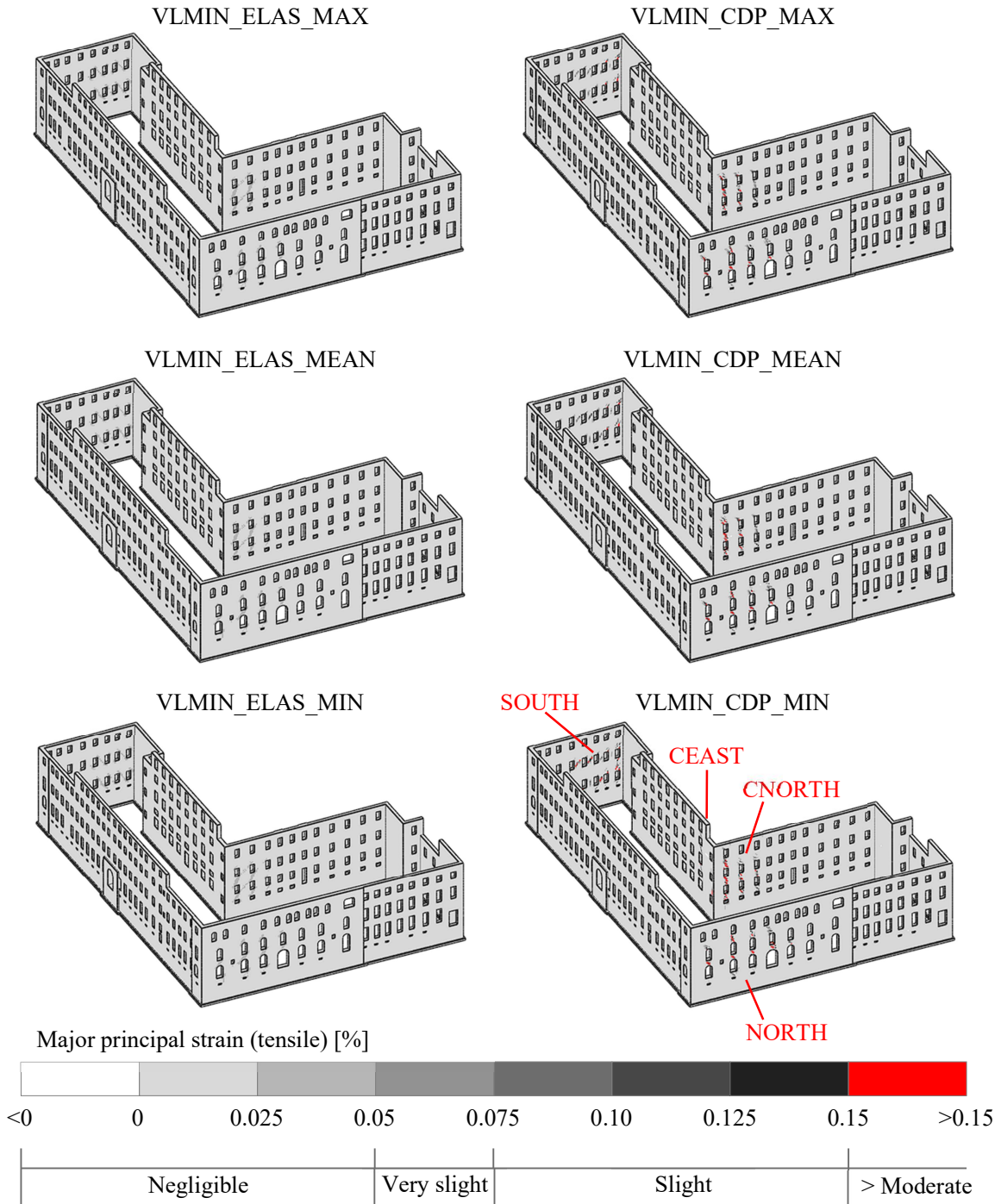


Figure 6.72. Uncoupled model: Major principal strains of the facades for the VLMIN models with both ELAS and CDP masonry constitutive behaviors

From the figure above, although it will be revised in more detail per facade below, it results that the tensile strains are negligible for all elastic models (ELAS), showing no

differences between the ELAS MAX, MEAN and MIN models. This is also demonstrated in next Figure 6.73, which is based on Table 2.1 related to the damage categories suggested by Burland et al. (1996) and Boscardin and Cording (1989). Indeed, the tensile strains experienced by the perimetral facades of the ELAS models fall completely (100%) in the damage category 0 for negligible severity (in reality, a very small percentage equal to 0.02% falls in category 1, related to the NORTH facade). This percentage is obtained by calculating the portion of finite elements that enter each category, from a total of 141350 elements that compose the building model.

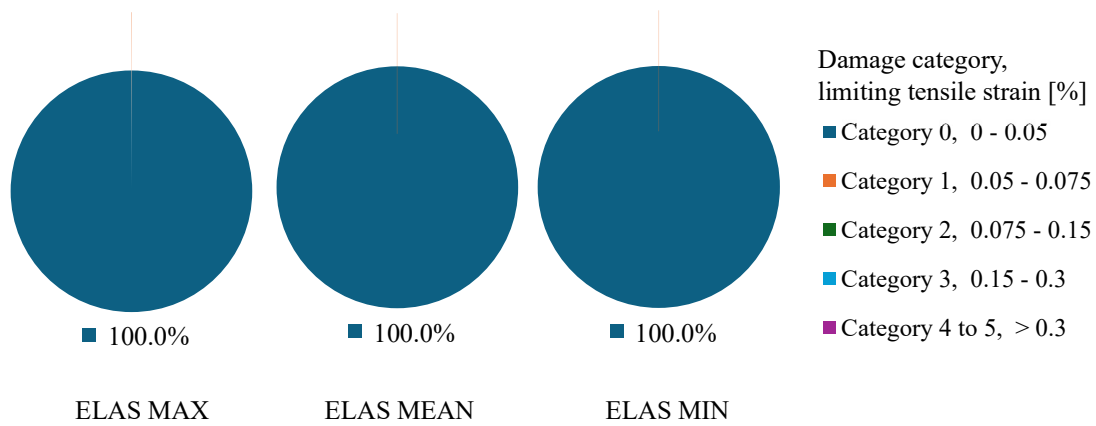


Figure 6.73. Uncoupled model: Cumulative portions of the facades belonging to the damage categories based on the limiting tensile strain, for the VLMIN models with the ELAS masonry constitutive behavior

For the elastoplastic models the effect of changing the CDP constitutive behavior is barely noticeable. In the next section where the individual facades are analyzed it is somewhat visible how some portions of the walls enter into more severe damage categories, the weaker the constitutive model becomes; nevertheless, the variations from one CDP model to the other appear trivial in the long run. For all, the elastoplastic models (CDP) always predict higher severity of damage in more extent areas of the facades than the elastic models (ELAS), supporting the findings of other authors reviewed in the past heading 3.2.2. In particular, based on Table 2.1 related to the damage categories suggested by Burland et al. (1996) and Boscardin and Cording (1989), according to Figure 6.74 the tensile strains experienced by the perimetral facades of the CDP models fall mainly (99.4% to 99.5%) in the damage category 0 for negligible severity, while a 0.2% enters in category 1 for very slight severity of damage, a 0.2% in the category 2 for slight severity, .0.1% in category 3 for moderate severity and up to 0.1% concern the categories 4 and 5 for severe to very severe level. These percentages are obtained by calculating the portion of finite elements that enter each category, from a total of 141350 elements that compose the building model.

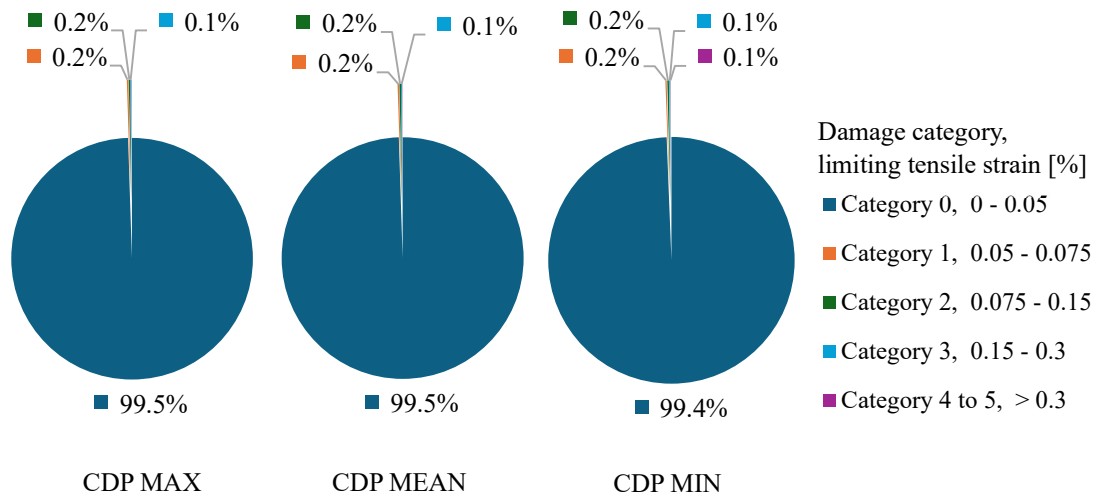


Figure 6.74. Uncoupled model: Cumulative portions of the facades belonging to the damage categories based on the limiting tensile strain, for the VLMIN models with the CDP masonry constitutive behavior

These past figures, however, are too coarse as they account for large volumes of facades that are far from entering into interaction with the basin of subsidence. For example, the WEST facade (refer to Figure 5.19) is still included in the pie charts from before summing entirely for the percentage of category 0 of damage, given that it is relatively far from the tunnel axis and thus, it is seldom affected by the excavation. In this way, in the next section the facades that present the most propagated, higher major principal strains are individually analyzed to determine how affected they are by the excavation.

### 6.2.3.2 Individual facades

For all the models, the facades that present the most propagated, higher strains are those with a near orthogonal orientation to the tunnel axis, directly the NORTH, CNORTH and SOUTH facades. The CEAST facade also shows high strains but only at the corner where it enters in interaction with the CNORTH facade. The next Figure 6.75, Figure 6.76 and Figure 6.77 show in detail the results of the parametric analyses for these facades.

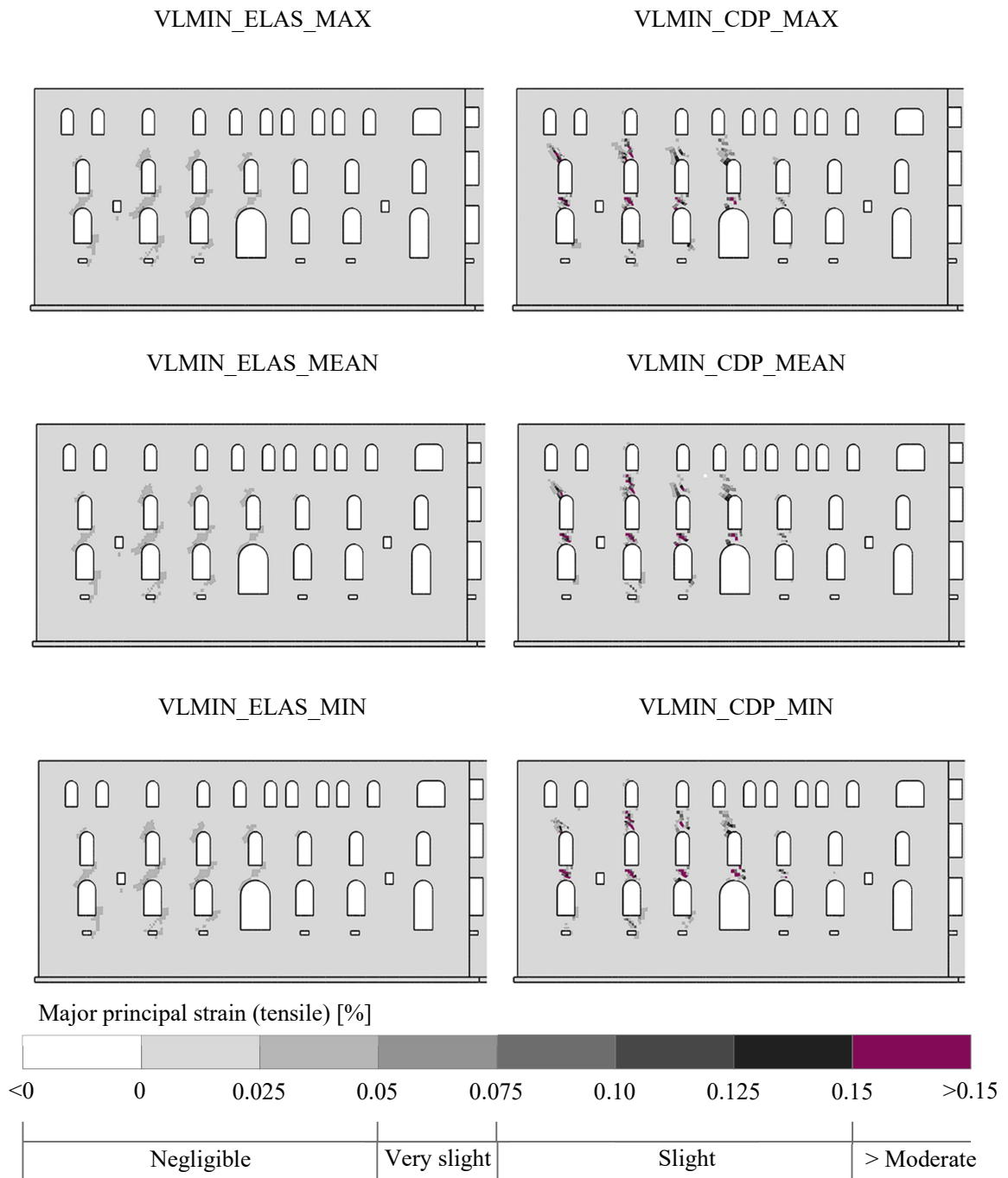


Figure 6.75. Uncoupled model: Major principal strains of the NORTH facade for the VLMIN models with both ELAS and CDP masonry constitutive behaviors

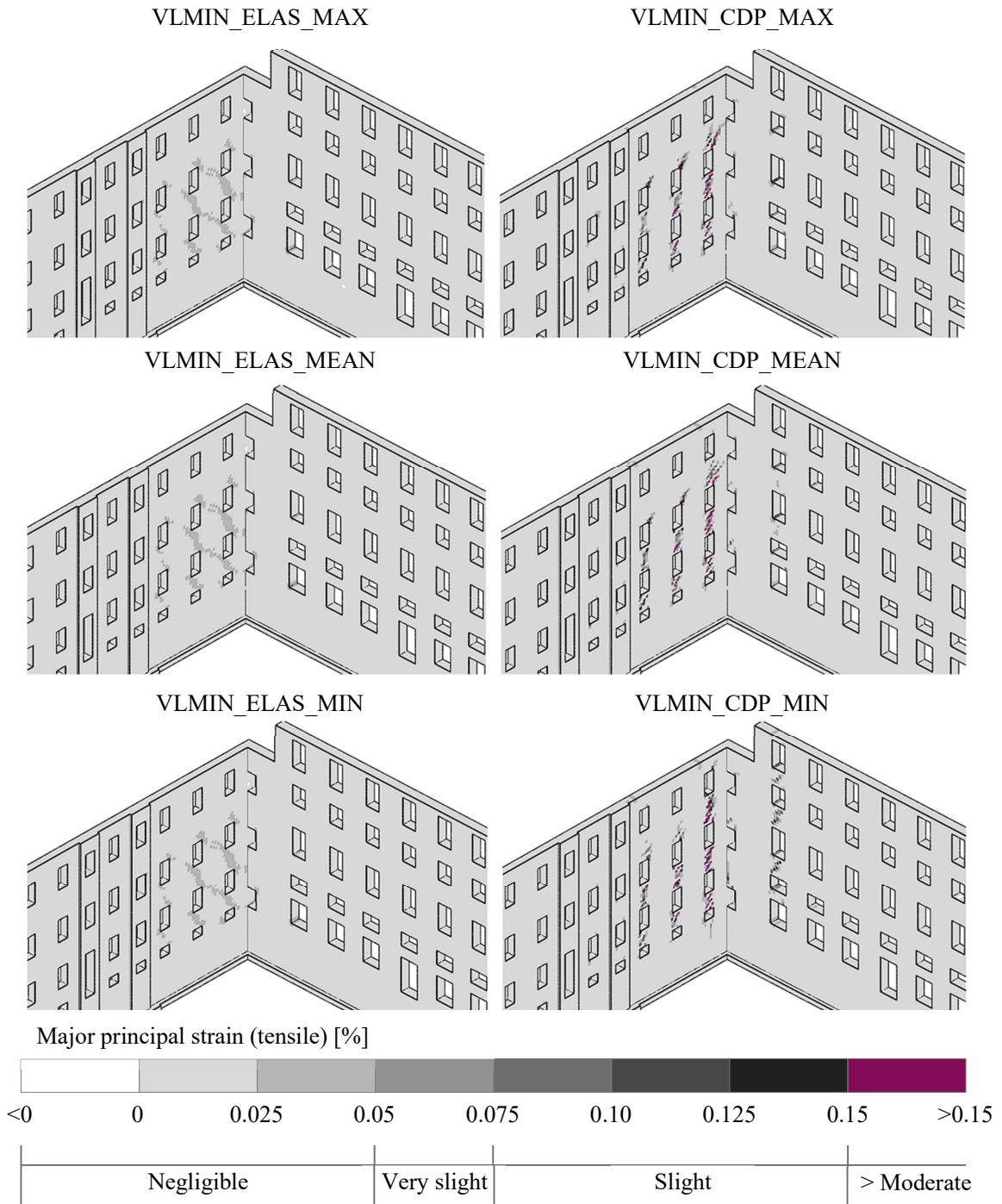


Figure 6.76. Uncoupled model: Major principal strains of the CNORTH and CEAST facades for the VLMIN models with both ELAS and CDP masonry constitutive behaviors

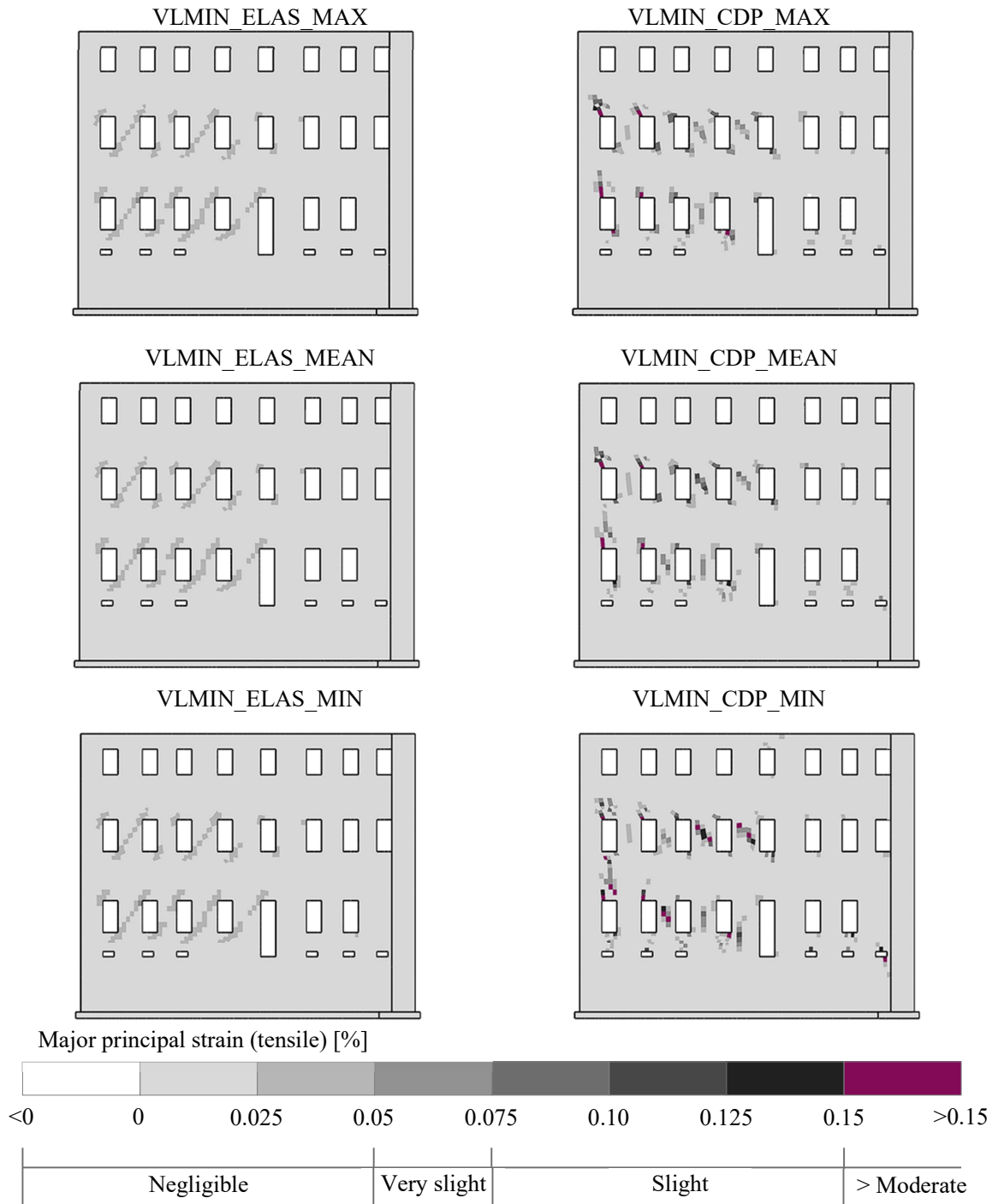


Figure 6.77. Uncoupled model: Major principal strains of the SOUTH facade for the VLMIN models with both ELAS and CDP masonry constitutive behaviors

Once again, based on Table 2.1 related to the damage categories suggested by Burland et al. (1996) and Boscardin and Cording (1989), the next figures show the proportion of risk of damage experienced by each individual facade.



For the NORTH facade the results of the ELAS and CDP models show respectively:

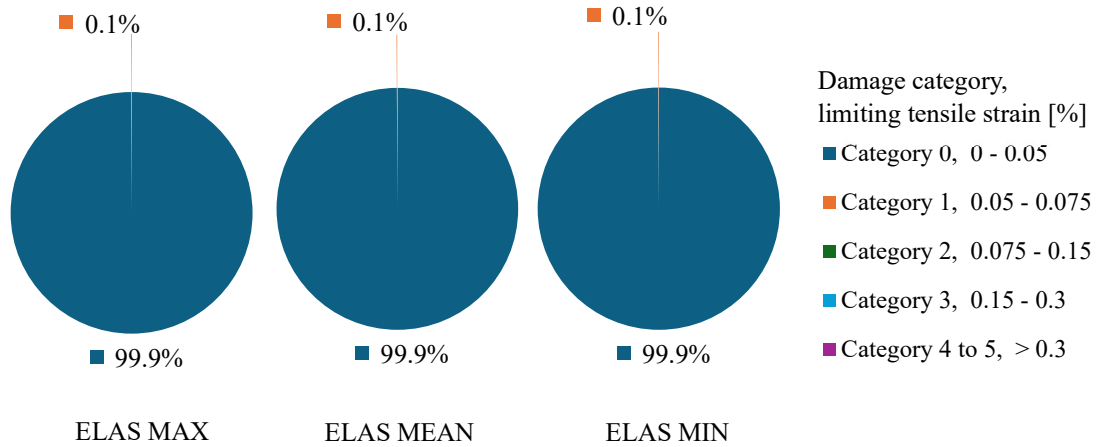


Figure 6.78. Uncoupled model: Cumulative portions of the NORTH facade belonging to the damage categories based on the limiting tensile strain, for the VLMIN models with the ELAS masonry constitutive behavior

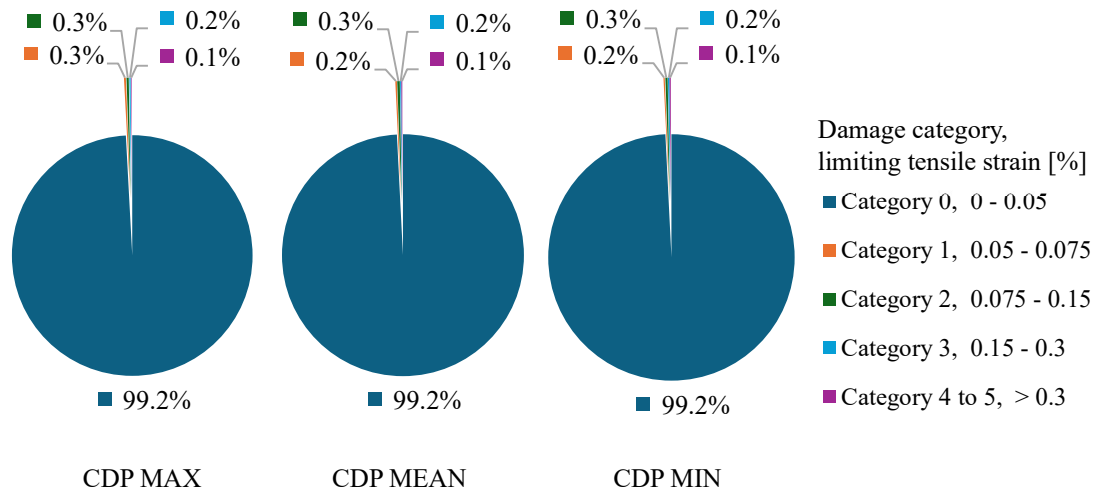


Figure 6.79. Uncoupled model: Cumulative portions of the NORTH facade belonging to the damage categories based on the limiting tensile strain, for the VLMIN models with the CDP masonry constitutive behavior

These percentages are obtained by calculating the portion of finite elements that enter each category, from a total of 41563 elements that compose the NORTH facade model. Particularly, for the CDP MAX model the detailed damage category map shows:

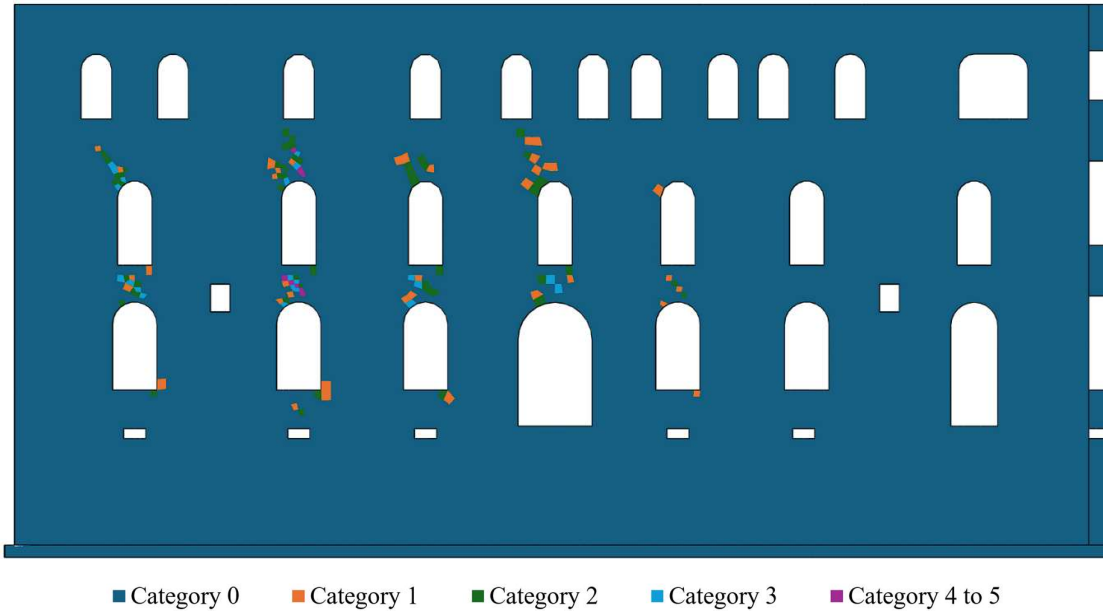


Figure 6.80. Uncoupled model: Damage category map of the NORTH facade for the VLMIN models with the CDP MAX masonry constitutive behavior

For the SOUTH facade the results of the ELAS and CDP models show respectively:

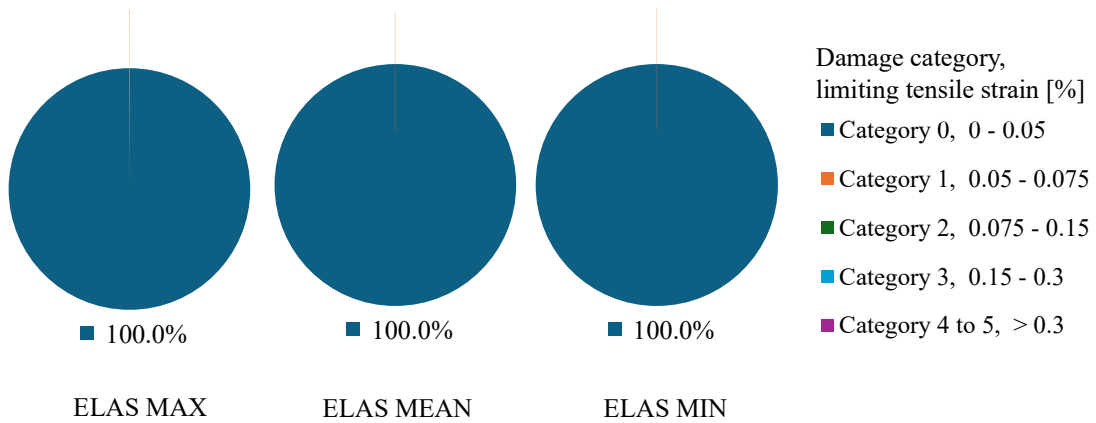


Figure 6.81. Uncoupled model: Cumulative portions of the SOUTH facade belonging to the damage categories based on the limiting tensile strain, for the VLMIN models with the ELAS masonry constitutive behavior

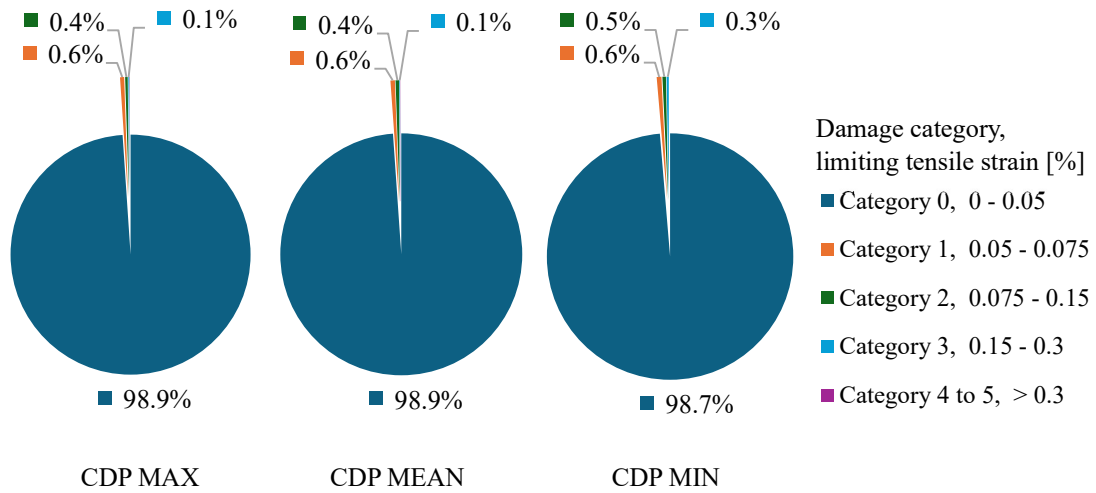


Figure 6.82. Uncoupled model: Cumulative portions of the SOUTH facade belonging to the damage categories based on the limiting tensile strain, for the VLMIN models with the CDP masonry constitutive behavior

These percentages are obtained by calculating the portion of finite elements that enter each category, from a total of 12014 elements that compose the SOUTH facade model. Particularly, for the CDP MAX model the detailed damage category map shows:

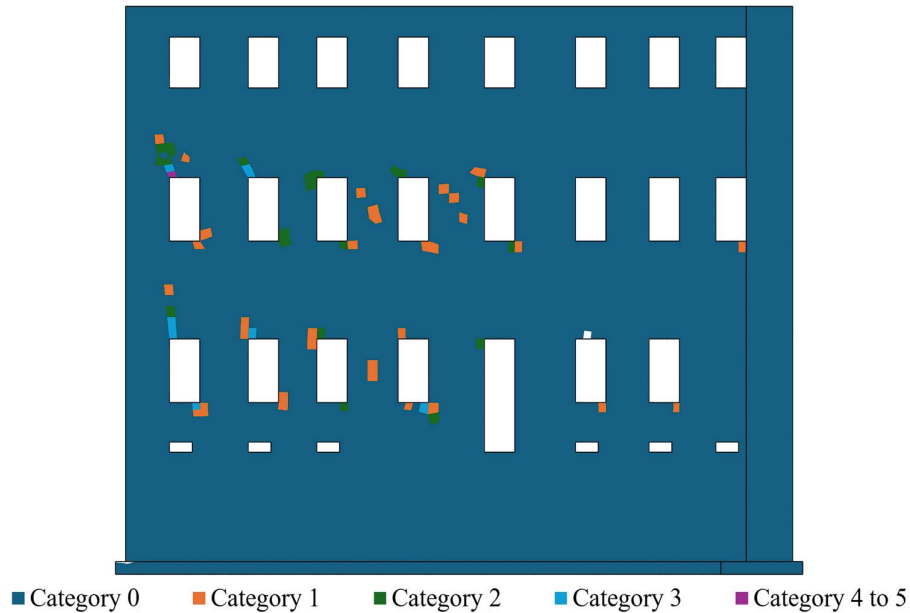


Figure 6.83. Uncoupled model: Damage category map of the SOUTH facade for the VLMIN models with the CDP MAX masonry constitutive behavior

For the CEAST and CNORTH facades the results of the ELAS and CDP models show respectively:

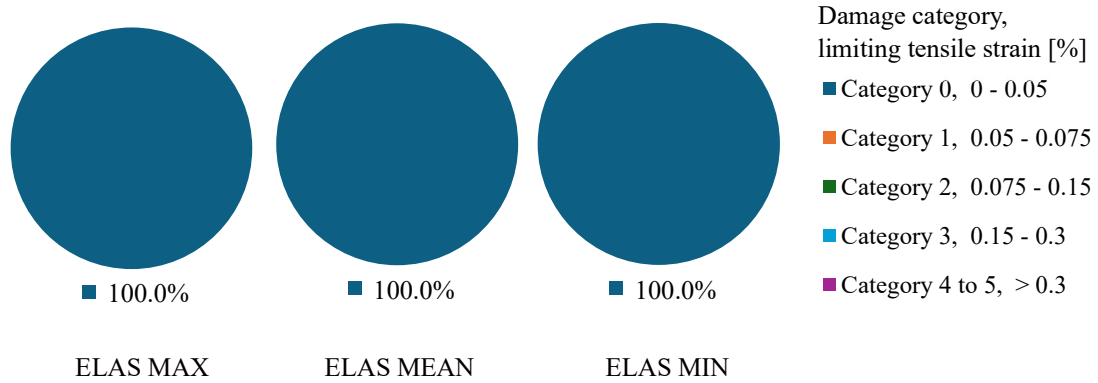


Figure 6.84. Uncoupled model: Cumulative portions of the CEAST and CNORTH facades belonging to the damage categories based on the limiting tensile strain, for the VLMIN models with the ELAS masonry constitutive behavior

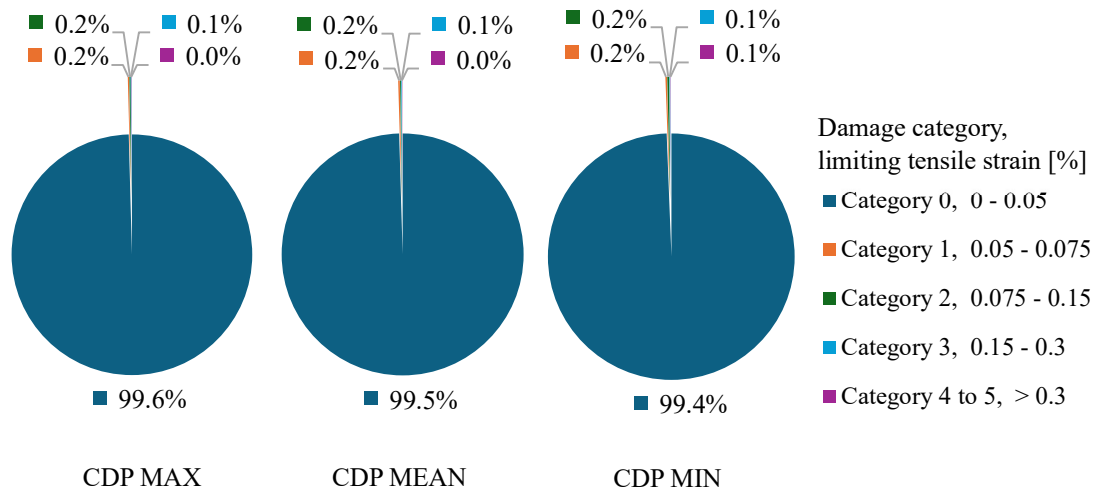


Figure 6.85. Uncoupled model: Cumulative portions of the CEAST and CNORTH facades belonging to the damage categories based on the limiting tensile strain, for the VLMIN models with the CDP masonry constitutive behavior

These percentages are obtained by calculating the portion of finite elements that enter each category, from a total of 61233 elements that compose the CEAST and CNORTH facade models. Particularly, for the CDP MAX model the detailed damage category map shows:

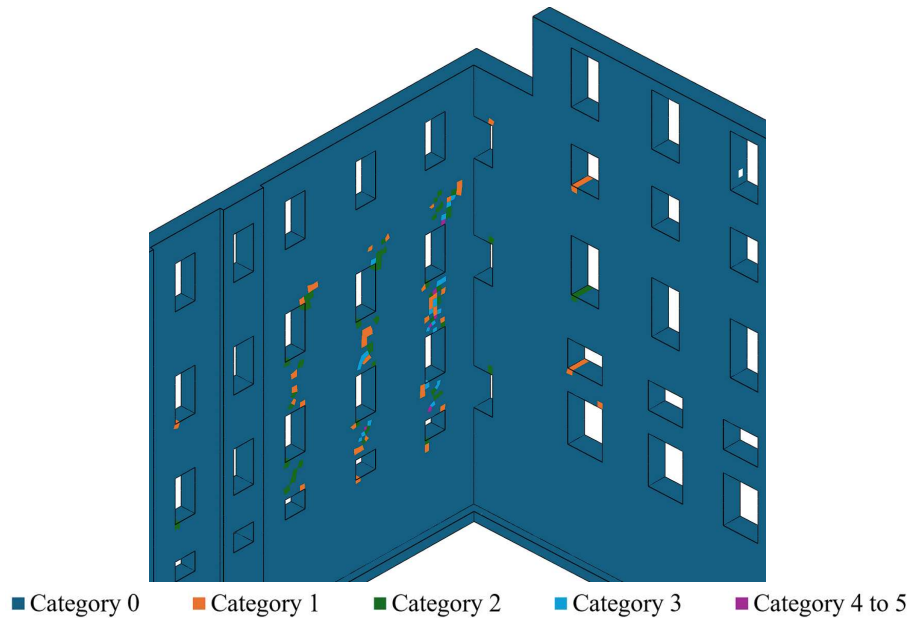


Figure 6.86. Uncoupled model: Damage category map of the CEAST and CNORTH facades for the VLMIN models with the CDP MAX masonry constitutive behavior

From all these graphs, the facade that shows the most concentrated damage risk is the SOUTH facade, only because it has the lowest amount of elements of the four. This facade, nevertheless, in comparison to the other three does not contain elements in the categories 4 or 5 of damage (it has only two). In elasticity all the facades belong to the category 0 for negligible severity of damage (except for the NORTH facade that has 31 elements out of 41563 in category 1 for very slight damage). In elasto-plasticity, the NORTH facade shows the highest amount of elements surpassing category of damage 0 (negligible) with 336 elements out of 41563, and it also has the largest number of elements entering categories of damage 3 to 5, above the threshold of 0.15% for the limiting tensile strain, with 112 elements out of 41563. This information is presented here both in terms of percentage (from past pie charts) and number of elements because none of these results by themselves serve to identify the most critical facade, but at most they can be paired with Figure 6.75 to Figure 6.77 to focus accordingly the monitoring of the facades during the tunnelling works.

#### 6.2.4 Comparison between uncoupled model results

From the conducted parametric analyses, the first point to become clear is that the variations between elastic models ELAS MAX, ELAS MEAN and ELAS MIN are negligible if not inexistent, as well as the variations between elastoplastic models CDP

MAX, CDP MEAN and CDP MIN are marginal, both from the facade damage category maps and the portions in the pie charts, for any level of subsidence applied. This suggests that, in the range of parameters selected for the masonry for the current model of the perimetral facades, any of these elastic or elastoplastic models can provide consistent results. This will be of great advantage when computing the coupled soil – structure interaction models, because it will permit to reduce the number of parametrical analyses while using the constitutive formulations that had the higher performance, especially the elastoplastic ones. As an example, a typical CDP MAX model would compute in half the time of a CDP MIN model. In this case, the computationally expensive coupled interaction model will be configured with the stronger CDP MAX formulation, given that it reduces considerably the run-time while resulting in marginally different results from the weaker CDP MIN model.

The second point is that all ELAS models resulted in degrees of severity lower than *moderate*, and it is reminded that in real life, damage related to these can result from a variety of causes, even shrinkage or thermal effects from the building itself. It is, therefore, that the facades are regarded to be at “low risk” of damage if elasticity alone is used for prediction, meaning that structural integrity is not compromised and repair works can be performed easily and economically (Mair, Taylor, & Burland, 1996).

On the other hand, if elasto-plasticity is summoned, damage risk becomes clearer and more severe the higher the settlement volume loss becomes. For all the NORTH, CNORTH, CEAST, and SOUTH facades, the finite elements enter in degrees of severity equal to and higher than *moderate*; however, this is witnessed in localized areas that should be the focus of careful monitoring during the construction of the tunnel.

Still, from the most pessimistic (VLMAX for the maximum volume loss, same model emulating the TBM steering gap of 6 cm, before referred to as GAP6 model) to the most optimistic (VLMIN for the minimum volume loss, same model including the presence of the jet grouting umbrella, before referred to as JET model) greenfield volume loss models, a clear improvement of the building’s state post excavation is observed. The next analyses will be effected for the CDP MAX models, seeing that they evidence minor differences with the rest of the elasto-plastic constitutive proposals.

In the next Figure 6.87 of the NORTH facade, the VLMAX model shows the greatest extension and intensification of tensile strains, seemingly worsening with the elevation in correspondence to the hogging deformation mode (see some strain concentrations appear at the eaves of the facade). On the contrary, the VLMIN model mainly experiences concentrated strains at the levels of the slabs of the second and third floors. Since in the simulation the stiffening contribution of the slabs in the vertical was neglected and the joint slab – facade was not modelled, it could be argued that these strains in the real case might be absorbed by the slab.

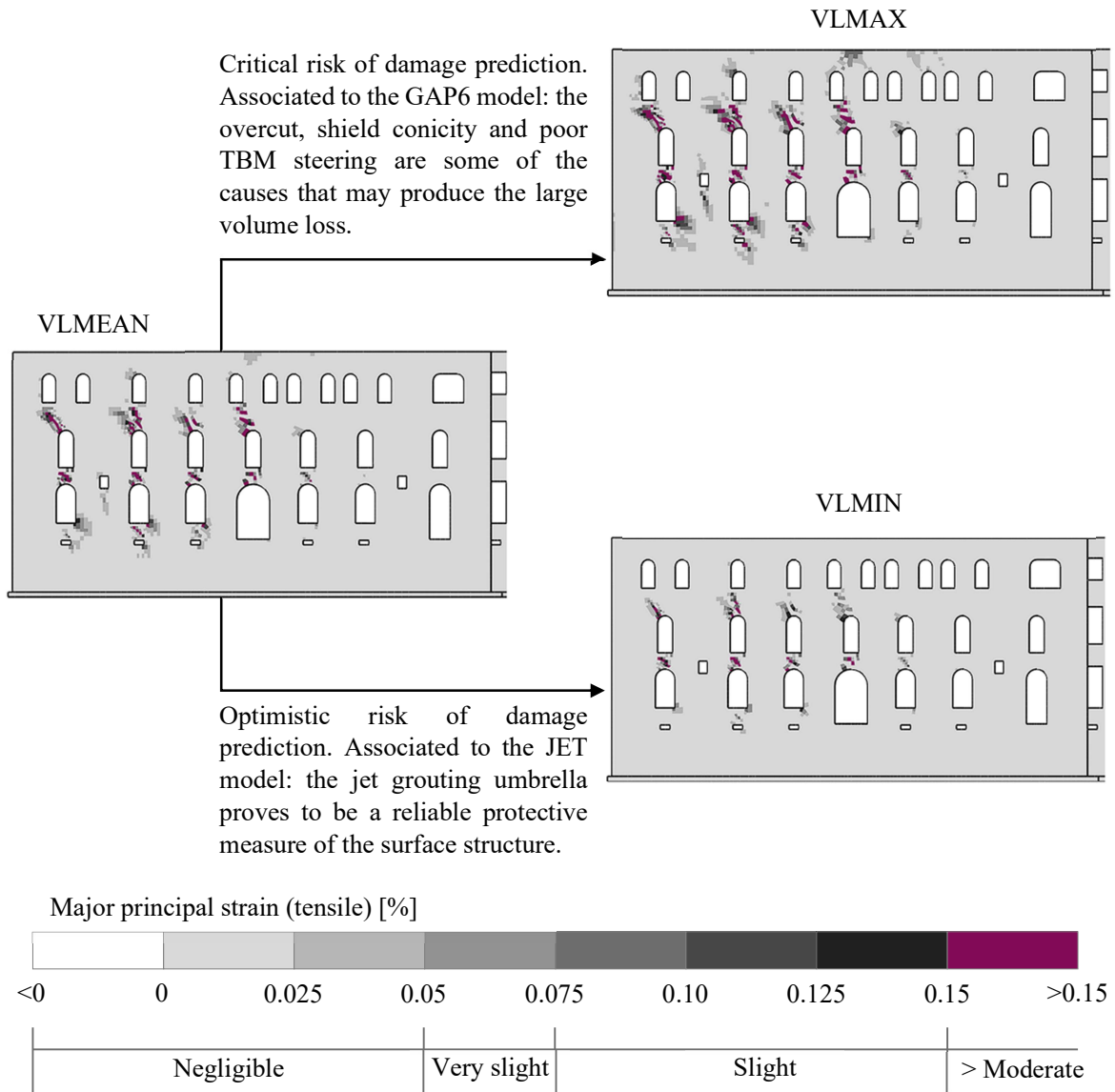


Figure 6.87. Uncoupled model: Comparison of the potential effects of the greenfield volume loss models in the NORTH facade

The CNORTH and CEAST facades perform similarly. In this case, however, the concentration of high tensile strains (above 0.15%) in the CEAST facade occurs especially in the VLMAX model, whereas it is non-existent in the VLMIN one:

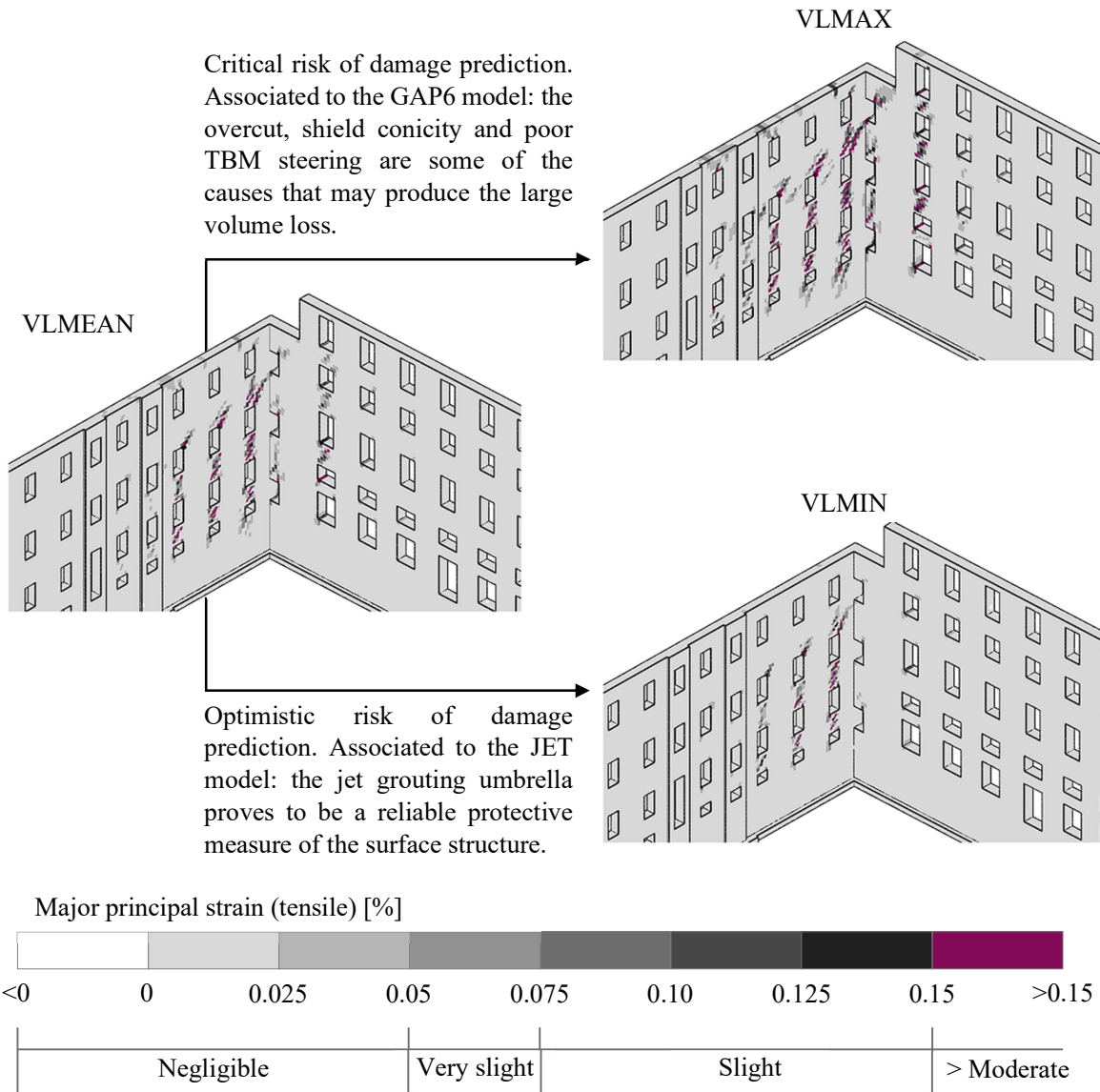


Figure 6.88. Uncoupled model: Comparison of the potential effects of the greenfield volume loss models in the CEAST and CNORTH facades

And for the SOUTH facade, in the VLMIN model the presence of tensile strains higher than 0.15% is also minor, compared to the other two predictions:



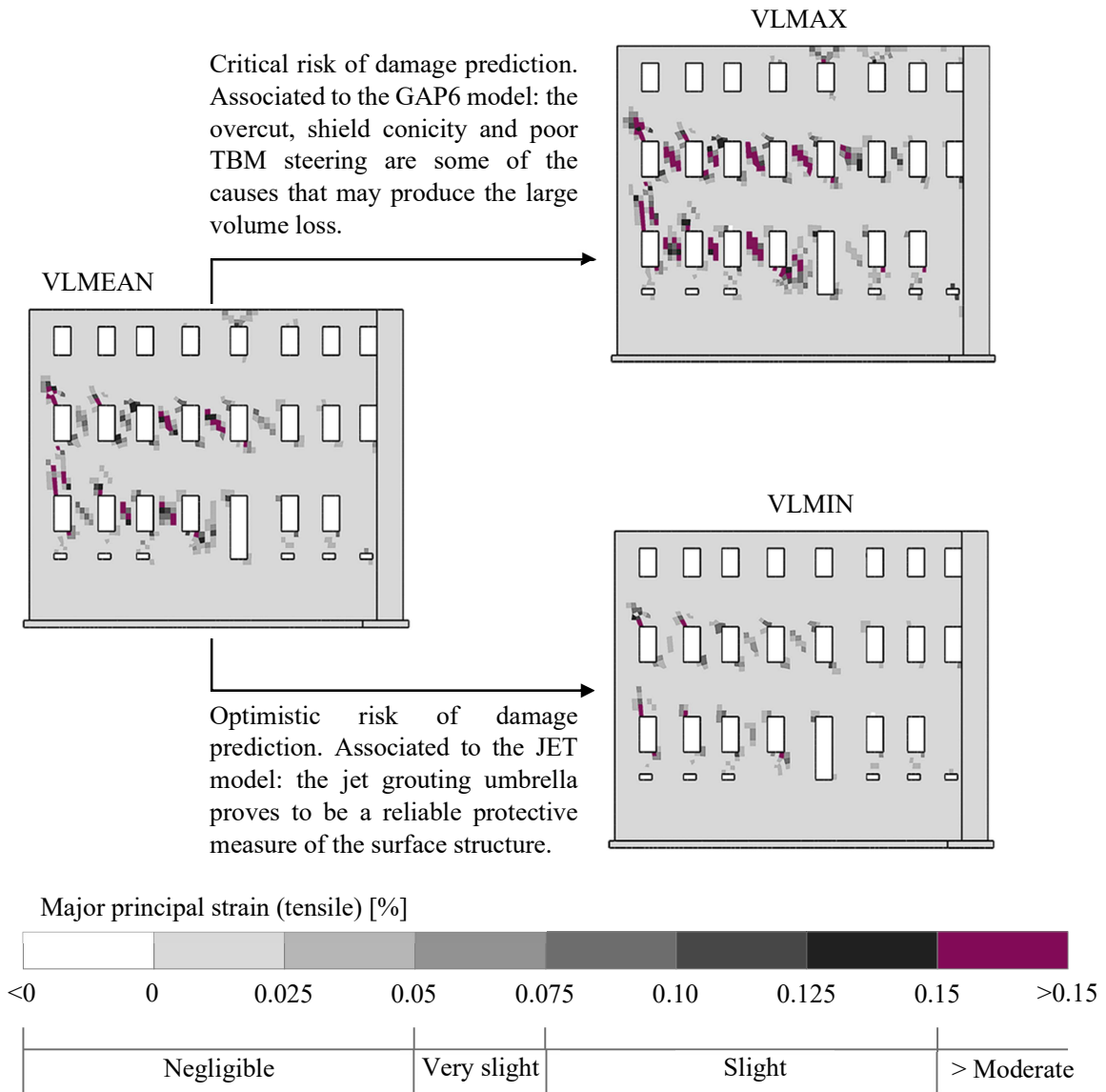


Figure 6.89. Uncoupled model: Comparison of the potential effects of the greenfield volume loss models in the SOUTH facade

### 6.3 Building risk of damage estimation with the EBA method

Contrary to the framework for the building risk of damage assessment of Figure 2.19 in which before formulating complex numerical models, the EBA method (explained in section 2.4.1) should be applied to estimate the building damage from greenfield settlement troughs, here the method is applied after for two reasons: first, as explained in Chapter 4, Infratrasporti. To had already identified that the building Palazzo Campana could present high degrees of damage severity using the EBA method, therefore from the beginning the main interest was to produce a more complex three-dimensional

numerical evaluation. Second, because the particularities of the situation, directly the non-conventional building layout and skewed angle with respect to the tunnel excavation axis, presented a challenge when considering which portion of the facades of the building to evaluate, with the high possibility of producing unreliable analyses if the settlement trough was regarded as completely orthogonal to any particular facade. Therefore, hereon the settlements imposed below the facades of the uncoupled building models are analyzed with the EBA method and are compared against the elasto-plastic model results. For the NORTH facade:

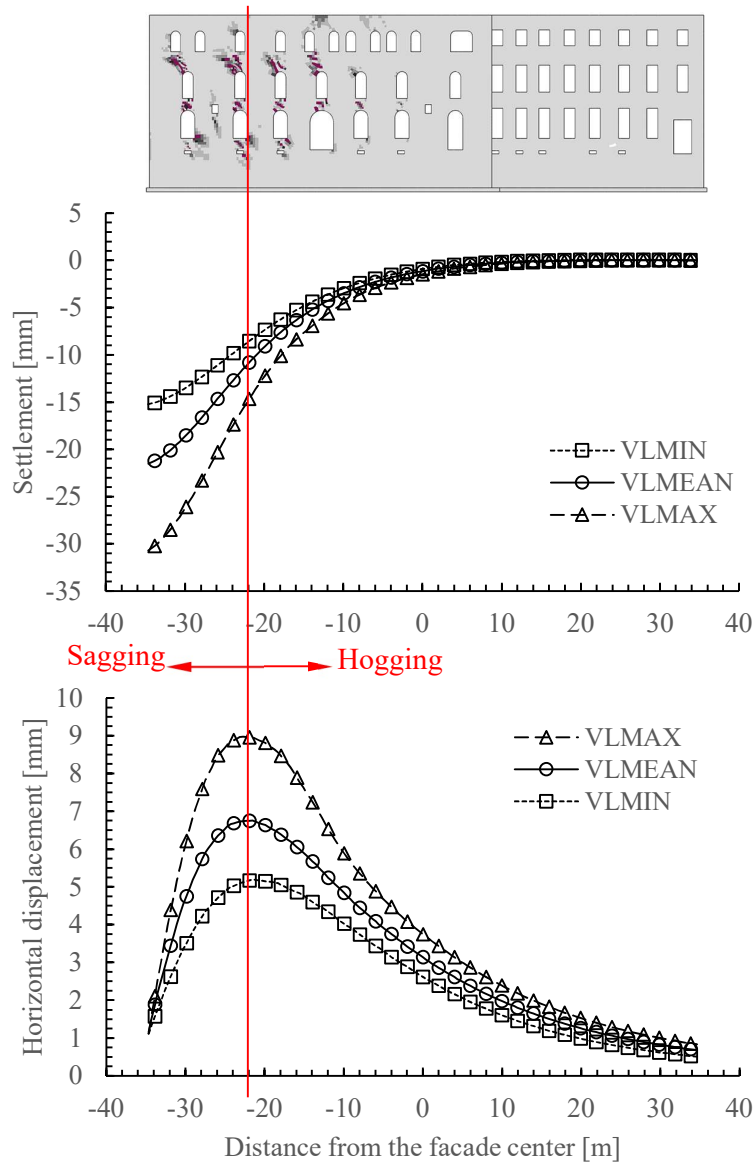


Figure 6.90. Greenfield settlements and horizontal displacements induced below the NORTH facade

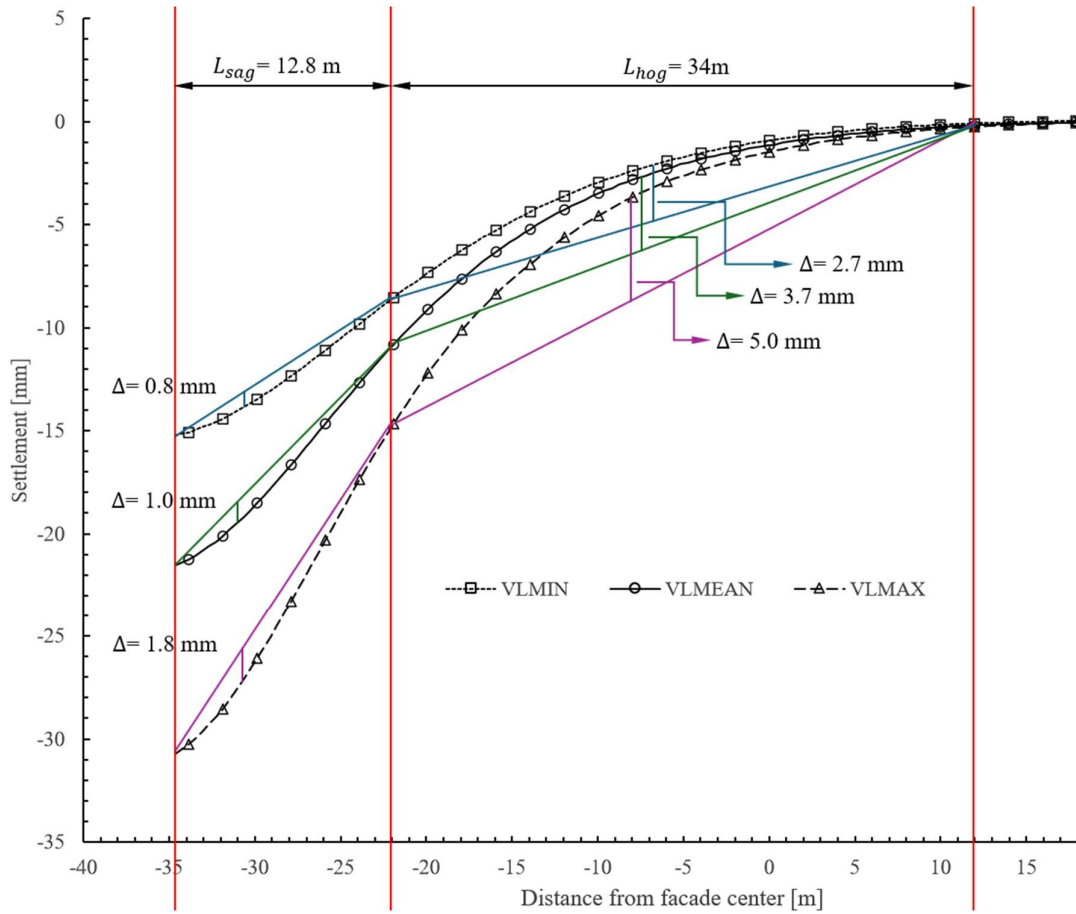


Figure 6.91. Parameters for the calculation of the deflection ratio of the NORTH facade in greenfield conditions

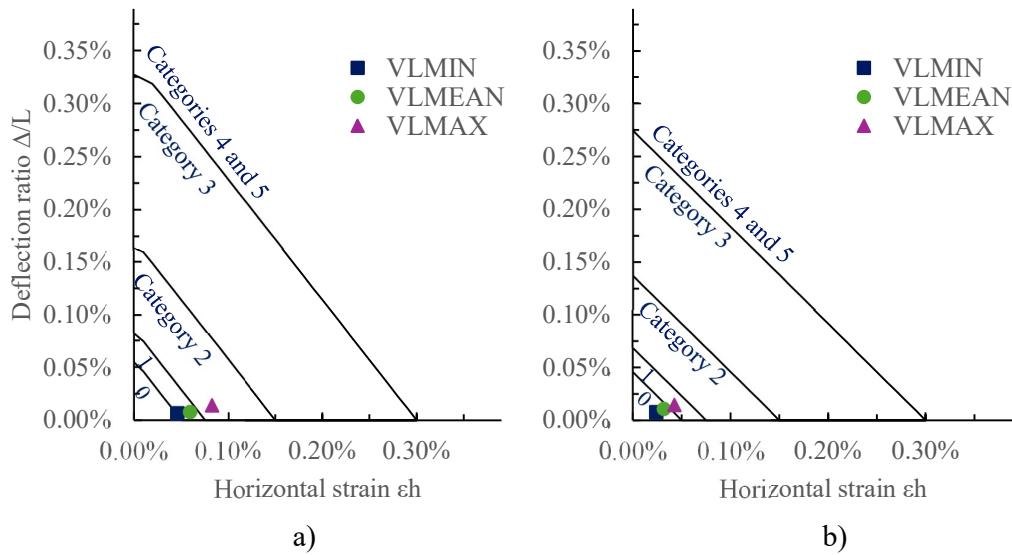


Figure 6.92. Damage category charts for the NORTH facade in greenfield conditions and ELAS MAX parameters, for a) sagging and b) hogging deformation modes

For the CNORTH facade:

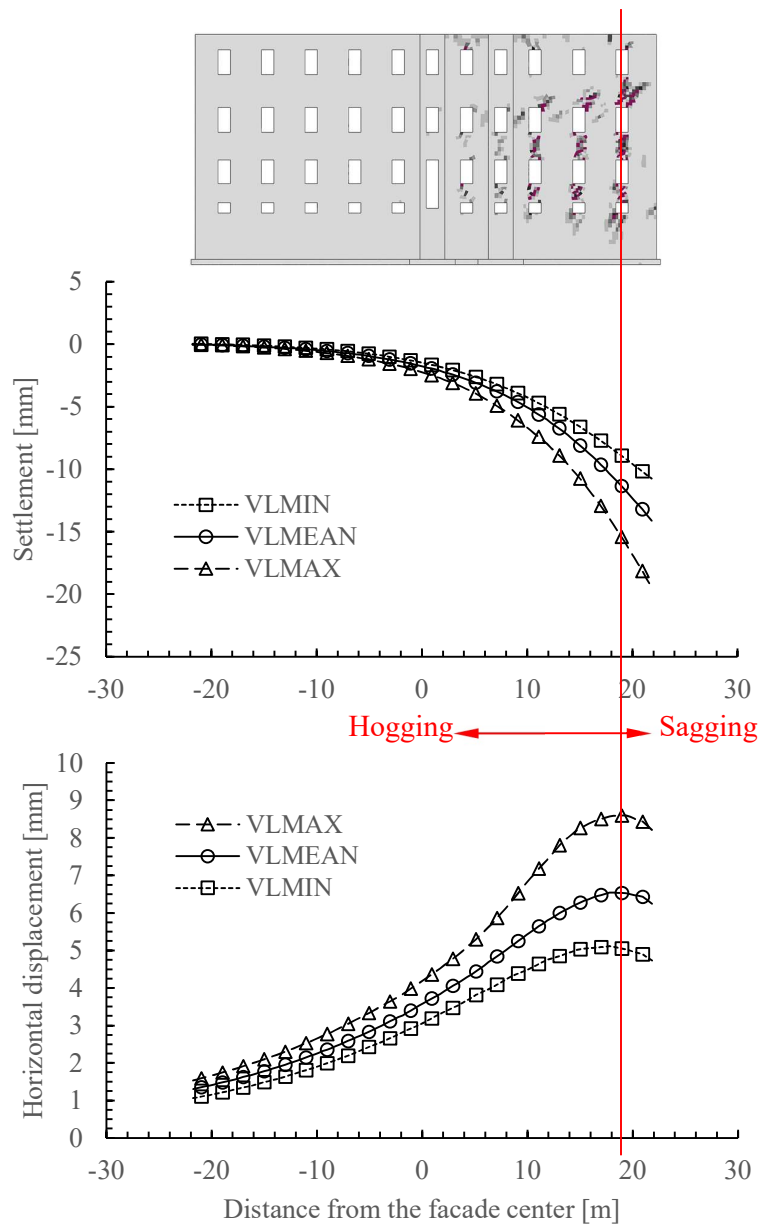


Figure 6.93. Greenfield settlements and horizontal displacements induced below the CNORTH facade

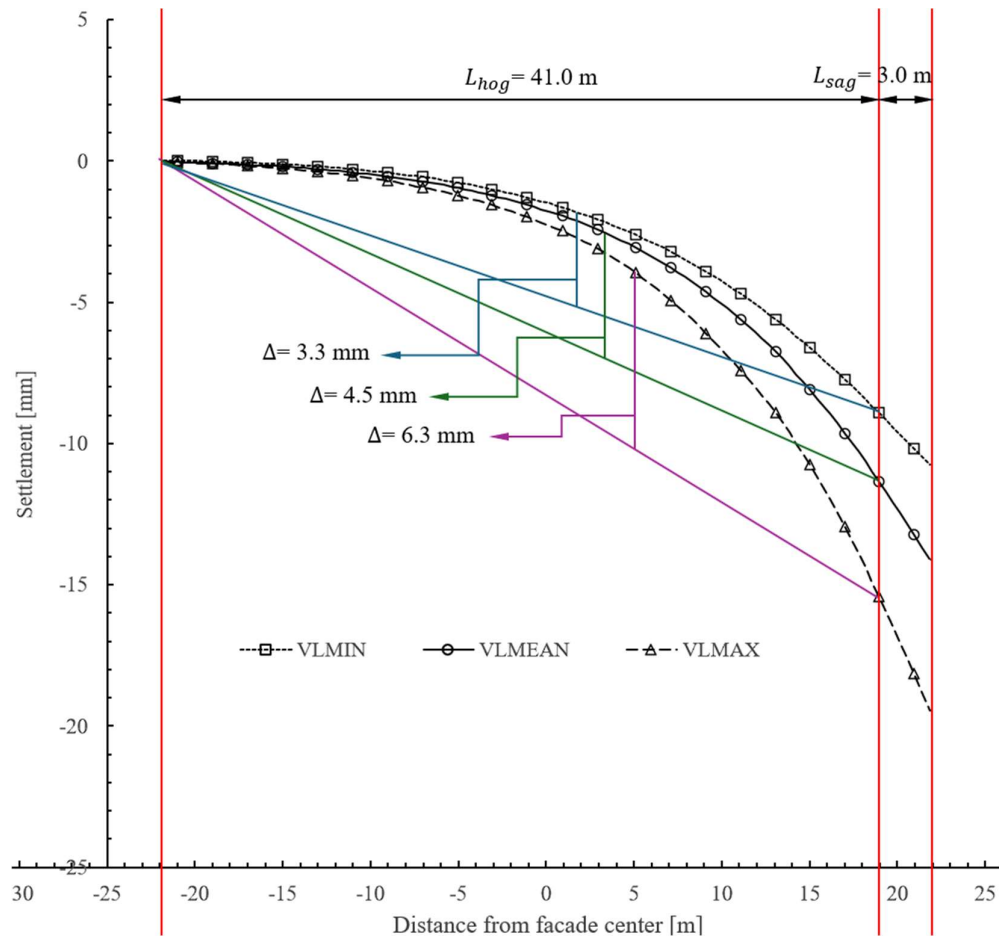


Figure 6.94. Parameters for the calculation of the deflection ratio of the CNORTH facade in greenfield conditions

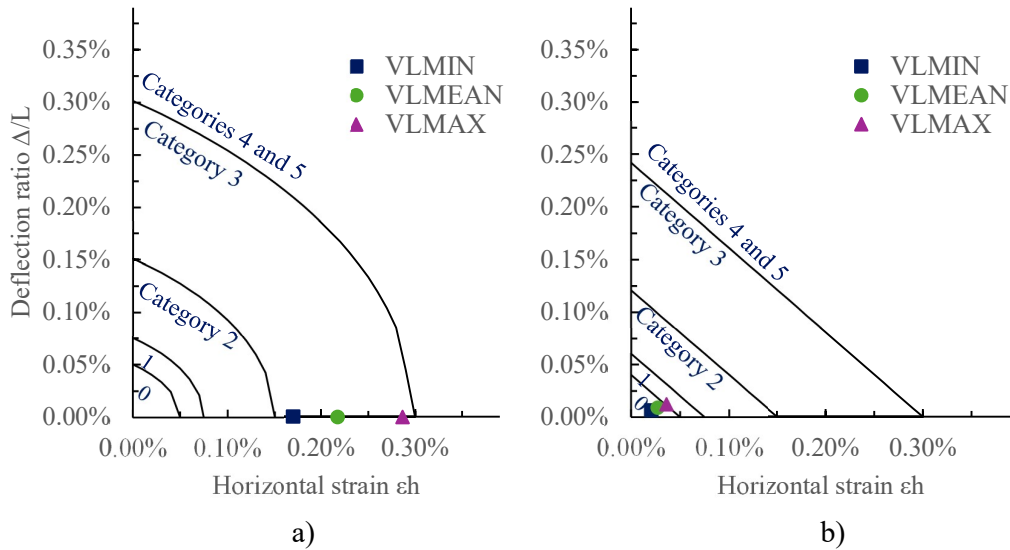


Figure 6.95. Damage category charts for the CNORTH facade in greenfield conditions and ELAS MAX parameters, for a) sagging and b) hogging deformation modes

And for the SOUTH facade:

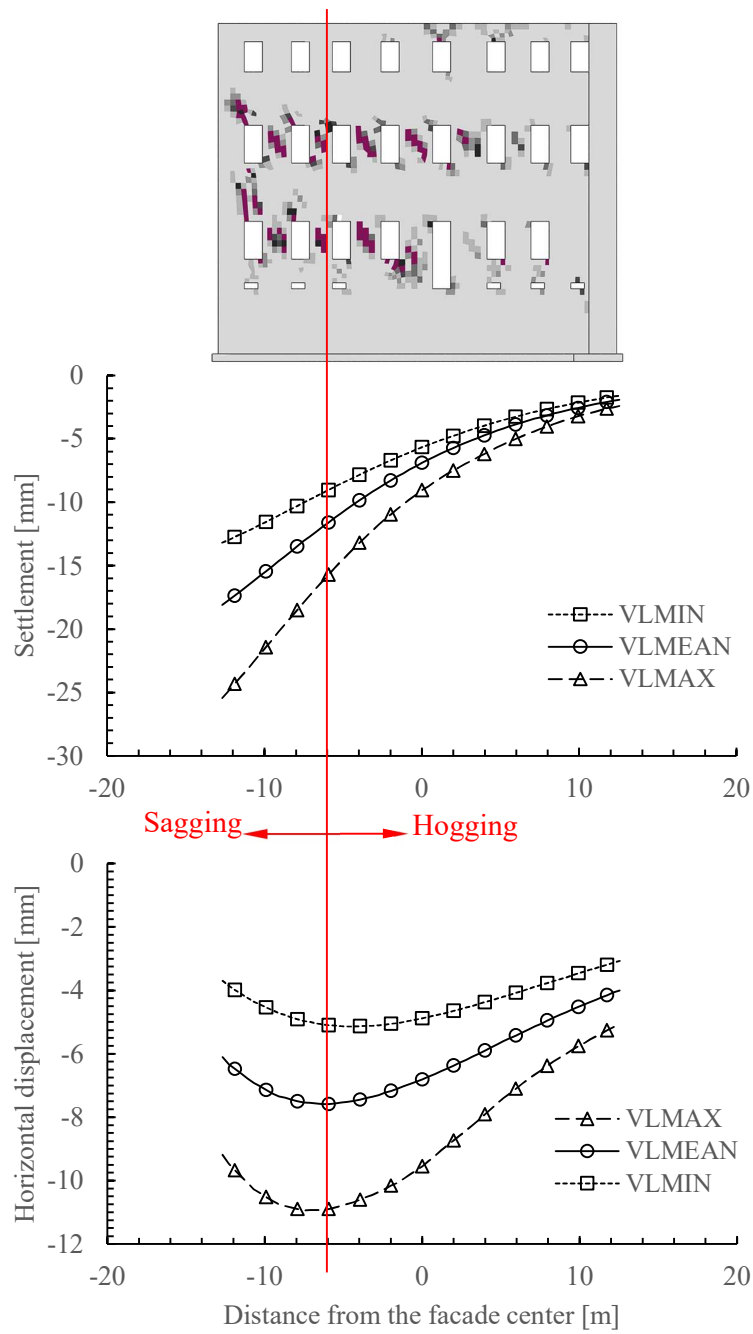


Figure 6.96. Greenfield settlements and horizontal displacements induced below the SOUTH facade

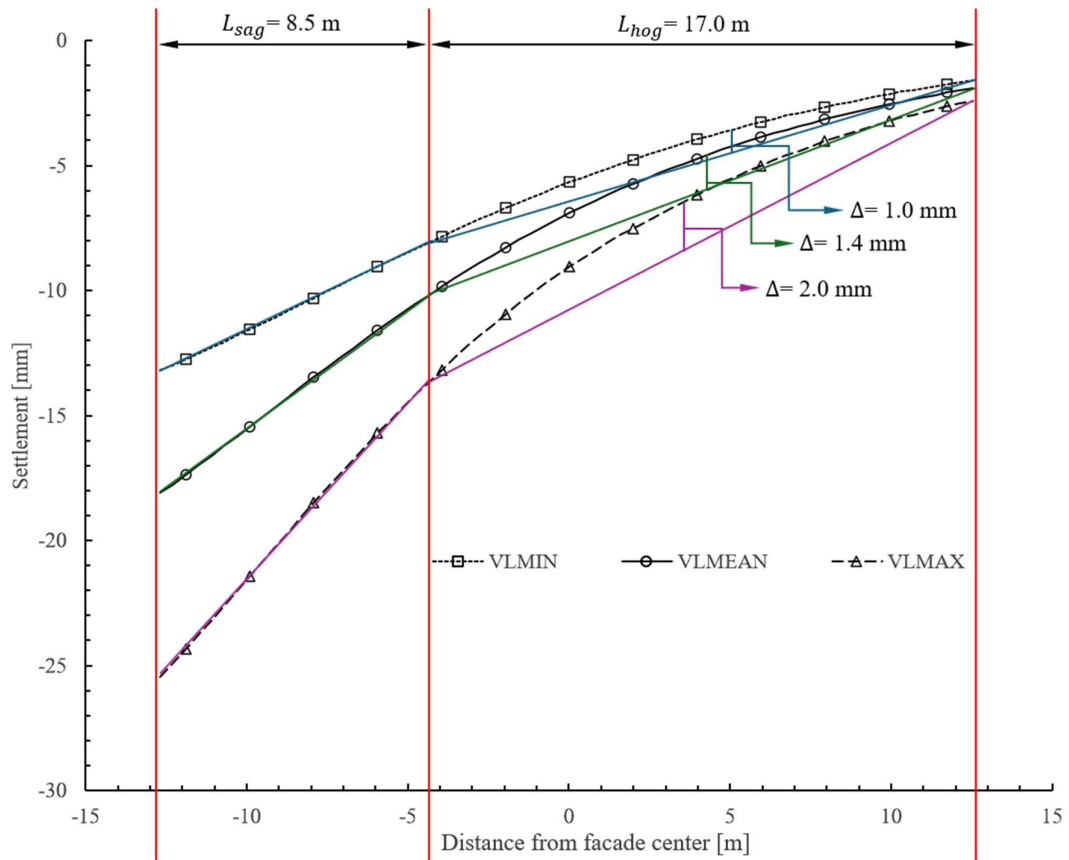


Figure 6.97. Parameters for the calculation of the deflection ratio of the SOUTH facade in greenfield conditions

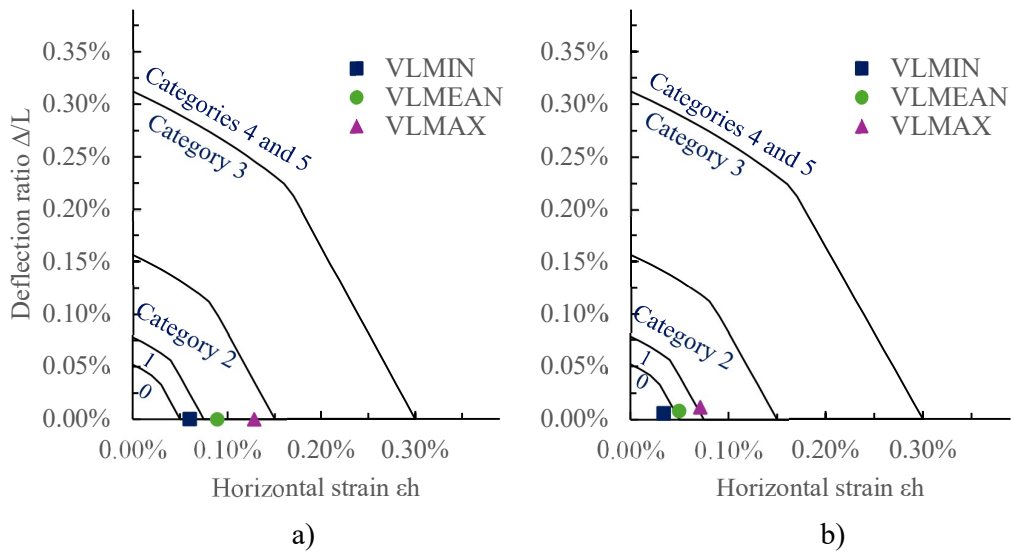


Figure 6.98. Damage category charts for the SOUTH facade in greenfield conditions and ELAS MAX parameters, for a) sagging and b) hogging deformation modes

As a general comment, for all the damage category charts the sagging deformation mode seems to yield more severe predictions of damage risk, for the CNORTH facade even entering in the category of damage 3 (see Figure 6.95). This is mainly explained due to the shorter spans and higher differential displacements of the sagging zones.

It is also interesting to remark that for all the facades (apart from the sagging zone of the CNORTH) the EBA method predicts *slight* damage risks at the most even, with the critical VLMAX models. This is not in accordance with the results found with the elasto-plastic CDP models as these showed some areas entering into *moderate* to *very severe* risks of damage. However, if the results from the elastic ELAS models are recalled, these also indicated that the building would experience *slight* damage risks at most. It is not strange to conclude, then, that the EBA method is best to describe the behavior of elastic-like masonry walls (such as walls well restrained by capable slabs), as it is not able to estimate localized plastic damage in the facades of a building, and this would seem evident from the beginning since the method is formulated based on average critical tensile strains, ignoring localized plasticization, and on top of that it is formulated in the theory of elasticity, which could disregard the real fragile failure kinematics of the masonry (recall Figure 5.35).

## 6.4 Coupled models: soil – structure interaction

Acknowledging the initial requirements of Infratrasporti.To S.r.l., which constrain the contractors to provide a jet grouting umbrella to minimize the settlements induced by the tunnelling activities below Palazzo Campana, and also keeping in mind that the interaction models are significantly more demanding in computational terms than previous models, both increasing the run time and absorbing more CPU and RAM resources, the decision is made to compute only the combined VLMIN with ELAS MAX and CDP MAX models. The VLMIN, in greenfield called JET model, precisely corresponds to the situation in which the jet grouting umbrella is present within the soil, being this the most realistic representation of the real tunnelling problem once the civil work starts. The elastic ELAS MAX and elasto-plastic CDP MAX constitutive behaviors are solely for the building model, analyzed in more detail in the previous Chapter 6.2 and identified to vary negligibly from their weaker counterparts. In this framework, two soil – structure interaction models are simulated: INT\_VLMIN\_ELAS\_MAX and INT\_VLMIN\_CDP\_MAX, with the code INT preceding the VLMIN as an indicator that it corresponds to the interaction model.

### 6.4.1 Steady-state, permanent deformations at the end of tunnelling

#### 6.4.1.1 Building risk of damage estimation

First, for the elastic building models the results in the permanent state of deformation after tunnelling are displayed next. For the entire building:



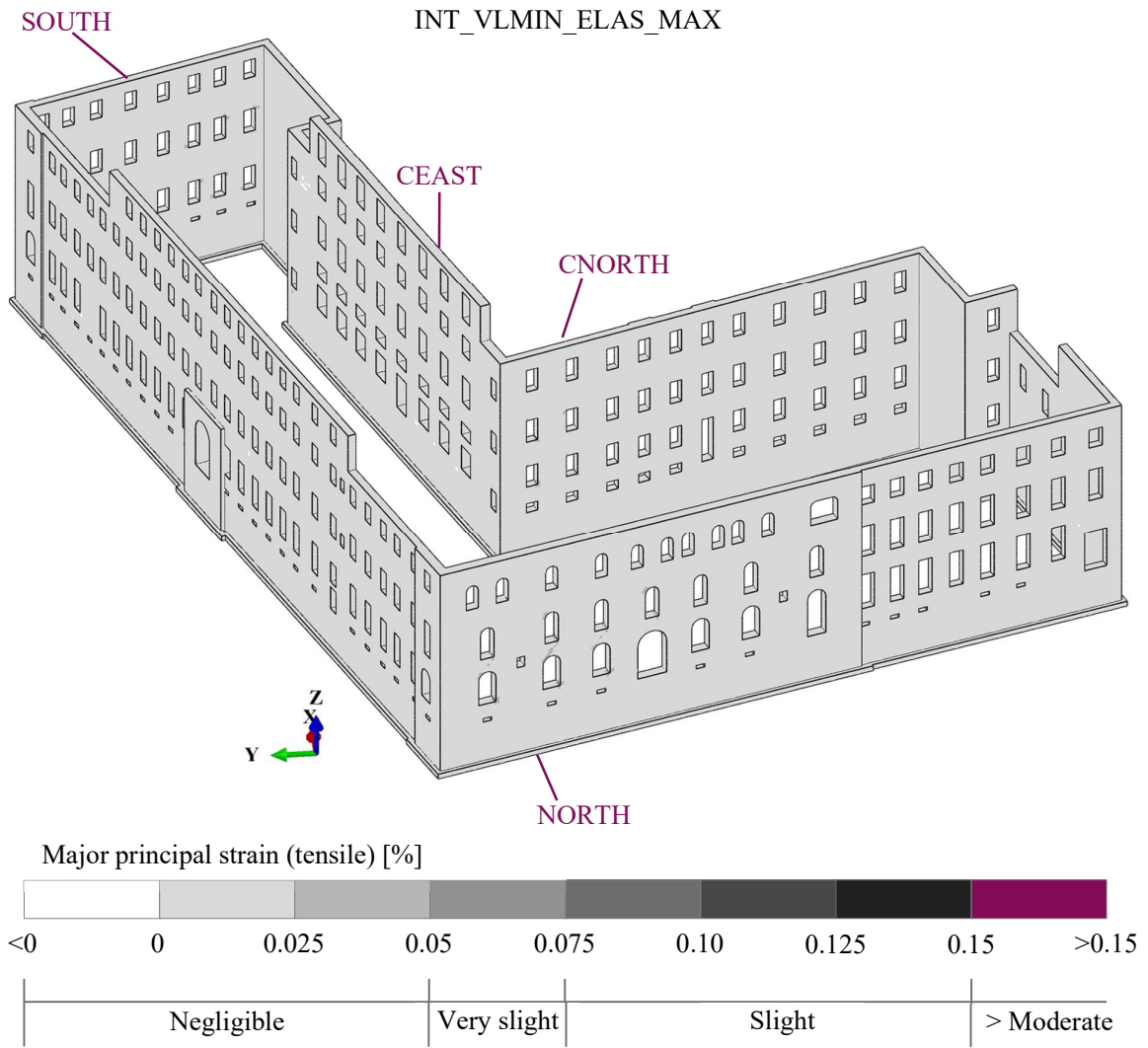


Figure 6.99. Interaction model: Major principal strains of the entire building for the INT\_VLMIN condition with ELAS MAX masonry constitutive behavior

And, analyzing the NORTH, CNORTH, CEAST and SOUTH facades, compatibly with the framework followed for the uncouple building models, the individual facades exhibit:

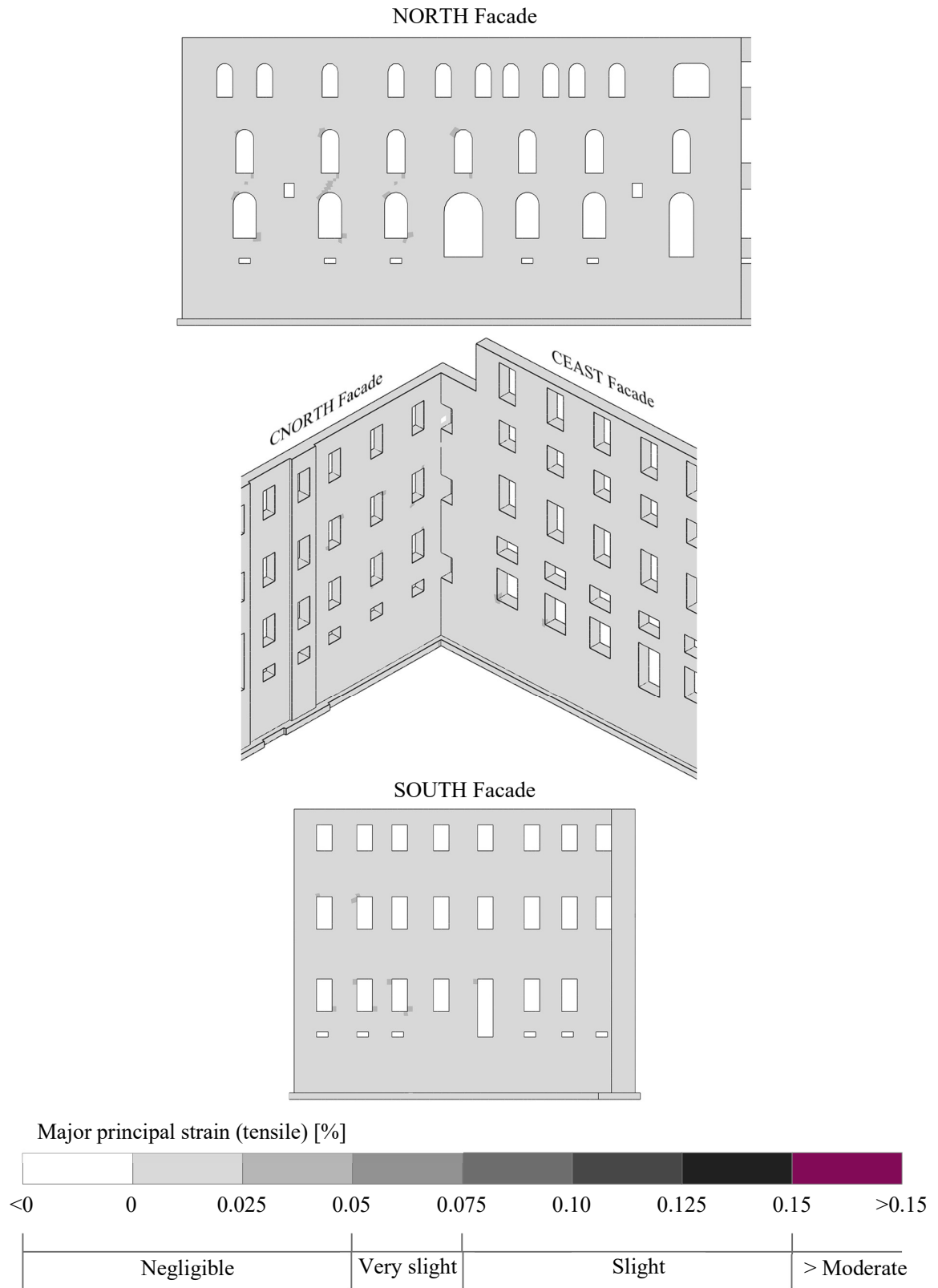


Figure 6.100. Interaction model: Major principal strains of the individual facades for the INT\_VLMIN condition with ELAS MAX masonry constitutive behavior

Notice anything from the previous two figures? It is indeed not easy to identify that there is a very limited number of zones showing a slightly darker tone of gray (still below 0.05%). Apart from these, the entirety of the facades shows strains falling below 0.025%, resulting in a constantly negligible degree of severity. It is, therefore, that the facades are regarded to be at “low risk” of damage if elasticity alone is used for prediction, meaning that structural integrity is not compromised and repair works can be performed easily and economically (Mair, Taylor, & Burland, 1996).

On the other hand, with the elasto-plastic CDP model some localized and relevant tensile strains are still predicted, as is displayed in the next figures. On top of that, the CEAST facade sees new zones present higher strains, as well as a new facade, the CSOUTH, is now showing signs of being affected by the tunnelling works. This will be better detailed under the next 6.4.2 section.

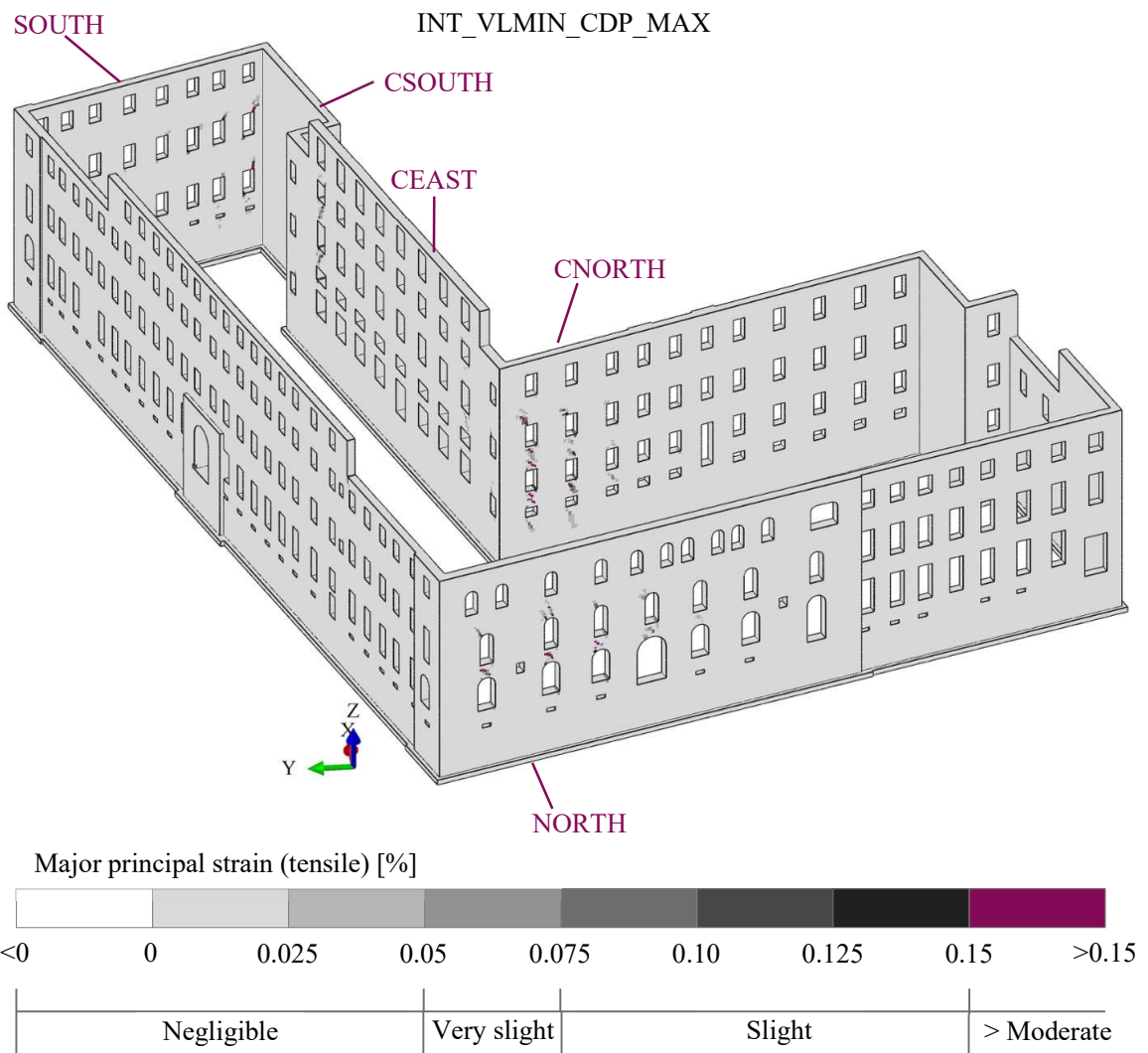


Figure 6.101. Interaction model: Major principal strains of the entire building for the INT\_VLMIN condition with CDP MAX masonry constitutive behavior



Figure 6.102. Interaction model: Major principal strains of the individual facades for the INT\_VLMIN condition with CDP MAX masonry constitutive behavior

6.4.1.2 Comparison against greenfield results

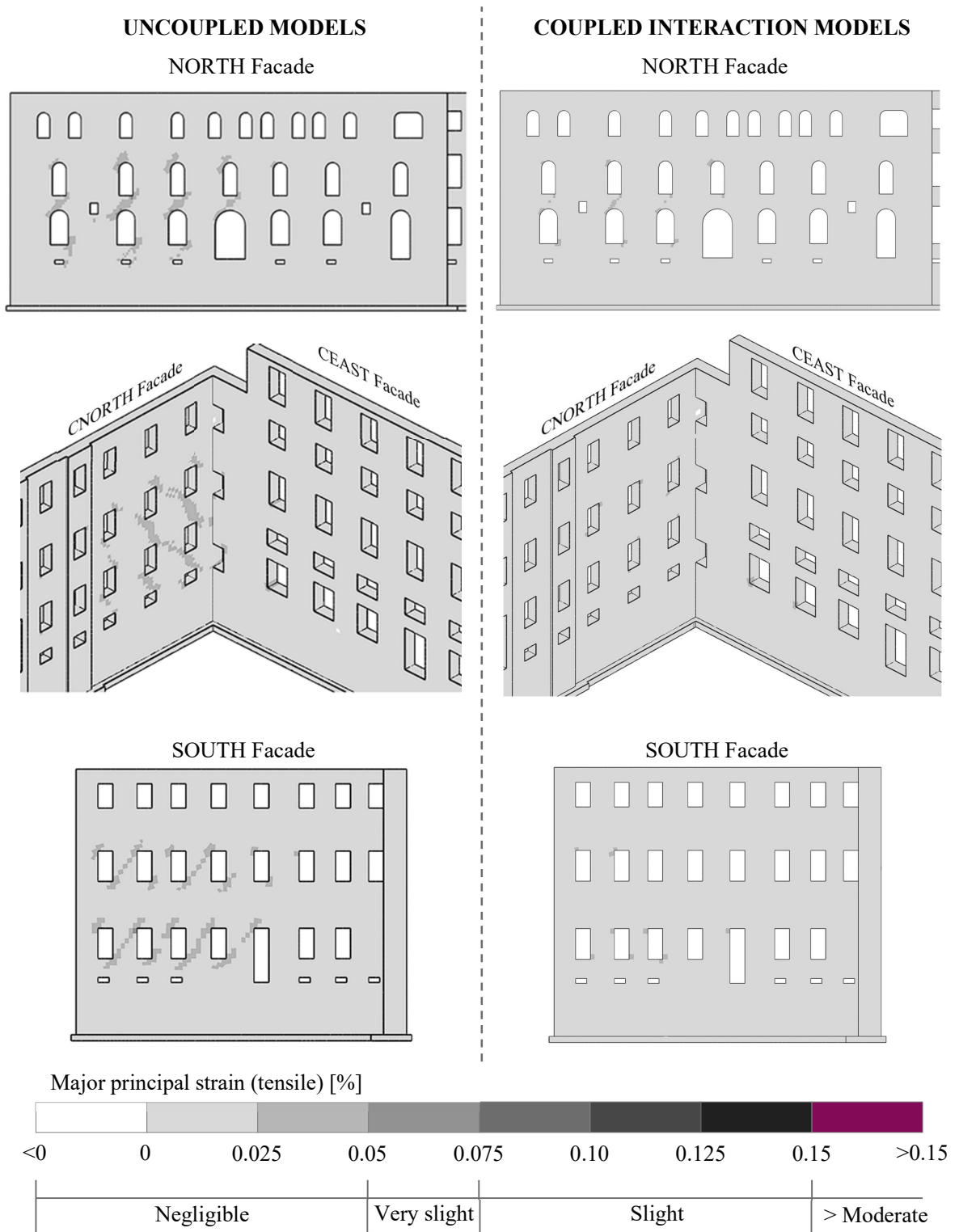


Figure 6.103. Comparison of major principal strains between individual facades of the uncoupled and coupled interaction models, for the VLMIN condition with ELAS MAX masonry constitutive behavior

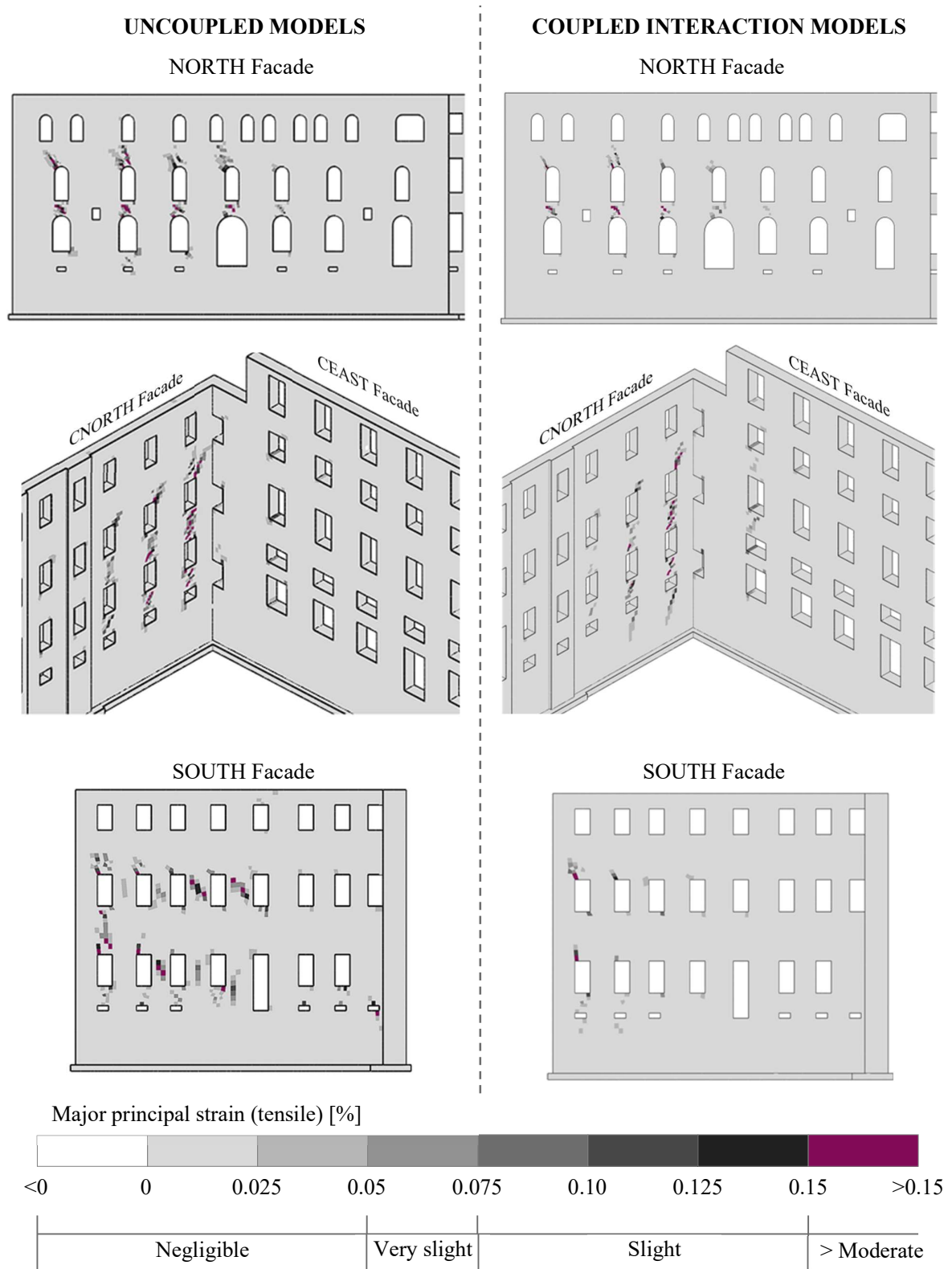


Figure 6.104. Comparison of major principal strains between individual facades of the uncoupled and coupled interaction models, for the VLMIN condition with CDP MAX masonry constitutive behavior



Figure 6.105. Comparison of damage category maps between individual facades of the uncoupled and coupled interaction models, for the VLMIN condition with CDP MAX masonry constitutive behavior

From here, consistent with the literature, the damage risk predictions are of a lower extension and degree of severity when a coupled soil – structure interaction model is evaluated in comparison to an uncoupled scheme. The risk of damage in elasto-plasticity is still not nullified, exhorting for detailed monitoring efforts during the excavations in the above identified critical zones.

### 6.4.2 Most critical excavation steps and the influence of three-dimensionality

In elasto-plasticity, it is confirmed from an in-depth analysis of each facade that, for the entire step-by-step simulation, the most critical step is always the final step when the excavation is concluded. This is because the plastic strains are cumulative and not recoverable, which is especially true with the CDP constitutive model here configured since a tensile damage parameter was defined, reducing progressively the stiffness of the finite elements entering in the plastic domain, without recovery. In elasticity, the most critical step for an individual facade is most of the time when the TBM is passing below the respective facade or when it is near and advancing towards it; surely in the latter case the longitudinal trough has a predominant influence over the transversal one. Moreover, in the elasto-plastic models it is also true that the plastic tensile strains of the building start accumulating before the TBM arrives below each individual facade, being produced because of the longitudinal trough but more generally, because of the complete three-dimensional basin of subsidence.

An excellent example is that of the CSOUTH facade, which until now has only been mentioned once in the heading 6.4.1.1, formerly never considered as a critical facade. In this line, the next Figure 6.106 shows the total tensile strains of the CEAST and CSOUTH facades for the uncoupled VLMIN\_CDP\_MAX model. Yes, truthfully. Although unbelievable, these facades seldom suffer after the steady-state greenfield subsidence (permanent soil deformations after the excavation) is imposed at the supporting layer below the foundation (recall sections 5.2.2.2 and 6.2). The maximum strain here recorded is equal to  $1.23\text{e-}03$  (top-right corner of the figure) at the intersection between the CEAST and the CNORTH facades. The CSOUTH facade is completely void of total tensile strains, or at least they are hidden to the color spectrum.

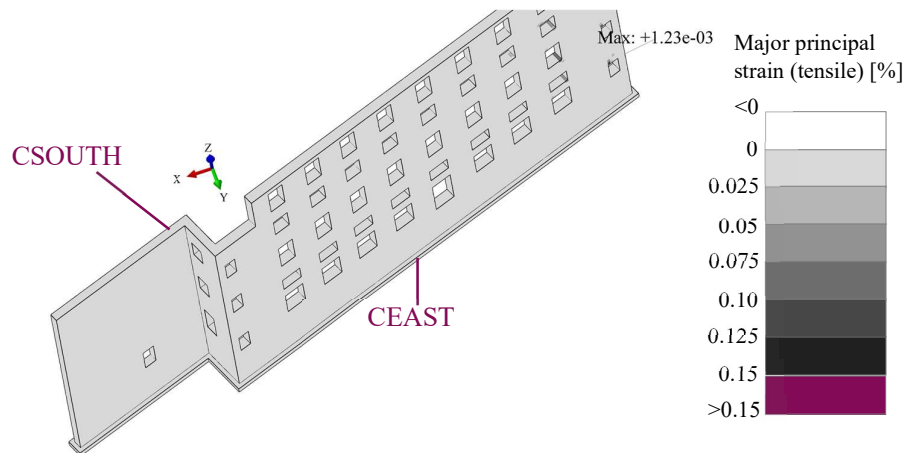


Figure 6.106. Total tensile strains of the uncoupled VLMIN\_CDP\_MAX model of CEAST and CSOUTH facades

Conversely, the next Figure 6.107 shows the evolution of the total tensile strains in both CEAST and CSOUTH facades for the coupled interaction INT\_VLMIN\_CDP\_MAX model. It is particularly critical for the CSOUTH facade, compatibly with previous affirmations that the most affected walls are practically orthogonal to the tunnel alignment. In this case, contrary to the uncoupled model, the evolution of the total



tensile strains is evident in the CSOUTH facade even when the front of the TBM's shield is nearly 12 meters from the wall. When the shield is 6 m far from the wall, the tensile strains are already the 53% of the final steady-state strains. This is a clear hint that the facade is not only suffering from the transversal settlement trough, but from the whole three-dimensional effects of the excavation and on top of that, it suffers from the interaction with the CEAST facade, as better depicted in the subsequent Figure 6.108.

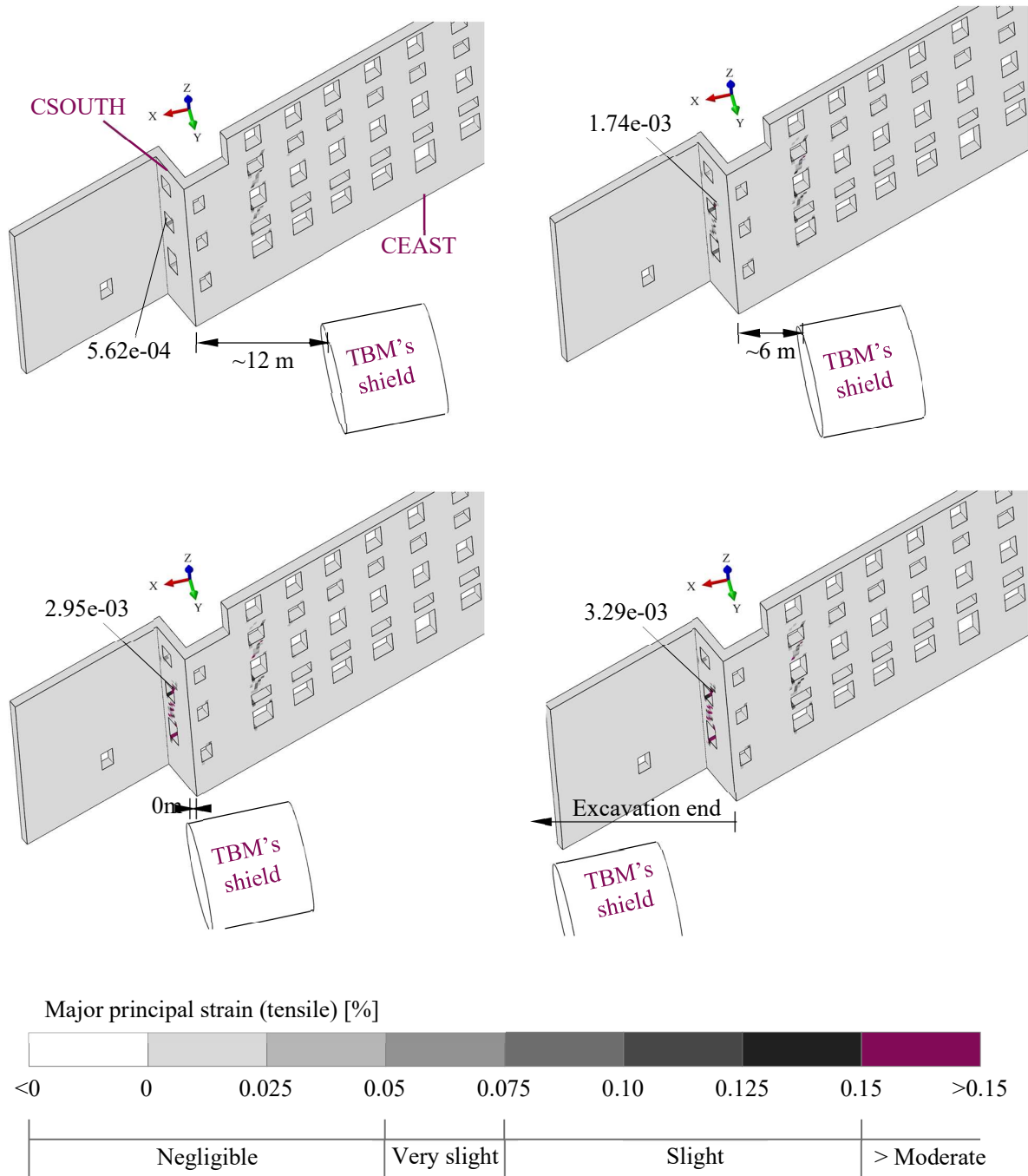


Figure 6.107. Effect (tensile) of the step-by-step excavation and the three-dimensionality in the CSOUTH facade

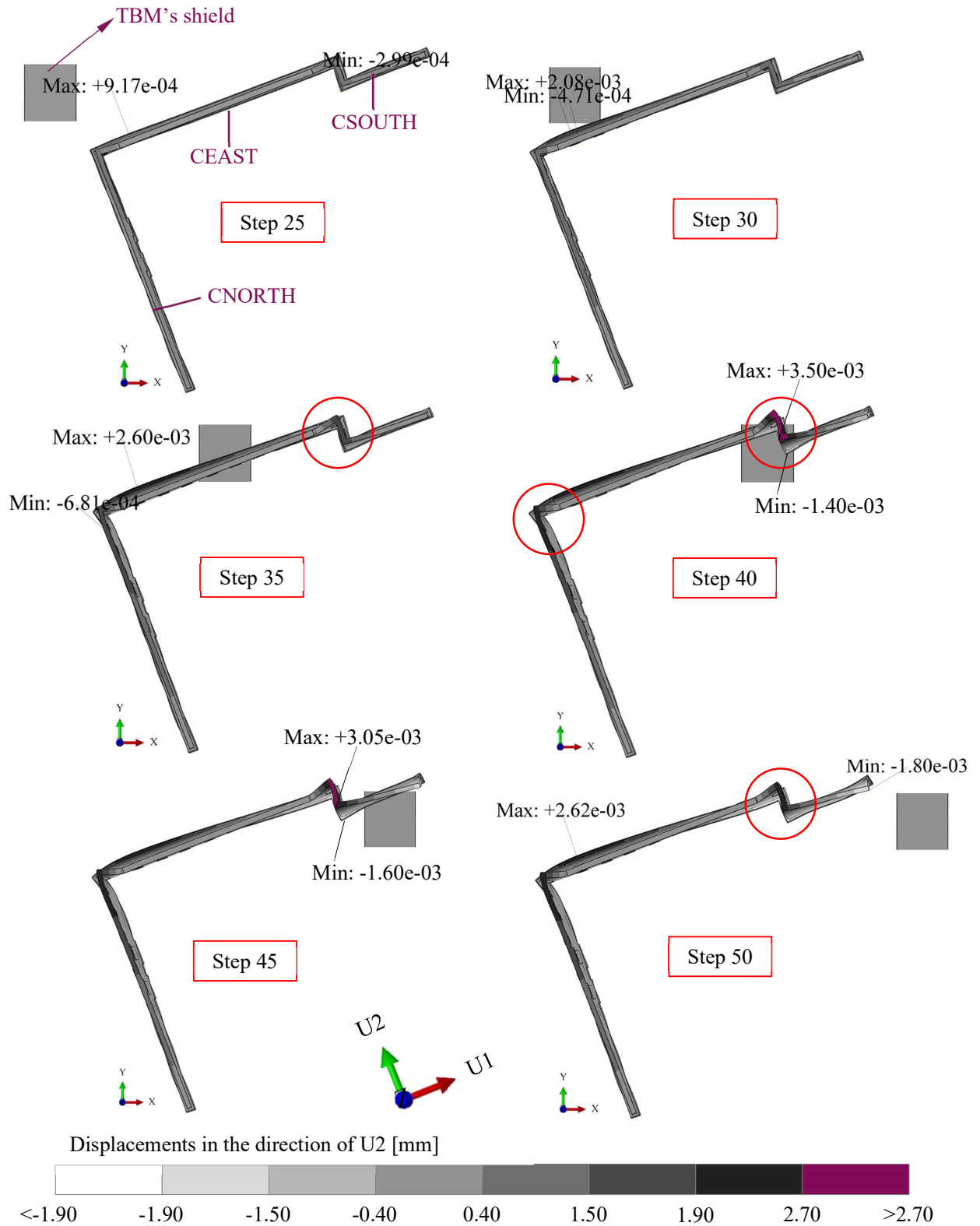


Figure 6.108. Displacements ( $U_2$  in meters for the labels, exaggerated deformation by 500 times) of the CNORTH, CEAST and CSOUTH facades and their three-dimensional interaction in the step-by-step excavation

In the Figure 6.108 above the deformed shape of the CNORTH, CEAST and CSOUTH facades is displayed, exaggerating the deformations by 500 times. The displacements in the direction of U2 are plotted as these are the in-plane movements of both CNORTH and CSOUTH, and the out-of-plane movements of CEAST. Starting from Step 35, near 15 meters from the CSOUTH facade, a slight torsion of both CSOUTH and CEAST can be seen, reaching its maximum value of 3.5 mm for Step 40 when the TBM is below CSOUTH, and then recovering to smaller values in subsequent steps. A torsional deformation also appears in Step 40 for the intersection between CNORTH and CEAST, occurring interestingly 15 steps after the TBM has passed below said intersection, while advancing 45 meters, indicating that the steady-state deformations are already present in that zone.

The torsional deformations are the product of the boundary conditions imposed. Even though the displacements are constrained at the level of the slabs, after confirming that the slabs act rigidly as a diaphragm, these are not constrained at the level of the foundation, because in the blueprints of the building both CEAST and CSOUTH have no slab at the foundation level (review Appendix B.1). The movements of the facades are also not constrained at the level of the roof, since during the on-site visual inspections it was confirmed that the roof was wooden and therefore, its stiffening action was disregarded during the modelling process.

The combined effect of the torsional deformations and the longitudinal subsidence contribute to the development of the localized and severe tensile strains witnessed in the CSOUTH facade. It is here argued, therefore, that it is futile evaluating these effects from the elastic beam assessment (EBA) method, since the interaction between the facades is neglected. Furthermore, an alarm is raised when performing only two-dimensional or three-dimensional uncoupled, single-step models as the longitudinal trough is usually not evaluated in these schemes.

## Chapter 7

### Conclusions and recommendations

#### 7.1 Conclusions

##### 7.1.1 Greenfield models

In general, it was found a reasonable agreement between the empirical and analytical methods for the basing of subsidence estimation with the reference REF greenfield three-dimensional model.

From greenfield parametrical analyses, the extreme (lowest and highest) settlement volume losses were produced for the GAP models, which varied the steering gap of the machine from 2, 4 and 6 cm to account for possible overcutting and shield conicity during the tunnelling works. The lowest settlement volume losses were produced in the GAP2 model of 2 cm steering gap, while the largest were present in the model GAP6 of 6 cm steering gap. This result, over all the rest of parameters that were varied, highlights the impact of the steering gap on the basin of subsidence, in agreement with the literature which shows that the largest settlements are always produced during the passing of the shield of the machine (except in the cases where long-term consolidation is also modelled). Surprisingly, not even the soil improvement measures (jet grouting or permeation grouting in the JET model) were as effective in reducing the basin of subsidence as delivering a correct steering of the TBM while trying to provide the smallest steering gap possible, in comparison to the GAP2 model, reminding the project managers and contractors alike of the importance of involving cautious and experienced operators in the excavation.

Furthermore, with the current modelling assumptions, most of the settlement volume losses sit around 0.88%, clearly reflecting the dominance of the parameters assumed for the REF model, especially the steering gap of 4 cm seeing that the GAP models are among the most impactful. If the reader can agree that the steering gap equal to 4 cm represents a reasonably average condition in tunnelling, then it is rational to conclude that the volume losses adopted by Infratrasporti.To (2024) during their empirical and two-dimensional numerical modelling assessments equal to 0.5 and 1.0% are not entirely conservative. In fact, the value of 0.5% would appear to underestimate the settlement trough while the 1.0% would only sit above the average condition by a little.

The face pressure parametrical analyses also produced some interesting results when implementing the face stability meta-models of Proutzopoulos' (2012). The meta-model showed that only the case for which the face pressure was null, FP0, resulted in

an instable excavation face. However, to validate this result the maximum principal absolute plastic strains were also plotted, where the plastic zone only covered a limited area in the vicinities of the excavation walls, supported by the shield and liner, and at the front of the excavation in a much more reduced magnitude. No plastic strain propagation was witnessed from the face of the excavation towards the surface. Therefore, if the method by Prountzopoulos' (2012) indicates face instability for the FP0 condition, it may have only been locally.

On the other hand, if the face pressure was reduced to the 25 or 50% of the horizontal geostatic stress, in correspondence with the FP25 and FP50 models, according to Prountzopoulos' (2012)  $\Omega_F - \Lambda_{FP}$  curve, the face was not instable. This is in good agreement with experiences in underground excavation in the Torino subsoil which, as described before when introducing the material in Chapter 4, has an inherently variable degree of cementation that grants it notable mechanical properties. This is by no means supporting the use of open-faced TBMs during the Metro-Line 2 works, but rather it provides a sense of tranquility if the worst-case scenario happens during the excavations: the EPB TBM is jammed and the conditioned soil loses its pressurized properties with the degradation of the foam, leading to a drop in the face pressure. In this case, at least the soil is known to be capable of providing some limited self-support while the problem is solved.

### 7.1.2 Uncoupled building models

From the conducted parametric analyses, the first point to become clear is that the variations between elastic models ELAS MAX, ELAS MEAN and ELAS MIN were negligible if not inexistent, as well as the variations between elastoplastic models CDP MAX, CDP MEAN and CDP MIN were marginal, both from the facade damage category maps and the portions in the pie charts, for any level of subsidence applied. This suggests that, in the range of parameters selected for the masonry for the current model of the perimetral facades, any of these elastic or elastoplastic models could provide consistent results. This was of great advantage when computing the coupled soil – structure interaction models, because it permitted to reduce the number of parametrical analyses while using the constitutive formulations that had the higher computational performance, especially the elastoplastic ones.

The second point is that all ELAS models resulted in degrees of severity lower than *moderate*, and it is reminded that in real life, damage related to these can result from a variety of causes, even shrinkage or thermal effects from the building itself. It is, therefore, that the facades were regarded to be at “low risk” of damage if elasticity alone was used for prediction, meaning that structural integrity was not compromised and repair works could be performed easily and economically (Mair, Taylor, & Burland, 1996).

On the other hand, if elasto-plasticity was summoned, damage risk became clearer and more severe the higher the settlement volume loss became. For all the NORTH, CNORTH, CEAST, and SOUTH facades, the finite elements entered in degrees of severity equal to and higher than *moderate*; however, this was witnessed in localized

areas (refer to heading 6.2.4 to see the specific locations) that should be the focus of careful monitoring during the construction of the tunnel.

Still, from the most pessimistic (VLMAX for the maximum volume loss, same model emulating the TBM steering gap of 6 cm, before referred to as GAP6 model) to the most optimistic (VLMIN for the minimum volume loss, same model including the presence of the jet grouting umbrella, before referred to as JET model) greenfield volume loss models, a clear improvement of the building's state post excavation is observed, with smaller areas presenting tensile strains of critical values.

When comparing the results against the EBA method, as a general comment, for all the damage category charts the sagging deformation mode yielded more severe predictions of damage risk, for the CNORTH facade even entering in the category of damage 3 (see Figure 6.95). This is mainly explained due to the shorter spans and higher differential displacements of the sagging zones.

It is also interesting to remark that for all the facades (apart from the sagging zone of the CNORTH) the EBA method predicted *slight* damage risks at the most, even with the critical VLMAX (maximum volume loss) models. This was not in accordance with the results found with the elasto-plastic CDP models as these showed some areas of the facades entering into *moderate* to *very severe* risks of damage. However, if the results from the elastic ELAS models are recalled, these also indicated that the building would experience *slight* damage risks at most. It is not strange to conclude, then, that the EBA method is best to describe the behavior of elastic-like masonry walls (such as walls well restrained by capable slabs), as it was not able to estimate localized plastic damage in the facades of the building, and this would seem evident from the beginning since the method is formulated based on average critical tensile strains, ignoring localized plasticization, and on top of that it is formulated in the theory of elasticity, which could disregard the real fragile failure kinematics of the masonry (recall Figure 5.35).

### 7.1.3 Coupled soil – structure interaction models

In general, consistently with the literature, the damage risk predictions are of a lower extension and degree of severity when a coupled soil – structure interaction model is evaluated in comparison to an uncoupled scheme. This owing to the possibility of including the building stiffness, inducing much more rigid deformations in the soil. Nevertheless, the risk of damage in elasto-plasticity is still not nullified, exhorting for detailed monitoring efforts during the excavations in the identified critical zones (see 6.4.1.2 and 6.4.2).

In elasto-plasticity, it was confirmed from an in-depth analysis of each facade that, for the entire step-by-step simulation, the most critical step was always the final step when the excavation was concluded. This was because the plastic strains were cumulative and not recoverable, which was especially true with the CDP constitutive model here configured since a tensile damage parameter was defined, reducing progressively the stiffness of the finite elements entering in the plastic domain, without recovery. In elasticity, the most critical step for an individual facade was most of the time when the TBM was passing below the respective facade or when it was near and advancing

towards it; surely in the latter case the longitudinal trough had a predominant influence over the transversal one. Moreover, in the elasto-plastic models it was also true that the plastic tensile strains of the building started accumulating before the TBM arrived below each individual facade, being produced because of the longitudinal trough but more generally, because of the complete three-dimensional basin of subsidence.

For the CSOUTH facade which showed damage risk predictions not before seen in the uncoupled building models, the combined effect of the torsional deformations and the longitudinal subsidence contributed to the development of the localized and severe tensile strains. It is here argued, therefore, that it is futile evaluating these effects from the elastic beam assessment (EBA) method, since the interaction between the facades is neglected. Furthermore, an alarm is raised when performing only two-dimensional or three-dimensional uncoupled, single-step models as the longitudinal trough is usually not evaluated in these schemes.

## References

- Acito, M., Bocciarelli, M., Chesi, C., & Milani, G. (2014). Collapse of the clock tower in Finale Emilia after the May 2012 Emilia Romagna earthquake sequence: Numerical insight. *Engineering Structures*, 70-91.
- Acito, M., Magrinelli, E., Milani, G., & Tiberti, S. (2020). Seismic vulnerability of masonry buildings: Numerical insight on damage causes for residential buildings by the 2016 central Italy seismic sequence and evaluation of strengthening techniques. *Journal of Building Engineering*, 1-28.
- Amorosi, A., & Sangirardi, M. (2021). Coupled three-dimensional analysis of the progressive tunnelling-induced damage to masonry buildings: is it always worth it? *Tunnelling and Underground Space Technology*, 118: 1-17.
- Anecchiarico, M., Portioli, F., & Landolfo, R. (2010). Micro and macro-finite element modeling of brick masonry panels subject to lateral loadings. *COST ACTION C26: Urban Habitat Constructions under Catastrophic Events - Proceedings of the Final Conference*, (pp. 315-320).
- Antunes, P. (2012). Testing Procedures for Two-Component Annulus Grouts. *North American Tunneling Proceedings, April 10*, 14-22.
- Aoki, T., Sabia, D., & Rovesti, M. (2022). A Methodological Approach to Evaluate Seismic Vulnerability of Masonry Cathedrals. *INTERNATIONAL JOURNAL OF ARCHITECTURAL HERITAGE VOL. 18, NO. 3*, 370-388.
- Attewell, P., & Woodman, J. (1982). Predicting the dynamics of ground settlement and its derivatives caused by tunnelling in soil. *Ground Engineering 15 (7)*, 13-22.
- Avgerinos, V., Potts, D., & Standing, J. (2016). The use of kinematic hardening models for predicting tunnelling-induced ground movements in London Clay. *Geotechnique*, 1-15.
- Barla, G., Barla, M., & Leuzzi, G. (2012). 3D numerical modelling and settlement monitoring during excavation of the Metro-Torino South extension. *Geotechnical Aspects of Underground Construction in Soft Ground – Viggiani (ed)*, 911-918.
- Barla, G., Barla, M., Bonini, M., & Crova, R. (2005). Back analysis of monitoring data for Metro Torino. *Geotechnical Aspects of Underground Construction in Soft Ground Volume: 1*. Amsterdam: Proceedings of the 5th International Symposium TC28.
- Barla, G., Barla, M., Bonini, M., & Gamba, F. (2005). Two and three dimensional modelling and monitoring of the Metro Torino. *11th International Conference of Iacmag*. Turin.



- Barla, M., & Barla, G. (2005). Assessing design parameters for tunnelling in a cemented granular soil by continuum and discontinuum modelling. *11th International Conference of Iacmag*, (pp. 475-484). Turin.
- Barla, M., & Barla, G. (2012). Torino subsoil characterization by combining site investigations and numerical modelling. *Geomechanics and Tunnelling* 5, 214-231.
- Benz, T. (2007). *Small-strain stiffness of soils and its numerical consequences*. Stuttgart: [Doctoral dissertation]. Universität Stuttgart.
- Boldini, D., Losacco, N., Bertolin, S., & Amorosi, A. (2018). Finite Element modelling of tunnelling-induced displacements on framed structures. *Tunnelling and Underground Space Technology*, 222-231.
- Boscardin, M., & Cording, E. (1989). Building response to excavation-induced settlement. *Journal of Geotech. Engineering, ASCE*, 115(1), 1-21.
- Bottino, G., & Civita, M. (1986). Engineering geological features and mapping of subsurface in the metropolitan area of Turin, North Italy. *5th International IAEG Congress*, (pp. 1741-1753). Buenos Aires.
- Bowers, K., Hiller, D., & New, B. (1996). Ground movement over three years at the Heathrow Express Trial Tunnel. *Geotechnical Aspects of Underground Construction in Soft Ground*, 647-652.
- Burland, J. (1995). Assessment of risk of damage to buildings due to tunnelling and excavations. *Invited Special Lecture to IS-Tokyo '95: 1st Int. Conf. on Earthquake Geotechnical Engineering*. Tokyo.
- Burland, J. (2001). Assessment methods used in design. In J. Burland, J. Standing, & F. Jardine, *Building response to tunnelling: Case studies from construction of the Jubilee Line Extension, London. VOLUME 1 PROJECTS AND METHODS* (pp. 23-43). London: Thomas Telford.
- Burland, J. (2001). Results of the research. In J. Burland, J. Standing, & F. Jardine, *Building response to tunnelling: Case studies from construction of the Jubilee Line Extension, London. VOLUME 1 PROJECTS AND METHODS* (pp. 321-325). London: Thomas Telford.
- Burland, J., & Wroth, C. (1974). *Settlement of buildings and associated damage*. Cambridge: University Engineering Department.
- Cattari, S., Camilletti, D., D'Altri, A., & Lagomarsino, S. (2021). On the use of continuum Finite Element and Equivalent Frame models for the seismic assessment of masonry walls. *Journal of Building Engineering* 43, 1-21.
- CEN. (2005). Eurocode 6 - Design of masonry structures - Part 1-1: General rules for reinforced and unreinforced masonry structures. Brussels.
- Chiriotti, E., Marchionni, V., & Grasso, P. (2001). *Porto Light Metro System, Lines C, S and J. Interpretation of the Results of the Building Condition Survey and Preliminary Assessment of Risk. Methodology for Assessing the Tunnelling Induced Risks on*

- Buildings along the Tunnel Alignment*. Porto: Normetro – Transmetro, Internal technical report [in Italian and Portuguese].
- Dalgic, K., Gulen, B., Liu, Y., Acikgoz, S., Burd, H., Marasli, M., & Ilki, A. (2023). Masonry buildings subjected to settlements: Half-scale testing, detailed measurements, and insights into behaviour. *Engineering Structures* 278, 1-11.
- Dassault Systemes. (2024, 07). *SIMULIA User Assistance 2024*. Retrieved from 3DS.COM: <https://help.3ds.com/>
- De Rienzo, F., & Oreste, P. (2011). Analyses of the Distribution and Nature of the Natural Cementation of Quaternary Sediments: The Case of the Turin Subsoil (Italy). *Geotech Geol Eng*, 29, 319-328.
- Designers Riuniti. (1983). *Palazzo Campana. Memoria e progetto, in Un progetto per l'Università. La riorganizzazione funzionale e fisica di Palazzo Campana a sede universitaria*. Torino: Designers Riuniti.
- Di Giulio, A., Bavasso, I., Di Felice, M., & Sebastiani, D. (2020). A preliminary study of the parameters influencing the performance of two-component backfill grout. *GALLERIE E GRANDI OPERE SOTTERRANEE n. 133*, 27-33.
- Epel, T., Mooney, M., & Gutierrez, M. (2021). The influence of face and shield annulus pressure on tunnel liner load development. *Tunnelling and Underground Space Technology*, 1-15.
- Fargnoli, V. (2015). *Soil-structure interaction during tunnelling in urban area: observations and 3D numerical modelling*. Bologna: [Doctoral dissertation]. Alma Mater Studiorum Università di Bologna. Retrieved from <http://amsdottorato.unibo.it/id/eprint/6926>
- Flores, Q. (2015). *Physical and Mechanical Behavior of a Two Component Cement-Based Grout for Mechanized Tunneling Application*. Rio de Janeiro: [Doctoral dissertation]. Universidade Federal do Rio de Janeiro.
- Giardina, G., van de Graaf, A., Hendriks, M., Rots, J., & Marini, A. (2013). Numerical analysis of a masonry façade subject to tunnelling-induced settlements. *Engineering Structures* 54, 234-247.
- Giordano, A., Mele, E., & De Luca, A. (2002). Modelling of historical masonry structures: comparison of different approaches through a case study. *Engineering Structures* 24, 1057-1069.
- González, C., & Sagaseta, C. (2001). Patterns of soil deformations around tunnels. Application to the extension of Madrid Metro. *Computers and Geotechnics*, 28, 6-7, 445-468.
- Herrenknecht AG. (2024, 07). *EPB Shield*. Retrieved from Herrenknecht: <https://www.herrenknecht.com/en/products/productdetail/epb-shield/>
- Hoek, E., & Brown, E. (1997). Practical estimates of rock mass strength. *International Journal of Rock Mechanics and Mining Sciences*, 1165-1186.

- Hoek, E., & Marinos, P. (2007). A brief history of the development of the Hoek-Brown failure criterion. *Soils and Rocks, No.2*, 1-13.
- Hoek, E., Carranza-Torres, C., & Corkum, B. (2002). Hoek-Brown criterion – 2002 edition. *Proc. NARMS-TAC Conference, Toronto, 1*, 267-273.
- Infratrasporti.To S.r.l. (2023). *INDAGINI GEOGNOSTICHE: RELAZIONE TECNICA DESCRITTIVA DELLE INDAGINI GEOGNOSTICHE ESEGUITE*. Torino: Città di Torino: Geoportale e Governo del Territorio [in Italian]. Retrieved from <http://geoportale.comune.torino.it/web/linea-2-della-metropolitana-torinese-progetto-definitivo>
- Infratrasporti.To S.r.l. (2024, 07). *Città di Torino: Geoportale e Governo del Territorio*. Retrieved from LINEA 2 DELLA METROPOLITANA TORINESE: Tratta Rebaudengo - Politecnico [in Italian]: <http://geoportale.comune.torino.it/web/linea-2-della-metropolitana-torinese-progetto-definitivo>
- Irace, A., Marcelli, I., Fioraso, G., Festa, A., Catanzariti, R., Raco, B., . . . Doveri, M. (2024). Subsurface geology of the Torino metropolitan area (Westernmost Po Plain, NW Italy). *Journal of Maps*, 1-11.
- ISTORETO. (2002). *Istituto piemontese per la storia della Resistenza e della società contemporanea 'Giorgio Agosti': Casa Littoria (ora Palazzo Campana) [in Italian]*. Retrieved from TORINO 1938-45. Luoghi memoria: <https://www.istoreto.it/torino38-45/littoria.htm>
- Kasper, T., & Meschke, G. (2004). A 3D finite element simulation model for TBM tunnelling in soft ground. *INTERNATIONAL JOURNAL FOR NUMERICAL AND ANALYTICAL METHODS IN GEOMECHANICS*, 28: 1441-1460.
- Kavvadas, M., Litsas, D., Vazaios, I., & Fortsakis, P. (2017). Development of a 3D finite element model for shield EPB tunnelling. *Tunnelling and Underground Space Technology*, 65: 22-34.
- Kirsch, E. (1898). The theory of elasticity and the needs of strength theory. *Zeitschrift des Vereines deutscher Ingenieure*, 797-807.
- Lasciarrea, W., Amorosi, A., Boldini, D., de Felice, G., & Malena, M. (2019). Jointed Masonry Model: A constitutive law for 3D soil-structure interaction analysis. *Engineering Structures* 201, 2-14.
- Lee, J., & Fenves, G. (1998). Plastic-Damage Model for Cyclic Loading of Concrete Structures. *Journal of Engineering Mechanics*, 124, 892–900.
- Lee, K., Rowe, R., & Lo, K. (1992). Subsidence owing to tunnelling. I. Estimating the gap parameter. *Canadian Geotechnical Journal*, 29, 929-940.
- Litsas, D., Sitarenios, P., & Kavvadas, M. (2017, October-December). Parametric investigation of tunnelling-induced ground movement due to geometrical and operational TBM complexities. *RIVISTA ITALIANA DI GEOTECNICA*, pp. 22-34.

- Loganathan, N., & Poulos, H. (1998). Analytical prediction for tunneling-induced ground movements in clay. *Journal of Geotechnical and Geoenvironmental Engineering*, 846-856.
- Losacco, N. (2011). *Development and testing of a simplified building model for the study of soil-structure interaction due to tunnelling in soft ground*. Rome: [Doctoral dissertation]. Sapienza Università di Roma.
- Losacco, N., & Viggiani, G. (2019). Class A prediction of mechanised tunnelling in Rome. *Tunnelling and Underground Space Technology*, 87: 160-173.
- Lublinter, J., Oliver, J., Oller, S., & Oñate, E. (1989). A Plastic-Damage Model for Concrete. *International Journal of Solids and Structures*, 25, 299–329.
- Mair, R., & Taylor, R. (1997). Bored tunnelling in the urban environment. *Theme Lecture, 14th ECSMGE*, (pp. 2353-2385). Hamburg.
- Mair, R., Taylor, R., & Burland, J. (1996). Prediction of ground movements and assessment of risk of building damage due to bored tunnelling. *Geotechnical Aspects of Underground Construction in Soft Ground*, 713-718.
- Meschke, G., Kropik, C., & Mang, H. (1996). Numerical analyses of tunnel linings by means of a viscoplastic material model for shotcrete. *International Journal for Numerical Methods in Engineering*, vol. 39, 3145-3162.
- Migliazza, M., Chiorboli, M., & Giani, G. (2009). Comparison of analytical method, 3D finite element model with experimental subsidence measurements resulting from the extension of the Milan underground. *Computers and Geotechnics*, 36: 113-124.
- Ministero delle Infrastrutture e dei Trasporti. (2018, February). Norme tecniche per le costruzioni NTC - Capitolo 8: Costruzioni Esistenti, ed Appendici [in Italian].
- Miraei, S. (2020). *Tunnelling-induced deformation and damage on framed structures with masonry infills*. Bologna: [Master thesis]. Alma Mater Studiorum Università di Bologna.
- Mohammadzamani, D., Lavasan, A., & Wichtmann, T. (2023). The role of hydro-mechanical properties of the tail void grouting material in mechanized tunnelling. *10th European Conference on Numerical Methods in Geotechnical Engineering*, (pp. 1-6). London.
- Mollon, G., Dias, D., & Soubra, A. (2012). Probabilistic analyses of tunneling-induced ground movements. *Acta Geotechnica* 8 (2), 181-199.
- Mooney, M., Grasmick, J., Kenneally, B., & Fang, Y. (2016). The role of slurry TBM parameters on ground deformation: Field results and computational modelling. *Tunnelling and Underground Space Technology*, 257-264.
- Morais, J., Marques, A., Morais, P., Veiga, M., Santos, C., Candeias, P., & Gomes, J. (2020). Modulus of elasticity of mortars: Static and dynamic analyses. *Construction and Building Materials* 232, 1-9.
- Nemorini, F. (2010). *MODELLAZIONE NUMERICA DI GALLERIE METROPOLITANE [Italian]*. Parma: [Master thesis]. Università degli Studi di Parma.

- Nikakhtar, L., Zare, S., & Mirzaei-Nasirabad, H. (2020). Numerical Modelling of Backfill Grouting Approaches in EPB Tunneling. *Journal of Mining and Environment (JME)*, 301-313.
- O'Reilly, M., & New, B. (1982). Settlements above tunnels in the United Kingdom – their magnitude and prediction. *Proc. Tunnelling '82 Symposium, Institution of Mining and Metallurgy*, (pp. 55-64). London.
- Oggeri, C., Oreste, P., & Spagnoli, G. (2021). The influence of the two-component grout on the behaviour of a segmental lining in tunnelling. *Tunnelling and Underground Space Technology*, 1-17.
- Oggeri, C., Oreste, P., & Spagnoli, G. (2022). Creep behaviour of two-component grout and interaction with segmental lining in tunnelling. *Tunnelling and Underground Space Technology*, 1-13.
- Oh, J., & Ziegler, M. (2014). Investigation on Influence of Tail Void Grouting on the Surface Settlements during Shield Tunneling Using a Stress-Pore Pressure Coupled Analysis. *KSCE Journal of Civil Engineering*.
- Oreste, P., Sebastiani, D., Spagnoli, G., & de Lillis, A. (2021). Analysis of the behavior of the two-component grout around a tunnel segmental lining on the basis of experimental results and analytical approaches. *Transportation Geotechnics*, 1-12.
- Oteo, C., & Moya, J. (1979). Estimation of the soil parameters of Madrid in relation to the tunnel construction. *Proc. 7th Euro conference on soil mechanics and foundation engineering, vol. 3*, (pp. 239-247). Brighton.
- Papantonopoulos, C., & Atmatzidis, D. (1993). A failure criterion for natural and artificial soft rocks. In *Anagnostopoulos et al. (eds): Geotechnical Engineering of Hard Soils-Soft Rocks*. Rotterdam: Balkema.
- Park, B., Choi, S., Lee, C., Kang, T., Do, S., Lee, W., & Chang, S. (2023). A Geometric Model for a Shield TBM Steering Simulator. *Applied Sciences*, 13, MDPI, 1-27.
- Peck, R. (1969). Deep excavations and tunnelling in soft ground. . *Proc. 7th International Conference on Soil Mechanics and Foundation Engineering*, (pp. 225-290). Mexico City.
- Peila, D. (2023, March 28). *Lecture: Soft ground mechanized tunnelling*. Retrieved from Politecnico di Torino: [www.polito.it](http://www.polito.it)
- Peila, D., Chierigato, A., Martinelli, D., Salazar, C., Shah, R., Boscaro, A., . . . Picchio, A. (2015). Long term behavior of two component back-fill grout mix used in full face mechanized tunneling. *Geingegneria Ambientale e Mineraria, Anno LII, n. 1*, 57-63.
- Pelizza, S., Peila, D., Sorge, R., & Cignitti, F. (2012). Back-fill grout with two component mix in EPB tunneling to minimize surface settlements: Rome Metro—Line C case history. *Geotechnical Aspects of Underground Construction in Soft Ground – Viggiani (ed)*, 291-299.


- Pinto, F., & Whittle, A. (2014). Ground Movements due to Shallow Tunnels in Soft Ground. I: Analytical Solutions. *Journal of Geotechnical and Geoenvironmental Engineering* 140, no. 4, 1-42.
- Prountzopoulos, G. (2012). *Investigation of the excavation face stability in shallow tunnels*. Athens: [Doctoral dissertation]. National Technical University of Athens.
- Rahmati, S., Chakeri, H., Sharghi, M., & Dias, D. (2022). Experimental study of the mechanical properties of two-component backfilling grout. *Proceedings of the Institution of Civil Engineers – Ground Improvement* 175(4), 277-289.
- Rainone, L., Tateo, V., Casolo, S., & Uva, G. (2023). About the Use of Concrete Damage Plasticity for Modeling Masonry Post-Elastic Behavior. *MDPI Buildings* 13, 1-31.
- Rampello, S., Callisto, L., Viggiani, G., & Soccodato, F. (2012). Evaluating the effects of tunnelling on historical buildings: the example of a new subway in Rome. *Geomechanics and Tunnelling* 5, 275-299.
- Romo, M., & Diaz, C. (1981). Face stability and ground settlements in shield tunneling. *Proc. International conference 10th on soil mechanics and foundation engineering, vol. 1*, (pp. 357-360). Stockholm.
- Rowe, R., & Kack, G. (1983). A theoretical examination of the settlements induced by tunnelling: four case histories. *Can. Geotech. J.* 20, 299-314.
- Sagaseta, C. (1987). Analysis of undrained soil deformation due to ground loss. *Geotechnique* 37, 3, 301-320.
- Schiavoni, M., Giordano, E., Roscini, F., & Clementi, F. (2023). Numerical modeling of a majestic masonry structure: A comparison of advanced techniques. *Engineering Failure Analysis*, 1-19.
- Terzaghi, K., & Peck, R. (1948). *Soil mechanics in engineering practice*. New York: J. Wiley & Sons.
- Thewes, M., & Budach, C. (2009). Grouting of the annular gap in shield tunneling – an important factor for minimisation of settlements and production performance. *Proceedings of the ITA-AITES World Tunnel Congress*, (pp. 23-28). Budapest.
- Thomaz, W., Miyaji, D., & Possan, E. (2021). Comparative study of dynamic and static Young's modulus of concrete containing basaltic aggregates. *Case Studies in Construction Materials* 15, 1-17.
- Tiberti, S., Acito, M., & Milani, G. (2016). Comprehensive FE numerical insight into Finale Emilia Castle behavior under 2012 Emilia Romagna seismic sequence: Damage causes and seismic vulnerability mitigation hypothesis. *Engineering Structures*, 397-421.
- Todaro, C., & Pace, F. (2022). Elastic properties of two-component grouts at short curing times: The role of bentonite. *Tunnelling and Underground Space Technology*, 1-12.
- Todaro, C., Peila, L., Luciani, A., Carigi, A., Martinelli, D., & Boscaro, A. (2019). Two component backfilling in shield tunneling: laboratory procedure and results of a test

- campaign. *ITA-AITES World Tunnel Congress (WTC)* (pp. 3210-3223). Naples: CRC Press/Balkema.
- Todaro, C., Saltarin, S., & Cardu, M. (2022). Bentonite in two-component grout applications. *Case Studies in Construction Materials*, 1-14.
- Università di Torino. (2017, February 14). *Università di Torino: Progetti di edilizia universitaria*. Retrieved from Adeguamento normativo di Palazzo Campana: <https://www.unito.it/ateneo/strutture-e-sedi/sedi/piano-di-sviluppo-edilizio/progetti-di-edilizia-universitaria-0>
- Uriel, A., & Sagaseta, C. (1989). *General report/discussion session 9: Selection of design parameters for underground construction*. Madrid.
- Vermeer, P., & de Borst, R. (1984). Non-associated plasticity for soils, concrete and rock. *HERON vol. 29*, 1-62.
- Verruijt, A., & Booker, J. (1996). Surface settlements due to deformation of a tunnel in an elastic half plane. *Geotechnique* 46, 753-756.
- Working Groups 2 & 14 SIG. (2014). Thrust Force Requirements for TBM. In Società Italiana Gallerie, *Thrust Force Requirements for TBM* (p. 32). Milan: Società Italiana Gallerie.
- Yiu, W. (2018). *Finite Element Analysis of Short-Term and Long-Term Building Response to Tunnelling*. Oxford: [Doctoral dissertation]. University of Oxford.
- Zizi, M., Corlito, V., Lourenco, P., & De Matteis, G. (2021). Seismic vulnerability of masonry churches in Abruzzi region, Italy. *Structures* 32, 662-680.

# Appendix A

## Geotechnical studies near Piazza Carlo Alberto

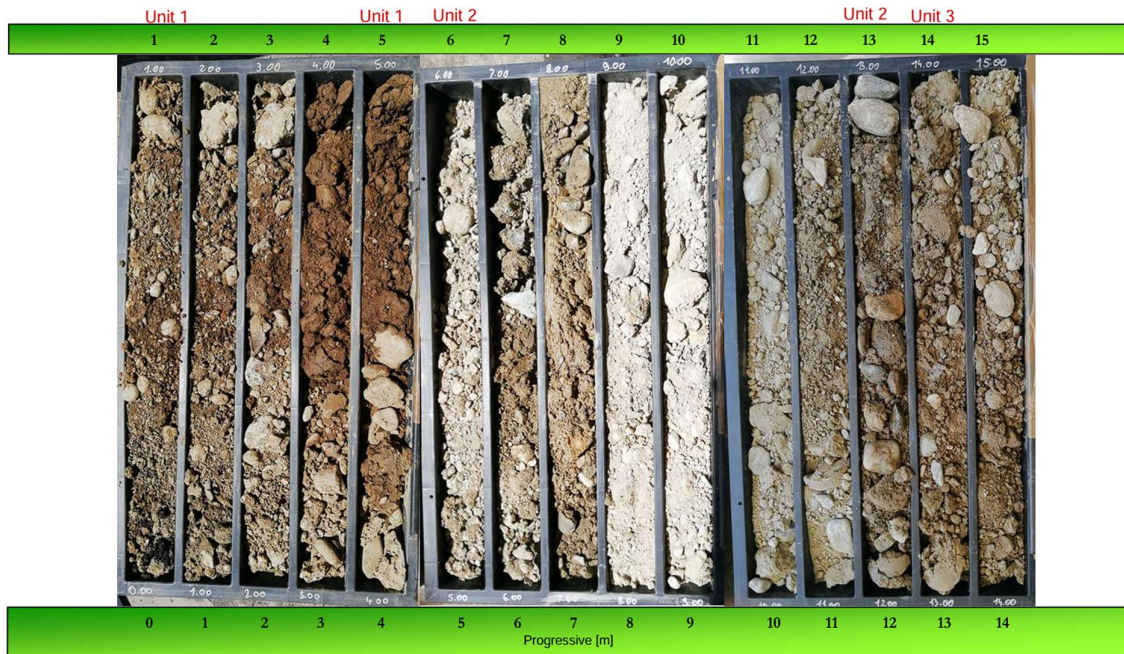
### A.1 SP-D12 stratigraphy, courtesy of Infratrasporti.To S.r.l. (2024)

 Veri 7.5.4 rev. 00 RILIEVO STRATIGRAFICO DI PERFORAZIONE <small>UNI EN ISO 27475-1:2007 UNI EN ISO 14688-1:2003 e 14689-1:2004</small>		SONDAGGIO													
Committente: Infratrasporti.To srl Cantiere: Metropolitana Autom. di Torino - Linea 2 - Lotto 1- Subtratta Politecnico - Pozzo Verona Località: Via Maria Vittoria c/o n°7 - Torino Perforazione: inizio: 02/08/2021 fine: 04/08/2021 Sonda: Geomarc G1000A Merlo Coordinate: N= 45°4'3.75" E= 7°41'5.96" Scala 1: 130 Accettazione n. 21016 Certificato n. 21016/33 del 11/08/2021		Compressa n. 21016 Lo Sperimentatore Dr. A. Carlu Il Direttore del Laboratorio Dr. Paolo Giorgio Sola													
		SP-D12 Pagina 1 di 1													
Profondità dal p.c. [m]	potenza dello strato [m]	sezione stratigrafica	descrizione litologica	falda	metodo e diam. di perforazione	diametro rivestimenti	percentuale di carotaggio	piezometro tubo aperto	inclinometro	S.P.T.	pocket penetrometer	pocket vane test	campioni indurimenti	campioni rimarraggiati	permeabilità [m/s]
0.00	0.15		Asfalto bituminoso.												
0.15	1.35		Terreno di riporto ghiaioso-sabbioso con subordinati frammenti lateritici.												
1.50	3.50		Ghiaia eterometrica con sabbia siltosa a tratti abbondante, ciottolosa (diam max 13-15 cm), da moderatamente addensata ad addensata, colore nocciola-brunastro. <b>As interpreted in 4.11 GEOTECNIA E SISMIKA, #02 Unit 1</b>							3.00 10-13-12 PC				3.00 CR1 3.50	
5.00	6.80		Ghiaia eterometrica con sabbia siltosa a tratti prevalente, ciottolosa (diam max 10-11 cm), da addensata a molto addensata con livelli cementati, colore grigio-nocciola. <b>Unit 2</b>							6.00 22-25-26 PC				6.00 CR2 6.50	
11.80	1.20		Ciottoli (diam max 13-15 cm) e ghiaia eterometrica in matrice sabbioso-debolmente limosa, molto addensata con livelli debolmente cementati, colore grigio-nocciola. <b>Unit 2</b>							9.00 R (1cm) PC				9.00 CR3 9.50	
13.00	12.30		Ghiaia eterometrica con sabbia debolmente limosa talora abbondante e/o prevalente, ciottolosa (diam max 12-13 cm), molto addensata con livelli cementati, colore nocciola. <b>Unit 3</b>							12.00 R (5cm) PC				12.00 CR4 12.50	
17.55										15.00 39-R (4cm)PC				15.00 CR5 15.50	
18.00										18.00 35-R (7cm)PC				18.00 CR6 18.50	
21.00										21.00 17-25-30 PC				21.00 CR7 21.50	
22.50										24.00 18-27-28 PC				24.00 CR8 24.50	
25.30	1.70		Ghiaia eterometrica in matrice sabbioso-debolmente limosa, talora limosa a livelli prevalente, debole alterazione talora discreta, molto addensata, colore nocciola-grigiastro. <b>Unit 2</b>							27.00 R (1cm) PC				27.00 CR9 27.50	
27.00	2.50		Ghiaia eterometrica con sabbia debolmente limosa a tratti abbondante, rari ciottoli, molto addensata con livelli cementati, talora intensamente (28.30m), colore nocciola. <b>Unit 2</b>							30.00 26-37-R (6cm)PC				30.00 CR10 30.50	
29.50	5.50		Alternanza di passate pluridecimetriche di ghiaia eterometrica con sabbia debolmente limosa e subordinati ciottoli generalmente molto addensate con livelli cementati, con analoghe passate intensamente alterate ed ossidate molto addensate, colore nocciola con screziature ocracee d'ossidazione. <b>Unit 4</b>							33.00 R (5cm) PC				33.00 CR11 33.50	

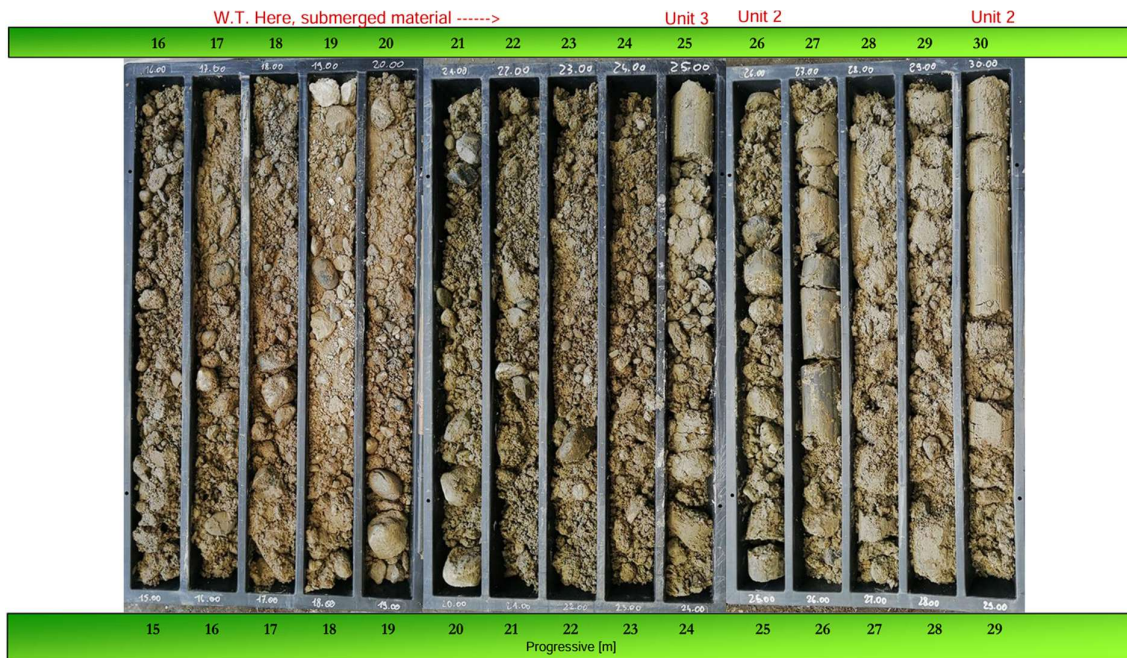
Coordinate Gauss Boaga 4391332.84N, 1395504.56E; quota 236.8 m s.l.m.  
 Il foro di sondaggio è stato attrezzato per tutta la sua lunghezza con tubo piezometrico in PVC del diametro di 2" con tratto fenestrato compreso tra -15.00m e -35.00m dal p.c.  
 PA - prove SPT a punta aperta. PE - prove SPT a punta chiusa.  
 Deposito cassotto: magazzino comunale in corso Orbassano n°444 - Torino



## A.2 Details of the samples from the SP-D12 stratigraphic borehole



Cassette 1-3 da 0.00 m a 15.00 m da p.c.



Cassette 4-6 da 15.00 m a 30.00 m da p.c.



Cassetta 7 da 30.00 m a 35.00 m da p.c.





A.4 SP-D13 stratigraphy, courtesy of Infratrasporti.To S.r.l. (2024)

 <p>Decreto di autorizzazione n. 4965 del 04/08/2010 per esecuzione e certificazione di indagini geotecniche e prove in sito ai sensi dell'art. 59 del D.P.R. n. 380/01</p>	Mod. 7.5.4 rev. 00	RILIEVO STRATIGRAFICO DI PERFORAZIONE	UNI EN ISO 22475-1:2007 UNI EN ISO 14583-1:2000 e 14689-1:2004	SONDAGGIO
	Committente	Infratrasporti.To srl		<b>SP-D13</b>
	Cantiere	Metropolitana Autom. di Torino - Linea 2 - Lotto 1-Subtratta Politecnico-Pozzo Verona		Pagina 1 di 1
	Località	Piazza Carlo Alberto - Torino	Commessa n. 21016	
Perforazione	inizio: 06/08/2021 fine: 10/08/2021	Sonda: Geomarc G1000A Merlo	Lo Sperimentatore Dr. A. Carlu	Il Direttore del Laboratorio Dr. Geol. Giorgio Sola
Coordinate:	N= 45°4'8.37" E= 7°41'11.42"	Scala 1: 130	<i>Dr. A. Carlu</i>	<i>Dr. G. Sola</i>
Accettazione n. 21016	Certificato n. 21016/37	del 11/08/2021		

profondità dal p.c. [m]	potenza dello strato [m]	sezione stratigrafica	descrizione litologica	felda	miscele e diam. di perforazione	diámetro rivestimenti	percentuale di carotaggio	piezometro tipo Casagrande	incinometro	S.P.T.	procket penetrometer	procket vane test	campioni indisturbati	campioni rimaneggiati	permeabilità [m/s]
0.00	0.10		Cotica erbosa.												
0.10	3.10		<b>Terreno di riporto</b> limoso-debolmente sabbioso con subordinata ghiaia fine e frammenti minuti lateritici, poco consistente, colore bruno-nocciola. <b>As interpretet in 4.11 GEOTECNIA E SISMICA, #02</b> <b>Unit 1</b>							3.00 7-7.8 FA			3.00 CR1 3.50		
3.20	0.70		Terreno di riporto limoso-argilloso con sporadica ghiaia fine e rari frammenti minuti di laterizio, poco consistente, colore bruno.							6.00			6.00 CR2 6.50		
3.90	0.45		Terreno rimaneggiato limoso-argilloso con sporadici frammenti lateritici minuti, colore nocciola-brunastro.							9.00			9.00 CR3 9.50		
4.35	1.25		Ghiaia eterometrica in matrice da limoso-debolmente argillosa a sabbioso-limoso con la profondità, da intensa a discreta ossidazione, moderatamente addensata, colore da nocciola-brunastro con screziature ocracee d'ossidazione a nocciola-grigiastro.							12.00 R (4cm) PC			12.00 CR4 12.50		
5.60	17.40		<b>Ghiaia eterometrica</b> in matrice <b>sabbioso-siltosa</b> a tratti abbondante e/o prevalente, <b>ciottolosa</b> (diam max 13-15 cm), <b>da addensata a molto addensata</b> con subordinati <b>livelli cementati</b> , colore grigio-nocciola. <b>Unit 2</b>							15.00 25-31-R (3cm)PC			15.00 CR5 15.50		13.50 <b>2.42E-05</b>
										18.00 28 <b>32-34</b> PC			18.00 CR6 18.50		15.00
							60-100 %			21.00 35-R (7cm)PC			21.00 CR7 21.50		<b>3.27E-05</b>
23.00	2.20		<b>Ghiaia eterometrica con sabbia debolmente limosa, rari ciottoli, molto addensata con livelli cementati, colore nocciola.</b> <b>Unit 2</b>							24.00 R (5cm)PC			24.00 CR8 24.50		
25.20	4.80		<b>Ghiaia eterometrica</b> in matrice <b>sabbioso-debolmente limosa</b> a livelli prevalente, <b>rari ciottoli, molto addensata</b> con subordinati <b>livelli debolmente cementati</b> , colore nocciola. <b>Unit 2</b>							27.00 20- <b>21-24</b> PC			27.00 CR9 27.50		
30.00	1.30		<b>Ghiaia eterometrica con sabbia debolmente limosa, subordinati ciottoli, molto addensata con livelli cementati, colore nocciola.</b> <b>Unit 2</b>							30.00 31-39-R (4cm)PC			30.00 CR10 30.50		
31.30	2.00		<b>Ghiaia eterometrica</b> in matrice <b>sabbioso-debolmente limosa</b> a livelli prevalente, <b>rari ciottoli, molto addensata</b> con subordinati <b>livelli debolmente cementati</b> , colore nocciola. <b>Unit 2</b>							33.00 33-R (4cm) PC			33.00 CR11 33.50		
33.30	2.80		<b>Ghiaia medio-fine</b> in matrice <b>sabbioso-limoso</b> a livelli prevalente, <b>rari ciottoli</b> , discreta ossidazione ed alterazione, <b>molto addensata</b> , colore nocciola con deboli screziature ocracee d'ossidazione. <b>Unit 2B</b>							36.00 R (2cm)PC			36.00 CR12 36.50		
36.10	3.90		<b>Ghiaia prevalentemente medio-fine con sabbia debolmente limosa</b> a tratti abbondante, <b>rari ciottoli</b> , debole ossidazione, <b>molto addensata</b> , colore nocciola. <b>Unit 2</b>							39.00 37-R (2cm) PC			36.00 CR13 36.50		
40.00													39.00 CR13 39.50		

Coordinate Gauss Roma 4991473.43N, 1306625.48E; quota 236.6 m s.l.m.  
 Nel foro di sondaggio è stata installata una cella Casagrande alla profondità di 39.50m dalla quale si dipartono due tubi piezometrici ciechi rispettivamente del diametro di 1"1/2 e 1/2".  
 PA : prova Spt a punta aperta. PC : prova Spt a punta chiusa.  
 Deposito cassette : magazzino comunale in corso Orbassano n°444 - Torino

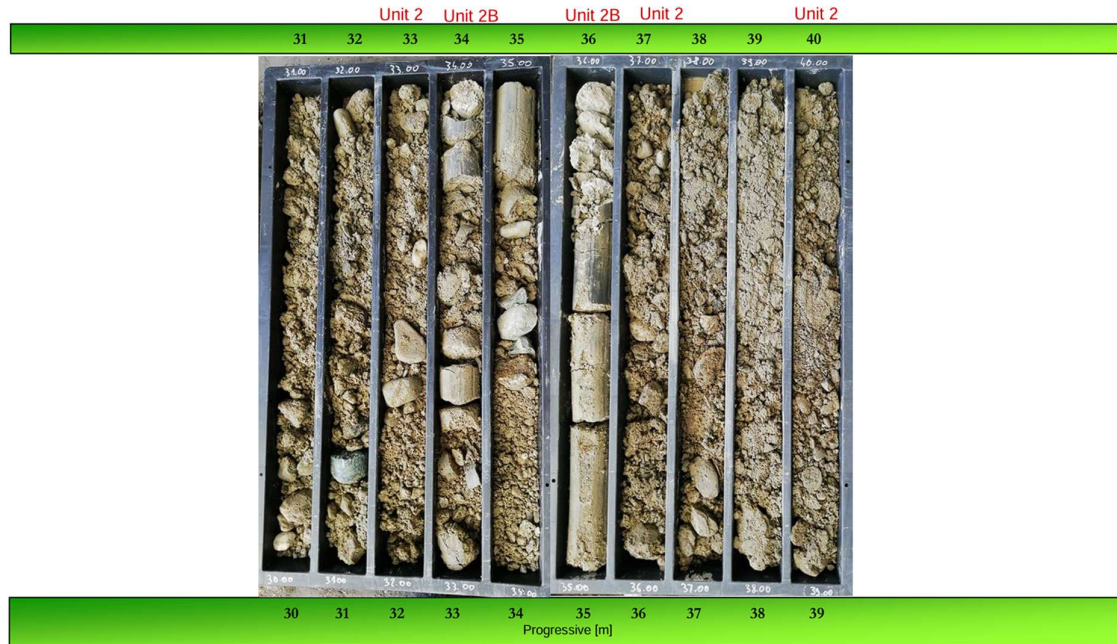
### A.5 Details of the samples from the SP-D13 stratigraphic borehole



Cassette 1-3 da 0.00 m a 15.00 m da p.c.



Cassette 4-6 da 15.00 m a 30.00 m da p.c.



Cassette 7-8 da 30.00 m a 40.00 m da p.c.





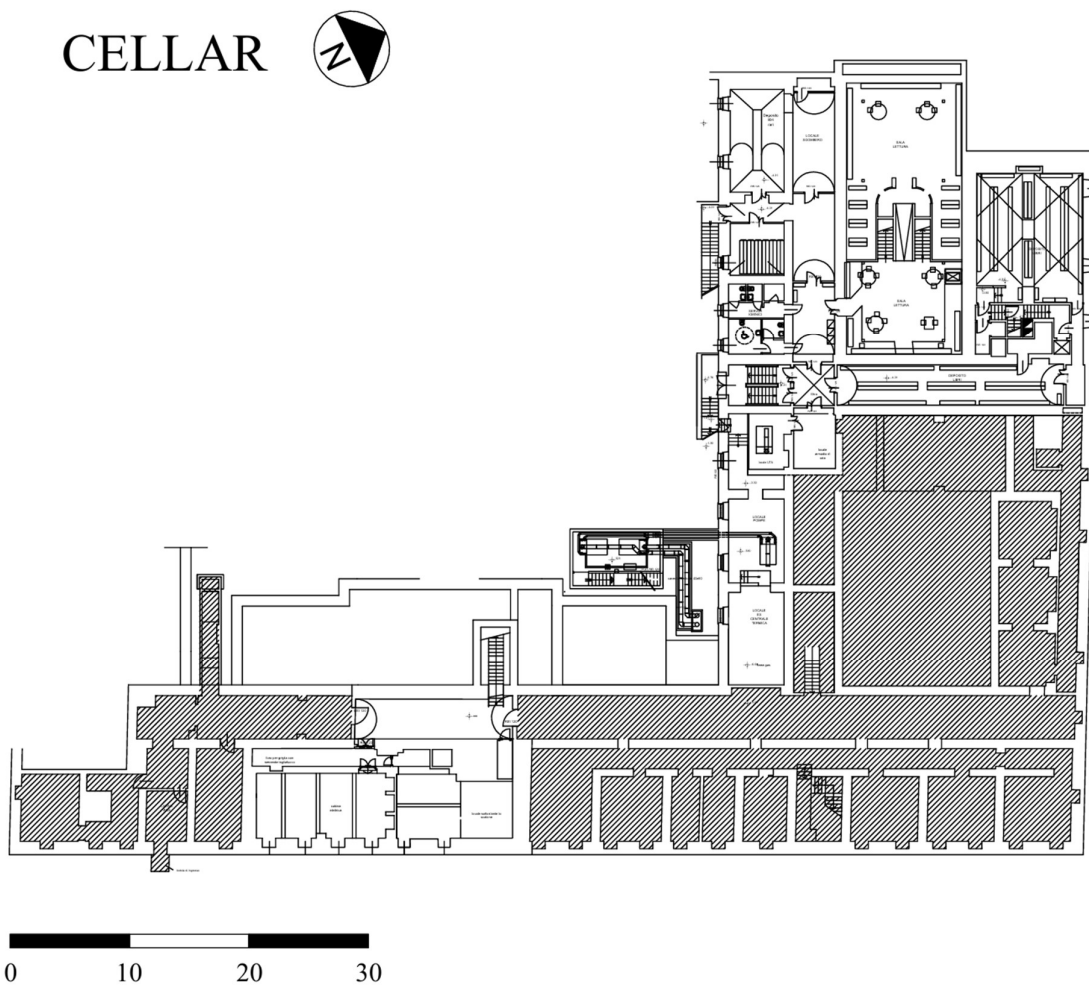


## Appendix B

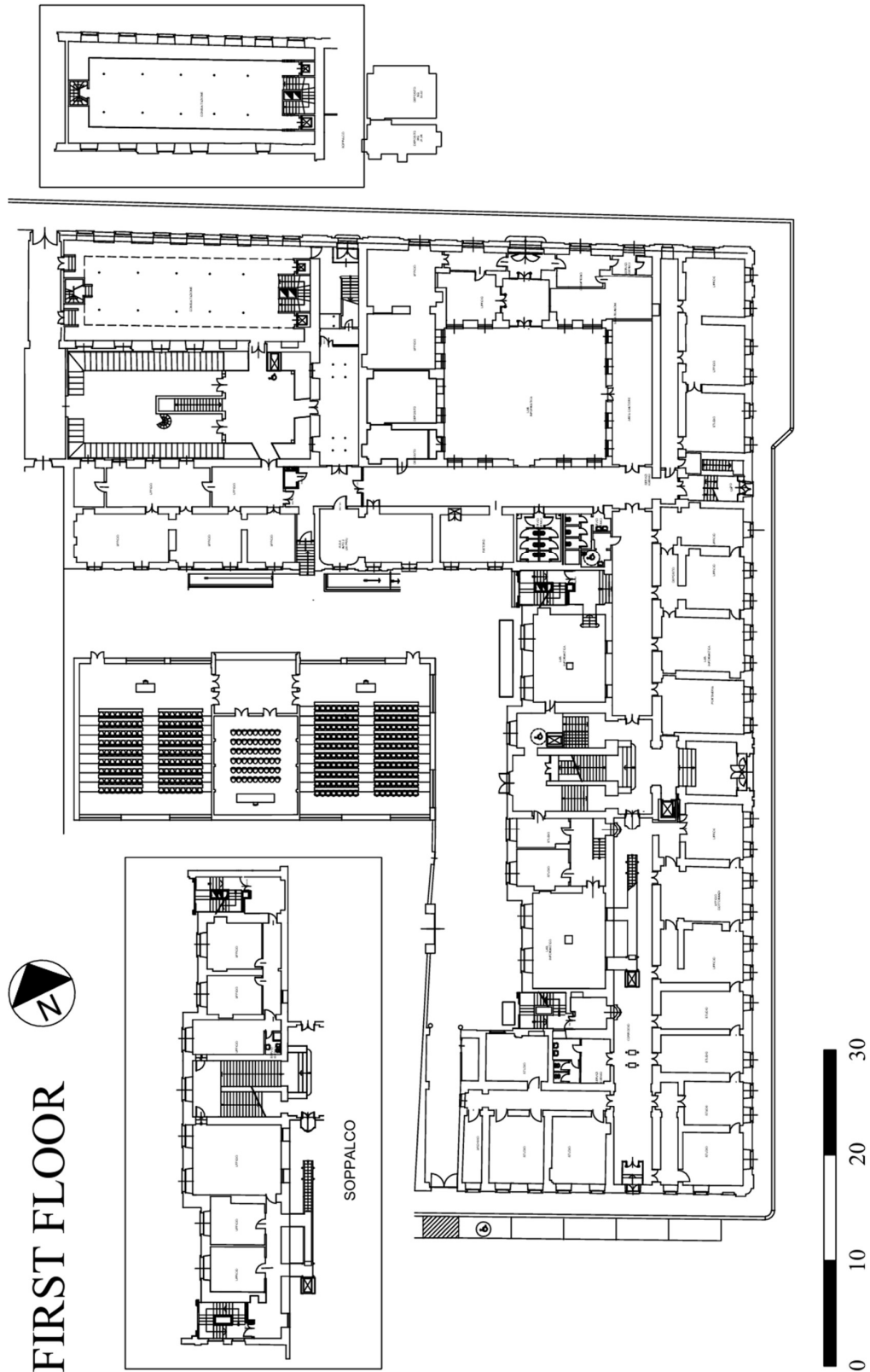
### Blueprints of Palazzo Campana

The blueprints are courtesy of the Building and Sustainability Directorate of the Università degli Studi di Torino.

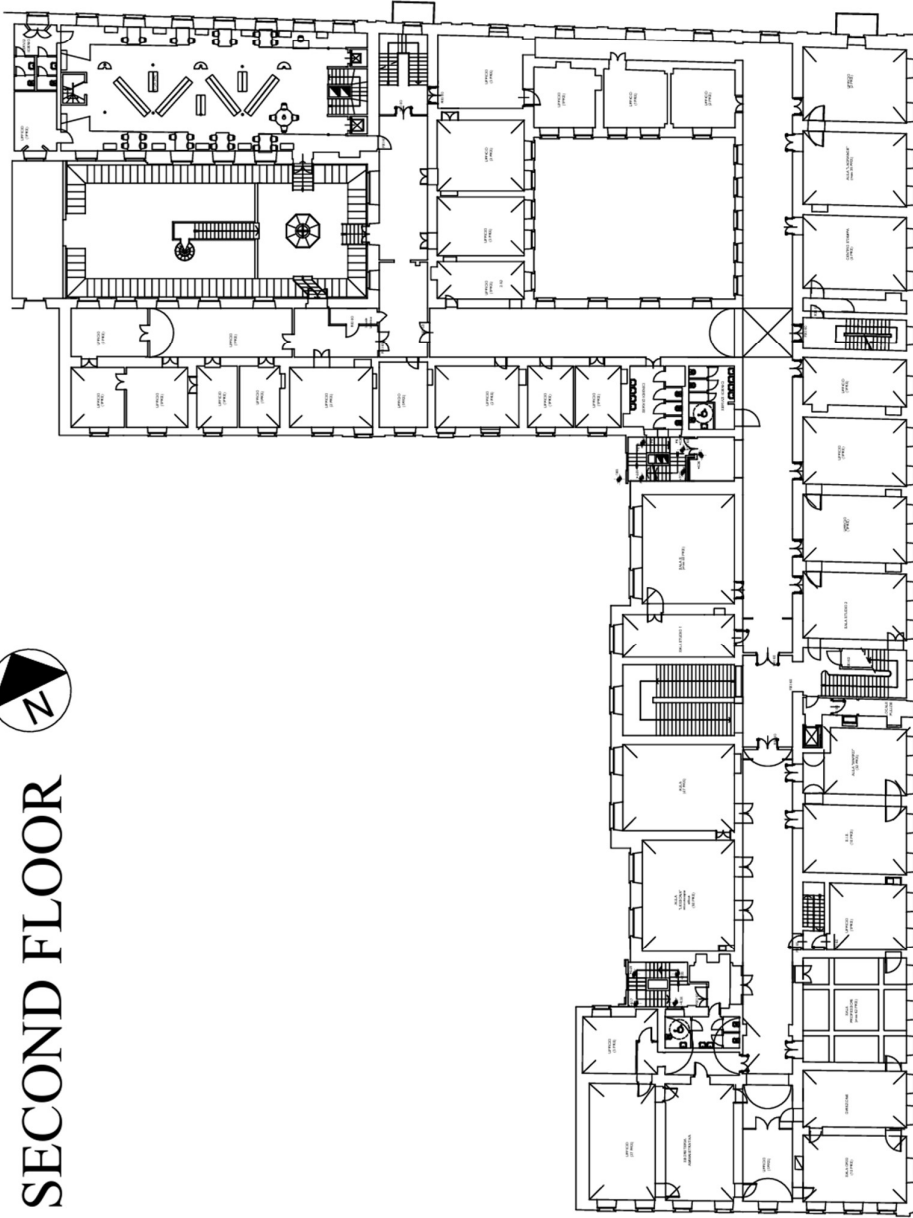
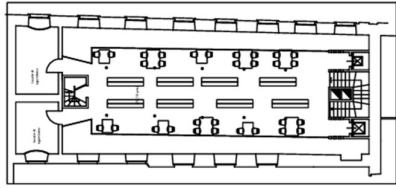
#### B.1 Cellar, top view



### B.2 First floor, top view



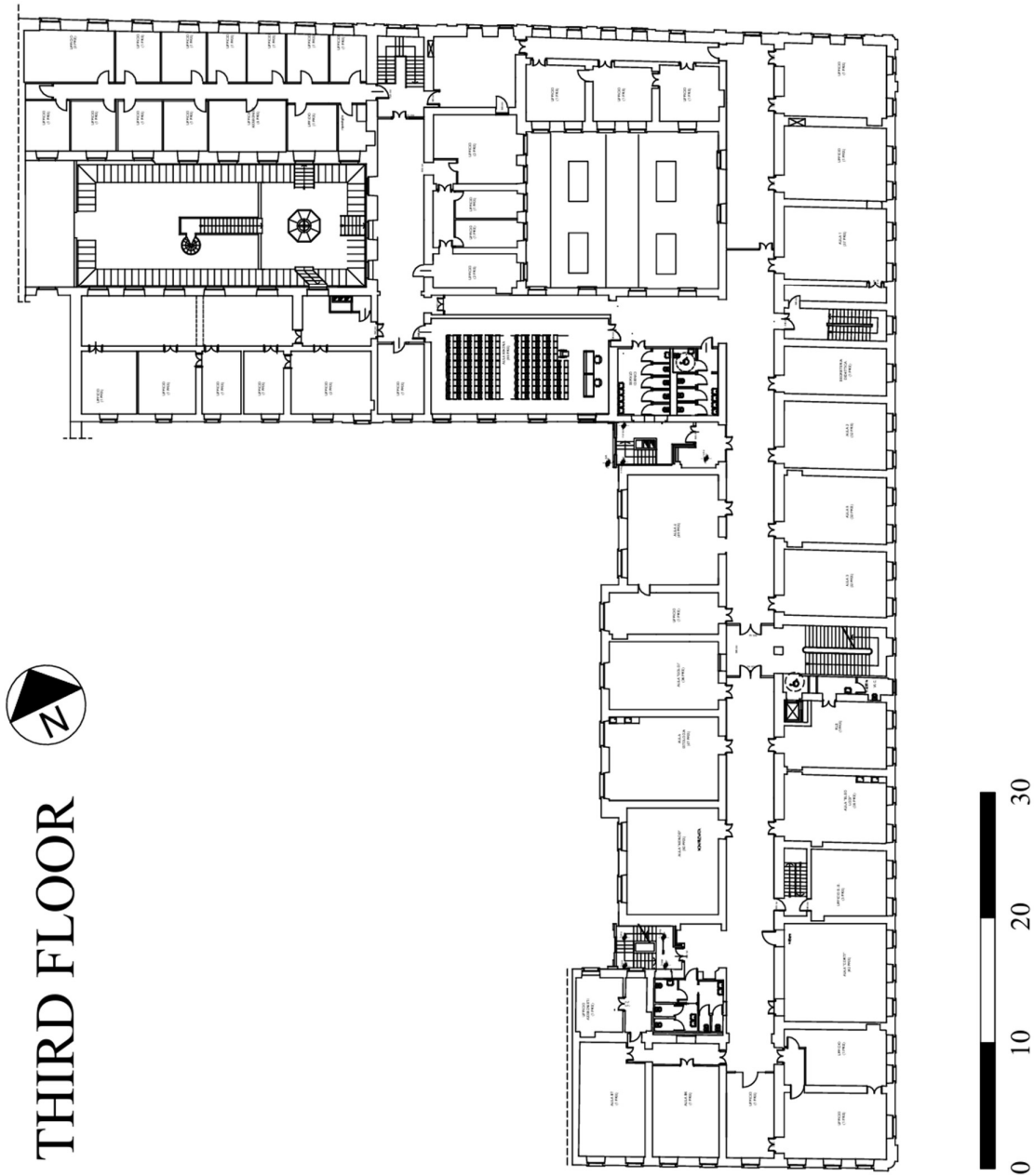
### B.3 Second floor, top view



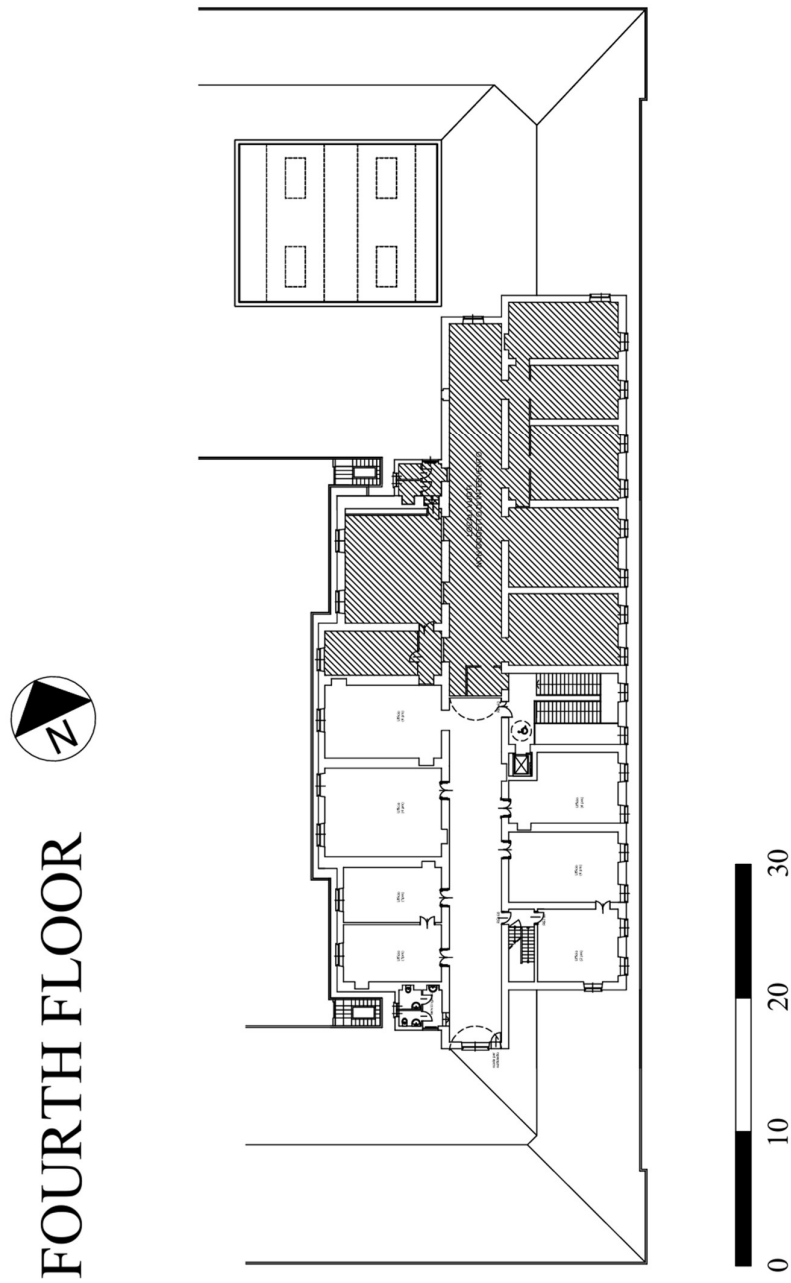
SECOND FLOOR



**B.4 Third floor, top view**

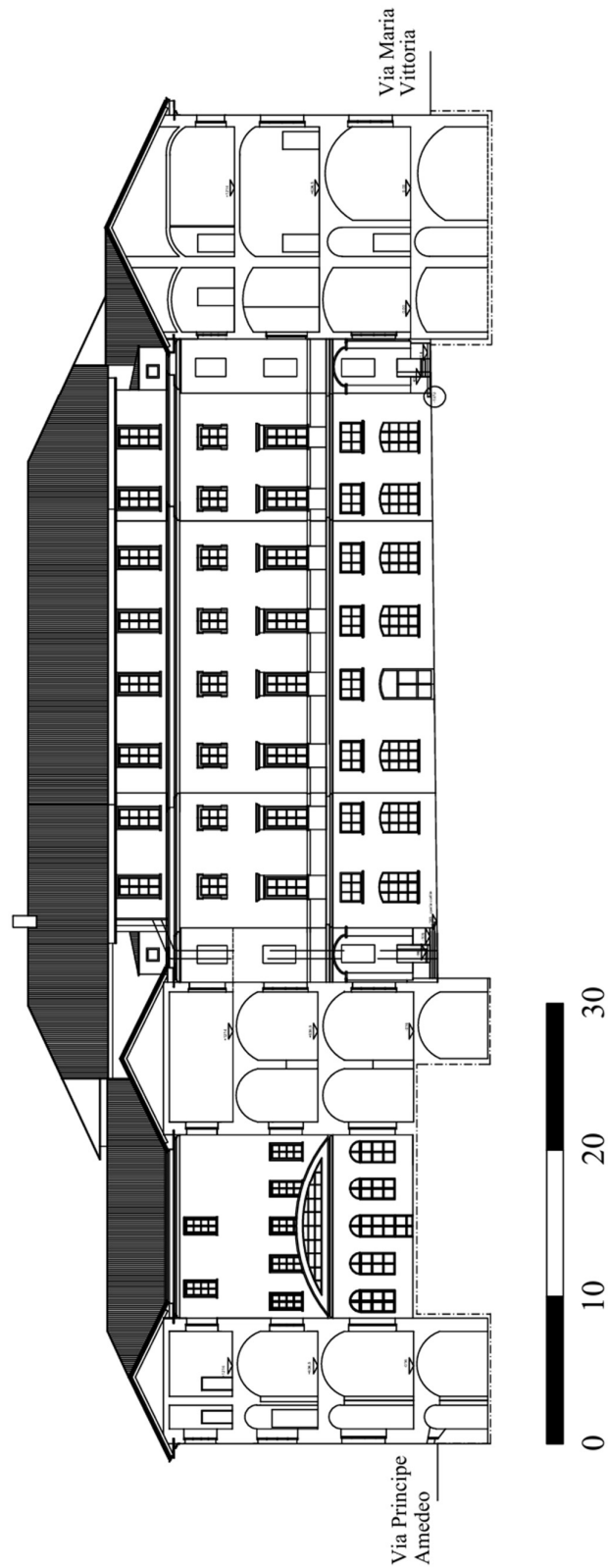


**B.5 Fourth floor, top view**



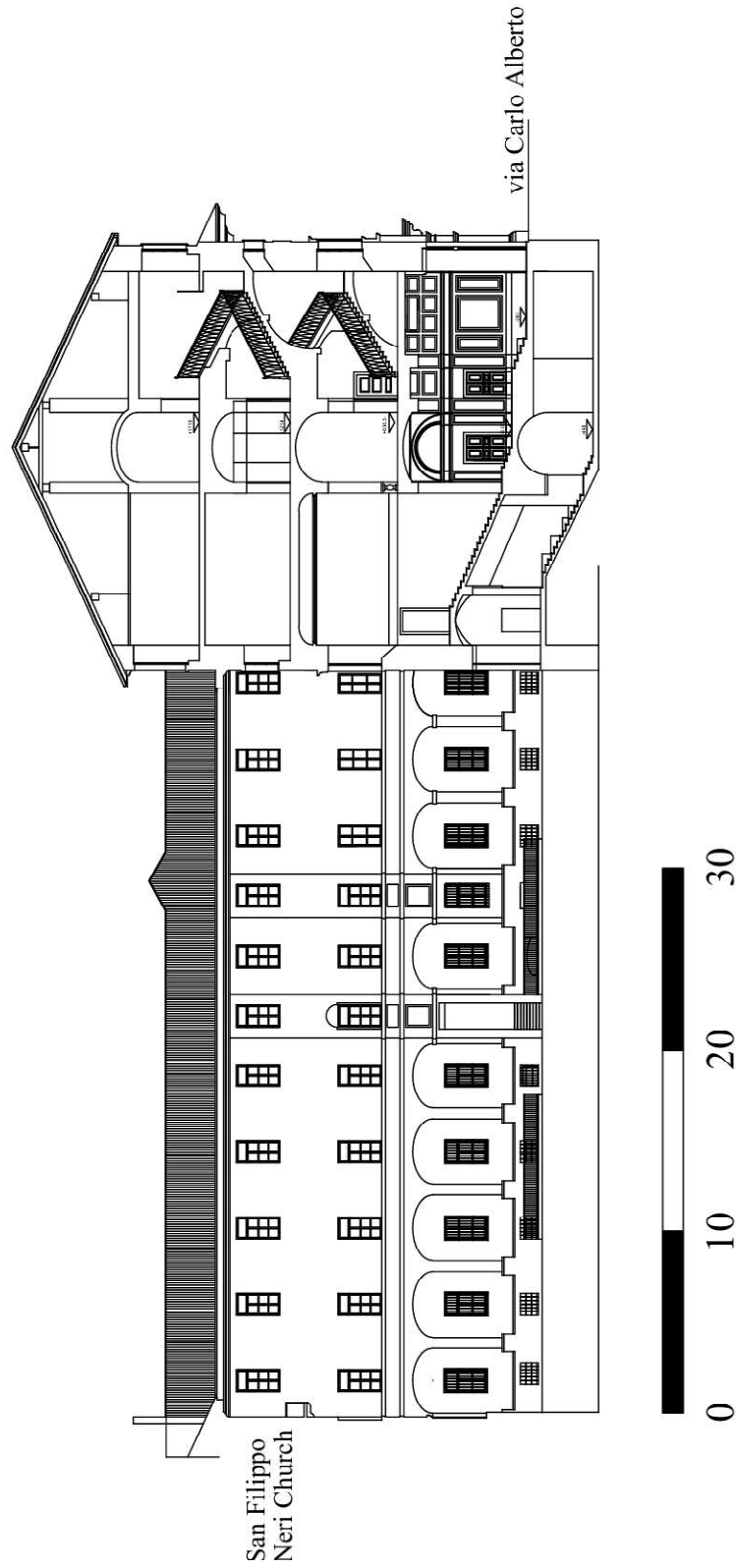
**B.6 Interior courtyard elevation, Via Carlo Alberto wing**

**Interior courtyard elevation, Via Carlo Alberto wing**



**B.7 Interior courtyard elevation, Via Principe Amedeo wing**

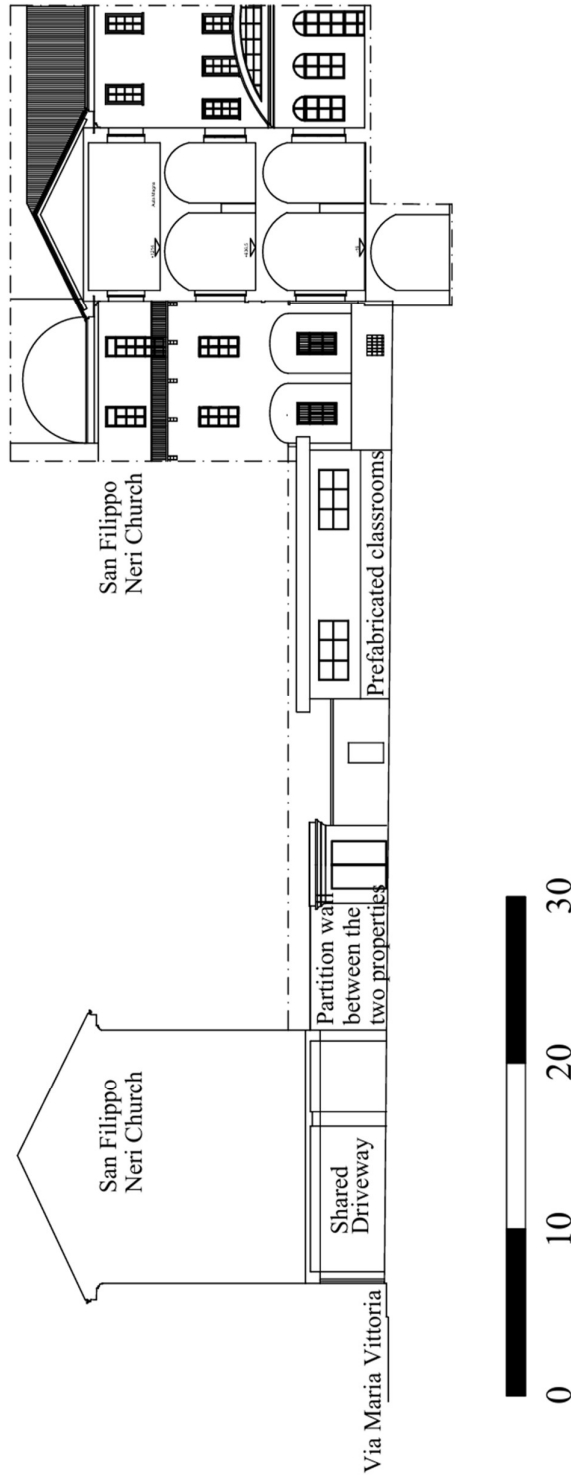
Interior courtyard elevation, Via Principe Amedeo wing





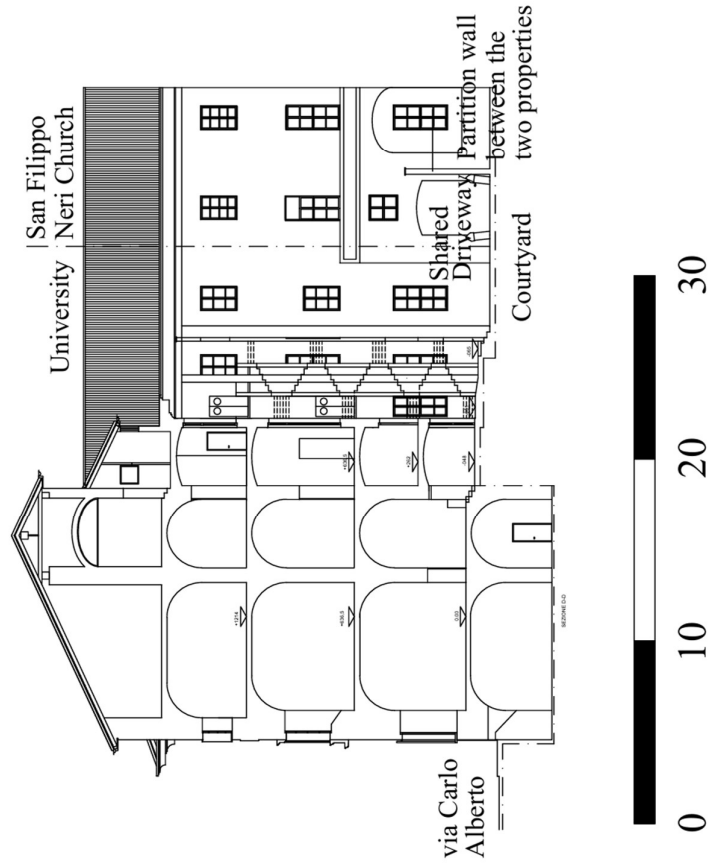
**B.8 Interior courtyard elevation, Via Accademia delle Scienze wing**

Interior courtyard elevation, Via Accademia delle Scienze wing



**B.9 Interior courtyard elevation, Via Maria Vittoria**

**Elevation, Via Maria Vittoria wing**



# Appendix C

## Building risk of damage assessment

### C.1 Empirical assessment for Palazzo Campana (PNCA43) with a volume loss of 1.0%, courtesy of Infratrasporti.To (2024)

DATI INPUT EDIFICIO		
<b>Codice Edificio</b>	[ID]	<b>PNCA43</b>
Progressiva	[pk]	8+850
Ubicazione		Via Carlo Alberto n. 8 - n. 10, Via Principe Amedeo n. 8 - n. 10, Via In asse galleria
Indice di vulnerabilità "Iv"	Breve termine	<b>76</b>
	Lungo termine	<b>69</b>
Fattore di riduzione categorie di danno	"Fr"	<b>1,75</b>
Tipo struttura [2]		M/C **
Destinazione d'uso		Università di Torino
Presenza di fratture		SI
Grado di conservazione		Mediocre
Altezza rispetto al p.c	[m]	22,83
Profondità fondazioni al di sotto del p.c	[m]	12,95
Numero di piani fuori terra	[n°]	5
Numero di piani interrati [n°]	[n°]	2
Lunghezza edificio L <sub>2</sub> [3]	[m]	33
Distanza bordo dall'asse x1	[m]	-66,00
Distanza bordo dall'asse x2	[m]	5,40
Quota sotterraneo	[m]	223,16
Quota asse galleria	[m]	211,10
Copertura rispetto a calotta galleria [4]	[m]	7,06
Rapporto moduli di deformazione [5]	E/G	12,5
SPOSTAMENTI E DISTORSIONI ANGOLARI		
Diametro di scavo galleria	[m]	10,00
Parametro di forma K	[-]	0,40
Volume perso Vp	[%]	1,00%
Perdita di volume	[m³/m]	78,54
Distanza flesso "f"	[m]	4,82
Picco curva subsidenza (in green field)	[mm]	65
Lunghezza max area di Hogging "Bh <sub>max</sub> "	[m]	7,2
Lunghezza area di Sagging "Bs"	[m]	9,6
Cedimento massimo Edificio "Smax"	[mm]	65
Distorsione angolare massima (1/β)	[-]	122
Spostamento orizzontale max. "Umax"	[mm]	15,78
Def orizzontale max in Hogg eh <sub>h</sub> [6]	[%]	0,178
Def orizzontale max in Sagg eh <sub>s</sub> [7]	[%]	0,000
CATEGORIA DI DANNO		
Deformaioni orizzontali (con ε <sub>n</sub> ≠ 0)		
Def. di trazione max hogg ε <sub>max,h</sub>	[%]	0,2119
Def. di trazione max sagg ε <sub>max,s</sub>	[%]	0,2794
<b>Valutazione del danno:</b>	<b>Pericolo a molto grave</b>	<b>4</b>
Deformaioni orizzontali (con ε <sub>n</sub> = 0)		
Def. di trazione max hogg (%)		0,0943
Def. di trazione max sagg (%)		0,2794
<b>Valutazione del danno:</b>	<b>Pericolo a molto grave</b>	<b>4</b>

Planimetria con edifici interferenti

Foto edificio PNCA43

Grafico curva di subsidenza e deformazioni edificio (sez. perpendicolare ad asse galleria)

--- curva subsidenza  
— Sagging  
— Hogging  
... Punto di flesso

Determinazione classe di danno

Indice di vulnerabilità dell'edificio	Basso		Medio		Alto	
	0 < Iv < 20	20 < Iv < 40	40 < Iv < 60	60 < Iv < 80	80 < Iv < 100	Iv > 100
Fattore di riduzione	Fr = 1.00	Fr = 1.25	Fr = 1.50	Fr = 1.75	Fr = 2.00	
Parametro di controllo	ε <sub>max</sub> [%]		ε <sub>max</sub> [%]		ε <sub>max</sub> [%]	
	min	max	min	max	min	max
0	0.000	0.050	0.000	0.040	0.000	0.033
1	0.050	0.075	0.040	0.060	0.033	0.050
2	0.075	0.150	0.060	0.120	0.050	0.100
3	0.150	0.300	0.120	0.240	0.100	0.200
4	> 0.300	> 0.240	> 0.200	> 0.171	> 0.150	> 0.125

ε<sub>max</sub> [%] color scale: 0.00 (green) to 0.279 (red)

**Legenda:**  
 [1] \*: Posizione rispetto alla direzione di avanzamento della TBM  
 [2] \*\*: [C]=cemento armato, [M]=muratura, [M/C]=struttura mista  
 [3] Dimensione nella direzione perpendicolare all'asse della galleria  
 [4] Copertura in calotta rispetto alla quota fondazione  
 [5] 12.5 per fabbricati in c.a. o misti e 2.6 per fabbricati in muratura  
 [6] Def. orizzontale max in Hogg calcolata tra i bordi dell'edificio  
 [7] Def. orizzontale max in Sagg posta pari a 0 a vantaggio di sicurezza